



Università degli Studi di Trieste

Sede Amministrativa del Dottorato di Ricerca

Facoltà di Scienze Matematiche, Fisiche e Naturali

XXIII Ciclo del Dottorato di Ricerca in FISICA

II Ciclo delle Scuole

**Study of the strange resonance Σ (1385)
as a tool for the analysis of the dynamics
of the Quark Gluon Plasma in the
ALICE experiment at LHC**

(Settore scientifico-disciplinare: FIS/04 FISICA NUCLEARE E SUBNUCLEARE)

Dottorando:

Massimo VENARUZZO

Coordinatore del Collegio dei Docenti:

Prof. **Paolo CAMERINI**

Firma: _____

Relatore e Tutore:

Dott. **Giacomo-Vito MARGAGLIOTTI**

Firma: _____

Anno Accademico 2009/2010

mail to:

massimo.venaruzzo@ts.infn.it



Marzo 2011. Dipartimento di Fisica, Trieste.

Alla mia famiglia

Ad Elisa

Riassunto

La presente tesi si basa sul lavoro da me effettuato nell'ambito della collaborazione ALICE. L'obiettivo scientifico principale dell'esperimento é quello di investigare le proprietà della materia fortemente interagente fino alle elevatissime densità di energia (> 10 GeV/fm³) e temperatura ($\gtrsim 0.2$ GeV) che verranno fornite da LHC e che ci si aspetta caratterizzino il mezzo formato nelle collisioni tra ioni pesanti a questi regimi. Calcoli di Cromo Dinamica Quantistica (QCD) su reticolo prevedono che in tali condizioni, il confinamento dei quark in adroni privi di carica di colore scompaia e si formi un plasma di quark e gluoni, denominato Quark-Gluon Plasma (QGP). Nelle ultime due decadi, numerose indicazioni della formazione di questo stato della materia sono state osservate negli esperimenti al CERN-SPS ($\sqrt{s_{NN}} = 17.3$ GeV) e al BNL-RHIC ($\sqrt{s_{NN}} = 200$ GeV). ALICE, quindi, grazie alle energie con cui opera e potrà operare in futuro, aprirà una porta in un regime totalmente nuovo e sinora inesplorato nel campo della fisica delle interazioni forti.

Il primo capitolo della tesi descrive per linee generali i fondamenti della QCD descrivendo le basi della fisica del Plasma di Quark e Gluoni. Si sofferma quindi nella descrizione di grandezze caratteristiche del tipo di fisica sotto esame e delle osservabili (*probes*) che possono testimoniare la comparsa del QGP nelle collisioni fra ioni pesanti, con attenzione particolare riguardo a quelle legate alla produzione di stranezza. Vengono inoltre illustrati alcuni dei risultati principali ottenuti dagli esperimenti all'SPS e a RHIC nonché alcune delle primissime misure effettuate da ALICE.

Nel secondo capitolo é presentata una breve descrizione della macchina LHC seguita da un'ampia panoramica delle varie componenti del rivelatore ALICE, delle rispettive prestazioni, nonché del framework di calcolo messo a punto per la gestione e l'analisi dell'enorme mole di dati prodotti dall'esperimento.

Il terzo capitolo approfondisce in maniera più specifica uno degli aspetti più rilevanti della fisica studiata da ALICE, ovvero la fisica delle risonanze strane quale strumento per lo studio della evoluzione dinamica del QGP, in particolare durante la fase di raffreddamento. Tra le numerose risonanze strane oggetto di possibile indagine, alcuni modelli teorici conferiscono particolare rilevanza alla risonanza $\Sigma(1385)$ della quale verranno discusse le caratteristiche e gli studi che la concernono effettuati dall'esperimento STAR a RHIC.

Il quarto capitolo entra quindi nell'ambito specifico del lavoro svolto per questa tesi, ovvero lo studio della $\Sigma(1385)$ in ALICE, in collisioni protone-protone, nel canale di decadimento forte $\Lambda \pi$. Verranno dapprima illustrati gli studi effettuati su simulazioni protone-protone all'energia di 10 TeV nel centro di massa, realizzati al fine di mettere a punto la procedura di analisi. Saranno descritte la procedura implementata per l'estrazione del segnale, la valutazione del fondo ed il fit ai dati, nonché lo studio por-

tato avanti per l'ottimizzazione dei tagli implementati al fine di massimizzare il rapporto segnale su rumore e la valutazione delle incertezze sistematiche.

Il quinto ed ultimo capitolo illustrerà l'applicazione delle procedure descritte ai dati raccolti in collisioni protone-protone alle energie di 900 GeV e 7 TeV nel centro di massa, analisi fondamentale per il tuning dei modelli esistenti nonchè come riferimento per le analisi in collisioni piombo-piombo che non rientrano nell'ambito di questa tesi. I tagli applicati sono stati quindi nuovamente ottimizzati in modo da verificare la bontà del metodo messo a punto su dati simulati e sono state valutate le incertezze sistematiche. Il capitolo termina con l'illustrazione dei risultati ottenuti. Dapprima i valori di massa e larghezza estratti dalle distribuzioni integrali in massa invariante, riscontrati in accordo con i valori riportati nel Particle Data Book; poi gli spettri differenziali in funzione del momento e della massa trasversi opportunamente fittati. I risultati vengono infine confrontati sia con le simulazioni prodotte alla medesima energia realizzate sulla base di diversi modelli teorici sia, in via del tutto preliminare, con i risultati ottenuti da STAR a $\sqrt{s} = 200$ GeV.

Contents

Riassunto	i
Index	iii
Introduction	1
1 The Physics Of Relativistic Heavy-Ion Collisions	3
1.1 The Standard Model	4
1.1.1 The QCD	6
1.2 Phase Transition in QCD	8
1.2.1 Characteristics of QGP	10
1.2.2 Deconfinement and chiral symmetry restoration	11
1.3 The Lattice QCD predictions	11
1.4 The Bjorken Picture	12
1.5 The QGP Signatures	14
1.5.1 Particle multiplicity	16
1.5.2 Energy density estimation	19
1.5.3 Collective flow	20
1.5.4 Particle production	28
1.5.5 Electromagnetic probes: photons and dileptons	35
1.5.6 Heavy-quark and quarkonium production	36
1.5.7 High p_t and Jet Quenching	40
1.5.8 Identical Particle Interferometry	45
1.5.9 Chiral-Symmetry Restoration	45
1.5.10 Fluctuations	45
1.6 The Quark Gluon Plasma at the LHC	46
1.6.1 Hard partons at the LHC	48
1.6.2 Parton Distribution Functions at low Bjorken- x : nuclear shadowing effect	49
2 The ALICE Experiment at LHC	51
2.1 The Large Hadron Collider	52
2.1.1 The LHC Design Features	52

2.1.2	StartUp and Status	55
2.2	The ALICE Physics Program	56
2.3	Luminosity in Pb-Pb collisions	56
2.4	Dose rates and neutron fluences	57
2.5	The ALICE Detector Layout	58
2.5.1	The Central Barrel	62
2.5.2	The Muon Spectrometer	79
2.5.3	Forward, Trigger and Multiplicity Detectors	80
2.5.4	The Data Acquisition and The Trigger System	84
2.5.5	The ALICE Offline Software Framework	86
3	Strange Resonances As Heavy	
	Ions Physics Probe	93
3.1	Strangeness and QGP Freeze-Out Dynamics	93
3.2	Dynamical Freeze-Out Constraint with Resonances	97
3.3	Sigma(1385) Features	107
3.4	Sigma(1385) studies in the STAR Experiment	108
3.4.1	Invariant Mass Analysis	109
3.4.2	Spectra	110
3.4.3	Average Transverse Momentum	111
3.4.4	Particle Ratios	114
3.4.5	Nuclear Modification Factor	117
3.4.6	Time Scale for Au+Au collisions	118
4	$\Sigma(1385)$: Proton - Proton Simulations Analysis	121
4.1	Data Analysis Description	122
4.1.1	Event Selection	122
4.1.2	$\Sigma(1385)$ Candidates Selection	122
4.2	Data Reduction Description	125
4.2.1	Invariant Mass Distribution	125
4.2.2	Background Definition Techniques	125
4.2.3	Signal Extraction	128
4.2.4	Kinematical and quality Cuts	128
4.2.5	Systematic uncertainties evaluation	139
4.2.6	Transverse momentum and mass spectrum	140
4.2.7	Signal Significance	144
4.2.8	Dependence of mass and width from p_t	145
5	$\Sigma(1385)$: Proton - Proton Data	
	Analysis	149
5.1	900 GeV Data Analysis Description	149
5.1.1	Invariant Mass Distribution	149

5.1.2	Signal Extraction	151
5.1.3	Kinematical Cuts	151
5.1.4	Systematic uncertainties evaluation at $\sqrt{s} = 900$ GeV	155
5.1.5	Transverse momentum and mass spectrum	155
5.1.6	Signal Significance	164
5.1.7	Dependence of mass and width from p_t	165
5.2	7 TeV Data Analysis Description	166
5.2.1	Invariant Mass Distribution	166
5.2.2	Signal Extraction	166
5.2.3	Kinematical Cuts	168
5.2.4	Global Results	172
5.2.5	Systematic uncertainties evaluation at $\sqrt{s} = 7$ TeV	173
5.2.6	Transverse momentum and mass spectrum	175
5.2.7	Signal Significance	184
5.2.8	Dependence of mass and width from p_t	184
	Conclusions	189
	Bibliography	191
	Ringraziamenti	203

Introduction

This thesis work was carried out in the context of the ALICE collaboration. The ALICE (*A Large Ion Collider Experiment*) experiment [1, 2, 3] will study Pb-Pb collisions at the Large Hadron Collider (LHC) until the center of mass energy per nucleon pair $\sqrt{s_{NN}} = 5.5$ TeV, the highest ever reached. The main physics goal of the experiment is the creation and the investigation of the properties of the strongly-interacting matter in the conditions of high energy density (> 10 GeV/fm³) and high temperatures ($\gtrsim 0.2$ GeV), expected to characterize the medium formed in central heavy-ion collisions at these energies. Under these conditions, according to lattice Quantum Chromo Dynamics (QCD) calculations, quark confinement into colorless hadrons should fade and a deconfined Quark-Gluon Plasma (QGP) should be formed. In the past two decades, experiments at CERN-SPS ($\sqrt{s_{NN}} = 17.3$ GeV) and BNL-RHIC ($\sqrt{s_{NN}} = 200$ GeV) have gathered ample evidences for the formation of this state of matter. ALICE, therefore, thanks to the energies available now and in the next future, will open a door in a whole and completely unexplored new regime for the physics of the strong interactions.

The first chapter of this thesis describes at a general level the cornerstones of the QCD and of the Quark-Gluon Plasma physics. Then it concentrates on the description of the main quantities related to the topics under analysis and on the so-called *probes* of the creation of the QGP in heavy-ion collisions. Particular attention will be put on the strangeness production related probes. Moreover some of the most important results obtained by the experiments at SPS and RHIC will be presented together with the very first measurements performed by ALICE.

A very short description of the LHC machine and its features opens the second chapter followed by a wide overview of the ALICE detector and of its performances, in addition with a description of the computing framework built for the collection and the analysis of the huge amount of data provided by the experiment.

The third chapter will describe in more details one of the most relevant aspects of the physics studied by ALICE, i.e. the physics of the strange resonances as fundamental tool for the QGP dynamic evolution analysis, in particular during the freeze-out phase. Among them, some theoretical models consider much relevant the $\Sigma(1385)$. It will be described in detail, with particular attention to the studies performed on it by the STAR experiment at RHIC.

The forth chapter is dedicated to this specific topic, i.e. the $\Sigma(1385)$ study at ALICE in proton-proton collisions, in the strong decay channel $\Lambda \pi$. First of all the studies performed on simulated data at $\sqrt{s} = 10$ TeV will be described. They were realized in order to build a dedicated analysis procedure. The implemented method for the signal extraction, background evaluation and the data fit will be described together with the optimized cuts introduced in order to find an optimal set able to maximize the signal

over background ratio. Then the systematic uncertainties evaluation is presented.

The application of the described procedure to the data collected in proton-proton collisions at $\sqrt{s} = 900$ GeV and 7 TeV, is then presented in the fifth and last chapter. This analysis is crucial for the tuning of the existing models and is an important benchmark for the next lead-lead collisions analysis. A new cut optimization will be performed in order to check the consistence of the procedure built using the simulated data. The systematic uncertainties will be evaluated at both energies. The results obtained (both integral and differential in the transverse momentum) will be shown and discussed together with a comparison with some dedicated simulations provided at the same energy with different models and with a very preliminary comparison with the STAR results at $\sqrt{s} = 200$ GeV.

Chapter 1

The Physics Of Relativistic Heavy-Ion Collisions

The Standard Model is the theory of the elementary particles and their fundamental interactions. This theory includes the strong interactions due to the color charges of quarks and gluons and a combined theory of weak and electromagnetic interactions[4]. Proposed and developed since the 1960's, the Standard Model is today a well established theory applicable over a wide range of conditions: the high-energy physics has validated it and confirmed its predictions through a large variety of experiments. In this context, the relativistic heavy ions physics is aimed at the application of this theory to complex and evolving systems of finite size, in order to understand the relations between collective phenomena and the microscopic laws of elementary-particle physics. The collisions between relativistic heavy ions allow to study the nuclear matter under conditions of extremely high temperature and energy density. In these conditions, the Standard Model predicts that the nuclear matter undergo a new phase, where the quarks and the gluons are expected to be deconfined and to freely move. Lattice QCD calculations[5] predict for the new phase a critical temperature $T_c \simeq 170$ MeV, corresponding to a critical energy density $\epsilon_c \simeq 0.7$ GeV/fm³. This means the possibility to observe how the Universe was looking like about 10^{-6} seconds after the Big-Bang (Figure 1¹).

This phase transition toward this hot and dense state of matter should be accessible to experimental observations. Collisions of atomic nuclei have been studied for more than 20 years at sufficiently high energies to cross into the deconfined phase. The first attempts were done since 1986 with light nuclei at the Alternating Gradient Synchrotron (AGS) at the Brookhaven National Laboratory (BNL) and at the Super Proton Synchrotron (SPS) at CERN, with *Si* and *S* respectively. Then, in the early 1990's, the acceleration of heavy nuclei began at both facilities: *Au* at AGS and *Pb* at SPS. The center of mass energy per colliding nucleon-nucleon pair, ($\sqrt{s_{NN}}$), was 4.6 GeV at the AGS and 17.2

¹The Temperature is often expressed in eV instead of Kelvin. The conversion from eV to Kelvin is defined using the Boltzmann constant k_B : $\frac{1\text{eV}}{k_B} = \frac{1.60217653 \times 10^{-19} \text{J}}{1.3806505 \times 10^{-23} \text{J/K}} = 11604.505 \text{ K}$.

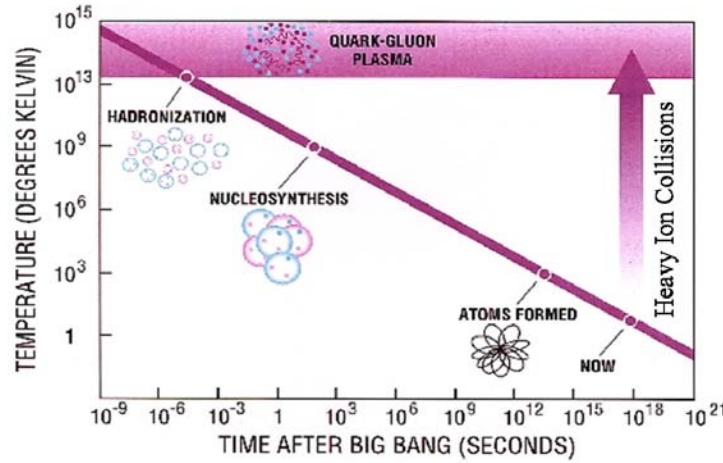


Figure 1.1: Evolution of the temperature of the Universe as a function of the time elapsed after the Big-Bang.

GeV at the SPS. Already in the late 1990's, at the CERN SPS, enough evidences were gathered to conclude that a new state of matter had been created. When the Relativistic Heavy Ion Collider (RHIC) went into operation at BNL, heavy-ion nuclei such as gold collided at a center of mass energy per nucleon-nucleon pair $\sqrt{s_{NN}} = 200$ GeV. The huge step in collision energy meant a much larger, hotter, longer living QGP “fireball” than at the SPS. Only with the LHC at CERN a similar (and even larger) step will be attained. Pb nuclei will collide at a center of mass energy of $\sqrt{s_{NN}} = 5.5$ TeV, about 30 times more than RHIC.

1.1 The Standard Model

The Standard Model describes the fundamental forces and the composition of matter. It is a gauge theory including the strong, weak, and electromagnetic forces and the related interactions; gravity is not part of the Standard Model and not further addressed. Matter is constituted out of point-like particles which having spin 1/2 and grouped into three families. Each family has two quarks and two leptons members (Table 1.1).

Leptons feel the weak force and the charged ones, the electromagnetic force. Quarks have a property called color playing the role of charge in the strong force. The color can take one out of three possible values (conventionally *red*, *green*, and *blue*). They do not appear freely, they are confined and appear in the form of hadrons that are colorless (also called *white*), i.e. in the corresponding SU(3)-algebra the colors of the constituent quarks sum to 0 (red + green + blue = white). Hadrons are grouped into baryons and mesons. Baryons consist of three quarks, qqq or $\bar{q}\bar{q}\bar{q}$ (e.g. the proton: uud). Mesons consist of two quarks, $q\bar{q}$ (e.g. the π^+ : $u\bar{d}$). Quarks feel the strong, weak, and electromagnetic forces. The forces are mediated by the exchange of gauge bosons, listed in Table 1.2 together with their relative coupling strengths.

Family	Quarks			Leptons		
	Name	Charge	Mass	Name	Charge	Mass
1	u	$2/3 e$	$1.7 - 3.3 \text{ MeV}/c^2$	e^-	$-e$	$0.511 \text{ MeV}/c^2$
	d	$-1/3 e$	$4.1 - 5.8 \text{ MeV}/c^2$	ν_e	0	$<2 \text{ eV}/c^2$
2	c	$2/3 e$	$1.27^{+0.07}_{-0.09} \text{ GeV}/c^2$	μ^-	$-e$	$106 \text{ MeV}/c^2$
	s	$-1/3 e$	$101^{+29}_{-21} \text{ MeV}/c^2$	ν_μ	0	$<0.19 \text{ eV}/c^2$
3	t	$2/3 e$	$172.0 \pm 1.6 \text{ GeV}/c^2$	τ^-	$-e$	$1.78 \text{ GeV}/c^2$
	b	$-1/3 e$	$4.19^{+0.18}_{-0.06} \text{ GeV}/c^2$	ν_τ	0	$<18.2 \text{ MeV}/c^2$

Table 1.1: Constituents of matter in the Standard Model[6].

Force	Strength	Gauge Boson(s)	Applies on
Strong force	1	8 Gluons (g)	Quarks, gluons
Electromagnetic force	$\simeq 10^{-2}$	Photon (γ)	All charged particles
Weak force	$\simeq 10^{-7}$	W^\pm, Z^0	Quarks, leptons
Gravitation	$\simeq 10^{-39}$	Gravitons	All particles

Table 1.2: Fundamental forces[6].

The strong force is mediated by gluons that have a color charge, and its theoretical framework is Quantum Chromo Dynamics (QCD). The Quantum Electro Dynamics (QED) describes the electromagnetic force, mediated by the exchange of photons. The weak force governed by the exchange of W^\pm 's and Z^0 's is described by the electroweak theory that includes the electromagnetic force. It has thus four gauge bosons (γ , W^\pm , and Z^0). The Standard Model has also, however, limitations that require extensions to keep the theory consistent. The most prominent example are the masses of the electroweak gauge bosons predicted to be zero within the theory. Something that is clearly inconsistent with experiment. This situation can be resolved by an additional gauge boson added to the theory, the Higgs boson[7]. The Higgs mechanism generates the masses for the W^\pm and the Z^0 while the γ remains massless. The puzzle about the existence of the Higgs boson is one of the topics addressed by the ATLAS and CMS experiments at the LHC.

1.1.1 The QCD

1.1.1.1 Historical Review

The strong interaction has been studied since the beginning of the 20th century soon after the discovery of the atomic nucleus. The existence of a binding force holding together the nucleons in the nuclei was postulated to assure nucleus stability. The discovery of the neutron and, later, of the pion provided a rather complete and satisfactory picture of the nucleus with the pion recognized as the long searched Yukawa particle of the strong interaction. Very early this turned out to be only a simplified picture of a small piece of what strong interaction concerns. Lots of new particles were produced in the experiments leading to a complete new scenario of both strong and weak interactions. The idea that the proton, as any strongly interacting particle (hadrons), were composed of more fundamental particles called *quarks*, emerged. Deep inelastic scattering experiments further clarified the quark structure of hadrons and the properties of strong interaction. The *quarks* exist in six different flavours and carry strong “colour” charge in three different types. The “mediators” of the strong force, playing the same role of the photon for electromagnetism, are called *gluons*, which come in eight colour combinations. A main difference with electromagnetism is that gluons do interact with each other while photons do not. The two main strong interaction features of interest for heavy-ion physics are:

- *Colour confinement*: “free” quarks have never been observed. Quarks are confined in particular “colourless” combinations inside hadrons.
- *Asymptotic freedom*: the value of the strong coupling constant, α_S , depends on the momentum transfer (Q^2) at which an observed process occurs (running coupling constant). α_S decreases with increasing energy and asymptotically, at infinite energy, tends to zero.

Another fundamental aspect concerns hadron masses: light mesons/baryons are mainly composed by two/three light quarks (u , d , s). However, summing the masses of the constituent quarks, only a small fraction of the hadron mass is obtained. For instance, the proton (uud) mass is $\sim 1 \text{ GeV}/c^2$ while the sum of the bare masses of its constituent quarks is $\leq 25 \text{ MeV}/c^2$. All these features are accomplished within the Quantum Chromo Dynamics theory of strong interaction described in the following section. This theory predicts that strong interaction properties in a complex system may differ from those observed in the vacuum. Quark confinement inside hadrons can disappear at energy densities higher than those typical of normal nuclear matter. The study of the modification of strongly interacting matter properties in a medium started relatively recently (in the 1970's).

1.1.1.2 The cornerstones of QCD

The QCD describes the interaction of quarks and gluons in the form of a gauge field theory, very similar to the way QED does for electrons and photons. In both cases we have spinor matter fields interacting through massless vector gauge fields. In QCD, however, the intrinsic colour charge is associated to the non-Abelian gauge group SU(3), in place of the Abelian group U(1) for the electric charge in QED. The quarks thus carry three colour charges, and the gluons, transforming according to the adjoint representation, carry eight different combinations of colours. The intrinsic charge of the gauge field (the gluon) is the decisive modification in comparison to QED; it makes the pure gluons system self-interactive, in contrast to the ideal gas of photons. As a result, the three-dimensional Laplace equation, which in non-relativistic QED leads to the Coulomb potential $V \sim 1/r$, for massive quarks becomes effectively one-dimensional, with the confining potential $V \sim r$ as the solution. The Lagrangian density of QCD is given by [8, 9]:

$$L = -\frac{1}{4}F_{\mu\nu}^a F_a^{\mu\nu} + \sum_f \bar{\psi}_\alpha^f (i\gamma_\mu D^\mu) \psi_\beta^f \quad (1.1)$$

with the non Abelian group tensor

$$F_{\mu\nu}^a = (\partial_\mu A_\nu^a - \partial_\nu A_\mu^a - gf_{bc}^a A_\mu^b A_\nu^c) \quad (1.2)$$

and

$$D_\mu = \partial_\mu + ig \frac{\lambda_a}{2} A_\mu^a \quad (1.3)$$

The fundamental degrees of freedom of the theory are the 3×6 quarks fermionic fields ψ and the eight gluonic fields A_μ . λ_a and f_{bc}^a are the eight SU(3) group generators (the 3×3 Gell-Mann matrices) and the structure constants. In the definition above, ψ represents, for each flavour, a vector $(\psi_{red}; \psi_{green}; \psi_{blue})$ of fermionic fields. Being based on a non abelian symmetry group, interaction terms between the vector bosons of the theory, the gluons, are present.

The inclusion of quark masses would add a term

$$L_m = \sum_f m_f \bar{\psi}_\alpha^f \psi^{f\alpha} \quad (1.4)$$

in Eq. 1.1. Equation 1.3 contains one dimensionless coupling constant g , and hence Eq. 1.1 provides no scale: QCD predicts only the ratios of physical quantities, not absolute values in terms of physical units. In QCD hadrons are colour-neutral bound states of quarks (baryons) or of quark-antiquark pairs (mesons); they are thus the chromodynamic analog of atoms as the electrically-neutral bound states in QED. The difference between the two theories becomes significant at large distances: while a finite ionization energy ΔE suffices to break up the electrodynamic bound, this is not possible in the

case of quark binding. This property of the QCD leads to the concept of “confinement”: quarks and gluons are confined inside hadrons. At short distances QCD shows another peculiar behaviour: the decrease of the colour charge with decreasing the distance from the colour-probe to the charge itself. This leads to the concept of “asymptotic freedom”, which implies that partons² inside hadrons interact weakly among themselves and can be considered as almost free.

1.1.1.2.1 Chiral symmetry and constituent quark masses

As already mentioned, for light hadrons, only a small fraction of the hadrons masses are recovered when the masses of the quarks they are composed of are summed. In the QCD theory this is motivated by the spontaneous chiral symmetry breaking mechanism. If the mass term is neglected, the QCD Lagrangian defined in Eq. 1.1 becomes chirally symmetric, i.e. invariant under separate flavour rotations of right- and left-handed quarks. Neglecting the mass term is a good approximation for the up and down quarks and quite good for the strange quark. The non-zero vacuum expectation value of the scalar quark density operator $\bar{\psi}\psi$ (“chiral condensate”) breaks this symmetry and generates a dynamic mass of order 300 MeV for the up and down quarks and about 450 MeV for the strange quarks. A pictorial view of the spontaneous chiral symmetry breaking mechanism can be seen in Figure 1.2.

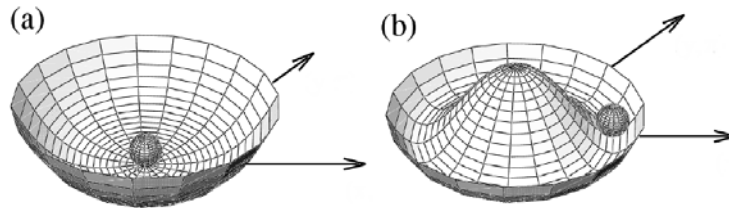


Figure 1.2: Pictorial view of the spontaneous breaking of the chiral symmetry. The quark, represented by the sphere, tends to occupy the minimum energy state: in the (a) configuration, it correspond to a symmetric state; in the (b) configuration, representing the confined quark in a nucleon, the parton is forced to break the symmetry and occupies an asymmetric state [10, 11].

1.2 Phase Transition in QCD

According to the Big Bang cosmological theory, a few microseconds after the Big Bang the early Universe was a very hot plasma of deconfined quarks and gluons. It evolved to its present state rapidly expanding and cooling, traversing a series of phase transitions predicted by the Standard Model. In these transitions, quarks and gluons became confined and the global features of our Universe, like the baryon asymmetry and the galaxy distribution, were originated. Today, the deconfined quarks and gluons are likely present in the core of the neutron stars, even if at lower temperature and higher density

²The basic constituents of hadrons, namely quarks and gluons.

than in the early Universe. The goal of the relativistic heavy-ion experiments is to form the deconfined phase colliding heavy ions at very high energy. In order to understand how the new phase forms, we can consider at first this picture, shown in Figure 1.3: composite nucleons with a finite spatial extension and made up of point-like quarks, if compressed, start to overlap above a critical density until each quark eventually finds within its immediate vicinity a considerable number of other quarks. It has no way to identify which of these had been its partners in a specific nucleon in the previous state at lower density. Therefore beyond a certain condition of high density, the concept of a hadron loses its meaning. At extreme densities, a medium constituted of unbound quarks forms[12].

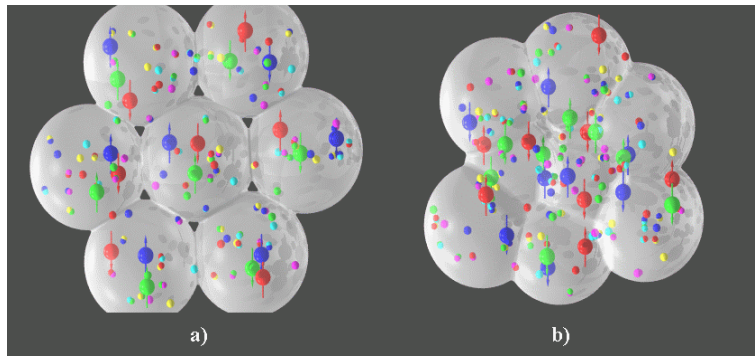


Figure 1.3: Pictorial view of the compression of the nuclear matter: the composite nucleons, with their finite spatial extension, are packed together (a); if compressed above a critical density, they start overlapping and the quarks can not identify their previous partners (b); the matter is thus deconfined.

In relativistic thermodynamics, higher densities can be obtained either by increasing the net baryon number³, or by “heating” the system, so that collisions between its constituents produce further hadrons. This leads to the phase diagram shown in Figure 1.4: for low values of temperature T and baryon density ρ_B , we have confinement and hence hadronic matter; for high T and/or ρ_B , deconfinement sets in and we get a particular phase of the matter called the Quark Gluon Plasma (QGP)[13, 14, 15].

Compressing the nuclear matter at $T = 0$, its properties can be understood in terms of a degenerate Fermi quark gas. By increasing T at low ρ_B , we are heating matter until it becomes a quark-gluon plasma. Strong interaction thermodynamics thus predicts the existence of new, deconfined state of matter at high temperatures and densities. In the following paragraphs, the creation of this state and its main features will be described.

³The net baryon number N_B is the difference between the number of baryons and of antibaryons present in a system. The variation of energy due to an increase in the N_B is the baryochemical potential $\mu_B = \frac{\partial E}{\partial N_B}$. It increases with the baryon density ρ_B , thus it is an alternative way to express the baryon content of a system.

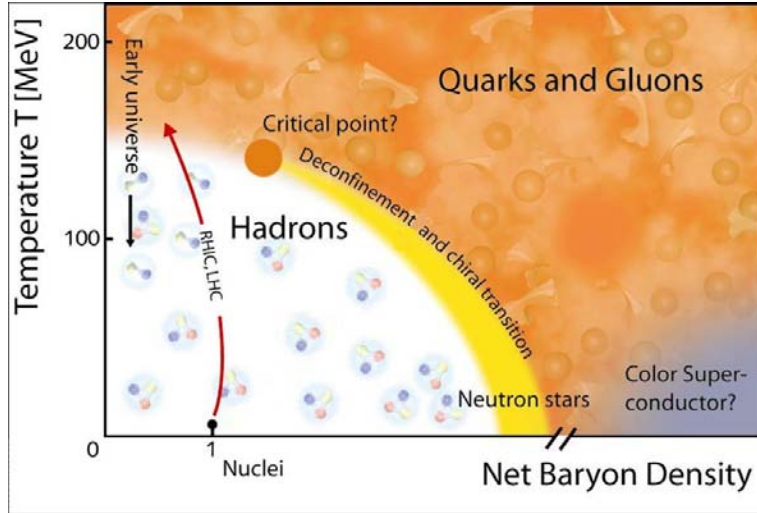


Figure 1.4: The nuclear matter phase diagram. For low temperature and baryon density the matter is in the ordinary nuclear conditions. Increasing the density and/or the temperature a phase transition to the Quark Gluon Plasma should occur. The red arrow shows approximately the range of temperature and density that are studied by the RHIC and LHC experiments.

1.2.1 Characteristics of QGP

Even before the formulation of the QCD, the existence of a phase transition to a new state of matter had been argued from the mass spectrum of resonances produced in hadronic collisions[16]. After the formulation of the QCD as an asymptotically free theory this observation has been related to a phase transition[17]. From QCD lattice predictions, the phase transition is expected at a critical temperature $T_c = 175$ MeV, corresponding to an energy density $\epsilon \simeq 1$ GeV/fm³. Starting from the ordinary nuclear matter, the ultra-relativistic heavy-ion collisions recreate the energy density conditions more favorable for the creation of this phase of coloured matter called the Quark Gluon Plasma (Figure 1.4). As suggested by the extrapolations of the asymptotic high temperature behaviour of QCD in the region of the transition from hadronic to partonic matter, the QGP was expected to behave as an ideal non-interacting gas: instead the observation performed by RHIC seems to suggest a rapid thermalization of the dense matter created in relativistic heavy-ion collisions. This suggests that the hot and denser medium created in these collisions is still strongly interacting. Also the early non-perturbative study have shown that the high temperature phase of QCD is far from being simply an ideal quark and gluon gas; even at temperatures $T \simeq (2-3)T_c$ large deviations from the ideal gas behavior have been deduced[18]. In order to compare the new scenario that should be accessible at LHC, the expected experimental conditions and the fireball characteristics are compared with the ones estimated at SPS and RHIC in Table 1.3.

	SPS	RHIC	LHC
$\sqrt{s_{NN}}$ (TeV)	0.017	0.2	5.5
T/T_c	1.1	1.9	3-4
ϵ (GeV/fm ³)	3	5	15-60
τ_{QGP} (fm/c)	<2	2-4	>10
V_f (fm ³)	few 10 ³	few 10 ⁴	few 10 ⁵

Table 1.3: Experimental conditions and QGP characteristics expected at LHC, compared with the corresponding values estimated at SPS and RHIC.

1.2.2 Deconfinement and chiral symmetry restoration

The phase transition from the hadronic matter to the QGP affects the masses of the quarks, due to the partial chiral symmetry restoration that takes place in this phase. When confined in hadrons, the quarks “dress” themselves with gluons to acquire an effective constituent quark mass of about 300 MeV (resulting as the equivalent to 1/3 of the proton or 1/2 of the ρ -meson mass). On the other hand, the basic bare quarks in the QCD Lagrangian are almost massless, so that the mass of the constituent quarks in the confined phase must be generated spontaneously through the confinement interaction (spontaneous breaking of chiral symmetry). Hence when deconfinement occurs, this additional mass is likely “lost” and the quarks go back to their intrinsic *bare* mass[12]. A Lagrangian with massless fermions possesses chiral symmetry; this allows a decomposition of the quarks into independent left- and right-handed massless spin one-half states, which for massive fermions become mixed. Hence the mass shift transition in QCD is often referred to as chiral symmetry restoration. It is important to stress that it does not necessarily coincide with deconfinement: when the hadrons are dissolved into quark constituents, the free and now coloured quarks may still interact to form coloured bound states.

1.3 The Lattice QCD predictions

The phase transition of ordinary QCD matter to a quark-gluon plasma state is quantitatively best studied in QCD thermodynamics within the framework of lattice QCD. Phase transitions are related to extended range phenomena in a thermal medium, to the collective behaviour and spontaneous breaking of global symmetries. In order to study such mechanisms in QCD a calculation approach able to deal with all non-perturbative aspects of the theory of strong interactions is needed: this is precisely the purpose of lattice QCD[19]. A discrete space-time lattice is introduced in this formulation of QCD, well suited for numerical calculations. Although the lattice calculations are affected by systematic errors, which are caused by the finite lattice cutoff and the use of quark

masses larger than those in nature, they have achieved important results in the study of the QGP phase transition: in particular, for zero baryochemical potential ($\mu_B = 0$), they expect it to occur at the critical temperature $T_c = 175 \pm 15$ MeV and the critical energy density $\epsilon_c \simeq (6 \pm 2)T_c^4 \simeq (0.3\text{-}1.3)$ GeV/fm³; the influence of the non-zero baryochemical potential expected at LHC is anyway estimated to be very small. Moreover, the estimates of the order of the transition and of the critical temperature depending on the number of flavours and the values of the quark masses indicate that in the more realistic limit of 2 zero mass quarks plus the s quark, the transition is a crossover at zero baryochemical potential and then a sort of second order phase transition. In Figure 1.5 the results of the lattice calculations are shown for what concerns the energy density in the limit of 2 and 3 zero mass quarks, as well as of 2 light and a heavier quark[5].

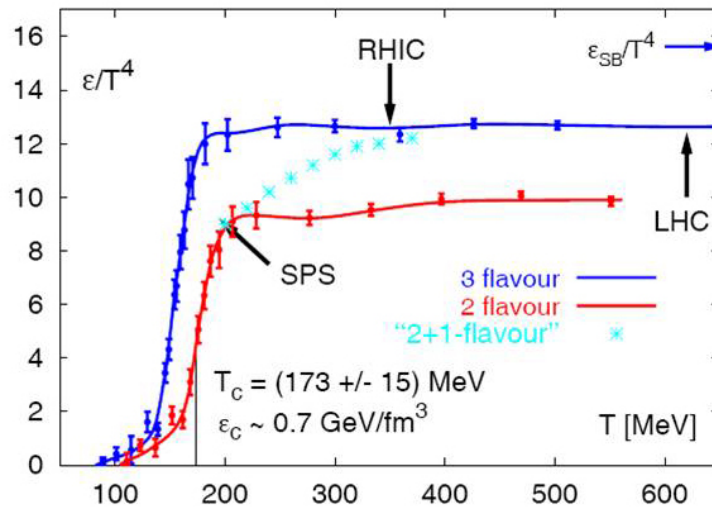


Figure 1.5: The energy density in QCD with 2 and 3 degenerate quark flavours as well as with two light and a heavier (strange) quark. The arrow on the right-side ordinates show the value of the Stefan-Boltzmann limit for an ideal quark-gluon gas.

1.4 The Bjorken Picture

In the collisions of heavy nuclei at every high energy, the density of matter is increased well beyond the ordinary nuclear matter density ($\rho_0 = 0.17$ nucleons/fm³); while the energy increases, the nuclei penetrate each other bringing the matter from highly excited states to a quark gluon plasma: at the LHC energy, the colliding nuclei pass through each other, leaving behind them the hot and dense matter that eventually decays into hadrons. After the collision, the high energy density allows to turn on the degree of freedom normally hidden in the ordinary nuclear matter that successively turn off during the expanding and cooling down phase. The different stages of the event evolution can be qualitatively described by the picture formulated by Bjorken[20, 21]. In Figure 1.6 it is possible to follow this space-time representation of the event, from the collision to the

final state:

1. At $t = 0$ the two nuclei collide: they are Lorentz contracted along the beam direction by a factor $\gamma = E_{beam}/M$ (E_{beam} is the beam energy per nucleon and $M \simeq 0.94$ GeV is the nucleon mass. $\gamma \sim 110$ at RHIC and ~ 3000 at the LHC), thus the longitudinal coordinate of each the nucleon is the same.
2. After impact, hard collisions with large momentum transfer $Q \sim 1$ GeV between partons inside the two nuclei (quarks, antiquarks and gluons) produce high energetic secondary partons. The hard scatterings happen at early times, $\sim 1/Q \ll 10^{-24}$ s. During the pre-equilibrium phase the system reaches the maximum energy density, forming a not yet thermalized system of quarks and gluons into a volume of some tens of fm³; prompt leptons and photons can be emitted.
3. The remnants of the original nuclei, called “spectator nucleons”, fly along the beam line. The “participant” nucleons that do not survive the collision form the mentioned fireball, so called because of the high energy density of the system and its rapid expansion. Then, thanks to the interactions among the partons, the system starts to thermalize: in these conditions and before the energy density drops below the critical value, the quark gluon plasma forms and the matter deconfinement takes place, at a time estimated of order 1 fm/c after the collision (QGP phase); direct leptons and photons and hard jets are produced. Soft collisions with small momentum exchange $Q \ll 1$ GeV produce many more particles and thermalize the QGP. The resulting thermalized QGP fluid expands hydrodynamically and cools down approximately adiabatically.
4. The partons from different nucleon-nucleon collisions rescatter leading to local thermal equilibrium and generating a thermodynamic pressure which brings to a collective expansion of the matter; the system cools down and the surface, already at a temperature below T_c evaporates into a hadron gas (hadronization stage).
5. The generated hadrons stop to interact ~ 20 fm/c after the collision: the evaporation is completed and the hadron gas, now expanded in a region of about $10^4 - 10^5$ fm³ around the interaction point, should have reached its final chemical composition (*chemical freeze-out*).
6. The hadrons continue to interact quasi-elastically, cooling the fireball until the *kinetic* (or *thermal*) *freeze-out*, defined as the moment in which all interactions among particles cease. Unstable particles, like resonances, decay and the decay products stream freely towards the detector.

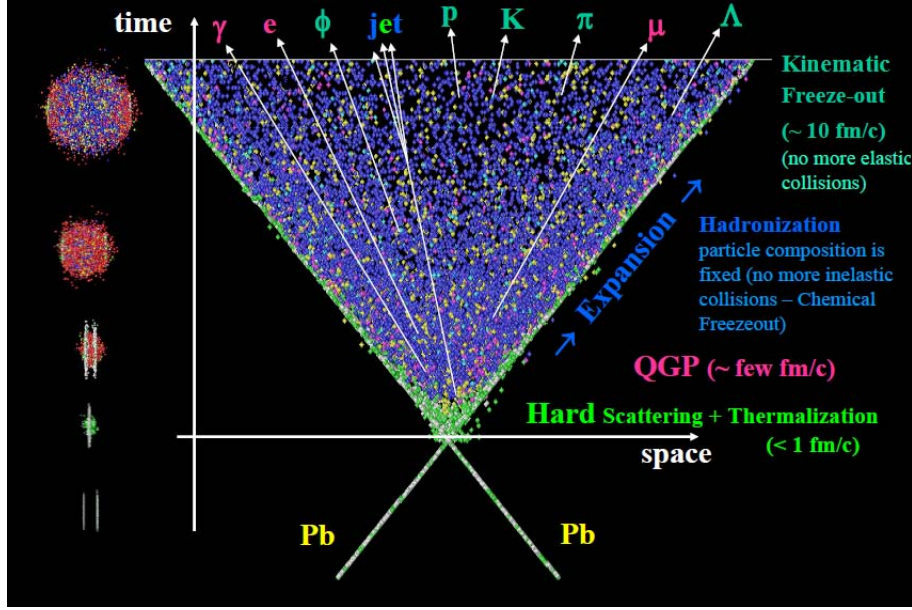


Figure 1.6: The space-time evolution of the heavy-ion collision. The various stages of the collision, drawn on the left part of the figure, are described, moving along the down-up direction, by the space-time representation and indicated with the conventional names on the right; on top, the particle types produced in the different stages of the evolutions are summarized.

1.5 The QGP Signatures

Since it is impossible to directly observe this short lived (\sim some fm/c) QGP system, the heavy-ion experiments like ALICE take the challenge to study the different behaviour of observables to infer on the existence and on the properties of this matter phase. Many of the signatures considered require the comparison of collisions where a QGP is suspected to have formed and collisions where no QGP is expected. The collective effects in heavy-ion collisions need to be disentangled from effects already present in lighter systems (p+p or p+heavy-ion) where no QGP is expected to form. For this purpose the same observables in heavy and light collision systems are usually directly compared. A further possibility is the comparison of central and peripheral heavy-ion collisions. In this case one can calculate the nuclear modification factors R_{AA} . These are the ratios of yields in heavy-ion collisions (N_{AA}) and in light collisions systems like p+p (N_{pp}) normalized to the number of independent binary nucleon-nucleon collisions (N_{coll}):

$$R_{AA}(p_t) = \frac{1}{N_{coll}} \frac{d^2 N_{AA}/dydp_t}{d^2 N_{pp}/dydp_t} \quad (1.5)$$

Depending on the compared systems, an isospin correction has to be taken into account owing to the different mixture of protons and neutrons in the two systems. In a likewise way, the factor R_{CP} denotes the ratio of central and peripheral collisions. The estimation of the number of participants in peripheral collisions, N_{coll} , is model dependent, therefore the systematic error in this comparison is larger than for the comparison

to a light collision system. Generally, it is of big advantage to use the same experimental setup for subsequent measurements under conditions as similar as possible. In this way many systematic uncertainties that are present in the measurements almost cancel out. In the following paragraphs, signatures of the QGP are outlined with special focus on the need for p+p reference data.

The signatures of the QGP can be divided in different categories, related to the different stages considered by the evolution picture described before: the deconfined medium (QGP), a possible interacting hadronic medium, and the final hadronic state[22]. The main direct hard probes of the creation of the QGP phase are:

- **Hard emission of thermal dileptons and photons.** These are a sort of internal probe: they are produced by the QGP itself and are not affected by the subsequent states of the medium, since they undergo only weak and electromagnetic interactions after their formation; therefore, they bear the imprints of the bulk properties of the early stages of the interaction and can be used as a thermometer of the medium, since they are produced also by the confined matter. However, this is also the main drawback of this study: it is very difficult to separate thermal dileptons and photons from the abundant hadronic production; moreover, the presence of a prompt component produced by early hard parton interactions in the primary and pre-equilibrium stages, has to be taken into account and separated as well.
- **Production of quarkonium states (J/ψ , Υ) in the primary parton collisions.** These states are produced before the existence of any medium but their dissociation is possible in a deconfined medium; their observed behaviour indicates therefore whether the subsequent medium was deconfined or not, resulting in a sort of external probe.
- **Jet quenching.** The energy loss of partons passing through the hot deconfined medium is expected to be larger than through the hadronic matter.

Information about the evolution of the hadronic system, in particular about its last stage, where the hadrons are still interacting, can be provided by:

- **In-medium modifications of resonances observable in their decays.** The changes of their masses or widths can originate from the large rescattering cross section in the medium, where the final state interactions influence in particular the hadronic decays. The study of these changes should be useful to distinguish between different expansion and freeze-out scenarios.

The expected QGP probes produced in the hadronization phase, the so called soft probes, which appear when the density of the medium has dropped sufficiently to allow the existence of hadrons, are:

- **Strangeness enhancement.** A hot QGP should contain the different quark species in almost equal amounts, which, if preserved up to hadronization, should

result in more abundant strangeness production than observed in p-p interactions, where the strange quark abundance is suppressed.

- **Collective flow and transverse momentum broadening.** Compared to p-p interactions, a hot initial QGP could lead to more pronounced expansion and specific expansion patterns.

In this sections, the main heavy-ion observables that are measured and studied by the ALICE experiment as probes and signatures of the QGP are discussed (with particular attention to those more related to the topic of this thesis), giving an overview of the present results, achieved by the previous experiments at SPS and at RHIC, and the perspectives for these topics research. Where necessary, the measurements of the same observables in proton-proton collisions will be discussed as a reference for nucleus-nucleus collisions.

1.5.1 Particle multiplicity

In the heavy-ion collisions, it is possible to determine the initial geometry of the collision and the way in which the initial available center-of-mass energy is redistributed in the accessible phase space studying the global properties of the final state. The collision geometry, moreover, is an essential prerequisite to the study of any physics observable. One of the most important observables that ALICE has measured, already from the first days of collisions, is the charged particles multiplicity. The quantities related to the event geometry, like the impact parameter b , the number of participant nucleons in the interaction N_{part} and the number of nucleon-nucleon collisions, can be extracted from the measurement of the multiplicity in a rather model-independent way. Reconstructing the centrality of the collisions, it is possible to study the physics observables as a function of b or N_{part} in order to locate the onset of the phase transition from the hadronic to the deconfined matter. A complete characterization of the event will be finally provided by the information about the temperature and the energy density reached in the collision, that can be inferred from the charged particle rapidity⁴ density dN_{ch}/dy and the p_t distributions.

In the following paragraphs the expectations of the particle multiplicity in proton-proton and in nucleus-nucleus collisions will be discussed.

1.5.1.1 Multiplicity in p-p collisions

The ALICE experiment started measuring the charged particle multiplicity in proton-proton events, as a benchmark for the further study in A-A events but also to extract information about the phase transition to QGP from the multiplicity fluctuations. From

⁴The rapidity for a particle with four-momentum (E, \vec{p}) is defined as $y = \frac{1}{2} \ln \frac{E+p_z}{E-p_z}$ where z is the beam direction. For particles in the relativistic limit ($E \simeq p$) it is often approximated with the pseudo-rapidity $\eta = \frac{1}{2} \ln \frac{p+p_z}{p-p_z} = -\ln[\tan(\theta/2)]$ with θ being the polar angle with respect to beam direction.

the observations, the hadron rapidity density can be parametrized for charged particles by a quadratic polynomial in $\ln(s)$. At SPS energies, $\sqrt{s} = 20$ GeV, the charged-particle rapidity density is about 2 at $y = 0$; at RHIC energies, it is about 2.5 and it is 3.81, 4.70, 6.01 at ALICE energies (0.9, 2.36 and 7 TeV respectively) while in Figure 1.7 the charged particles multiplicity as a function of center of mass energy (right graph) and the comparison with the considered models (left graph) are shown.

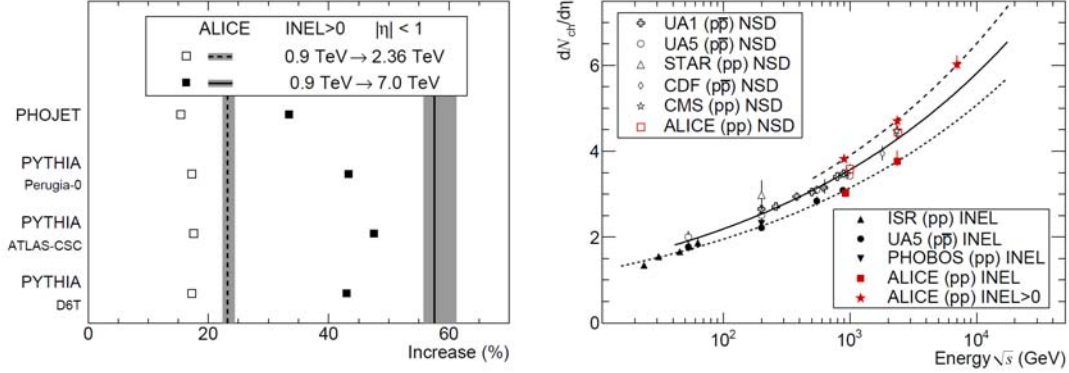


Figure 1.7: **Left:** Relative increase of the charged-particle pseudorapidity density, for inelastic collisions having at least one charged particle in $|\eta| < 1$, between $\sqrt{s} = 0.9$ TeV and 2.36 TeV (open squares) and between $\sqrt{s} = 0.9$ TeV and 7 TeV (full squares), for various models. Corresponding ALICE measurements are shown with vertical dashed and solid lines; the width of shaded bands correspond to the statistical and systematic uncertainties added in quadrature. **Right:** charged-particle pseudorapidity density in the central pseudorapidity region $|\eta| < 0.5$ for inelastic and non-single-diffractive collisions and in $|\eta| < 1$ for inelastic collisions with at least one charged particle in that region (INEL $>0_{|\eta|<1}$), as a function of the center-of-mass energy. The lines indicate the fit using a power-law dependence on energy. The data points at the same energy have been slightly shifted horizontally for visibility[23].

The measured values are higher than those from the models considered, except for PYTHIA tune ATLAS-CSC for the 0.9 TeV and 2.36 TeV data, and PHOJET for the 0.9 TeV data, which are consistent with the data. At 7 TeV, the data are significantly higher than the values from the models considered, with the exception of PYTHIA tune ATLAS-CSC, for which the data are only two standard deviations higher. The relative increase of pseudorapidity densities of charged particles between the measurement at 0.9 TeV and the measurements at 2.36 TeV and 7 TeV have also studied. An increase of $57.6\% \pm 0.4\%(\text{stat.})^{+3.6\%}_{-1.8\%}(\text{syst.})$ between the 0.9 TeV and 7 TeV data, compared with an increase of 47.6% obtained from the closest model, PYTHIA tune ATLAS-CSC. The 7 TeV data shows that the measured multiplicity density increases with increasing energy significantly faster than in any of the models considered.

1.5.1.2 Multiplicity in A-A collisions

The measurement of the particle multiplicity was one of the first topic addressed by the ALICE experiment when started its first heavy-ions data taking activity, last Novem-

ber 2010, with lead beams. In particular, the charged-particle pseudo-rapidity density $dN_{ch}/d\eta$ was the topic of the first ALICE article concerning the heavy-ion collisions at the CERN-LHC[24]. Infact the first step in characterizing the system produced in these collisions is the measurement of the charged-particle pseudo-rapidity density, which constrains the dominant particle production mechanisms and is essential to estimate the initial energy density. This measurements was performed using the Pb-Pb collisions provided by the LHC at $\sqrt{s_{NN}} = 2.76$ TeV and comparisons to model predictions and to previous measurements in nucleus-nucleus collisions at lower energies at the SPS and RHIC, as well as to pp and $p\bar{p}$ collisions over a wide energy range. This measurement provides new insight into particle production mechanisms in high energy nuclear collisions and enables more precise model predictions for a wide array of other observables in nuclear collisions at the LHC. In order to compare bulk particle production in different collision systems and at different energies, and to compare with model calculations, the charged particle density is scaled by the number of participating nucleons. The density of primary charged particles at mid-rapidity was found to be $dN_{ch}/d\eta = 1584 \pm 4$ (stat.) ± 76 (sys.). Normalizing per participant pair, $dN_{ch}/d\eta/(0.5N_{part}) = 8.3 - 0.4$ (sys.) with negligible statistical error. In Figure 1.8, this value is compared to the measurements for Au-Au and Pb-Pb, and non single diffractive (NSD) pp and $p\bar{p}$ collisions over a wide range of collision energies. The energy dependence can be described by $s_{NN}^{0.11}$ for pp and $p\bar{p}$, and by $s_{NN}^{0.15}$ for nucleus-nucleus collisions. A significant increase, by a factor 2.2, in the pseudo-rapidity density is observed at $\sqrt{s_{NN}} = 2.76$ TeV for Pb-Pb compared to $\sqrt{s_{NN}} = 0.2$ TeV for Au-Au.

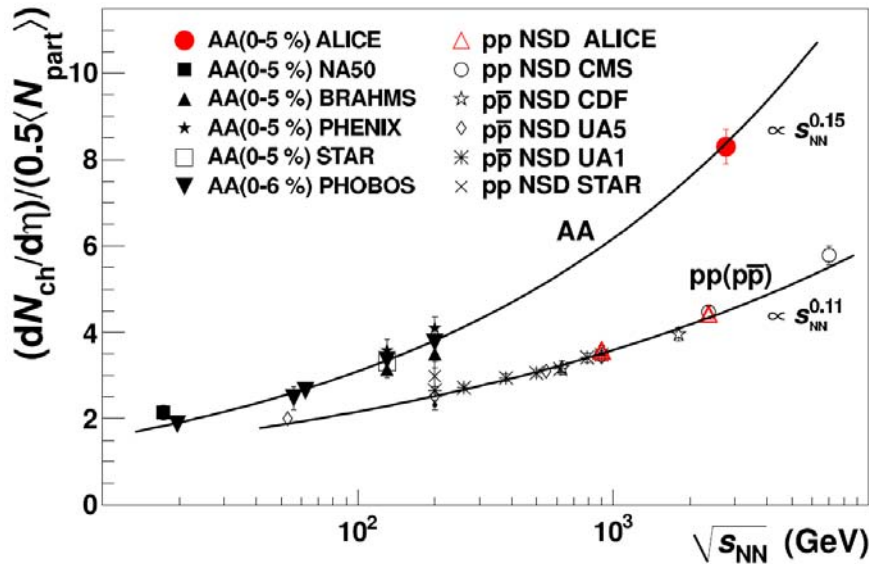


Figure 1.8: Charged particle pseudo-rapidity density per participant pair for central nucleus-nucleus and non-single diffractive $pp/p\bar{p}$ collisions, as a function of $\sqrt{s_{NN}}$. The energy dependence can be described by $s_{NN}^{0.15}$ for nucleus-nucleus, and $s_{NN}^{0.11}$ for $pp/p\bar{p}$ collisions.[24].

Figure 1.9 compares the measured pseudo-rapidity density to model calculations that

describe RHIC measurements $\sqrt{s_{NN}}$ 0.2 TeV, and for which predictions at $\sqrt{s_{NN}}$ 2.76 TeV are available.

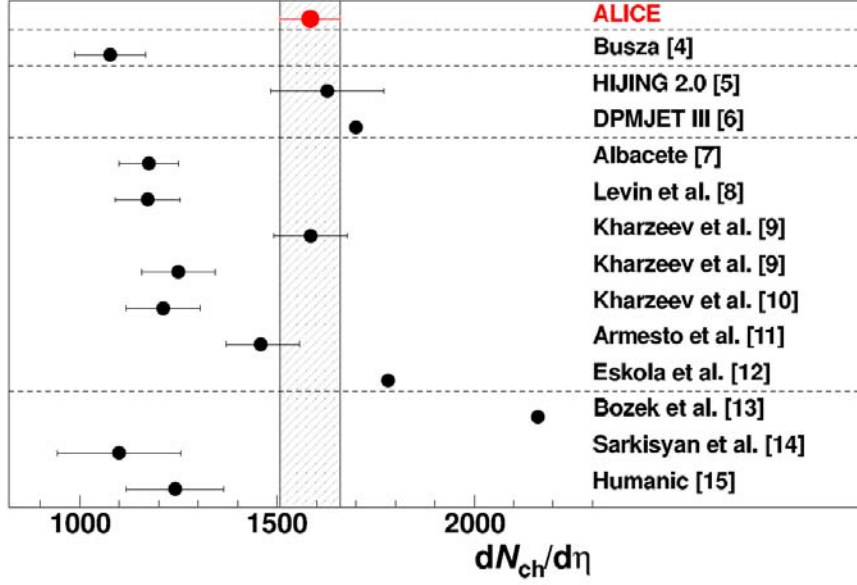


Figure 1.9: Comparison of this measurement with model predictions. Dashed lines group similar theoretical approaches.[24].

Perturbative QCD-inspired Monte Carlo event generators, based on the HIJING model tuned to 7 TeV pp data or on the Dual Parton Model, are consistent with the measurement while, for instance among the other models, an hydrodynamic model in which multiplicity is scaled from pp collisions overpredicts the measurement.

1.5.2 Energy density estimation

The energy density of the central rapidity region in the collision zone can be estimated via the Bjorken formula[20]:

$$\epsilon_{Bj}(\tau) = \frac{1}{S_{\perp} \tau} \frac{dE}{dy} \Big|_{y=0} \quad (1.6)$$

where τ is the evaluation time, S_{\perp} is the transverse overlap area of the colliding nuclei and E is the total energy. Usually $\frac{dE}{dy} \Big|_{y=0}$ is approximated to $\frac{dE}{dy} \Big|_{y=0} \approx \langle E_T \rangle \frac{dN}{dy} \Big|_{y=0}$ with $\frac{dN}{dy} \Big|_{y=0}$ the hadron multiplicity at $y = 0$ and $\langle E_T \rangle$ the average hadron transverse energy in the same rapidity interval. The Bjorken formula is based on the assumptions of longitudinal boost invariance and formation of a thermalized central region at an initial time τ_0 . Usually, a reference *QGP formation time* τ_0 is considered even if its value is not exactly defined and different choices, between 0.2 and 1 fm/c, are used. At the SPS with $\tau_0 = 1$ fm/c the estimated energy density was $\epsilon_{Bj} = 3.1 \pm 0.3$ GeV/fm³[25], a sufficient value for the phase transition to occur. In Figure 1.10, the estimated values of ϵ_{Bj} (from STAR at RHIC[26]) are reported as a function of the centrality parameter

N_{part} , for two different collision energies. The energy density is estimated to lie between 5 and 25 GeV/fm³, depending on the chosen formation time.

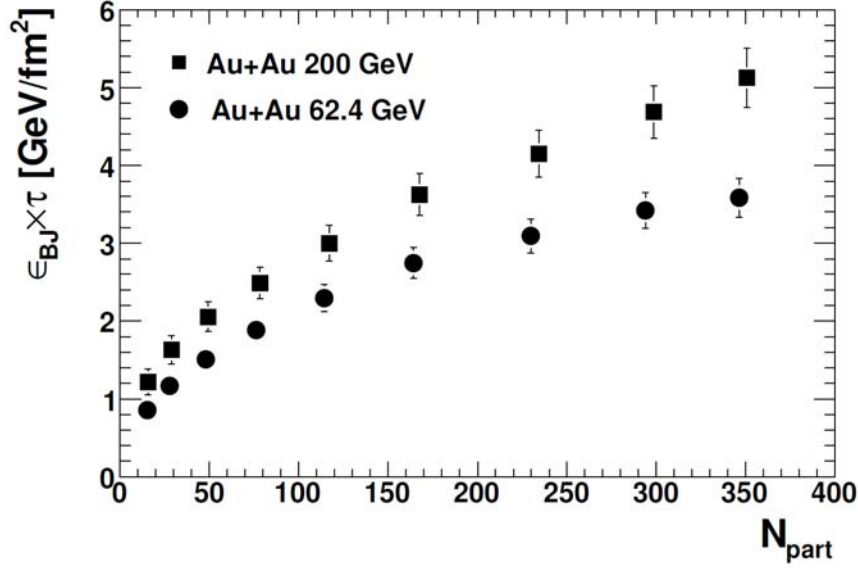


Figure 1.10: Estimate of the product of the Bjorken energy density and the formation time as a function of centrality N_{part} at RHIC (from STAR)[26].

1.5.3 Collective flow

Another collective observable that can provide information about the evolution of the matter in the heavy-ion collisions is the flow. The flow can be defined as a collective expansion of the matter and can follow different possible patterns, evolving both with an isotropic expansion and with a non-isotropic component, like in non-central collisions. In particular, this phenomenon affects all the particles involved in an event, showing the presence of multiple interactions between them. In proton-proton collisions this effect is absent, while it was observed in every nucleus-nucleus collision class, from the low energy fixed-target reactions below 100 A MeV up to the RHIC collision at $\sqrt{s_{NN}} = 200$ GeV; it is as well expected to be observed by ALICE. Different medium effects can influence the flow, depending on the energy of the collision: at low energies, flow effects are mostly caused by the nucleons belonging to the incoming ions and can be interpreted as caused by two-body interactions and mean field effects. At high energy, the larger number of produced particles dominates the flow effects while the initial nucleons are supposed to give a minor contribute, especially at central rapidities. Measuring the flow, it is thus possible to distinguish if it originates from partonic matter or from the hadronization stage. In Figure 1.11 the three most common flow phenomena are schematically represented. The *radial flow* interests central collisions: here the initial state is symmetric in azimuth, causing an isotropic azimuthal distribution even of the particles in the final stage (see Figure 1.11a). The relevant observables to study such

effects are the transverse momentum distributions of the various particle species.

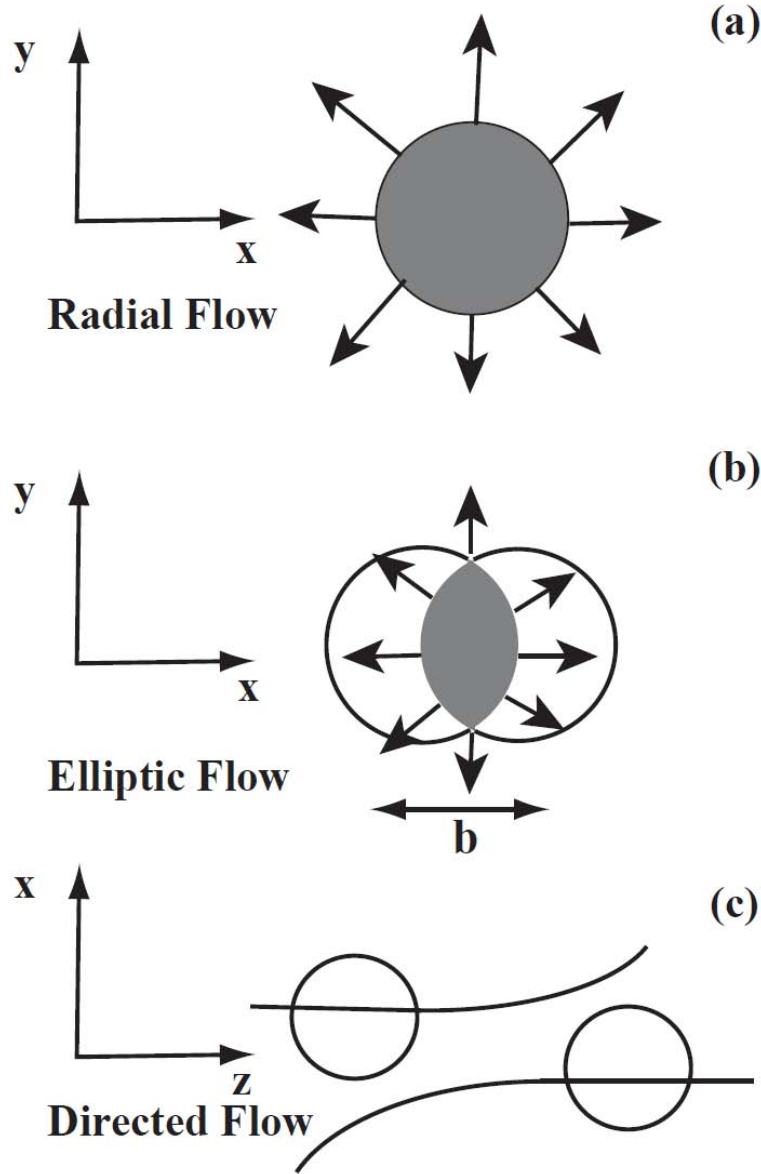


Figure 1.11: Illustration of the three most common flow phenomena.

Instead, in non-central collisions the pressure gradients are in general azimuthally asymmetric. These pressure gradients cause a correlation between the event configuration and the momentum distributions. For this anisotropic flow, the pattern depends on the collision energy, the considered phase-space region and the particle species. The flow of the nucleons from the nuclei have its maximum in the plane determined by the impact parameter and the beam axis, i.e. the reaction plane. Moreover, the flows of particles originating from the two nuclei are equal in magnitude but opposite in direction, thus it is called *directed flow* (see Figure 1.11c). At ultra-relativistic energies the particles are mostly produced within the interaction volume and can exhibit additional flow patterns;

this results in the so-called *elliptic flow* (see Figure 1.11b). Several different methods has been proposed to measure the anisotropic flow, based for example on the event-by-event reconstruction of the reaction plane, performed by correlating the directions of the produced particles with the event plane, or on the study of the two-particle correlations without reconstructing the reaction plane.

1.5.3.1 Kinetic freeze-out temperature and radial flow

A common flow velocity field results in a larger transverse momentum for heavier particles, leading to a dependence of the observed spectral shape on the particle mass. The kinetic freeze-out temperature T_{kin} , defined as the temperature at the surface of “last scattering”, is estimated by the analysis of the measured transverse momentum spectral shapes of different particles. Figure 1.12 shows a comparison of the measured transverse momentum spectra for π ’s, K ’s and \bar{p} ’s in p-p, d-Au and Au-Au for central and peripheral collisions.

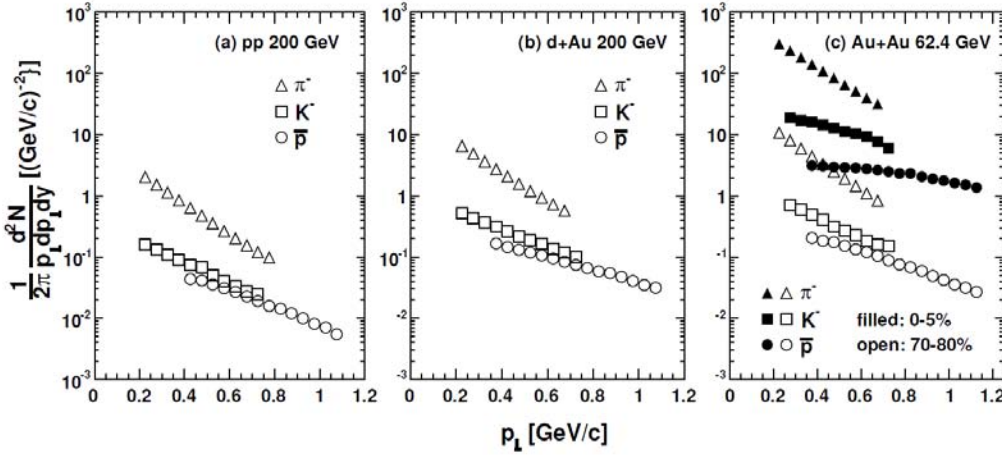


Figure 1.12: Comparison of π ’s, K ’s and \bar{p} ’s transverse momentum spectra observed by STAR in p-p and d-Au collisions ($\sqrt{s_{NN}} = 200$ GeV) and Au-Au collisions at ($\sqrt{s_{NN}} = 62.4$ GeV) for central (filled symbols) and peripheral (open symbols) collisions[26].

The spectra are described by the hydrodynamics-motivated blast-wave model[26]. The blast-wave model assumes that particles are locally thermalized at a kinetic freeze-out temperature and are moving with a common collective transverse radial flow velocity field. As reported in [26] (by STAR collaboration) the expected momentum spectral shape is used to fit six particle spectra (π^\pm , K^\pm , p , \bar{p}) simultaneously. Both T_{kin} and the average transverse flow velocity $\langle\beta\rangle$ are free parameters of the fit. In Figure 1.13, panel on the left, the kinetic freeze-out temperature obtained in different experiments is reported along with the chemical freeze-out temperature as a function of the collision energy. In the lower panel on the right the values recovered for $\langle\beta\rangle$ are shown.

The extracted average transverse flow velocity $\langle\beta\rangle$ increases with the centrality in Au-Au collisions as expected if a stronger pressure gradient develops in more central

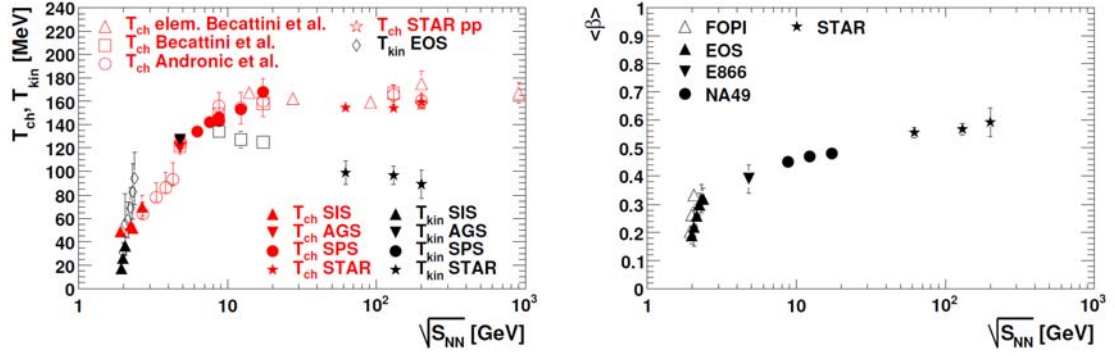


Figure 1.13: Chemical (T_{ch}) and kinetic (T_{kin}) freeze out temperatures (left) and average transverse-radial flow velocity ($\langle\beta\rangle$) (right) extracted in different experiments for central heavy-ion collisions as a function of the collision energy..

collisions. Quite large values of $\langle\beta\rangle$ are observed also in p-p and d-Au collisions mainly due to hard-scattering and jet production. If this latter contribution is subtracted, a value $\langle\beta\rangle_{flow} = 0.54$ is found in Au-Au collisions. The magnitudes of both the kinetic freeze-out temperature and the radial flow velocity found by STAR are very similar for $\sqrt{s_{NN}} = 62.4, 130, 200$ GeV, while they strongly depend on the charged particle multiplicity and, thus, on the initial energy density. This suggests that a higher initial energy density results in a larger expansion rate and longer expansion time, yielding a larger flow velocity and lower kinetic freeze-out temperature.

1.5.3.2 Elliptic flow

Flow anisotropies are generated mostly during the early stages of the collision. They are driven by spatial anisotropies of the pressure gradients due to the initial spatial deformation of the nuclear reaction zone in non-central collisions. This deformation decreases with time as a result of anisotropic flow: matter accelerates more rapidly in the direction where the fireball is initially shorter, due to larger pressure gradients. With the disappearance of pressure gradient anisotropies, the driving force for flow anisotropies vanishes, and, due to this “self-quenching” effect, the elliptic flow saturates early. If the fireball expansion starts at sufficiently high temperature, it is possible that all elliptic flow is generated before matter reaches T_c and hadronizes. In this case, elliptic flow is a clean probe of the equation of state of the QGP phase. Re-scattering processes among the produced particles transfer the spatial initial deformation onto momentum space, i.e. the initially locally isotropic transverse momentum distribution of the produced matter begins to become anisotropic. The momentum anisotropy manifests itself as an azimuthal anisotropy of the measured hadron spectra. The azimuthal particle distributions are studied by analyzing the differential production cross-sections in terms of a Fourier expansion:

$$\frac{dN}{p_t dp_t dy d\phi} = \frac{1}{2\pi} \frac{dN}{p_t dp_t dy} + 2 \sum_{i=1}^{\infty} v_i(y; p_t; b) \cos[i(\Phi - \Psi_{RP})] \quad (1.7)$$

where Ψ_{RP} is the reaction plane angle, y is the particle rapidity, b is the impact parameter of the collision and v_i are the Fourier coefficients. The sine terms in the expansion vanish due to reflection symmetry with respect to the reaction plane. The Fourier coefficients are given by:

$$v_i(y; p_t; b) = \langle \cos[i(\Phi - \Psi_{RP})] \rangle \quad (1.8)$$

the angular brackets denoting an average over the particles, summed over all events, in the $(p_t; y)$ bin of interest. The lowest order Fourier terms are the so called direct flow (v_1) and elliptic flow (v_2). For collisions between equal nuclei v_2 is, at mid-rapidity, the first non vanishing Fourier coefficient. The dependence on the centrality and on the spatial eccentricity reported in many papers (for instance [27, 28]) confirms that the v_2 is tied to the spatial asymmetry of non-central collisions. This indicates that a high level of collectivity is present at an early stage of the collision. Each particle species has its own v_2 coefficient: at low p_t the elliptic flow depends on the mass of the particle, being smaller for larger masses, as expected if a common radial flow velocity is present.

An overview of the v_2 measurements performed at RHIC can be found at [27], [28], [29], [30], [31] and [32].

Recently the ALICE experiment has provided its first v_2 measurement in Pb-Pb collisions at $\sqrt{s} = 2.76$ TeV collected in November 2010. The Figure 1.14a shows $v_2(p_t)$ for the centrality class 40-50% obtained with different methods. For comparison, the STAR measurements for the same centrality from Au-Au collisions at $\sqrt{s_{NN}} = 200$ GeV are shown indicated by the shaded area. It was found that the value of $v_2(p_t)$ does not change within uncertainties from $\sqrt{s_{NN}} = 200$ GeV to 2.76 TeV. The Figure 1.14b presents $v_2(p_t)$ for three different centralities, compared to STAR measurements. The transverse momentum dependence is qualitatively similar for all three centrality classes. At low p_t there is agreement of $v_2(p_t)$ with STAR data within uncertainties.

Figure 1.15 shows that the integrated elliptic flow increases from central to peripheral collisions and reaches a maximum value in the 50-60% and 40-50% centrality class.

The integrated elliptic flow measured in the 20-30% centrality class is compared to results from lower energies in Figure 1.16. It shows that there is a continuous increase in the magnitude of the elliptic flow for this centrality region from RHIC to LHC energies. In comparison to the elliptic flow measurements in Au-Au collisions at $\sqrt{s_{NN}} = 200$ GeV a $\sim 30\%$ increase in the magnitude of v_2 at $\sqrt{s_{NN}} = 2.76$ TeV. The increase of about 30% is larger than in ideal hydrodynamic calculations at LHC multiplicities but is in agreement with some models that include viscous corrections which at the LHC become less important[33].

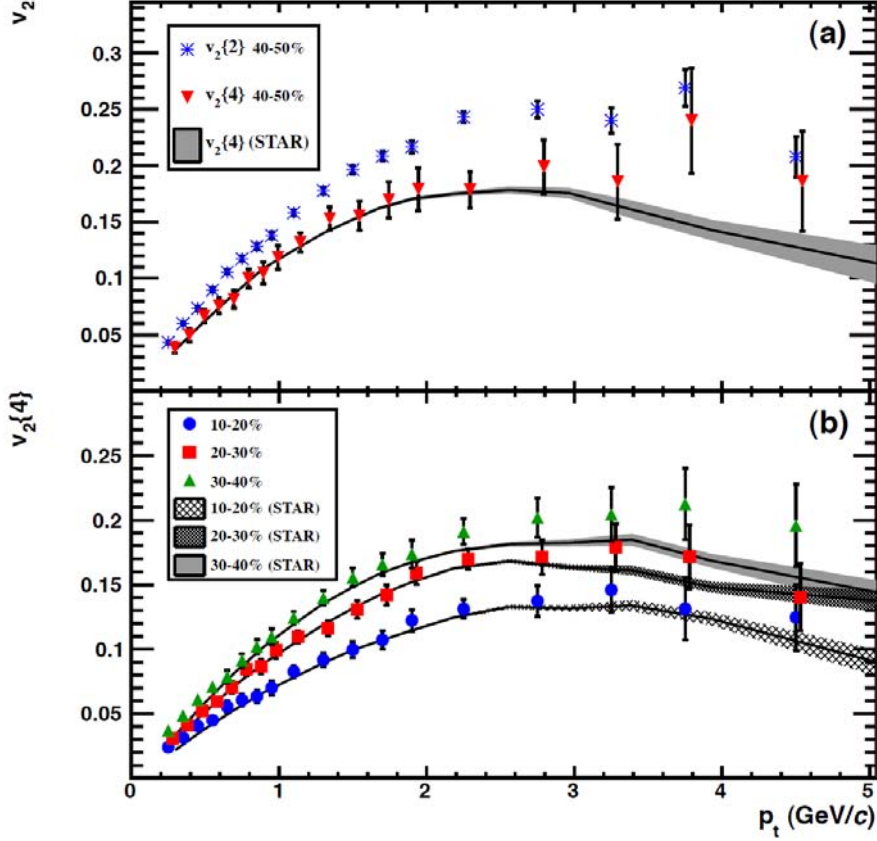


Figure 1.14: (a) $v_2(p_t)$ for the centrality bin 40-50% from the 2- and 4-particle cumulant methods for this measurement and for Au-Au collisions at $\sqrt{s_{NN}} = 200$ GeV. (b) $v_2\{4\}(p_t)$ for various centralities compared to STAR measurements. The data points in the 20-30% centrality bin are shifted in p_t for visibility[33].

1.5.3.3 Chemical freeze-out properties: temperature, baryon-chemical potential and strangeness suppression factor

The fireball produces hadrons that are in chemical equilibrium forming a statistical ensemble. In the chemical equilibrium model [26, 34], the system is described in a grand-canonical ensemble and distribution functions for each particle kind are derived via the Maximum Entropy Principle by imposing global energy, baryon and strangeness conservation. Particle abundances in a thermal system of volume V are then governed by only few parameters[26]:

$$N_i/V = \frac{g_i}{(2\pi)^3} \gamma_S^{S_i} \int \frac{1}{\exp\left(\frac{E_i - \mu_B B_i - \mu_S S_i}{T_{chem}}\right) \pm 1} d^3p. \quad (1.9)$$

In the above expression, N_i is the abundance of particle species i , g_i the spin degeneracy, B_i and S_i are the baryon and strangeness number carried by the particle species i , E_i is the particle energy and the integral is over the whole momentum space. The parameters in the model are the temperature of the system, the baryon and strangeness

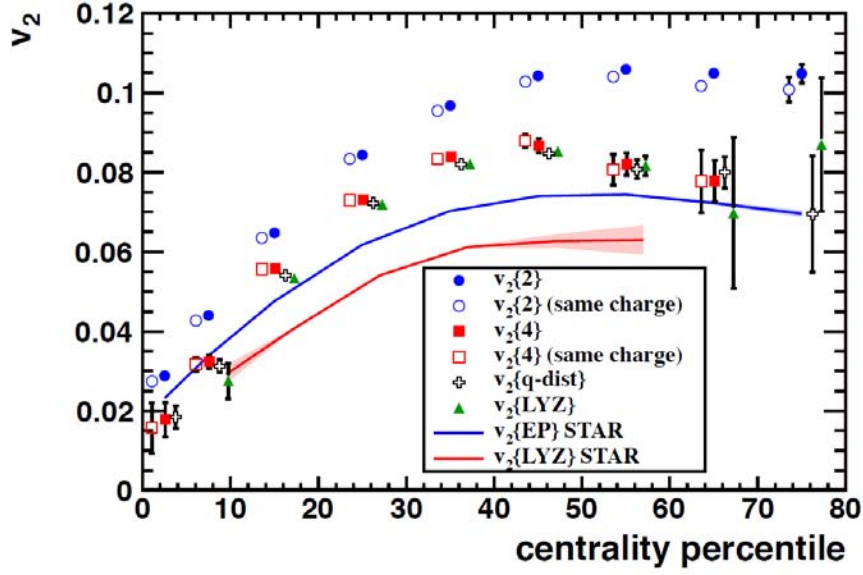


Figure 1.15: Elliptic flow integrated over the p_t range $0.2 < p_t < 5.0$ GeV/c, as a function of event centrality, for the 2- and 4-particle cumulant methods, a fit of the distribution of the flow vector, and the Lee-Yang Zeroes method. For the cumulants the measurements are shown for all charged particles (full markers) and same charge particles (open markers). Data points are shifted for visibility. RHIC measurements for Au-Au at $\sqrt{s_{NN}} = 200$ GeV, integrated over the p_t range $0.15 < p_t < 2.0$ GeV/c are shown by the solid curves[33].

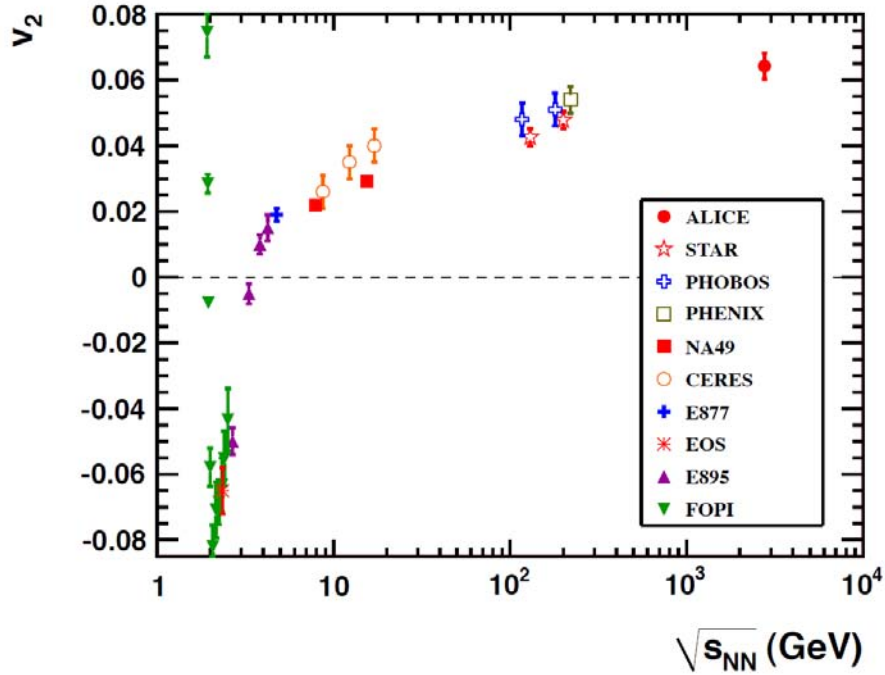


Figure 1.16: Integrated elliptic flow at 2.76 TeV in Pb-Pb 20-30% centrality class compared with results from lower energies taken at similar centralities[33].

chemical potentials, μ_B and μ_S and the ad-hoc strangeness suppression factor, γ_S . The measured particle abundance ratios are fit by the chemical equilibrium model to obtain the system parameters at the chemical freeze-out. In Figure 1.17 (left panel) the results obtained by the STAR collaboration for the ratio of different particle abundances are shown[27]. On the right panel the baryon chemical potential extracted from the fits in different experiments is reported as a function of the collision energy. It decreases smoothly with the collision energy, so that new baryons and anti-baryons can be created with increasing ease. This behaviour is confirmed by the recent measurements performed by ALICE in terms of p/\bar{p} ratio in pp collisions at $\sqrt{s} = 7$ TeV[35] and charged particle multiplicity in PbPb collisions at $\sqrt{s_{NN}} = 2.76$ TeV[24]. As shown in [26], the baryon chemical potential increases with centrality.

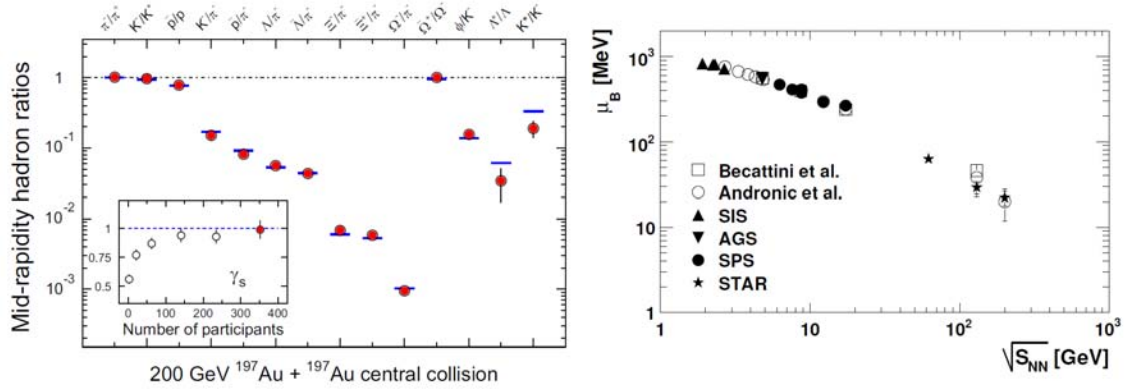


Figure 1.17: Left panel: ratios of p_t -integrated mid-rapidity yields for different hadron species measured in STAR for central Au-Au collisions at $\sqrt{s_{NN}} = 200$ GeV [27]. The horizontal bars represent statistical model fits to the measured yield ratios for stable and long-lived hadrons. The variation of γ_S with centrality is shown in the inset, including the value (leftmost point) from fits to yield ratios measured by STAR for 200 GeV p-p collisions. Right panel: the baryon chemical potential (μ_B) extracted in different experiments for central heavy-ion collisions as a function of the collision energy[26].

The chemical freeze out temperature T_{chem} , extracted from the data of many different experiments at many different collision energies (Figure 1.13, left panel), after an initial steep rise, plateaus abruptly near $\sqrt{s_{NN}} \simeq 10$ GeV at a value slightly higher than 160 MeV. It is remarkable that the same temperature is recovered for systems with different initial conditions, that is, different centralities, different colliding nuclei and different collision energies: central heavy-ion collisions at high energies can be characterized by a unique, energy independent chemical freeze-out temperature. This temperature is rather close to the critical temperature that should characterize the hadronization phase as estimated by lattice QCD calculations. Thus chemical freeze-out must occur very soon after or in the meanwhile of hadronization. The success of chemical equilibrium model in describing the data should not be readily taken as a proof of chemical equilibrium of each individual collision[36]. In p-p and other collisions between elementary particles, particles abundances are well described by the chemical equilibrium model (but with the

ad-hoc strangeness suppression factor significantly smaller than unity) suggesting that particle production in these collisions is a statistical process and the chemical temperature is a parameter governing the statistical production process. Some important points emerges from collective flow and chemical freeze-out properties. The medium created in heavy-ion collisions collectively expands very fast ($\langle\beta\rangle = 0.54$) and undergoes rapid cooling. Both $\langle\beta\rangle$ and the kinetic freeze-out temperature depends on the collision centrality while the chemical freeze-out does not. The former are controlled by a competition between local thermalization and expansion rate: the larger fireballs formed in central collisions live longer, develop more radial flow and cool down to lower kinetic freeze-out temperatures than in peripheral collisions. Conversely, T_{chem} is not the result of kinetic processes. The difference between the two freeze-out temperatures indicates that, after being formed, the hadrons continue to re-scatter quasi-elastically without changing their abundances. The hydrodynamical models describing the elliptic flow, along with many other signatures (see the following sections for some examples), support a scenario with the creation of a QGP. The chemical freeze-out temperature is very close to the critical temperature T_c predicted by lattice QCD at which the phase transition should occur. The rapid expansion (and thus cooling) along with the observation that strangeness is not suppressed as in elementary collisions (see next section) suggests the existence of a pre-equilibrium before hadronization because it would require time to reach the equilibrium starting from a non equilibrium condition, implying a larger difference between T_c and T_{chem} . This would enforce the idea that the chemical freeze-out is related more to a statistical formation of the hadrons rather than to a kinetic process involving inelastic scattering among them. If this is the case, the observed plateau in Figure 1.13 would indicate that a phase boundary is reached at a critical collision energy. Beyond that energy, all additional energy goes into heating the quark-gluon plasma which, in turn, cools again and freezes out at the critical temperature delimiting the phase boundary.

1.5.4 Particle production

The partonic matter created in the heavy-ion interactions at ultrarelativistic energies hadronizes into a large number of hadronic species. Through the study of the yields, the momentum spectra and the correlations of the produced particles, it is possible to extract information on the initial state matter phase and on the hadronization process, in order to understand the evolution of the system. As described by the Bjorken picture, a large fraction of particles will originate after the QGP phase, during the hadronization. The chemical freeze-out stage of the event, where the inelastic interactions stop, will govern the composition of the emitted hadrons; the elastic interactions will be still possible until the kinetic freeze-out is reached: thus, the measurements of the momentum spectra of the different particle types will allow a reconstruction of the event since the hard initial collisions until the soft final interactions. The different behaviour of chemical and kinetic freeze-out conditions in the $T-\mu_B$ plane is shown in Figure 1.18. The proposed empirical unified description shows that the hadronic composition of the final state is determined

by an average energy per hadron being approximately 1 GeV in the rest frame of the produced system[37].

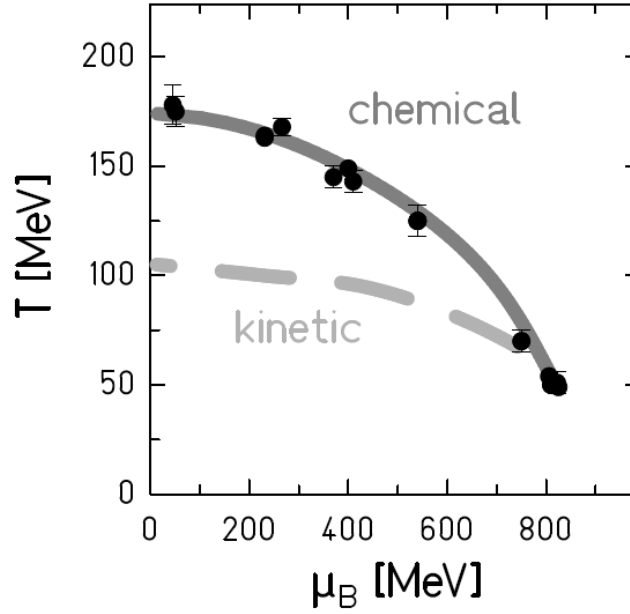


Figure 1.18: The chemical freeze-out condition (solid line) compared with the temperatures where kinetic freeze-out (dashed line) is observed[37]. The chemical freeze-out line is a phenomenological behaviour extrapolated from the parameters observed at SIS, AGS, SPS (40 AGeV and 160 AGeV) and RHIC. The resulting final state is composed of hadrons with 1 GeV average energy per hadron in the rest frame of the produced system.

1.5.4.1 Strangeness Enhancement

In order to observe the variations in the production of strange particles in presence of the QGP, it is useful to define the strangeness content as the ratio (Wroblewski coefficient)

$$W_s \equiv \frac{2 \langle s\bar{s} \rangle}{\langle u\bar{u} \rangle + \langle d\bar{d} \rangle} \quad (1.10)$$

where the quantities in brackets represent the number of quark-antiquark pairs[38]. The particle yields are studied with the aim to reconstruct the strange-to-light-quarks W_s ratio at the hadronization point before the decays, even if it is difficult since the u , d quark number increases significantly in the secondary decays. The production of strange particles is suppressed in the ordinary nuclear matter by the larger s quark mass with respect to the u and d masses. The absence of strange valence quarks in the colliding nucleons causes a suppression of the strange baryons production in the low-energy nucleon-nucleon collisions. Instead, the yields for strange-particle species in ultrarelativistic nucleus-nucleus collisions should be higher than the corresponding yields at the same energy in nucleon-nucleon collisions, if the deconfinement occurs: here

the reactions leading to strangeness production are partonic and have lower thresholds and higher cross sections, in particular if the strange mass is reduced by the partial restoration of the chiral symmetry. In these conditions the quarks should retain only their bare mass, decreasing from ~ 500 MeV to ~ 150 MeV for the s quark, and the threshold for the $s\bar{s}$ pairs should be consequently lowered allowing their production via gluon-gluon fusion in the QGP conditions. Moreover, in a system rich of baryons with respect to the antibaryons with high concentration of up and down quarks, the Pauli principle could block the production of $u\bar{u}$ and $d\bar{d}$ pairs: the energy of the lowest free level available for a light quark should grow enough to be comparable with the energy needed to create a $s\bar{s}$ pair.

In more details it is possible to summarize the ideas about the strangeness enhancements as follows. When color bonds are broken the chemically equilibrated deconfined state has an unusually high abundance of strange quarks. Perturbative QDC studies on the dynamical process of chemical equilibration has shown that only the gluon component in the QGP is able to produce strangeness rapidly, allowing formation of (nearly) chemically equilibrated dense phase of deconfined, hot, strangeness-rich, quark matter in relativistic nuclear collisions. Therefore strangeness enhancement is related directly to presence of gluons in QGP. The high density of strangeness formed in the reaction fireball favors formation of multi strange hadrons which are produced rarely if only individual hadrons collide[39].

The appropriate observable is the “enhancement” E of strange particle Y [40]:

$$E_Y = \frac{\langle N_Y^{A-A} \rangle \langle N_{part}^{p-A} \rangle}{\langle N_{part}^{A-A} \rangle \langle N_Y^{p-A} \rangle} \quad (1.11)$$

where $\langle N_{part}^{p-A} \rangle$ and $\langle N_{part}^{A-A} \rangle$ are the numbers of participant in a p-A (A-A) collision and $\langle N_Y^{p-A} \rangle$ and $\langle N_Y^{A-A} \rangle$ are the number of strange particles produced in a p-A (A-A) collision.

It is expected that $E_Y > 1$ and increasing with strangeness content of the particle. The reason is that strangeness-producing processes in a QGP

$$q q \leftrightarrow s s \quad g g \leftrightarrow s s \quad (1.12)$$

should equilibrate faster than the corresponding processes in a hadron gas (HG)

$$\pi^+ \pi^- \leftrightarrow K K \quad \pi N \leftrightarrow \Lambda K \quad (1.13)$$

This can be seen relatively quickly by computing the momentum exchange $\langle Q \rangle$ needed for these processes ($\langle Q \rangle \simeq 2m_s$ for Eq. 1.12, $\langle Q \rangle \simeq 2m_K$ for Eq. 1.13). Hence, the strangeness abundance should reach chemical equilibrium much faster in a quark gluon plasma than in a hadron gas. Since the initial strangeness abundance in collisions is zero, the number of strange particles in a system of a certain lifetime with a phase transition should be parametrically higher than for a similar system where the transition did not

occur. This is particularly true for multi-strange particles: in the hadron gas phase, these can only be produced sequentially

$$\pi \pi \pi N \leftrightarrow \pi \pi \Lambda K \leftrightarrow \pi \Xi K K \leftrightarrow \Omega K K K \quad (1.14)$$

In a hadronizing quark-gluon plasma, strange hadrons are presumably produced via *coalescence* of quarks. Hence, Λ , Ξ and Ω are “automatically” equilibrated to the same degree. In summary, strangeness particle abundance in a collision where a QGP is produced (a high energy A-A collision) should be enhanced with respect to a collision where hadronic dynamics is at play (a p-p or p-A collision, or an A-A collision where hadronic dynamics dominates). The onset of this enhancement could signal the appearance of a phase transition, or more generally a change in the degrees of freedom of the system[41]. Experimental data have confirmed this prediction [42][43][44]. Both at SPS and RHIC, enhancement defined with respect to p-p collisions is unity for p-A and d-A. At A-A, it increases with both N_{part} and strangeness content of the particle s , $\ln E \propto s \ln N_{part}$. The constant of proportionality does not vary between RHIC and SPS. This is exactly the behavior expected under the hypothesis that, in A-A (but not in p-A) systems the density of strangeness is higher than in p-p.

Some works were performed in order to review the hypotheses of strangeness enhancement, in particular how it scales with particle type, energy, system size[40]. The conclusion reached by these studies, analyzing both equilibrium and non equilibrium statistical models, is that different scenarios for the origin of strangeness enhancement within the statistical model give, generally, different scaling observables controlling the strangeness enhancement. The numerous competing effects, however, render it non-trivial to conclusively establish which model is more physically appropriate by scaling studies alone. The results of an explicit calculation of enhancements from both the equilibrium and non-equilibrium statistical model are shown in Figure 1.19

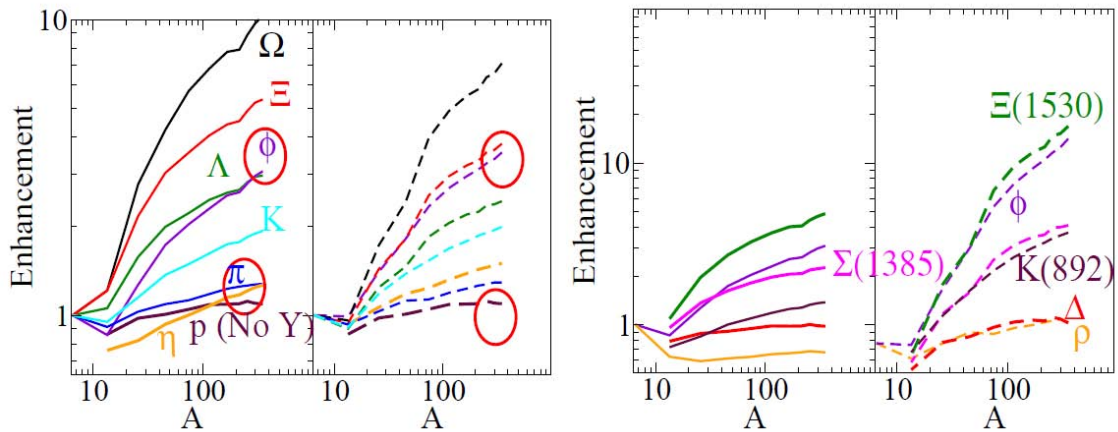


Figure 1.19: Enhancement factors of different stable particles (left panel) and resonances (right panel) for the equilibrium (dashed lines) and non-equilibrium (solid lines) statistical models. Red ellipses show where the scaling in the models differs[40].

The resulting enhancement in the strange particle production has been observed by the NA57 and WA97 experiments (Figure 1.20).

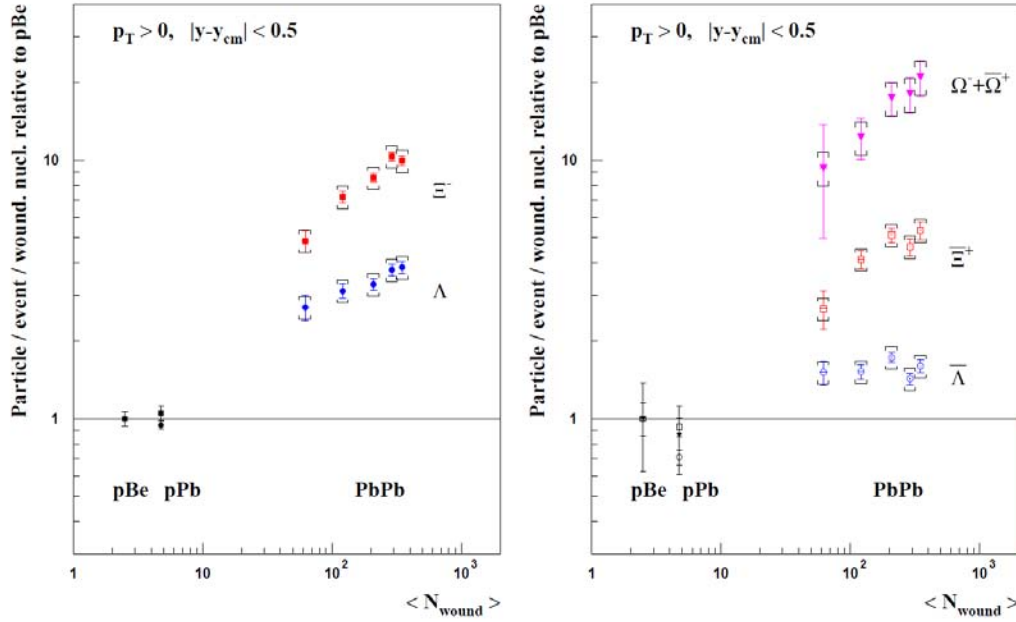


Figure 1.20: The strangeness enhancement as observed at SPS. The yields of the different hyperons in p-Be, p-Pb and Pb-Pb collisions, normalized to the p-Be production are plotted as a function of the number of participants.

No enhancements are seen for p-Pb, while for Pb-Pb the enhancement exists and increases with the centrality of the collision. Moreover, the enhancements are systematically larger according to the strangeness content of the particle: for the Ω 's, the enhancement reaches the value of 20 for the most central collisions[45]. The STAR experiment at RICH has observed an enhanced strange-baryon production in Au-Au collisions compared to pp collisions at $\sqrt{s_{NN}} = 200$ GeV[46]. The enhancement observed increases with the strangeness content of the baryon, and increases for all strange baryons with collision centrality (Figure 1.21).

At LHC, the expected enhancement should follow the same behaviour observed at SPS and RHIC, but some non-equilibrium models predict even greater enhancements. Anyway, ALICE is capable to measure this factor in order to understand the strangeness production mechanisms in different systems at the same energy.

1.5.4.2 ALICE Strange Prospects Measurements

In recent years some studies were performed in order to try to analyze what would be the scenarios of the strangeness measurements at the LHC energies and, in particular, in the ALICE Experiment[47]. Assuming that particle production in heavy-ion collisions, as shown at SPS and RHIC is described by a thermal source, some statistical observables can be extrapolated up to LHC energies. Indeed, a chemical freezeout temperature

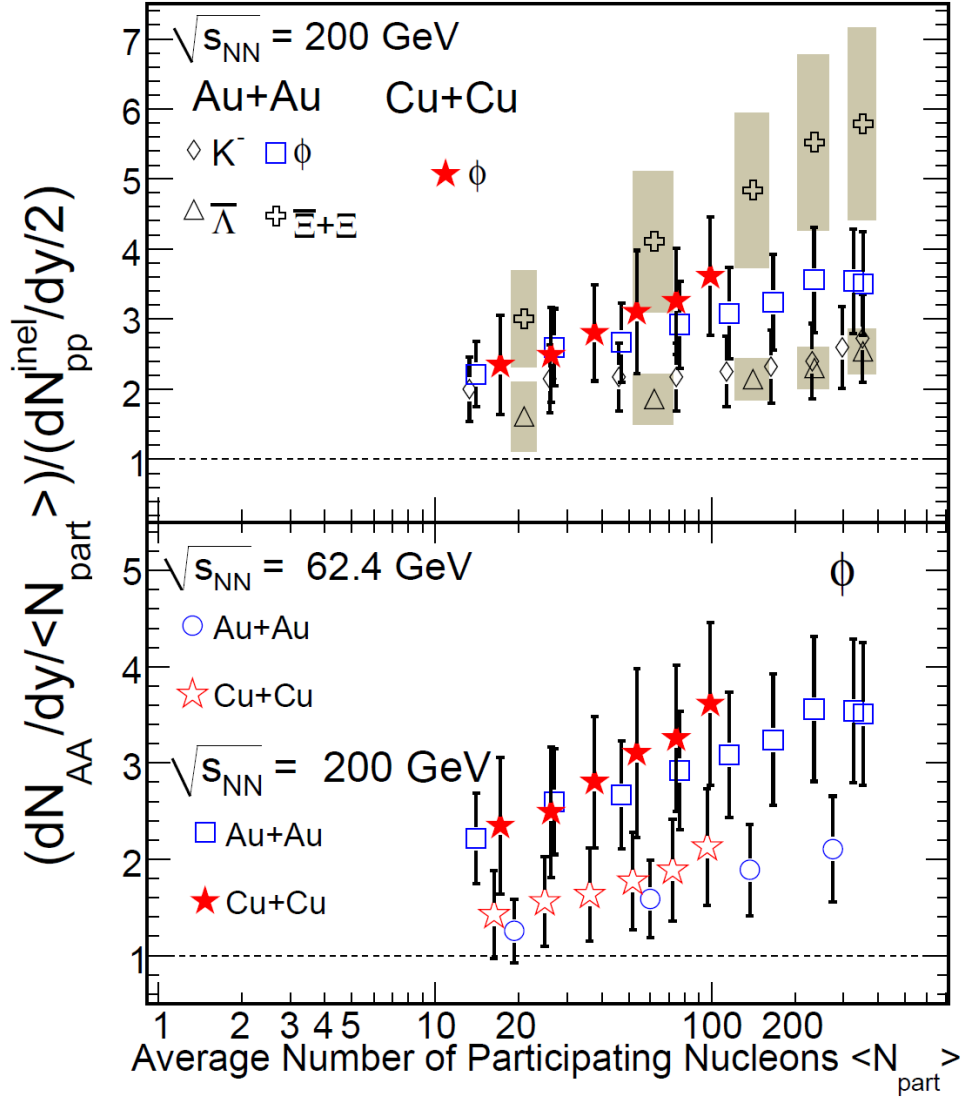


Figure 1.21: Strangeness enhancement measured by the STAR experiment. Upper panel: the ratio of the yields of K^- , ϕ , $\bar{\Lambda}$ and $\Xi + \bar{\Xi}$ normalized to $\langle N_{part} \rangle$ in nucleus-nucleus collisions and to corresponding yields in inelastic pp collisions as a function of $\langle N_{part} \rangle$ at $\sqrt{s} = 200$ GeV. Lower panel: same as above for ϕ mesons in Cu-Cu collisions at 200 and 62.4 GeV.

and a finite baryo-chemical potential in the statistical thermal model approach can be obtained at equilibrium using a constant average energy per hadron close to 1 GeV which approximately gives $T = 165$ MeV and $\mu_B = 1$ MeV at $\sqrt{s_{NN}} = 5.5$ TeV. For what concern the overall strange quark production, most of the information is contained in the Wroblewski factor. From RHIC to LHC energies, this factor should stay almost constant and reach ~ 0.43 and ~ 0.20 for respectively PbPb and pp collisions. The models may consider differently the degree of strangeness equilibration in the final state, which can be related to the QGP cooling under several assumptions. Figure 1.22 displays the estimates for particle ratios for two models. Introducing, for the strange quarks, the phase space occupancy factor γ_s , the equilibrium model (THERMUS[48]) shown here

assumes complete equilibrium of strangeness in the final (hadronic) state ($\gamma_s^H = 1$) whereas for the non-equilibrium model (SHARE[49]), equilibration for strange quarks in the QGP ($\gamma_s^{QGP} = 1$) can lead to an over-saturation after sudden hadronization ($\gamma_s^H = 3 \div 5$).

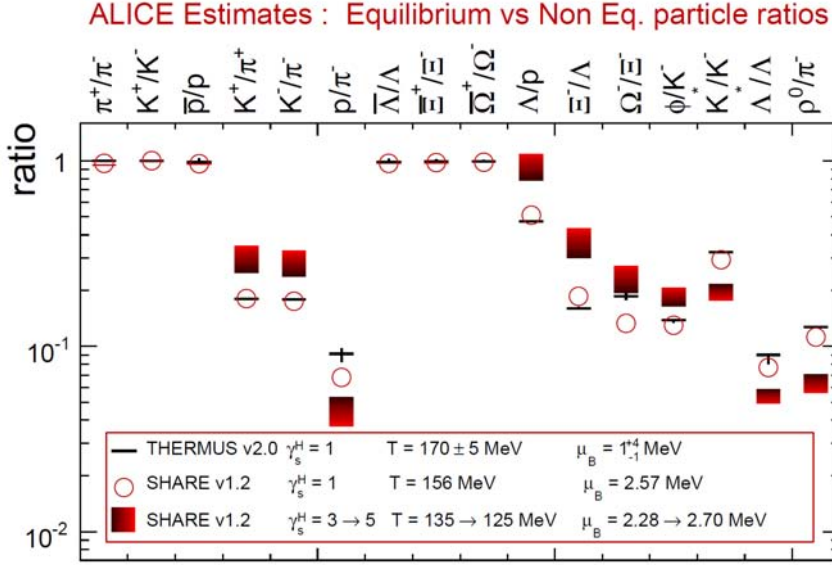


Figure 1.22: Estimates of particle ratios in central Pb-Pb collisions at LHC energies for equilibrium (THERMUS[48]) and non equilibrium (SHARE[49]) statistical models with different assumptions related to chemical freeze-out conditions: i) for the equilibrium model, a chemical freeze-out temperature of $T = 170 \pm 5$ MeV and a chemical potential $\mu_B = 1_{-1}^{+4}$ MeV were extrapolated from RHIC thermal fits; ii) for the non-equilibrium model, the strangeness equilibration is reflected in the strange quark phase space occupancy γ_s and the image of strangeness equilibrium in the deconfined source, $\gamma_s^{QGP} = 1$, results in an over-saturation $\gamma_s^H = 3 \div 5$ after sudden hadronization. Strangeness saturation in the hadronic phase i.e. $\gamma_s^H = 1$ for the non equilibrium model is shown as a reference (open circles) and systematics comparison for the chemical freeze-out conditions ($T = 156$ MeV and $\mu_B \simeq 2.6$ MeV). Expected values for resonances are presented with no in-medium effects[47].

Within errors, THERMUS ratios correspond exactly to the former values of T and μ_B and all antiparticle to particle ratios at LHC are shown to be unity. For non-identical species ratios, the differences between THERMUS and SHARE equilibrium results can be interpreted as a systematical variation of the chemical temperature. On the contrary non-identical species ratios are very sensitive to the equilibrium hypothesis: significant deviations are observed especially where strange baryons are involved. From these comparisons and assuming that contributions from hard processes are marginal for these studies, the distinction between non-equilibrium and equilibrium scenarios should be within the reach of the ALICE experiment[47]. Moreover additional studies were performed to estimate the ALICE strangeness capability at top LHC energies for K_s^0 , Λ , Ξ and Ω and also for some resonances such as $K^0(892)$ and $\Phi(1020)$ [50].

1.5.5 Electromagnetic probes: photons and dileptons

The importance of the observation of collision products that undergo only electromagnetic and weak interactions has been stressed in the introduction of this overview of the QGP observables: probes with such characteristics can provide information about the different stages of the event evolution without being influenced by the traversed matter. In this section the study of the electromagnetic probes, namely photons and dileptons, is discussed.

1.5.5.1 Photons

The photons are produced in all the different stages of a heavy-ion collision and, owing to their small electromagnetic coupling, they do not interact with the surrounding matter[51, 52]. In particular the different production stages can be summarized qualitatively as follows:

1. The “prompt” photons are produced early in the pre-equilibrium stage of the collision, by parton-parton scattering in the primary nucleus-nucleus (or nucleon-nucleon) collisions. In the high p_t domain ($p_t > 10$ GeV/c), the photons are produced in QCD hard-scattering processes. Although their rate decreases as an inverse power of p_t , photons up to several hundred GeV are expected to be detected at LHC: their yield should be suppressed by the nuclear shadowing and the in-medium parton energy loss, but should be increased thanks to the partonic transverse momentum and to the photon radiation induced by the medium. The production nuclear effects and the medium effects have to be disentangled comparing the Pb-Pb observations with the p-p and the p-Pb ones. The data from Tevatron experiments on p-p events and from RHIC appears to be well described by perturbative QCD. It has to be stressed that an important background to direct photon production is the decay $\pi^0 \rightarrow \gamma\gamma$ produced in similar hard partonic processes.
2. In the equilibrium stage of the collision, the quark gluon plasma is expected to be formed with a temperature of up to 1 GeV. In the thermal bath, photons are radiated off by the quarks which collide with other quarks and gluons. This production adds to the prompt photons in the low p_t domain ($p_t < 10$ GeV/c).
3. After the QGP phase, the plasma expands and cools. At the critical temperature a hadronic phase is formed. In this phase, photons can be produced in the scattering of π , ρ , ω or in resonance decays. This mechanism continues until the resonances stop to interact, when the freeze-out temperature of ~ 100 MeV is reached. The theoretical predictions of the direct thermal photon spectra are based on two step calculations: the photon production rates from an equilibrated QGP and hadron gas are calculated and then convoluted with a model for the space-time evolution of the fireball.

4. After freeze-out, further photons can be produced by the decay of π^0 , η and higher resonances, with energies in the range of up to a few hundred MeV.

Photons produced by π decays, either from the primary collisions or final-state contribution, constitute a large but reducible background to direct photon production over the whole p_t range. Thus they can be subtracted from the data. Instead, the prompt photons provide an irreducible background but its estimate is necessary to extract the rate of thermal photons.

1.5.5.2 Dileptons

Another important tool for probing the temperature and the dynamical properties of the matter during the evolution of a relativistic heavy-ion collision is the production of lepton pairs, the so-called *dileptons*. Even for the dileptons production, as for the photons, it is possible to distinguish among prompt, thermal and freeze-out decay components:

- considering the dileptons mass range, above pair mass $M \sim 2 \text{ GeV}/c^2$ the prompt contribution is dominated by semi-leptonic decays of heavy-flavour mesons and by the Drell-Yan process ($q\bar{q} \rightarrow l^+l^-$). Since these leptons originate from hard scatterings, their rates can be calculated in perturbative QCD;
- at leptons pair masses above $\sim 1.5 \text{ GeV}/c^2$, since the thermal radiation is very sensitive to temperature variations, the dileptons production is expected to originate from the early hot phases, probably from $q\bar{q}$ annihilation. Similarly to the photons case, the thermal QGP radiation has to be discriminated from the large prompt background;
- finally, at low masses, less than $1.5 \text{ GeV}/c^2$, thermal dileptons spectra are dominated by the radiation process from the hot hadronic phase.

1.5.6 Heavy-quark and quarkonium production

Among the hard probes that could provide direct information on the deconfined medium produced in the heavy-ion events, charm and bottom quarks are very suitable to understand the dynamics of the collisions: their production takes place on a timescale of the order of $1/m_Q$ where m_Q is the heavy-quark mass. On the other hand, thanks to their long lifetime, charm and bottom quarks can live through the thermalization phase and be affected by its presence. In order to extract information about the plasma from the features of heavy-quarks production in A-A collisions it is very important to well understand their production in p-p and p-A interactions and compare some observables like the total production rates, the transverse momentum distributions and the kinematic correlations between the heavy quark and antiquark. Both the productions of bound states of $c\bar{c}$ and $b\bar{b}$ (quarkonia) and of open charm and bottom will be extensively studied by ALICE, either as different probes of the event evolution and as interrelated topics. The

study of the correlations between the properties of open charm and bottom and quarkonia spectra will allow to understand the dynamics of the dense medium: in the very low p_t region, which will be accessible to ALICE, the production of heavy quark-antiquark pairs should increase the probability of forming quarkonia. In the region of perturbative production, i.e. at large p_t , the quarkonium suppression should take place. Moreover, the different effects of enhancement in the productions of quark-antiquark pairs and of the quarkonium suppression, which will be introduced in the following paragraphs, should be disentangled by the study of the correlations between quarkonium and open heavy-quarks momentum spectra.

1.5.6.1 Open charm and beauty observation

The measurement of open charm and open beauty production allows one to investigate the mechanisms of heavy-quarks production, propagation and, at low momenta, hadronization in the hot and dense medium formed in high-energy nucleus-nucleus collisions. The open charm and open beauty cross sections are also needed as a reference to measure the effect of the transition to a deconfined phase on the production of quarkonia: a direct measurement of the D and B mesons yields would provide the normalization for charmonia and bottomonia production. Finally, the measurement of B meson production is necessary within the search for the quarkonia suppression, which will be further discussed, in order to estimate the contribution of secondary J/ψ (from $B \rightarrow J/\psi + X$) to the total J/ψ yield: B mesons decay into J/ψ mesons with a branching ratio of about 1%. Since B mesons are produced by a factor of 5 more abundantly than J/ψ mesons, and since direct J/ψ production might be further suppressed by QGP effects, secondary J/ψ mesons are conceivably contributing a large fraction to the observable J/ψ signal. The measurement of charm and beauty production in proton-proton and proton-nucleus collisions, besides providing the necessary baseline for the study of medium effects in nucleus-nucleus collisions, is intrinsically interesting as a test of both perturbative and non-perturbative sectors of QCD in a new energy domain.

1.5.6.2 Quarkonia observation

At the high temperature of the QGP phase, the quark-antiquark pairs can be produced and form quarkonium states: these states are bound by energies comparable with the mean energies of the plasma (\sim few hundred MeV) and therefore have large probability to break up. The dissociation of heavy-quarks bound states can be explained taking into account, for example, the J/ψ case, which is the $1S$ bound state of $c\bar{c}$ pair. In this picture the colour screening present in the hot medium of deconfined quarks and gluons, will dissolve the binding and separate the c and the \bar{c} . When the medium cools down to the confinement transition point, the separated quarks will be too far to see each other and to interact: the charm quark (antiquark) will thus combine with a light antiquark (quark) and form a D (\bar{D}). Therefore the J/ψ production will be suppressed by the presence of the QGP. Lattice-based potential models indicate that

the dissociation temperature for J/ψ is $T_{J/\psi} \sim 2.1 \times T_c$, while the excited states χ_c and ψ' are dissolved close to the critical temperature $T_{\chi_c} \sim 1.2 \times T_c$, $T_{\psi'} \sim 1.1 \times T_c$ [53]. Moreover, the detection of J/ψ and ψ' mesons through their leptonic decay to a pair of muons is particularly interesting since muons are not affected by the strong interactions in the later stages of the collision evolution. The NA38 and NA50 experiments at SPS have extensively studied the production of the charmonia (J/ψ and ψ'). The data refer to different systems, from O-U and S-U (NA38), with a projectile energy of 200 GeV per nucleon, to Pb-Pb (NA50) with a projectile energy of 158 GeV per nucleon[54]. Also p-p and p-nucleus interactions (with proton energy as high as 450 GeV) have been studied in detail as a benchmark to understand the nuclei-nuclei interactions. The data collected with protons, Oxygen and Sulphur beams on several targets show that the J/ψ yield is suppressed with respect to the Drell-Yan process ($q\bar{q} \rightarrow l^+l^-$) yield. Namely, the J/ψ to Drell-Yan ratio shows a suppression that increases with the mean length of nuclear matter crossed by the $c\bar{c}$ pair. This suppression is interpreted in terms of nuclear absorption of the $c\bar{c}$ pair prior to J/ψ formation. The extrapolation to the Pb-Pb system of the normal suppression pattern observed with lighter systems represents the baseline to which the Pb-Pb data can be compared and is indicated by the solid curve in Figure 1.23 as a function of the transverse energy E_T and in Figure 1.24. Conversely, the measured yield in Pb-Pb collision show a stronger suppression, growing more rapidly than expected with the E_T . This larger suppression is explained as an effect of the deconfined matter and the consequent colour screening.

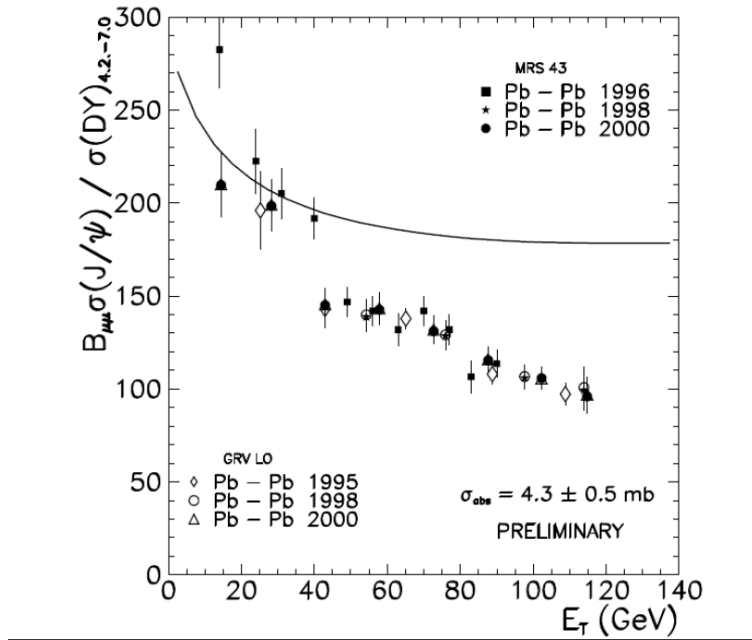


Figure 1.23: The J/ψ suppression observed in A-A collision (points), compared with the suppression extrapolated from p-p collisions data (black curve)[54].

The NA60 experiment has observed similar behavior in In-In collisions at the same

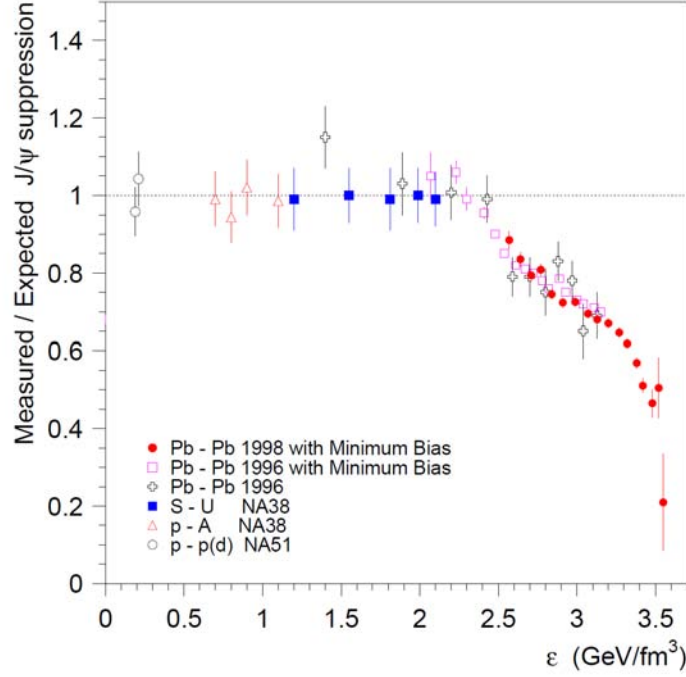


Figure 1.24: Measured J/ψ production yields at SPS, normalized to the yields expected assuming that the only source of suppression is the ordinary absorption by the nuclear medium. The data is shown as a function of the energy density reached in the several collision systems.[55].

energy (158 GeV/nucleon, Figure 1.25)

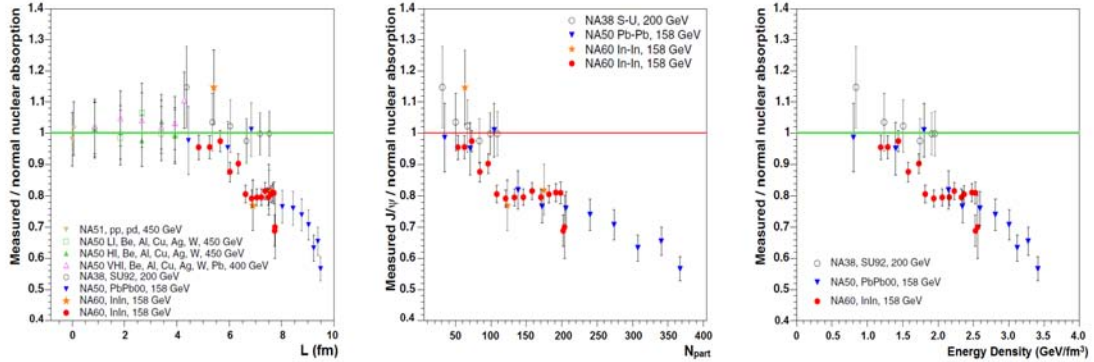


Figure 1.25: Ratio between the J/ψ data points and the absorption curve as a function of several centrality estimators: (a) length of nuclear matter crossed (L), (b) N_{part} , (c) energy density[56].

In addition, other effects have to be taken into account where higher center-of-mass energies are available (RHIC and LHC): the study of charmonia show significant differences with respect to the SPS energies. Here, in addition to prompt charmonia produced directly via hard scattering, secondary charmonia can be produced according to different mechanisms which might result in an enhancement instead of a suppression of charmo-

nium states. Since, at RHIC, QGP has a longer lifetime and reaches a higher energy density, straightforward extrapolations of the naive J/ψ melting scenarios predicted near-total suppression. The RHIC data apparently indicate a survival probability similar to that observed at the SPS. In Figure 1.26 the ratio between the measured J/ψ suppression and the expected suppression from normal nuclear absorption is shown as a function of the energy density, as observed at the SPS and RHIC[57].

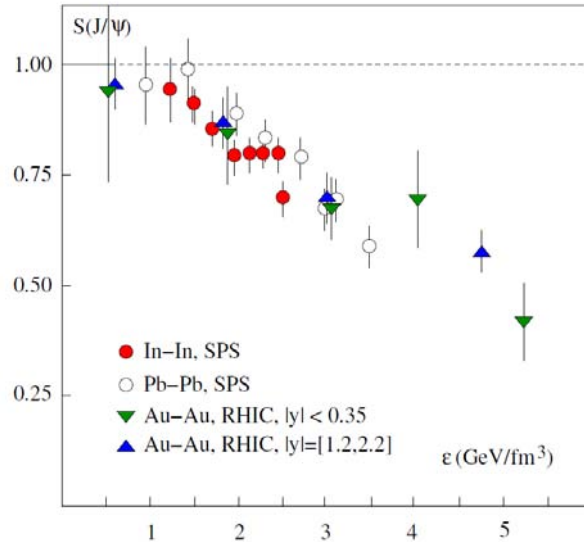


Figure 1.26: Ratio of measured J/ψ suppression over the expected suppression from nuclear absorption as a function of the energy density, as observed at the SPS and RHIC[57].

Recent data taken by the PHENIX experiment at RHIC exhibit a factor three suppression for most central Au-Au collisions at $\sqrt{s} = 200$ GeV[58]. In Figure 1.27 the J/ψ nuclear modification factor as a function of the number of participant compared to various models of final state interaction in the medium is shown.

The comparison with theoretical models suggests that it is necessary to consider the existence of recombination models in order not to overestimate the suppression in the extrapolation from the SPS experiments. The statistics of the present Au-Au data sample is too low to confirm those models. This problem is expected to be solved by the LHC statistics. Moreover, at LHC, the much higher energy offers the possibility of measuring with significant statistics the bottomonium yields providing another probe for QGP studies. In fact, the spectroscopy of the Υ , whose dissolution energy can not be reached at RHIC, should reveal at LHC energies new information on the characteristics of the QGP.

1.5.7 High p_t and Jet Quenching

In 1982 Bjorken stated that an “high-pt quark or gluon might lose tens of GeV of its initial transverse momentum while plowing through quark-gluon plasma produced in its local environment”[59]. Hard partons traversing the hot and dense medium created

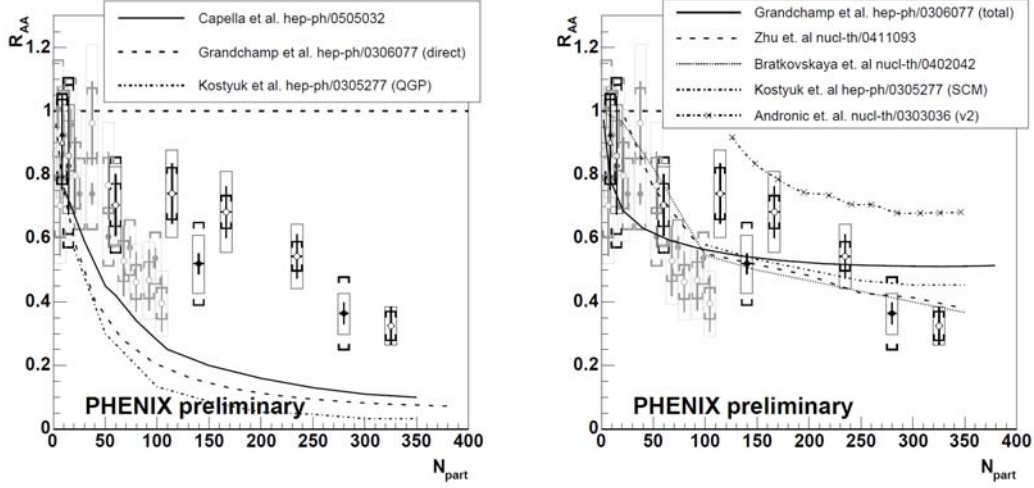


Figure 1.27: J/ψ nuclear modification factor as a function of the number of participant compared to various models of final state interaction in the medium. All the models involve additional final state interactions and reproduce both the CERN SPS results and the PHENIX low statistics results. The predictions plotted on the left panel overestimate the J/ψ suppression. The predictions plotted on the right panel show better agreement with the data or even underestimate the suppression[58].

in heavy-ion collisions lose energy by gluon radiation and/or colliding elastically with surrounding partons[60, 61]. This would have many observable consequences, of which the most directly measurable would be a depletion in the yield of high- p_t hadrons[62, 63, 64]. One of the most exciting results to date at RHIC is that the yield of π^0 at high transverse momentum in central $\sqrt{s_{NN}} = 200$ GeV Au-Au collisions is suppressed compared to the yield in pp collisions scaled by the number of underlying nucleon-nucleon collisions[65] (Figure 1.28).

Direct photons are not expected to undergo partonic energy loss, because they do not interact strongly and, thus, see the gluonic medium as “transparent”. Conversely, π^0 and η mesons do interact strongly. The magnitude of the suppression and its dependence from p_t of the particles and centrality of the collision are the same for η and π^0 , suggesting that the production of light neutral mesons at large p_t in nuclear collisions at RHIC is affected by the medium in the same way. This is expected if the suppression takes place at the parton level.

The observation that single-particle inclusive spectra in d-Au collisions at the same energy are not suppressed demonstrate that the strong suppression of the inclusive yield observed in central Au-Au collisions is due to final-state interactions with the dense medium generated in such collisions[66] (Figure 1.29).

The phenomenon is interpreted as a consequence of the so called *jet quenching* effect. Nuclear effects on hadron production in d-Au and Au-Au collisions are measured through comparison to the pp spectrum using the ratio

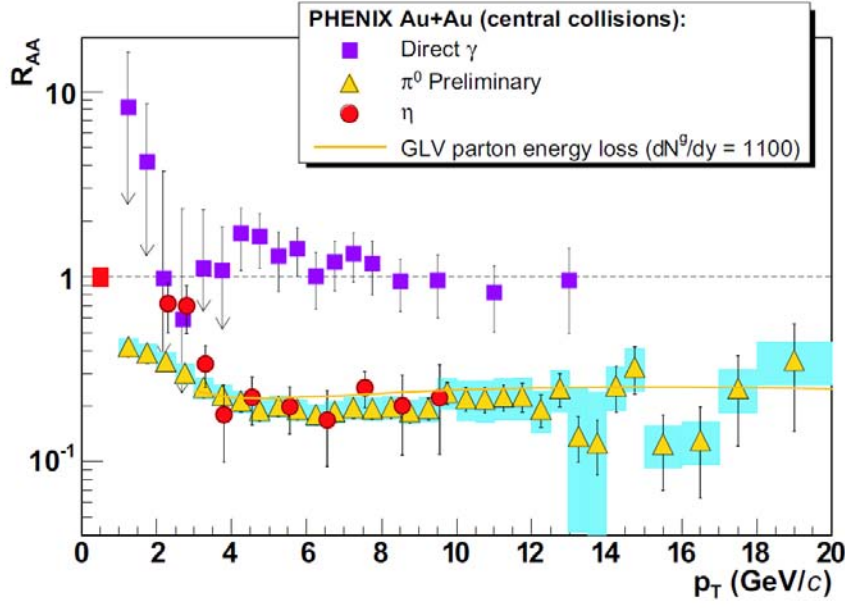


Figure 1.28: Nuclear modification factor R_{AA} from Eq. 1.5 of mesons π^0 (triangles), η (circles) and direct photons (squares), as measured by PHENIX[65].

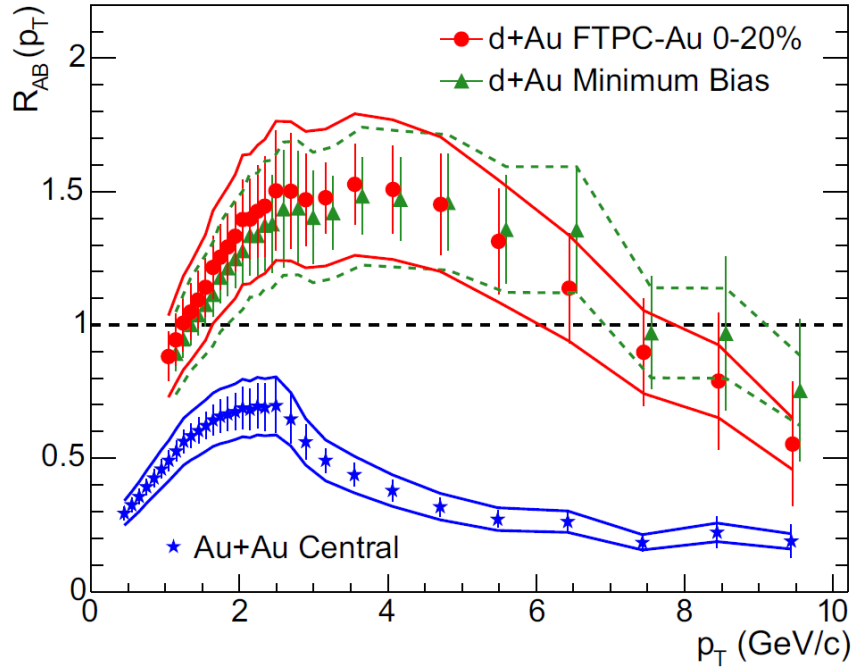


Figure 1.29: $R_{AB}(p_t)$ from Eq. 1.15 for minimum-bias and central d-Au collisions, and central Au-Au collisions, as measured by STAR. The minimum-bias data d-Au are displaced 100 MeV/c to the right for clarity[66].

$$R_{AB}(p_t) = \frac{d^2 N / dp_t d\eta}{T_{AB} d^2 \sigma^{pp} / dp_t d\eta} \quad (1.15)$$

where $d^2N/dp_t d\eta$ is the differential yield per event in the nuclear collision A-B, $T_{AB} = \langle N_{bin} \rangle / \sigma_{inel}^{pp}$ describes the nuclear geometry, and $d^2\sigma^{pp}/dp_t d\eta$ for pp inelastic collisions is determined from the measured pp differential cross section.

A hard hadronic collision at high energy may be pictured in the following way: partons distributed in the projectiles are involved in a hard scattering, with a large transfer of energy-momentum, whereas the non-colliding remnants of the incoming hadrons initiate what is called the “underlying event”. The energetic coloured partons produced by the hard subprocess undergo a cascade of branchings which degrade their energies and momenta. Finally the end points of this branching process and the remnants of the incoming projectile, fragment into colourless hadrons during the hadronization stage. In hadronic collisions, hard parton scatterings occurring in the initial interaction produce cascades of consecutive emissions of partons, called *jets*. At the end of the event evolution described in the previous sections, the jets fragment in hadrons during the hadronization phase. The final state is characterized by clusters of particles close in the phase space: their transverse momenta relative to the jet axis is small compared to the jet momentum and this collimation increases with increasing the jet energy. The jets lose their energy while propagating in the hot and dense medium due to the gluons radiation, resulting in the suppression of hard jets (the so-called *jet quenching* effect); the parton energy loss grows quadratically with the in-medium path length.

High-energy nucleus-nucleus collisions allow to study the properties of this medium through modifications of the jet-structure:

- **Suppressed particle yield:** the in-medium energy loss results in a suppression of the hard jets and in a reduction of the high- p_t particles yield.
- **Back-to-back azimuthal suppression:** the interaction of the hard jets with the deconfined medium leads also to a suppression in the production of jet pairs. Studies of the angular correlation of high- p_t particles shows a peak at opposite azimuthal angles. Instead in a deconfined matter, one of the two fast partons, covering a shorter distance to escape the medium, can emerge and be detected; the other one goes through a longer path with respect to its partner, loses its energy interacting with the medium and is not detected (Figure 1.30). In Figure 1.31 this effect as observed by the STAR experiment at RHIC is shown.

Clear correlation peaks are observed near $\Delta\Phi \sim 0$ and $\Delta\Phi \sim \pi$ in pp and d-Au data, while the disappearance of back-to-back $\Delta\Phi \sim \pi$ high- p_t hadron correlation in central Au-Au collisions seems to be consistent with large energy loss in a system that is opaque to the propagation of high-momentum partons or their fragmentation products[67, 68].

- **Impact parameter dependence:** since the characteristics and the size of the dense medium should depend on the centrality of the initial collision, a correlation of the *jet quenching* effect with the impact parameter is expected to be observed.

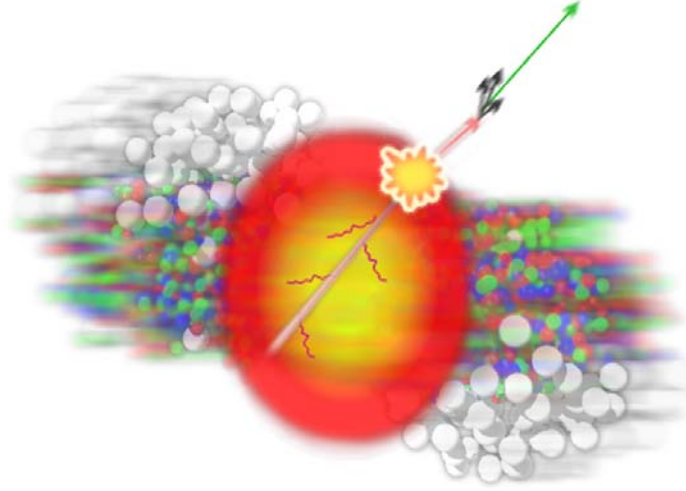


Figure 1.30: Drawing illustrating jet emission from the fireball surface and quenching of its inward-moving partner.

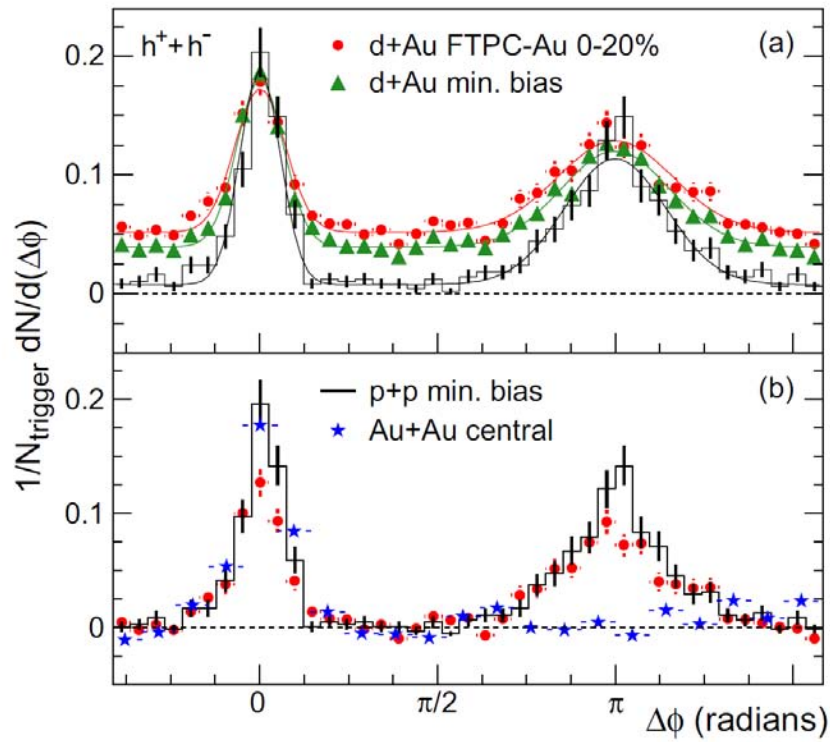


Figure 1.31: Two-particles azimuthal distribution for pp collisions (black line), central d-Au (filled points) and central Au-Au collisions (stars) observed at RHIC. The away-side jet disappears for central AA collisions[66].

Jets reconstruction is particularly challenging in heavy-ion collisions due to the large background induced by the high-multiplicity environment in these collisions. STAR has

recently shown the first results for the full reconstruction of jets in Au-Au collisions at $\sqrt{s_{NN}} = 200$ GeV[69, 70, 71]. At the LHC a much copious jets production is expected allowing a better separation from the background[72]. The comparison of full jet measurements at RHIC and the LHC will provide a crucial insight into the understanding of jet quenching and hot QCD matter. With the first Pb-Pb collisions data at $\sqrt{s_{NN}} = 2.76$ TeV, collected in 2010 all the three LHC major experiments (ALICE, ATLAS and CMS) spotted the first evidences of *jet quenching* in this new energy regime[73, 74, 75].

1.5.8 Identical Particle Interferometry

Two (or more) particle momentum correlations reveal information about the space-time dynamics of the collision. This procedure is analogous to Hanbury-Brown and Twiss (HBT) interferometry that has been successfully used in astrophysics to determine the angular diameter of stars[76]. In high-energy physics these correlations allow to measure the size, the lifetime, and the flow patterns of the fireball when the hadronization occurs.

1.5.9 Chiral-Symmetry Restoration

The Lagrangian of QCD implies approximate chiral symmetry. As a consequence the baryon number should be conserved for right-handed and left-handed quarks separately. In nature only the total baryon number is conserved thus chiral symmetry is broken. The symmetry breaking is twofold: to start with the symmetry is only approximate due to the finite, however small, bare quark masses that cause a so-called explicit symmetry breaking. Furthermore, the quarks acquire their constituent masses in the interaction with the QCD vacuum at low T which is a spontaneous breaking of the symmetry[77]. It is predicted that the spontaneous breaking of chiral-symmetry is restored at temperatures prevailing in the QGP phase. As a consequence the position and width of the masses of the light vector mesons (ρ , ω , and ϕ) may change[78]. Indications have been seen at the SPS in the NA60 experiment[79, 80].

1.5.10 Fluctuations

Any physical quantity measured in an experiment is subject to fluctuations which, in general, depend on the properties of the system under study. Fluctuations may reveal important insight into the system itself. The most efficient way to address fluctuations of a system created in heavy-ion collisions is via the study of event-by-event fluctuations: a given observable is measured on a event-by-event basis and the fluctuations of that observable are studied over an ensemble of events. Large-acceptance detectors allow a detailed analysis of individual collisions. Due to the hundreds or even thousands of particles produced in these collisions statistical methods can be applied. In the framework of statistical physics, fluctuations measure the so-called *susceptibility* of a system which determines the response of the system to external forces. Fluctuations allow to gain access to fundamental properties of the system just like in the experiments which

deal with macroscopic quantities. In general fluctuations may reveal information well beyond the thermodynamic properties of a system: as the system expands, fluctuations may have been frozen earlier, thus providing information about how the system was looking like before its thermal freeze-out set in. A beautiful example comes from astrophysics: fluctuations in the cosmic wave background radiation, first observed by COBE⁵. In heavy-ion collisions fluctuations of transverse momentum and charge have been studied so far. The former should be sensitive to temperature-energy fluctuations[82, 83, 84] which in turn provide a measure of the heat capacity of the system

$$\langle(\delta T)^2\rangle = \langle(T^2)\rangle - \langle(T)\rangle^2 = \frac{T^2}{C_V} \quad (1.16)$$

The QCD phase transition is associated with a maximum of the specific heat therefore temperature fluctuations should exhibit a minimum. Charge fluctuations[85, 86] are sensitive to fractional charges carried by the quarks. If an equilibrated partonic phase forms after heavy-ion collisions the charge fluctuation per entropy would be about a factor 2 or 3 smaller than in a hadronic scenario. Fluctuation of the ratio of positively to negatively charged particles has been proposed as one observable

$$\left\langle \delta \frac{N^+}{N^-} \right\rangle \simeq 4 \frac{\langle(\delta Q)^2\rangle}{\langle N_{ch} \rangle} \sim \frac{\langle(\delta Q)^2\rangle}{S} \quad (1.17)$$

Accounting for the fractional charge of the quarks, the variance of the ratio of positive and negative particles scaled by the total charged-particles multiplicity should be approximatively four times smaller than for a hadron gas. This prediction relies on the notion that quark-quark correlations can be neglected. However, they may be not negligible.

1.6 The Quark Gluon Plasma at the LHC

Starting from the estimates of the charged multiplicity, many parameters of the medium produced in the collision can be inferred. Table 1.4 presents a comparison of the most relevant parameters for SPS, RHIC and LHC energies[87].

At the LHC, the high energy in the center of mass is expected to determine a large energy density and an initial temperature at least a factor 2 larger than at RHIC. This high initial temperature extends also the lifetime and the volume of the deconfined medium. In addition, the expected large number of gluons favours energy and momentum exchange, considerably reducing the time needed for the thermal equilibration of the medium. To summarize, the LHC will produce *hotter, larger and longer – living* “drops” of QGP than the present heavy-ion facilities. The key advantage in this new scenario is that the quark-gluon plasma studied by the LHC experiments will be much more

⁵NASA’s COBE (Cosmic Background Explorer)[81] satellite was developed to measure infrared and cosmic microwave background radiation from the early Universe. COBE was launched on November 18, 1989.

Parameter	SPS	RHIC	LHC
$\sqrt{s_{NN}}$ [GeV]	17	200	5500
dN_{gluons}/dy	$\simeq 450$	$\simeq 1200$	$\simeq 5000$
dN_{ch}/dy	400	650	$\simeq 3000$
Initial temperature [MeV]	200	350	> 600
Energy density [GeV/fm ³]	3	25	120
Freeze-out volume [fm ³]	few 10 ³	few 10 ⁴	few 10 ⁵
Life-time [fm/c]	< 2	2-4	> 10

Table 1.4: Comparison of the parameters characterizing central nucleus-nucleus collisions at different energy regimes[87].

similar to the quark-gluon plasma that can be investigated from a theoretical point of view by means of lattice QCD. As mentioned, lattice calculations are mostly performed for a baryon-free system ($\mu_B = 0$). In general, $\mu_B = 0$ is not valid for heavy-ion collisions, since the two colliding nuclei carry a total baryon number equal to twice their mass number. However, the baryon content of the system after the collision is expected to be concentrated rather near the rapidity of the two colliding nuclei. Therefore, the larger the rapidity of the beams, with respect to their center of mass, the lower the baryo-chemical potential in the central rapidity region. The rapidities of the beams at SPS, RHIC and LHC are 2.9, 5.3 and 8.6, respectively. Clearly, the LHC is expected to be much more baryon-free than RHIC and SPS and, thus, closer to the conditions simulated in lattice QCD. In addition to this effect, also the higher temperature predicted for the LHC favours the comparison with theory. This point can be better understood by going back to the lattice results for ϵ/T^4 (Fig 1.5). If we now concentrate on the result obtained with 2+1 flavours, 2 light quarks plus a heavier one, we notice that ϵ/T^4 continues to rise for $T > T_c$, indicating that significant non-perturbative effects, not fully accounted for in the lattice formalism, are expected at least up to temperatures $T \simeq (2-3) T_c$. In Ref. [88] the strong coupling constant in this range is estimated as

$$\alpha_s(T) = \frac{4\pi}{18 \ln(5T/\Lambda_{QCD})} = 0.43 \text{ for } T = T_c ; 0.3 \text{ for } T = 2T_c ; 0.23 \text{ for } T = 4T_c \quad (1.18)$$

using the fact that the QCD scaling constant Λ_{QCD} is of the same order of magnitude as $T_c \sim 200$ MeV. These values confirm that non-perturbative effects are larger in the range $T < 2 T_c$. The conditions produced in heavy-ion collisions at SPS and RHIC are contained in this range ($T_{SPS} \approx 1.2 \times T_c$ and $T_{RHIC} \approx 2 \times T_c$), meaning that, in these cases, the comparison of experimentally determined quantities, such as temperature or energy density, to lattice QCD calculations is not fully reliable. With an initial

temperature of $\sim (4-5) T_c$ predicted for central Pb-Pb collisions at $\sqrt{s_{NN}} = 5.5$ TeV, the LHC will provide closer-to-ideal conditions (i.e. with smaller non-perturbative effects), allowing a direct comparison to the theoretical calculations. In this sense, the regime that will be realized at the LHC may be defined as “deep deconfinement”.

1.6.1 Hard partons at the LHC

The higher energy accessible at the LHC will imply not only a new regime concerning the properties of the produced QGP but will also allow to test them with new probes, in particular with hard-probes. At the LHC, hard processes contribute significantly to the total Pb-Pb cross-section. Hard partons are ideal probes of the medium because:

1. They are produced in the early stage of the collision in primary partonic scatterings, $gg \rightarrow gg$ or $gg \rightarrow q\bar{q}$, with large virtuality Q and, thus, on temporal and spatial scales, $\Delta\tau \sim 1/Q$ and $\Delta r \sim 1/Q$, which are sufficiently small for the production to be unaffected by the properties of the medium.
2. Given the large virtuality, the production cross-sections can be reliably calculated with the perturbative approach of pQCD. In fact, since

$$\alpha_s(Q^2) \propto \frac{1}{\ln(Q^2/\Lambda_{QCD}^2)} \quad (1.19)$$

in an expansion of the cross-sections in powers of α_s , for large values of Q^2 , the higher order terms (in general higher than next-to-leading order, $O(\alpha_s^3)$) are small and can be neglected. In this way, as already mentioned, one can safely use pQCD for the energy interpolations needed to compare p-p ,p-A and A-A and disentangle initial and final state effects.

3. While propagating through the medium they lose energy via QCD energy loss mechanisms which depend on the medium density, opacity and extension. Thus, from their attenuation, it is possible to gain information on the early stage of the medium evolution, before hadronization.

The estimated yields for charm and beauty production are expected to be 10 and 100 times larger, respectively, at the LHC than at RHIC. At the LHC also weakly interacting hard probes become accessible[1]. Direct photons (but in principle also Z^0 and W^\pm bosons) produced in hard processes will provide information about nuclear parton distributions at very large virtuality (Q^2). Z^0 and W^\pm bosons that do not interact strongly could be an ideal unbiased reference to better clarify and understand the energy loss mechanisms.

1.6.2 Parton Distribution Functions at low Bjorken- x : nuclear shadowing effect

Parton distribution functions (PDF) naively express the probability to find a parton with a given fraction (called Bjorken- x) of the proton (or nucleus) momentum. The PDF calculation is not possible from first principles starting from the QCD Lagrangian defined in Eq. 1.1. They are extracted from global fits to experimental data, mainly from deep inelastic scattering (DIS) experiments. By means of the DGLAP (Dokshitzer-Gribov-Lipatov, Altarelli-Parisi) evolution equations[89] describing the PDF Q^2 dependence, PDF values can be predicted at different Q^2 . In Figure 1.32 (left panel) an example of proton PDF at $Q^2 = 5 \text{ GeV}^2$ obtained with CTEQ 4L parametrization is reported, highlighting the different x regions accessible at RHIC and LHC.

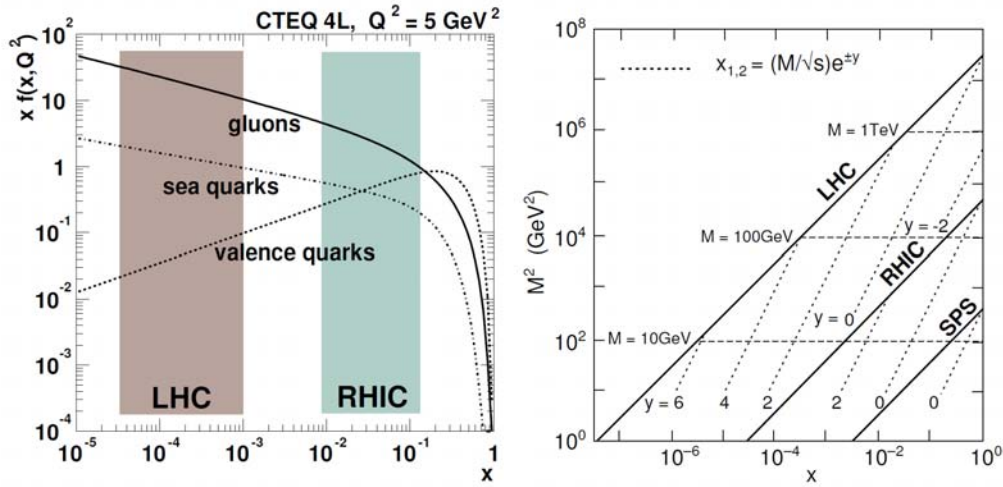


Figure 1.32: On the left: example of proton Parton Distributions Functions, obtained with CTEQ 4L parametrization at $Q^2 = 5 \text{ GeV}^2$. On the right: the range of Bjorken- x and M^2 relevant for particle production in nucleus-nucleus collisions at the top SPS, RHIC, and LHC energies. Lines of constant rapidity are shown for LHC, RHIC and SPS.

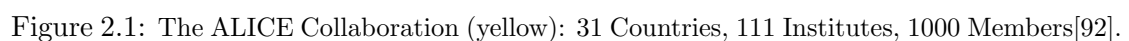
Reference PDFs for LHC, obtained from global fits from HERA data and using different schemes can be found in [90]. The large cross-sections for hard-scattering processes with large virtuality will allow to access the lowest Bjorken- x values ever access, as shown in Fig 1.32 for nucleus-nucleus collisions. The extension of the x range to values below 10^{-4} implies that, in a very simplified picture, a large- x parton in one of the two colliding nuclei “sees” the other incoming nucleus as a superposition of $\approx A \times 1/10^{-4} \approx 10^6$ gluons. These gluons are so many that the probability that the lower momentum ones merge together is not negligible: two gluons, with momentum fractions x_1 and x_2 , merge in a gluon with momentum fraction $x_1 + x_2$ (i.e. $g_{x_1} g_{x_2} \rightarrow g_{x_1+x_2}$, where g stands for the gluon parton distribution function). As a consequence of this “migration” towards larger values of x , the nuclear parton densities are depleted in the small- x region (and slightly enhanced in the large- x region) with respect to the proton

parton densities. This phenomenon is known as nuclear shadowing effect and it has been experimentally studied in electron-nucleus DIS experiments in the range $5 \cdot 10^{-3} < x < 1$ [91]. Experimental data in the x range covered by the LHC are not available yet: the existing data provide only weak constraints for the gluon PDF. ALICE will probe a continuous range of x as low as about 10^{-5} , accessing a novel x regime where strong nuclear gluon shadowing is expected.

All the physics topics here presented will be extensively studied by ALICE with a very composite detector that will be described in the next chapter.

The ALICE Experiment at LHC

ALICE is built and operated by a collaboration of more than 1000 members from about 30 countries (Figure 2.1).



The ALICE physics program includes dedicated runs at the maximum LHC energy in order to collect reference data and to develop a specific p-p program. In addition it will take data on protons and lighter ions beams, also at lower energy. In this section the experimental conditions at LHC and the ALICE data taking program are briefly described. Then an overview of the ALICE detector is given: the design and technology features of the various components are considered in relation to their tasks and performances. A particular attention is devoted to the Inner Tracking System and to its role within the experiment. Moreover, all the LHC experiments will produce an unprecedented amount of data: they will be distributed and analyzed worldwide using the GRID framework. The ALICE software framework, developed for analysis on the GRID, is introduced in a dedicated section.

2.1 The Large Hadron Collider

The Large Hadron Collider (LHC)[93] at CERN is the biggest particle accelerator worldwide. First discussions on the project started in 1984. The LHC project was approved in 1994 and the construction work in the underground tunnel started in 2001 after dismantling of the LEP collider⁶. LEP was previously built into the tunnel which is located under the Swiss-French border area close to Geneva at a depth of 50 to 175 m. The LHC has a circumference of 27 km. Its largest achievable acceleration energies are 7 TeV for protons and 2.76 TeV per nucleon for lead ions, therefore providing collisions at $\sqrt{s} = 14$ TeV and $\sqrt{s_{NN}} = 5.5$ TeV, respectively. These are the largest energies that have ever been accessible in particles collisions experiments.

2.1.1 The LHC Design Features

The LHC is a synchrotron that accelerates two counter-rotating beams in separate beam pipes. One of its goals is to reach an high luminosity for protons beams (namely 10^{34} cm⁻² s⁻¹) and it is now on track to achieve it. The layout of the LHC is shown in Figure 2.2. It is segmented into octants, each having a straight section in its center, referred to as *points*. The arcs are called Sector xy where x and y are the numbers of the corresponding octants in clock-wise order, e.g. Sector 34. Four of the straight sections contain the experiments (points 1, 2, 5, and 8) which are the only locations where the beams cross. Particles are injected before point 2 and 8. The radio-frequency (RF) system that accelerates the particles is located at point 4; the beam dumping system is located at point 6. At point 3 and 7, collimation systems that “clean” the beam by removing particles that have either a too large spatial distance to their bunch (particles in the so-called beam-halo) or are too fast or too slow, thus separated in momentum-space, are placed. The cleaning prevents particles from being lost in an uncontrolled fashion within the accelerator.

⁶The Large Electron-Positron (LEP) Collider operated in the years 1989 to 2000 with a maximum center-of-mass energy of 209 GeV.

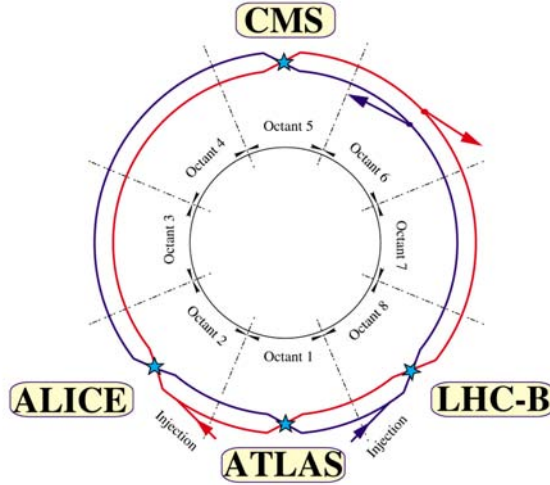


Figure 2.2: Schematic view of the LHC.

The main components of the machine are 1232 dipoles that bend the beam trajectories. An LHC dipole has a length of 14.3 m and contains superconducting magnets which operate at a temperature of 1.9 K, notably 0.8 K lower than the background temperature of the Universe. Powered by a maximum current of 11.7 kA the dipoles provide a magnetic field from 0.535 T during injection (beam energy of 450 GeV) to 8.33 T during nominal collisions (beam energy of 7 TeV). A pictorial view of a LHC dipole is shown in Figure 2.3. Eight RF cavities per beam deliver radio-frequency power to accelerate the beams, keep the bunches of particles well-localized and compensate for energy loss due to synchrotron radiation. The cavities produce a field of 5.5 MV/m.

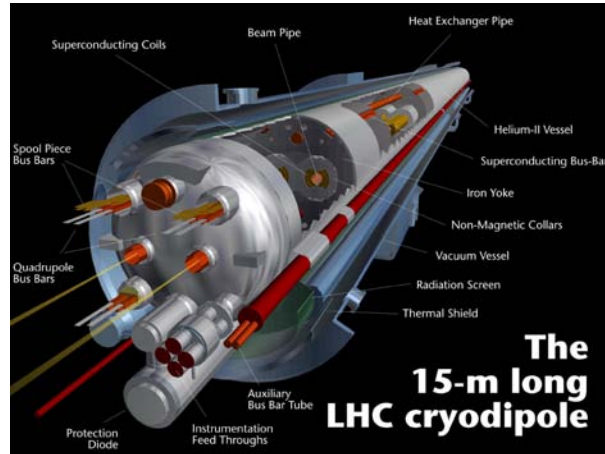


Figure 2.3: Schematic view of a LHC Dipole Magnet.

Injection of bunches into the LHC is preceded by acceleration in the LINAC2, PS booster, PS, and SPS accelerators. The acceleration sequence is slightly different for heavy ions, since bunches pass the LINAC3, LEIR, PS, and SPS accelerators. In Figure 2.4 all the different components composing the actual CERN accelerating chain are

shown.

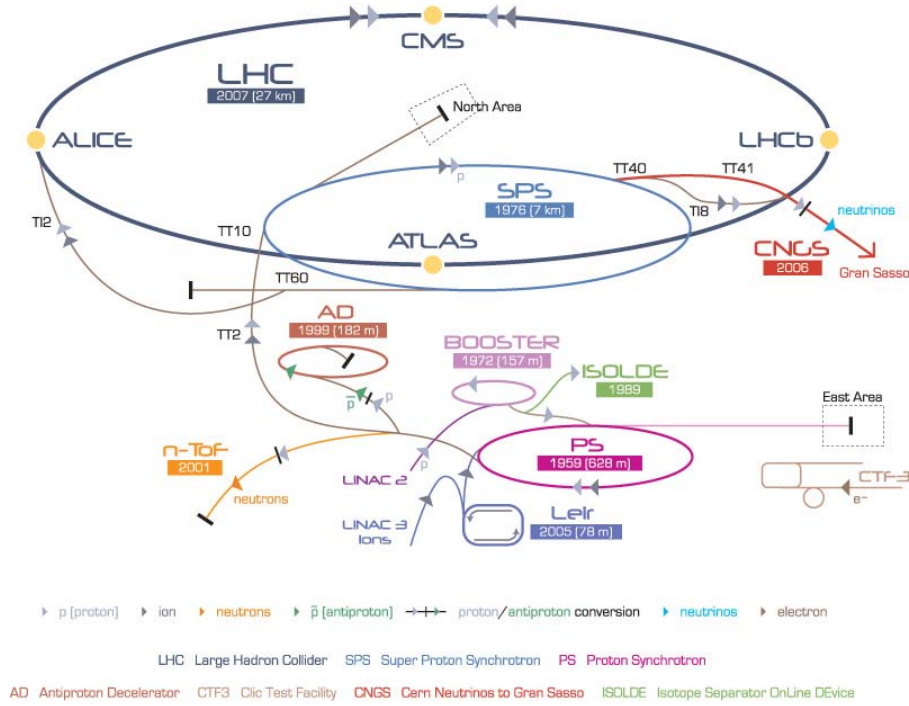


Figure 2.4: CERN Accelerators Scheme.

Several injections to the LHC are needed until all bunches of both beams are filled. The design parameters foresee nominal operation, where each beam is filled with 2808 bunches each consisting of 1.15×10^{11} protons. Bunches have a r.m.s. length between 11.24 cm at injection and 7.55 cm at collision. They are separated by 25 ns. LHC's design luminosity is $10^{34} \text{ cm}^{-2} \text{ s}^{-1}$ for protons and $10^{27} \text{ cm}^{-2} \text{ s}^{-1}$ for Pb ions. However, the LHC will deliver a significantly lower luminosity to the ALICE experiment during proton collisions (about $3 \times 10^{30} \text{ cm}^{-2} \text{ s}^{-1}$) by means of defocusing or displacing the beams. At nominal luminosity about 2.4×10^9 pp collisions are estimated to occur per second in the LHC.

Six experiments take place at the LHC:

- **ALICE (A Large Ion Collider Experiment)** which will be discussed in the following paragraphs.
- **ATLAS (A Toroidal LHC ApparatuS)**[94] and **CMS (Compact Muon Solenoid)**[95] are general-purpose proton-proton detectors that are built to cover the widest possible range of physics at the LHC. Specific topics are the search for the Higgs boson and physics beyond the Standard Model, e.g. new heavy particles postulated by supersymmetric extensions (SUSY) of the Standard Model and evidence of extra dimensions.

- **LHCb (The Large Hadron Collider beauty experiment)**[96] studies CP-symmetry violation processes in heavy b quark systems.
- **LHCf (Large Hadron Collider forward experiment)**[97] measures forward particles created during LHC collisions to provide further understanding of high-energy cosmic rays. The detector is placed close to the ATLAS experiment.
- **TOTEM (TOTAl Elastic and diffractive cross-section Measurement)**[98] measures the total cross-section, elastic scattering, and diffractive processes. The detector is located close to the CMS experiment.

In Figure 2.5 the location along the accelerator ring of the four major experiments is shown.

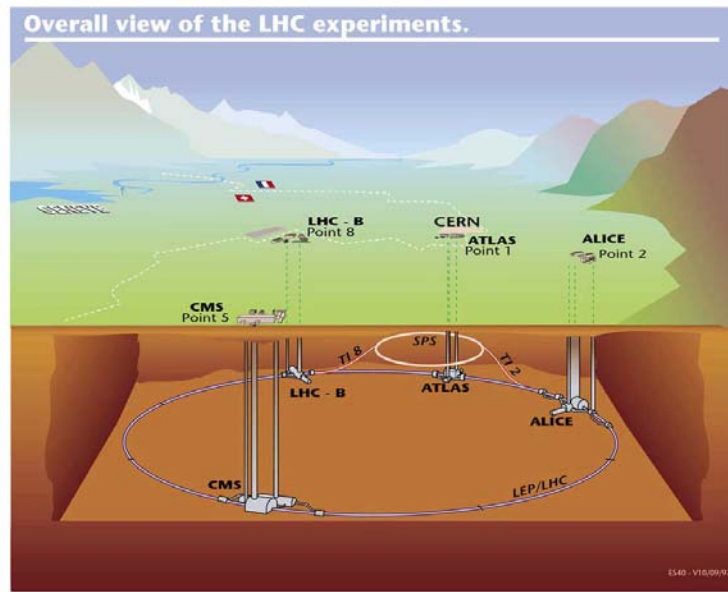


Figure 2.5: LHC accelerator and location of the four major experiments: ATLAS, CMS, ALICE, LHCb.

2.1.2 StartUp and Status

LHC started on the 10th September 2008 with great success. In less than an hour after the first injection the first beam had been sent successfully around the entire ring. During the same day the second beam in the opposite direction successfully passed through the ring. In a few days commissioning made important progress. The RF captured the beam successfully soon after and a stable circulating beam was achieved on the 12th of September. Unfortunately, a transformer failure in point 8 stalled the commissioning for about a week. On the 19th September when LHC was basically ready for collisions at $\sqrt{s} = 900$ GeV, an accident occurred during the 10 TeV magnet commissioning without beam in Sector 34, the last sector that was commissioned to this energy[99]. To repair

the damage that occurred in the machine the sector had to be warmed up, which delayed the LHC operations until late Autumn 2009. On 23 November 2009 LHC was able to start again its activity and collected the first 900 GeV pp collisions. After that, the beams energy was increased to 1.18 TeV per beam. During the 2010 spring the beam energy was increased to 3.5 TeV, and the machine has run with this conditions until the 2010 Autumn when the first PbPb collisions at $\sqrt{s} = 2.76$ TeV were provided.

2.2 The ALICE Physics Program

A comprehensive heavy-ion program at the LHC is aimed at two main objectives: colliding the largest available nuclei at the highest possible energy and a systematic study of different collision systems (p-p, p-A, A-A) at different beam energies. The LHC is expected to start with several months of pp running followed at the end of each year by several weeks of heavy-ion collisions. For rate estimates, all LHC experiments use an effective time per year of 10^7 s for pp and 10^6 s for heavy-ion operation. The ALICE program is summarized below:

- pp collisions at $\sqrt{s} = 900$ GeV and 7 TeV during 2010
- PbPb collisions at $\sqrt{s} = 2.76$ TeV in November 2010
- pp collisions at $\sqrt{s} = 7$ TeV during 2011
- PbPb collisions at $\sqrt{s} = 2.76$ TeV in Autumn 2011
- LHC technical stop in 2012
- pp collisions at $\sqrt{s} = 14$ TeV starting from 2013 and then regular runs
- Subsequent heavy-ion program
 - 1-2 years PbPb
 - 1 year pPb-like collisions (pPb, dPb or α Pb)
 - 1-2 years Ar-Ar.

The operation characteristics for a ten year period are summarized in Table 2.1.

2.3 Luminosity in Pb-Pb collisions

One of the most important experimental issues in the design of the experiment and of its physics program is the luminosity for Pb-Pb collisions. It depends on the limitations imposed by both the detector and the accelerator. Among the sub-detectors, the most constraining limits come from the main tracking device, the Time-Projection Chamber (TPC), and the forward muon spectrometer. The TPC limits the maximum usable luminosity because of event pile-up during the $88 \mu\text{s}$ drift time. The TPC is expected to

	pp	Ar-Ar	Ar-Ar	Pb-Pb	d-Pb
$\langle L \rangle$ ($\text{cm}^{-2} \text{s}^{-1}$)	3×10^{30}	3×10^{27}	10^{29}	10^{27}	8×10^{28}
σ_{inel} (mb)	70	3000	3000	8000	2600
Rate (s^{-1})	2×10^5	9×10^3	3×10^3	8×10^3	2×10^5
Runtime (s)	10^8	10^6	2×10^6	5×10^6	2×10^6
Events	2×10^{13}	9×10^9	6×10^{11}	4×10^{10}	4×10^{11}
Particles per event	100	2400	2400	14200	500
N_{tot}	2.1×10^{15}	2.2×10^{13}	1.4×10^{15}	5.7×10^{14}	2×10^{14}

Table 2.1: Experimental conditions for a ten-year period in different collision type periods.

be operated even at luminosities above $10^{27} \text{cm}^{-2} \text{s}^{-1}$, given that the multiplicity in the Pb-Pb collisions remains under 4000 per unit of pseudo-rapidity. On the other hand, the maximum acceptable illumination of the muon spectrometer trigger chambers limit the luminosity to $(2 - 4) \times 10^{28} \text{cm}^{-2} \text{s}^{-1}$. However, the limitations of the LHC are stronger than those imposed by the sub-detectors technologies: the machine will provide the nominal luminosity of $L_0 = 10^{27} \text{cm}^{-2} \text{s}^{-1}$. During the first ALICE PbPb run the luminosity was $\sim 10^{23} \div 10^{25} \text{cm}^{-2} \text{s}^{-1}$.

2.4 Dose rates and neutron fluences

Another important issue taken into account while designing the ALICE detector is the radiation level. Considering all the collision types, i.e. protons, light-ions and heavy-ion beams for different time periods and luminosities, the radiation load on the various parts of the detectors must therefore be calculated for a combination of beam conditions. The main sources of radiation in ALICE are: the particles produced in the collisions, the beam losses from the injection point of LHC and the beam-gas interactions in p-p runs. The dominant contribution comes anyway from particles produced at the interaction point. The ten-year integrated values for the doses and the neutron fluences in the various sub-detectors (Figure 2.9) and in the electronic racks are listed in Table 2.2. The radiation load reaches its maximum (2 kGy dose, 1×10^{12} neutrons cm^{-2}) close to the beam pipe, in the Silicon Pixel Detector region, and scales with $\sim 1/r^2$ that means that doses for the other subsystems can also be estimated from this table. In particular, the regions of the forward detectors, V0 and T0, close the beam pipe will receive doses and neutron fluences similar to those of the pixel detector[100].

System	Radius (cm)	Dose (Gy)	Neutron Fluence (cm^{-2})
SPD1	3.9	2.2×10^3	8.0×10^{11}
SPD2	7.6	5.1×10^2	5.6×10^{11}
SDD1	14	1.9×10^2	4.5×10^{11}
SDD2	24	1.0×10^2	4.2×10^{11}
SSD1	40	4.0×10^1	4.1×10^{11}
SSD2	45	2.6×10^1	4.1×10^{11}
TPC (in)	78	1.3×10^1	3.6×10^{11}
TPC (out)	278	2.0×10^0	2.4×10^{11}
TRD	320	1.6×10^0	1.5×10^{11}
PID	350	1.1×10^0	1.0×10^{11}
HMPID	490	5.0×10^{-1}	8.0×10^{10}
RackLoc1		5.6×10^{-1}	8.4×10^7
RackLoc2		3.8×10^{-1}	1.5×10^6
RackLoc3		2.2×10^{-6}	3.5×10^3
RackLoc4		7.8×10^{-6}	9.2×10^3

Table 2.2: Experimental conditions for a ten-year period in different collision type periods.

2.5 The ALICE Detector Layout

As mentioned in the Introduction, goal of this thesis is the study of the strange resonance $\Sigma(1385)$ in the strong decay channel $\Lambda\pi$. In order to be able to reconstruct the $\Sigma(1385)$ and Λ signal it is mandatory to reconstruct and identify their daughter particle, i.e protons and pions, even at low momenta values. To achieve this goal the central barrel detector plays a fundamental role and among them, in particular the Inner Tracking System (ITS), the Time Projection Chamber (TPC) and Time Of Flight (TOF) are necessary because of their particle identification capability. Especially in Pb-Pb collisions, where the particle multiplicity is very high and so the combinatorial background to the $\Sigma(1385)$ signal is huge, their features in terms of spatial, momentum and dE/dx resolution will be crucial. These sub-detectors together with all the others composing the ALICE detector will be described hereafter.

The ALICE detector, shown in Figure 2.6, 2.7 and 2.9, consists of a central detector system, covering mid-rapidity ($|\eta| < 0.9$) over the full azimuth, and several forward sub-detectors. The ALICE global reference frame is defined with the z axis parallel to the beam direction pointing in the opposite direction to the muon arm and the x and y axes

in the plane transverse to the beam direction, the x pointing towards the center of the LHC ring, the y axis pointing upward.

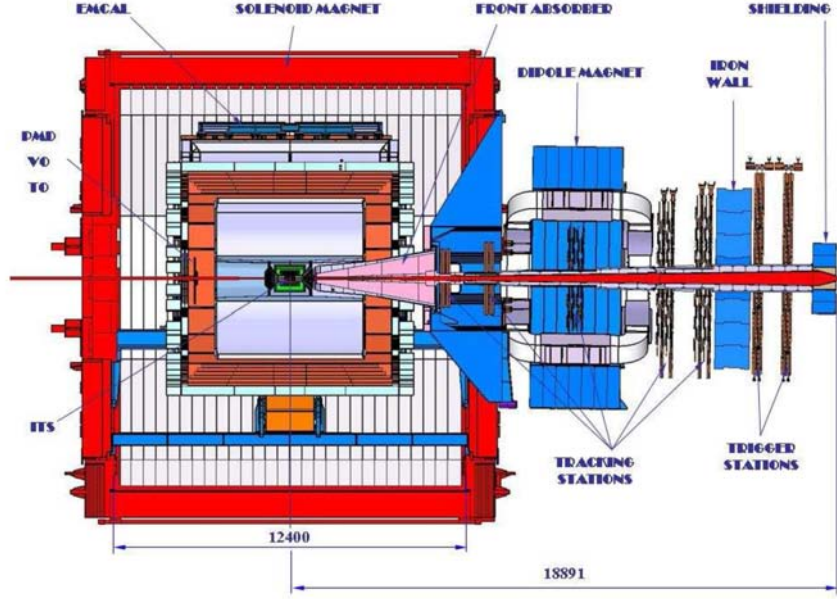


Figure 2.6: ALICE detector layout lateral view. Lengths in cm.

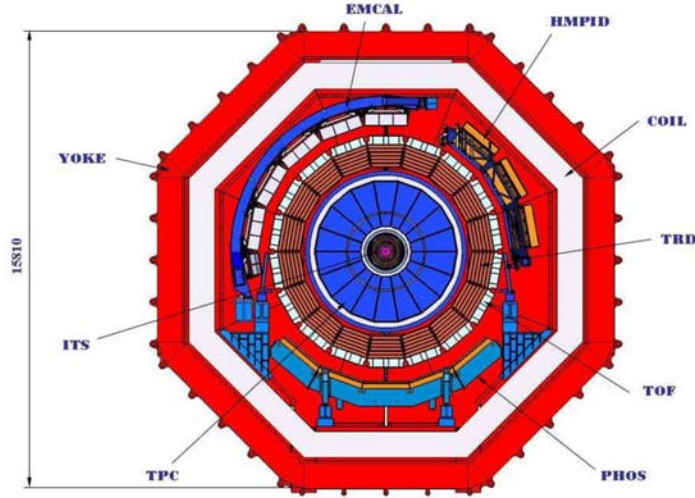


Figure 2.7: The ALICE detector layout frontal view. Lengths in cm.

The central detectors are placed inside the large solenoid magnet originally constructed for the L3 experiment at LEP, with an internal length of 12 m and a radius of 5 m and a 0.5 T nominal field. The field homogeneity in the volume of the detectors has been improved with respect to the L3 situation, reducing the variations below 2% of the nominal field value. The beam pipe is built in beryllium with an outer radius of 3 cm and a thickness of 0.8 mm, corresponding to 0.3% of radiation length X_0 . The central system includes, from the interaction vertex to the outside, six layers of high-resolution

silicon detectors (Inner Tracking System), the main tracking system of the experiment (Time-Projection Chamber), a transition radiation detector for electron identification (Transition-Radiation Detector), and a particle identification array (Time-Of-Flight). The central system is complemented by a small-area array of ring-imaging Cherenkov detectors for the identification of high-momentum particles (High-Momentum Particle Identification Detector), and two electromagnetic calorimeters, one consisting of a small arm of high-density crystals (PHOTon Spectrometer) for the photon and neutral mesons detection, and the other made of Pb-scintillators, for measuring jets properties, and called EmCal. The central barrel detectors are devoted to charged hadrons, electrons and photons reconstruction and identification in a very high-multiplicity environment like what will be produced in PbPb collisions.

Close to the L3 magnet doors and outside the L3 magnet, some detectors are placed for triggering (T0 and V0) or to measure global event characteristics (Photon Multiplicity Detector and Zero-Degree Calorimeter). The detection and identification of muons are performed with a dedicated Muon Spectrometer, placed outside the magnet, that exploits the beam-perpendicular field of a large warm dipole magnet.

Figure 2.8 shows the pseudorapidity acceptance of the subdetectors with an overlaid $dN_{ch}/d\eta$ prediction for p-p collisions by the event generator PYTHIA. The subdetectors have full coverage in azimuth except for the ones marked with an asterisk. SPD, SDD, and SSD are the subsystems of the ITS. Two ranges are given for the TPC, depending on the conditions imposed on the track length (full and reduced). ZN, ZP, and ZEM are the different parts of the ZDC.

In the following section an overview of the sub-detectors is given together with some considerations about their task and performances.

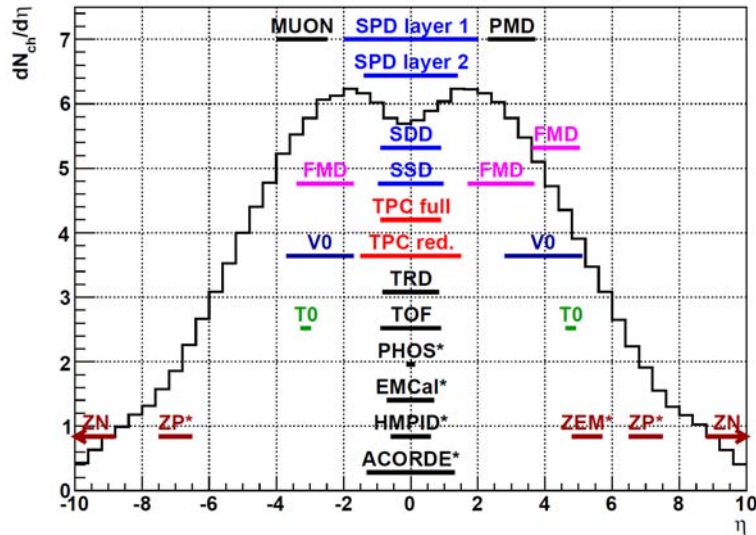


Figure 2.8: ALICE pseudorapidity acceptance.

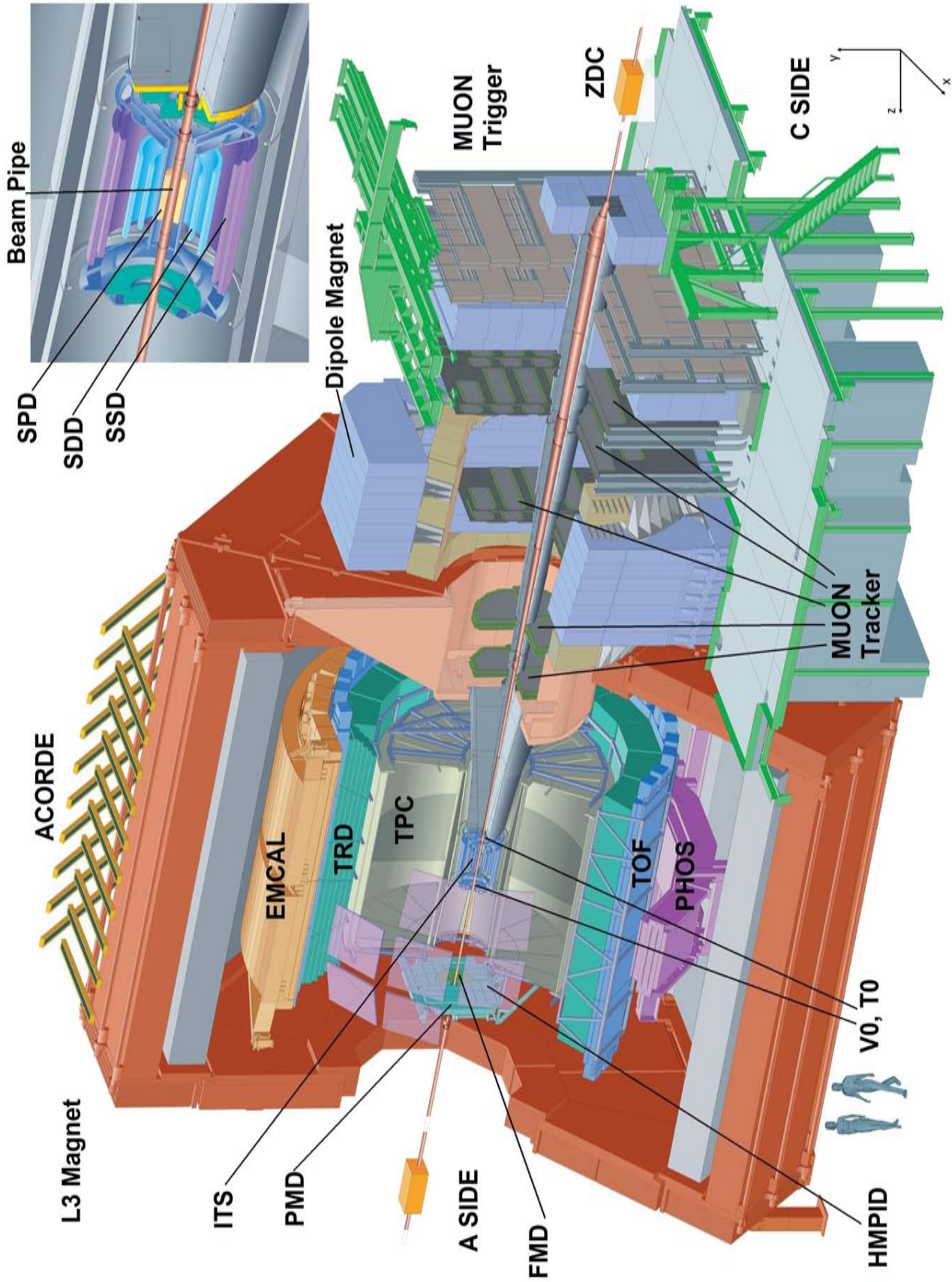


Figure 2.9: Schematic view of the ALICE detector.

2.5.1 The Central Barrel

2.5.1.1 The Inner Tracking System

The Inner Tracking System (ITS) is placed close to the interaction point and it was designed to accomplish some tasks which are crucial for the ALICE physics program. The number, position and segmentation of the ITS layers, as well as the detector technologies, have been optimized according to the following requirements:

- Efficient track finding in the high multiplicity environment predicted for central PbPb collisions at LHC, which was estimated up to 8000 particles per unit of rapidity at the time of the ALICE design. This calls for high granularity in order to keep the system occupancy at the level of a few per cent on all the ITS layers.
- High resolution on track impact parameter and momentum. The momentum and impact parameter resolution for low-momentum particles are dominated by multiple scattering effects in the material of the detector; therefore the amount of material in the active volume has been kept to a minimum. Moreover, for track impact parameter and vertexing performance, it is important to have the innermost layer as close as possible to the beam axis.
- Possibility to use the ITS also as a standalone spectrometer. For this reason, the four layers equipped with SDD and SSD provide also particle identification capability via dE/dx measurement.

In more details the ITS tasks are:

- to reconstruct the primary vertex with a resolution better than $100\ \mu\text{m}$;
- to reconstruct the secondary vertices and to measure the impact parameter for the decays of hyperons and D and B mesons;
- to track and identify the low- p_t ($< 100\ \text{MeV}$) particles, which are not seen from the outer detectors;
- to improve the TPC momentum resolution for the high- p_t particles;
- to track and identify the particles traversing the dead zones of the TPC.

Moreover, in cooperation with the other detectors, the ITS characteristics allow to improve the performances in the study of many ALICE physics topics: the global observables of the heavy-ion collisions, like the charged particle multiplicity and the particle spectra and correlations; the resonance production and possible variations in their parameters; a precise mass measurement of the heavy-quarks states to improve the signal-to-background ratio for the observation of the quarkonia suppression; the jet observation, covering also the TPC dead zones. These tasks will be accomplished by the ITS thanks to its design and construction characteristics, which are described hereafter.

ITS characteristics

The ITS is placed very close to the interaction point. It consists of six concentric cylindrical layers of silicon detectors, the innermost of them located at a radius $r = 3.9$ cm, the outermost at $r = 43.9$ cm (Figure 2.10), and it is placed inside the Time Projection Chamber.

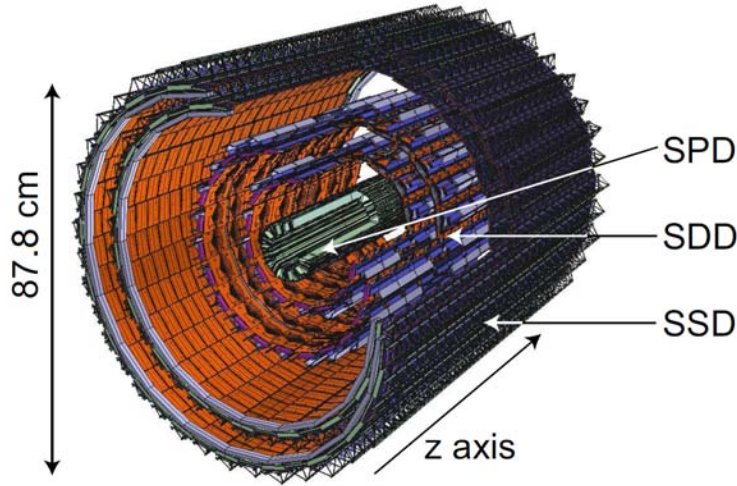


Figure 2.10: Schematic view of the ITS.

The number, position and segmentation of the layers are optimized for efficient track reconstruction and high impact-parameter resolution. In particular, the overall ITS dimensions are constrained by the geometry of the neighbouring parts of the ALICE apparatus: the inner radius is the minimum allowed by the beryllium beam pipe coaxial with the ITS detector layers; the outer radius is instead determined by the request to match the reconstructed tracks with those from the TPC. The layers dimensions along the beam axis allow to cover a rapidity range of $|\eta| < 0.9$ for all vertices located within the length of the interaction diamond, i.e. $\pm 1\sigma = \pm 10.6$ cm along the beam direction. The first layer covers a more extended range ($|\eta| < 1.98$) in order to provide, together with the Forward Multiplicity Detectors, a continuous coverage in rapidity for the measurement of the charged-particles multiplicity.

Besides the rapidity coverage, the ITS has been designed to meet the experimental requirements in terms of granularity, spatial resolution and particles discrimination. In the two innermost layers, where the particles density is expected to reach ~ 50 particles/cm², highly segmented pixel detectors have been chosen: their granularity allows to detect and resolve the particles keeping the occupancy low and to reconstruct the space points with high spatial precision. The other four layers provide also the dE/dx information on a large dynamic range for the particle identification, allowing the ITS to operate as a stand-alone low- p_t spectrometer: the central layers are equipped with silicon drift detectors, with true two-dimensional read-out like the pixels, providing high spatial precision in both directions; finally on the outermost layers, where the particle density is expected

to be lower and the granularity requirements are less stringent, double-sided microstrip detectors have been placed, assuring high precision in the bending direction ($\sim 20 \mu\text{m}$) and minimizing the fake track probability. Hereafter the detailed description of the three different types of silicon detectors is given, followed by a discussion of their tasks and performances.

Silicon Pixel Detector

The ALICE SPD is made of hybrid silicon pixel detectors, consisting of a two-dimensional matrix of reverse-biased silicon detector diodes bump-bonded to readout chips. The readout is binary: when the signal, pre-amplified and shaped by the read-out chip, surpasses the applied threshold, the corresponding cell outputs a logical 1. Two SPD modules are mounted together along the z direction to form a 141.6 mm long half-stave. Two half-staves are attached head-to-head along the z direction to a carbon-fibre support sector, which provides also the cooling. Each sector supports six staves: two on the inner layer and four on the outer layer. The assembly of half-staves on sectors provides an overlap of about 2% of the sensitive area along $r\phi$, while there is no sensor overlap along z , where, instead, there is a small gap between the two half-staves. Five sectors are then mounted together to form an half-barrel and finally the two (top and bottom) half-barrels are mounted around the beam pipe to close the full barrel, which is actually composed of 10 sectors. In Figure 2.11 the layout of the SPD is shown. The characteristics in terms of geometry, active area and other operating parameters are summarized in Table 2.3.

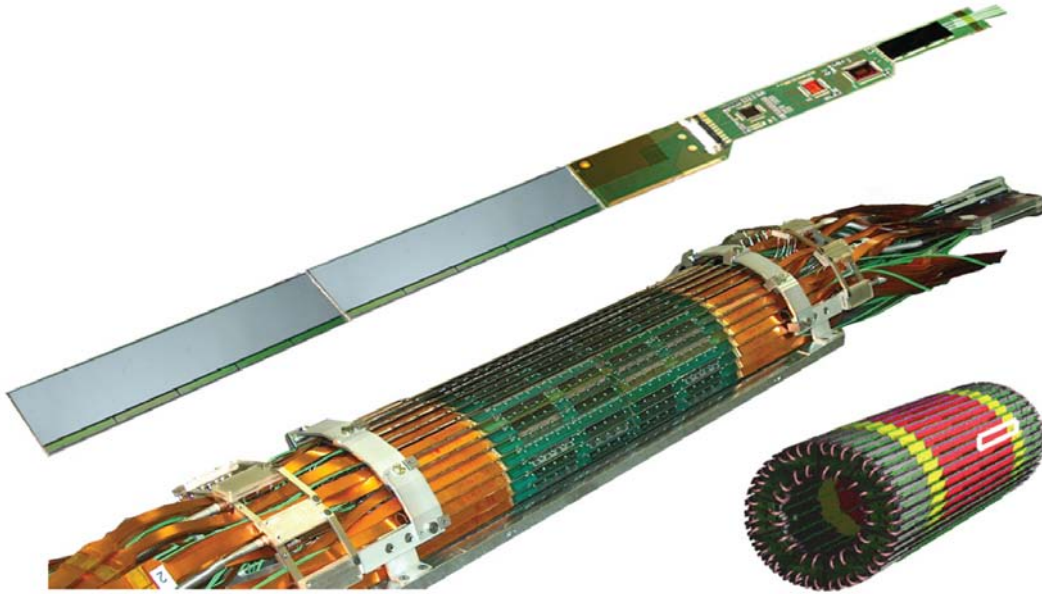


Figure 2.11: The Silicon Pixel Detector layout: an half stave (left) and the pixel barrel (right)[101].

Besides the high performances requested in terms of granularity and spatial preci-

sion, the SPD is radiation hardened in order to operate in a relatively high radiation environment: for the 10 years running period foreseen for the experiment, in the case of the inner layer, the integrated levels of total dose and fluence are estimated to be 220 krad (2.2 kGy) and $10^{12} \text{ n}\cdot\text{cm}^{-2}$ (1 MeV neutron equivalent), respectively. In addition, its design minimizes the material budget (down to $\sim 1\%$ of the radiation length X_0 per layer, for a straight track perpendicular to the surface) in order to reduce the Coulombian scattering of the traversing particles. The sensor is $200 \mu\text{m}$ thick; its high segmentation allows to keep the diode capacitance low, resulting in an excellent signal-to-noise ratio at high speed. The SPD is cooled with an evaporative system based on C_4F_{10} that allows the detector to operate at an average temperature range 25°C to 30°C : cooling capillaries are embedded in the supports, while a high thermal conductivity grease transfers the heat from the front-end electronics. Finally, exploiting the speed of the detector response, each pixel chip provides a *Fast – OR* digital pulse when at least one pixels in the matrix is hit. The pre-processed *Fast – OR* data can contribute to the Level 0 trigger decision in the ALICE acquisition[101]. This feature is very useful in particular in the case of events with very low multiplicities in pp runs and significantly improves the background rejection in these interactions and the event selection in heavy-ion runs.

Silicon Drift Detector

The two central layers of the ITS, where the charged particle density is expected to reach up to 7 cm^{-2} , are equipped with Silicon Drift Detectors (SDD). The Silicon Drift Detectors provide the localization of the impact point of a particle in two dimensions, exploiting the silicon segmentation on one coordinate and the measurement of the transport time of the deposited charge to measure the second coordinate. The high resolution and multi-track capability are provided at the expense of speed. They are therefore well suited to the ALICE experiment in which very high particle multiplicities are coupled with relatively low event rates. A SDD module has a series of parallel, implanted p^+ field strips, connected to a voltage divider on both surfaces of the high-resistivity n-type silicon wafer. The voltage divider is integrated on the detector substrate itself. The field strips provide the bias voltage to fully deplete the volume of the detector and they generate an electrostatic field parallel to the wafer surface, thus creating a drift region. Electron-hole pairs are created by the charged particles crossing the detector. The holes are collected by the nearest p^+ electrode, while the electrons are focused into the middle plane of the detector and driven by the drift field towards the edge of the detector where they are collected by an array of anodes composed of n^+ pads. The small size of the anodes, and hence their small capacitance, imply low noise and good energy resolution. The owing mechanism is shown in the scheme in Figure 2.12.

An ALICE SDD sensor is produced from homogeneous high-resistivity ($3 \text{ k}\Omega\cdot\text{cm}$) $300 \mu\text{m}$ thick Neutron Transmutation Doped (NTD) silicon. The layout is shown in Figure 2.13: the sensitive area is split into two drift regions by the central cathode strip, HV-biased with 2.4 kV. In each drift region the drift field parallel to the wafer surface

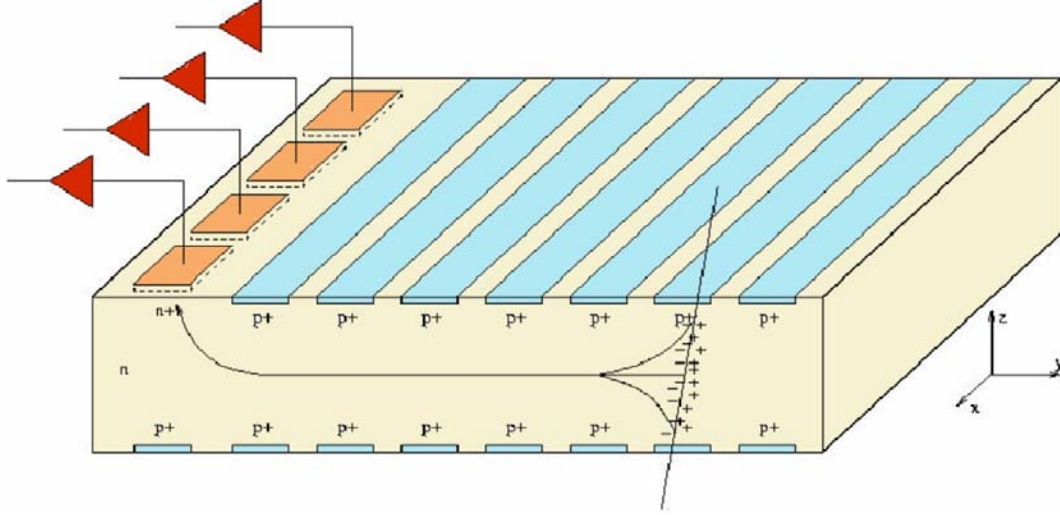


Figure 2.12: Schematic view of the charges drifting inside the SDD sensor.

is generated by the p^+ cathode strips that fully deplete the detector volume, a row of anodes collects the charges and three rows of MOS charge injectors monitor the drift velocity which depends on temperature[102].

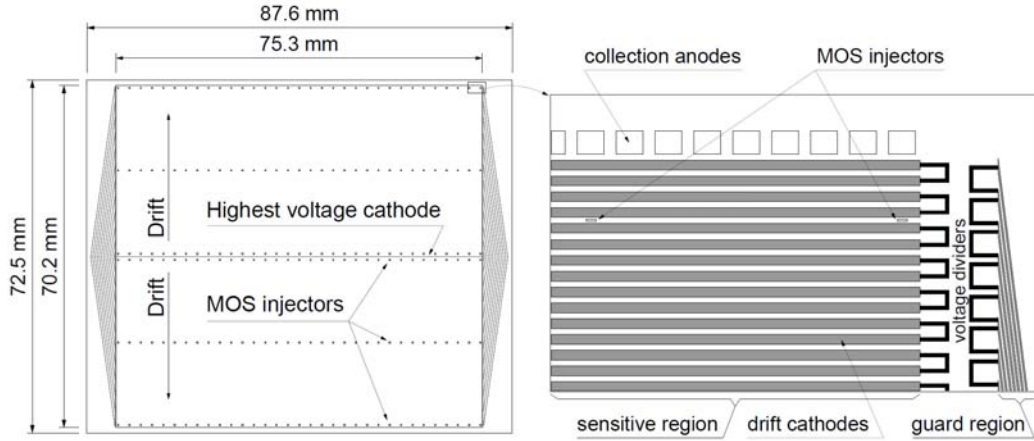


Figure 2.13: Schematic view of the ALICE SDD. The sensitive area is split into two drift regions by the central, highest voltage, cathode. On each drift region 256 anodes provide to collect the charges and three rows of 33 point-like MOS charge injectors are used to monitor the drift velocity[3].

This dependence ($v_{drift} \propto T^{2.4}$) causes a velocity variation of 0.8%/K at room temperature. Owing to the diffusion during the drift, the electrons reach the anode region with a Gaussian distribution. The coordinate perpendicular to the drift direction is given by the centroid of the collected charge. The coordinate along the drift direction is measured by the centroid of the signal in the time domain, taking into account the amplifier response. The SDD modules are mounted on linear structures called *ladders*. There are 14 *ladders* with six modules each on the inner SDD layer (layer 3), and 22

ladders with eight modules each on the outer SSD layer (layer 4). The modules are attached to the *ladder* space frame, which is a lightweight truss made of Carbon-Fibre Reinforced Plastic (CFRP) with a protective coating against humidity absorption, using ryton pins and have their anode rows parallel to the ladder axis (z). The *ladders* are mounted on a CFRP structure made of a cylinder, two cones and four support rings. The cones provide the links to the outer SSD barrel and have windows for the passage of the SSD services. The support rings are mechanically fixed to the cones and bear reference ruby spheres for the ladder positioning.

The SSD achieves a space precision as good as $35\ \mu\text{m}$ and $25\ \mu\text{m}$ along the drift direction ($r\phi$) and along the anode (z) respectively. Moreover, the detector provides two out of the four dE/dx samples needed for the ITS particle identification.

Silicon Strip Detector

The outer layers of the ITS are composed of Silicon Strip Detector (SSD) modules: they use $300\ \mu\text{m}$ thick double sided silicon sensors with 768 strips on each side; the strips, with a pitch of $95\ \mu\text{m}$, form a stereo angle of $35\ \text{mrad}$ between the two opposite module sides, which assures a stereo view and the reduction of ambiguities, even at high particle densities. The picture of an SSD module is visible in Figure 2.14.

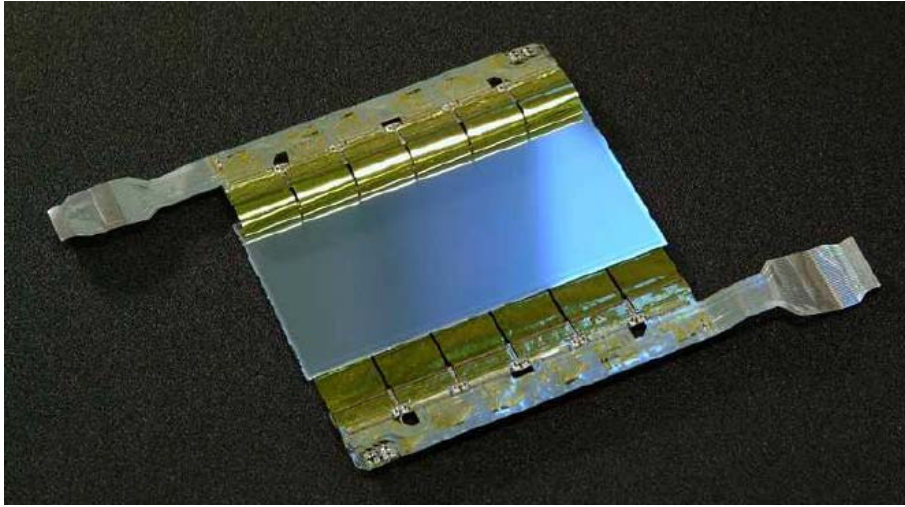


Figure 2.14: An SSD module during the construction, after the assembling of the sensor with the electronics.

The modules are assembled on *ladders* of the same design as those supporting the SDD (Figure 2.15). The innermost SSD layer (layer 5) is composed of 34 *ladders*, each of them being a linear array of 22 modules along the beam direction. Layer 6 (the outermost ITS layer) consists of 38 *ladders*, each of them made of 25 modules.

The 72 *ladders*, carrying a total of 1698 modules, are mounted on Carbon Fibre Composite support cones in two cylinders (Figure 2.16).

The spatial resolution of the SSD system is determined by the $95\ \mu\text{m}$ pitch of the sensor readout strips and by the charge-sharing between those strips. Without making

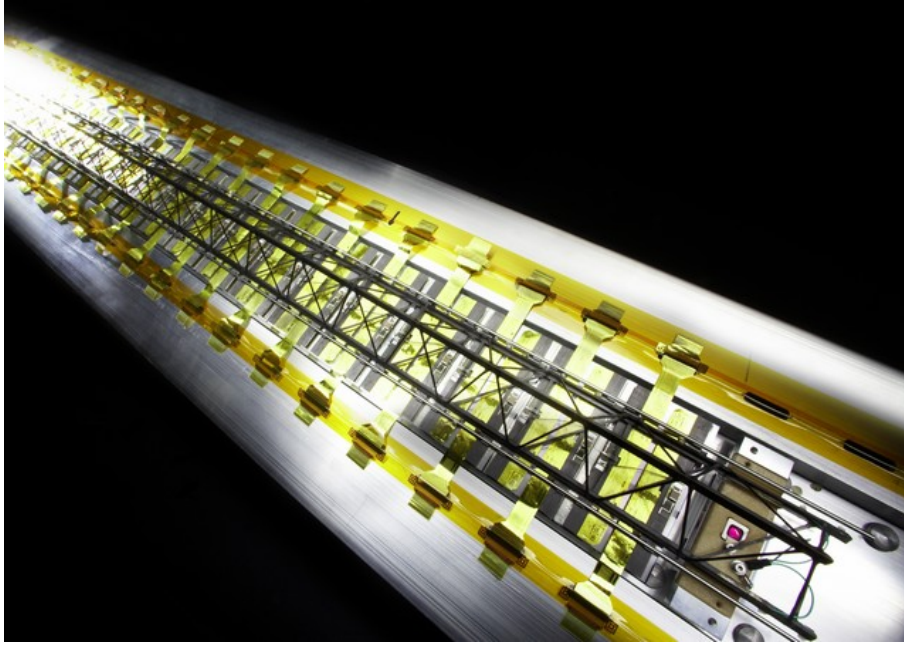


Figure 2.15: An SSD *ladder* during the assembling phase.

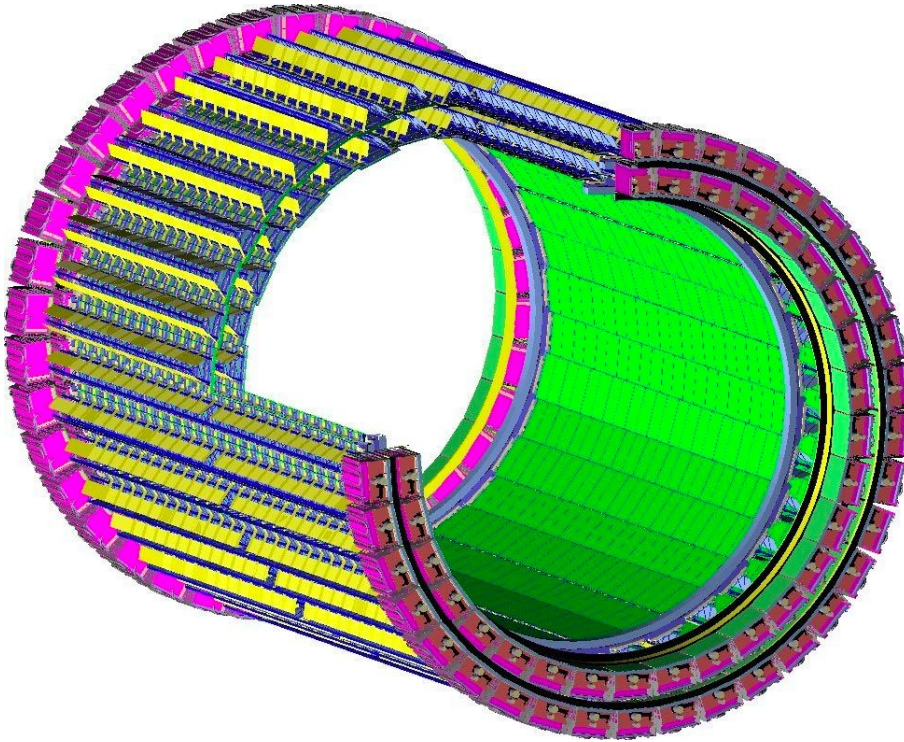


Figure 2.16: Scheme of the SSD cone. The *ladders* are progressively installed on the carbon fibre cones with the corresponding readout electronics modules, forming the two SSD cylindrical layers.

use of the analogue information the r.m.s spatial resolution is $27 \mu\text{m}$. Beam tests have shown that a spatial resolution of better than $20 \mu\text{m}$ in the $r\phi$ direction can be obtained

by analyzing the charge distribution within each cluster. In the direction along the beam the spatial resolution is about $830 \mu\text{m}$. The SSD layers are crucial for the matching of tracks from the TPC to the ITS. They provide a two dimensional measurement of the track position and dE/dx information to assist particle identification, in particular for low-momentum particles [103].

The ITS performances

In this section the basic performances of the ITS, as expected from Monte Carlo simulations, are discussed in relation to the main observables that will be studied by the experiment.

The geometrical parameters of the layers are summarized in Tables 2.3 and 2.4. As far as the material budget is concerned, it should be noted that the values reported in Table 2.4 account for sensor, electronics, cabling, support structure and cooling for particles crossing the ITS perpendicularly to the detector surfaces. Another 1.30% of radiation length comes from the thermal shields and supports installed between SPD and SDD barrels and between SDD and SSD barrels, thus making the total material budget for perpendicular tracks equal to 7.66% of X_0 .

Layer	Type	r [cm]	$\pm z$ [cm]	Number of modules	Active Area per module $r\phi \times z$ [mm ²]	Resolution $r\phi \times z$ [μm^2]	Material budget X/X ₀ [%]
1	pixel	3.9	14.1	80	12.8×70.7	12×100	1.14
2	pixel	7.6	14.1	160	12.8×70.7	12×100	1.14
3	drift	15.0	22.2	84	70.17×75.26	35×25	1.13
4	drift	23.9	29.7	176	70.17×75.26	35×25	1.26
5	strip	38.0	43.1	748	73×40	20×830	0.83
6	strip	43.0	48.9	950	73×40	20×830	0.86

Table 2.3: Characteristics of the six ITS layers.

- **Acceptance.** The rapidity acceptance of the ITS ($|\eta| < 0.9$) allows to study the global observables of the heavy-ion collisions, like the particles ratios, the p_t spectra and the particles correlations on an event-by-event basis. Within the covered rapidity range, the ITS is able to detect and track the thousands of particles emitted in each heavy-ion collision, resulting necessary in particular to detect the decay of large mass, low p_t particles. With its full azimuthal coverage, the ITS can provide also an efficient rejection of low-mass Dalitz decays. Moreover, the inner SPD layer, covering the range $|\eta| < 1.98$ for interactions taking place at $z = 0$, can provide a continuous coverage in rapidity for the measure of charged particles

Parameter	Pixel	Drift	Strip
Spatial precision $r\phi$ (μm)	12	35	20
Spatial precision z (μm)	100	25	830
Two track resolution $r\phi$ (μm)	100	200	300
Two track resolution z (μm)	850	600	2400
Cell size (mm^2)	50×425	202×294	95×40000
Active area per module (mm^2)	12.8×69.6	72.5×75.3	73×40
Readout channels per module	40960	2×256	2×768
Total number of modules	240	260	1698
Total number of readout channels (k)	9835	133	2608
Total number of cells (M)	9.84	23	2.6
Max. occupancy in Pb-Pb (layer 5) (%)	2.1	2.5	4
Max. occupancy in Pb-Pb (layer 6) (%)	0.6	1.0	3.3
Power dissipation in barrel (W)	1350	1060	850
Power dissipation EndCap (W)	30	1750	1150

Table 2.4: The parameters of the various ITS sub-detectors. The mentioned *module* represents a single sensor element.

multiplicity over about 8 η -units if combined with the Forward Multiplicity Detector (FMD). From simulation-based studies, it turns out that the measurement of the multiplicity and of the pseudorapidity distribution can be efficiently performed with the two SPD layers in their full acceptance regions ($|\eta| < 2$ for layer 1, $|\eta| < 1.4$ for layer 2).

- **Spatial precision and granularity.** The granularity of the ITS detectors is capable to cope with the expected thousands of particles per Pb-Pb event, since it was designed for a maximum track density of 8000 tracks per unit of rapidity, while more recent extrapolations from RHIC data set to ~ 4000 tracks the expected value for ALICE. The millions of effective cells that compose each layer of the ITS can keep the system occupancy low, at a few percent, even in events where it will detect about 10000 tracks simultaneously. The resolution of the vertices and the impact-parameter measurement is determined by the spatial resolution of the ITS detectors, that reaches the value of $12 \mu\text{m}$ for the first pixel layer: the simulations show a $10 \mu\text{m}$ resolution in the determination of the vertex z -position in case of heavy-ion collisions, and $110 \mu\text{m}$ ($70 \mu\text{m}$ in the transverse coordinate) for the average pp event ($dN_{ch}/d\eta = 6-7$) after the track reconstruction. With

these performances, the ITS allows to carry out for example the study of the open charm, through the observation of the D_0 weak decays, which have a proper decay length of few hundred microns ($c\tau = (123.0 \pm 0.4) \mu\text{m}$). For $p_t \simeq 1 \text{ GeV}/c$, the SPD layers allow a resolution of about $60 \mu\text{m}$ for the impact parameter projection in the bending plane: with this resolution it is possible to reduce the combinatorial background by selecting a few displaced tracks out of the large number of primary vertex tracks. This high resolution is fundamental also in the study of the suppression of the J/ψ production, in particular to discriminate prompt from secondary J/ψ originating from B decay. From the impact parameter measurement, indeed, it is possible to identify the e^+e^- pairs produced by a displaced vertex and to select them as secondary J/ψ decays. Moreover, the spatial precision is also crucial for the study of the strange baryon production.

- **Particle identification dE/dx measurement.** The ITS contributes to the particle identification through the measurement of specific energy loss. Four layers of the ITS (two silicon-drift and two silicon-strip detector layers) provide signal amplitude information, which can be used for PID in the low-momentum range by measuring ionization energy loss dE/dx . This is estimated as a truncated mean (using the two or three lowest amplitude signals out of four) in order to minimize the influence of Landau fluctuations. The dynamic range of the analogue readout must be large enough to provide dE/dx measurement for low-momentum, highly ionizing particles, down to the lowest momentum at which tracks can still be reconstructed with a reasonable ($> 20\%$) probability. Figure 2.17 shows the truncated mean dE/dx for a sample of ITS stand-alone tracks together with the PHOBOS parametrization of the expected most probable value[104].

The resolution of the ITS dE/dx measurements allows a good π/K separation up to $450 \text{ MeV}/c$ and a good K/p separation up to about $1 \text{ GeV}/c$. A typical ITS response function, for momenta in the range $400\text{-}425 \text{ MeV}/c$, is shown in Figure 2.18. The tails at lower dE/dx values for kaons and protons are due to the incorrect assignment of a cluster during track reconstruction. Such a cluster is with the largest probability due to a pion, therefore lowering the truncated mean amplitude. The size of this effect will depend on the track-quality selection criteria which will have to be optimized on the real data sample and on the experimental particle-species ratios.

- **Material budget.** While traversing the detector material, the multiple scattering worsens the resolution of the momentum and impact parameter measurement of particles with small transverse momenta. The silicon detectors have been designed and produced minimizing the total amount of material: as mentioned in the description of the various ITS sub-detectors, the pixel sensors were produced with the minimum achievable thickness of $200 \mu\text{m}$, while the drifts and the strips,

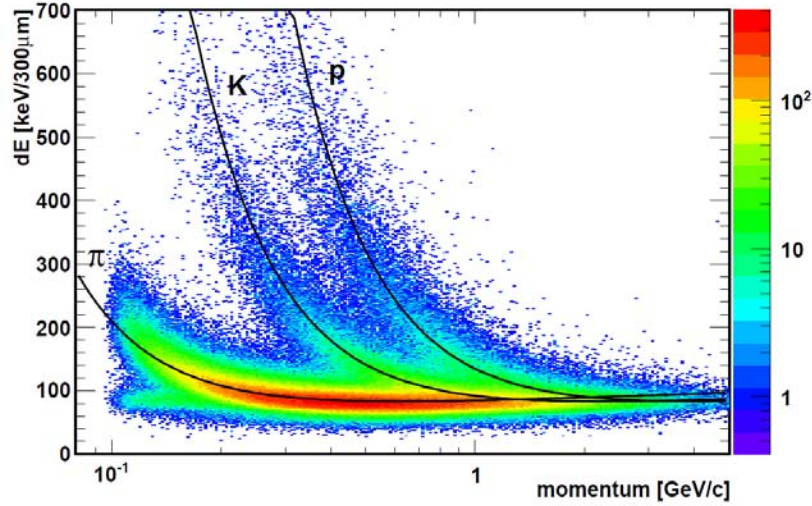


Figure 2.17: Specific energy loss dE/dx vs. momentum for tracks measured with the ITS in pp collisions at $\sqrt{s} = 900$ GeV. The solid lines are a parametrization of the detector response based on the Bethe-Bloch formula[104].

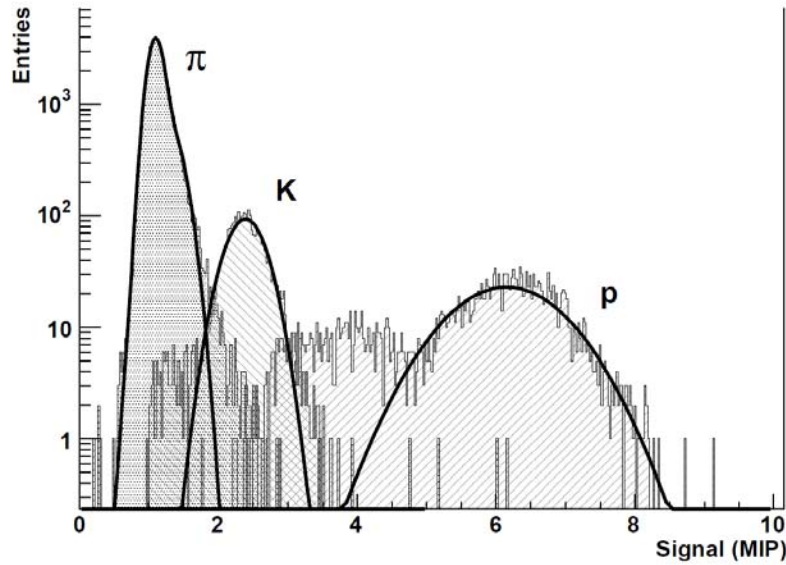


Figure 2.18: Distributions of the truncated mean SDD and SSD signals (MIP units) obtained with the HIJING generator for pions, kaons and protons for a reconstructed momentum of 400-425 MeV/c. The curves are the result of Gaussian approximations[3].

which measure the ionization density dE/dx , have the minimum thickness capable to provide a good signal-to-noise ratio, namely $\sim 300 \mu\text{m}$. Taking into account the overlaps needed for a full coverage of the entire solid angle and the incidence angles of tracks, the detectors effective thickness amounts to 0.4% of the radiation length X_0 . A comparable effective thickness is added by the electronics, cables, supports, cooling systems and other not sensible material. The resulting momentum resolution that can be achieved with ITS is better than 2% for pions with momentum

between 100 MeV/c and 3 GeV/c.

- **Readout rate.** The ALICE detector will acquire data in two different read-out configurations, triggered by different trigger classes that operate simultaneously. A first trigger activates the readout of the whole of ALICE, for the central collisions generating large events; the trigger of the muon arm activates instead the readout of a subset of fast readout detectors, including the two pixel layers of the ITS, and it is kept active even when the centrality trigger is disabled because of bandwidth saturation. This trigger system requires the readout time for the pixel detectors to be set at less than 400 μs .

2.5.1.2 The Time Projection Chamber (TPC)

The TPC is the main tracking device of the ALICE detector. It provides track finding, momentum measurement and particle identification through dE/dx measurement. It has a cylindrical shape with an internal radius of 80 cm determined by the maximum acceptable hit density (0.1 cm^{-2}) and an outer radius of 250 cm chosen in order to have an average particle path length in the chamber sufficient to get a dE/dx resolution better than 10%. The total active length of $\sim 500 \text{ cm}$ in the z direction allows the acceptance in the pseudorapidity range $-0.9 < \eta < 0.9$. The material budget of the TPC is kept as low as possible both for the field cage and for the adopted drift gas to ensure minimal multiple scattering and secondary particle production. The drift gas mixture Ne/CO₂ (90%/10%) is optimized for drift velocity, low electron diffusion and low radiation length. The radial thickness of the detector is of 3.5% of X_0 at central rapidity and grows to $\sim 40\%$ towards the acceptance edges. The TPC layout is shown in Figure 2.19.

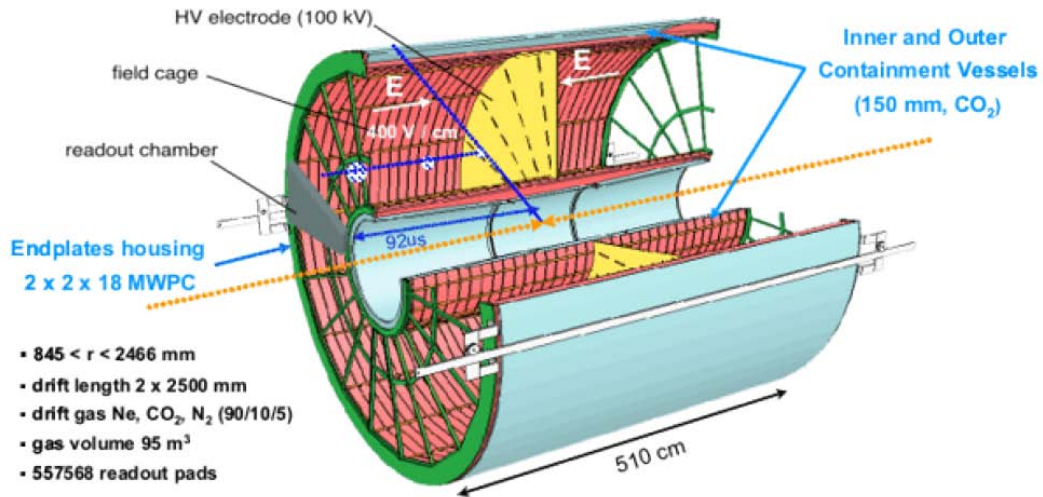


Figure 2.19: The Time Projection Chamber layout and main characteristics.

The TPC readout chambers are multi-wire proportional chambers with cathode-pad readout. The readout planes at the two ends of the large drift volume (88 m^3) are

azimuthally segmented in 18 sectors, each covering an angle of 20° . The non-active region between two adjacent sectors is 2.7 cm wide, implying an azimuthal acceptance of $\sim 90\%$ for straight tracks originating from the interaction point. A drift voltage of 100 kV stretches between the central electrode (at $z = 0$) and the two readout planes at $z = \pm 2.5$ m. A maximum of 160 clusters can be measured for a typical track which allows up to 20 000 tracks in one event to be reconstructed and identified. The TPC is, due to its drift time of about 90 μs , the slowest detector in ALICE. This has to be taken into account for the trigger: once an event is accepted, usually no other event is measured with the TPC within the next 90 μs . The large number of measured clusters allows the specific energy loss (dE/dx) of traversing particles to be calculated without being affected by the tails of the energy loss (Landau) distribution.

An high momentum resolution is required to the TPC both for the study of soft hadronic observables and for the hard probes in the high- p_t region. For low- p_t particles, between 100 MeV/c and 1 GeV/c, reconstructed in the TPC, the momentum resolution is between 1% and 2%, while it is larger than 10% at 20 GeV/c, quickly increasing with p_t . Thus it is necessary to use the TPC in combination with the other tracking detectors (ITS and TRD) to measure higher momenta: using these detectors we can achieve about 10% momentum resolution for tracks with p_t of 100 GeV/c at 0.5 T magnetic field. The TPC dE/dx measurement has an estimated resolution that slightly depends on the charged-particle density: for particles with momentum around 0.5 GeV/c, it changes from 5.5% for p-p events to 6.5% for central Pb-Pb collisions. The TPC provides a 3σ π/K and K/p separation in the region of $p_t < 1$ GeV/c, as well as good electron-pion separation up to a few GeV/c [3, 105].

2.5.1.3 The Transition Radiation Detector

The Transition Radiation Detector (TRD) has to provide electron identification in the central barrel for momenta above 1 GeV/c [3, 106]. Above 1 GeV/c, the transition radiation from electrons traversing a radiator can be exploited together with the specific energy loss in a suitable gas mixture measured by multi-wire proportional read-out chambers. This working principle is schematically presented in Figure 2.20.

The TRD is located at radii from 2.9 m to 3.7 m. It is segmented into 18 sectors where each consists of six layers. It is composed of 540 individual readout detector modules: each module consists of a radiator of 4.8 cm thickness, a multi-wire proportional read-out chamber and the front-end electronics for this chamber. The signal induced on the cathode pad is read-out. In the Xe/CO₂ (85%/15%) gas-mixture of the chambers, a minimum ionizing particle liberates 275 electrons cm^{-1} . The gas gain will be of the order of 5000. The readout electronics features 1.18 million channels. Average drift spectra for electrons and pions are shown in Figure 2.21.

The TRD was designed to derive a fast trigger for charged particles with high momentum. It can significantly enhance the recorded Υ -yields, high- p_t J/ψ , the high-mass part of the dilepton continuum as well as jets. The TRD achieves a pion rejection es-

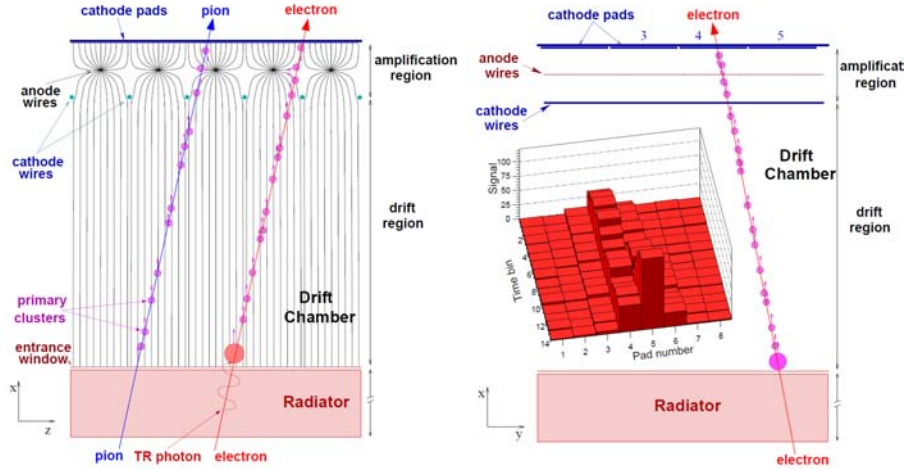


Figure 2.20: Schematic view of a detector module in $r\phi$ direction, illustrating the TRD working principle. The left panel shows a projection in the plane perpendicular to the wires. Electrons produced by ionization energy loss (dE/dx) and by transition radiation absorption drift along the field lines towards the anode wires. The right panel shows a projection in the bending plane of the ALICE magnetic field; the inset shows the charge deposit from an inclined track, used for the momentum reconstruction.

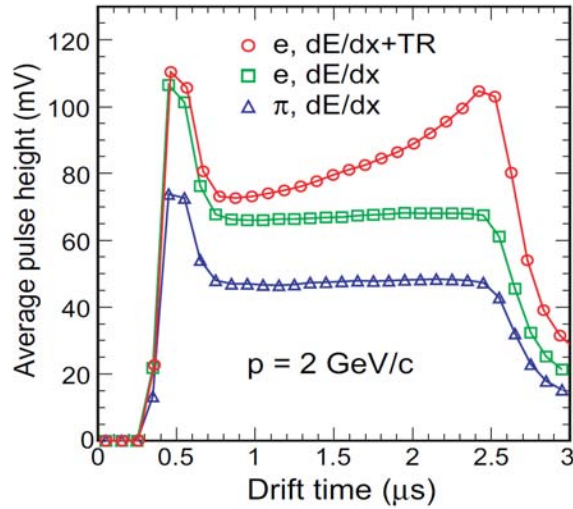


Figure 2.21: Average pulse height as a function of drift time for pions (triangles), electrons without a radiator (squares) and electrons with a radiator (circles) for 2 GeV/c particles.

timated in 1% of pions erroneously identified as electrons at an electron efficiency of 90%; matching the TPC, it allows an overall mass resolution of about $100 \text{ MeV}/c^2$ at the Υ -mass (for $B = 0.4 \text{ T}$).

2.5.1.4 The Time Of Flight Detector

The Time-Of-Flight (TOF) detector is a large area array of Multi-Gap Resistive-Plate Chamber (MRPC) strips covering the central pseudo-rapidity region ($|\eta| < 0.9$). Its

main task is the particle identification in the intermediate momentum range, below ~ 2.5 GeV/c for pions and kaons, up to 4 GeV/c for protons, with a π/K and K/p separation better than 3σ . The kaons identified by the TOF detector allow invariant mass studies, in particular the detection of open heavy flavoured states and vector-meson resonances such as the ϕ meson. The detector has a modular structure corresponding to 18 sectors in $r\phi$ and to 5 segments in z direction and is located at a radius of 3.8 m. The whole device thickness corresponds to 30% of a radiation length. The MRPC strips are placed inside modules that define and seal the gas volume, acting also as Faraday cages, and support the external front-end electronics and services. These are stacks of very thin structures (250 μm) featuring a high and uniform electric field and a $\text{C}_2\text{H}_2\text{F}_4/\text{i-C}_4\text{H}_{10}/\text{SF}_6$ gas mixture so that any traversing particle immediately triggers an avalanche. The setup achieves a very good time resolution of about 40 ps. Combined with other uncertainties, e.g. the uncertainty to determine the exact time of the interaction, the time of flight measurement for single particles has an overall resolution of better than 100 ps [107, 3]. The TOF detector has about 160,000 channels while the total active area of $\sim 140 \text{ m}^2$. A schematic layout of one supermodule inside the ALICE spaceframe and a photo of an assembled supermodule are shown in Figure 2.22.

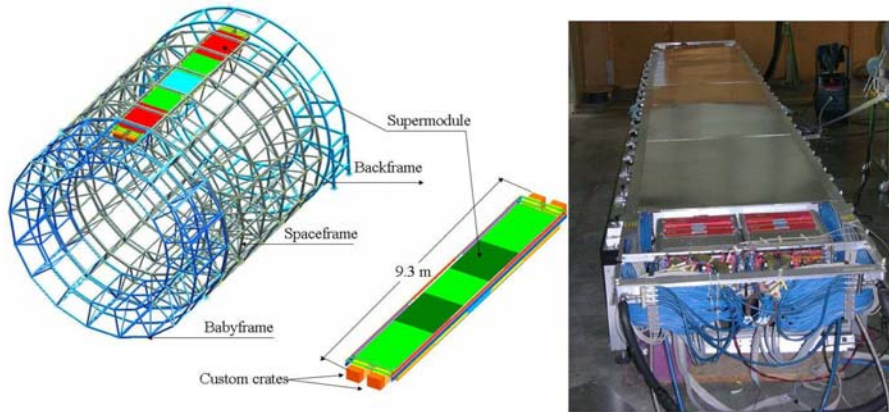


Figure 2.22: Schematic drawing of one TOF supermodule, consisting of 5 modules, in the ALICE spaceframe (left panel). A supermodule after assembly (right panel).

The Figure 2.23 presents a scatter plot of the measured momenta versus the estimated masses for particles produced in central Pb-Pb collisions generated with HIJING. The points corresponding to pions, kaons and protons are coloured in red, blue and green, respectively.

2.5.1.5 High-Momentum Particle Identification Detector

The High-Momentum Particle Identification Detector (HMPID) is dedicated to the identification of hadrons with $p_t > 1$ GeV/c. It extends ALICE's capability of π/K and K/p separation to 3 and 5 GeV/c, respectively, and therefore it plays an important role in the identification of particles beyond the momentum interval studied through energy loss by

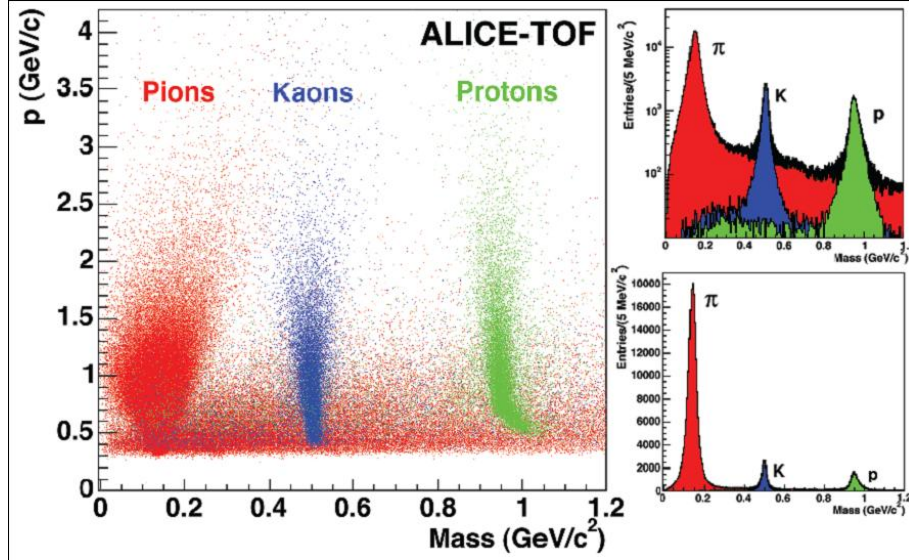


Figure 2.23: Momentum versus mass calculated (left) and reconstructed mass (right) from TOF for a sample of HIJING Pb-Pb events. Overall TOF system resolution: 120 ps; momentum range $0.5 < p < 2.5$ GeV/c, for 200 HIJING events at $B = 0.4$ T. The two plots on the right are the same graph in logarithmic (high) and linear (low) scale. Figure from [108].

the ITS and the TPC and through the time-of-flight measurements by the TOF detector. The HMPID is based on proximity-focusing Ring Imaging Cherenkov (RICH) counters: its working principle is schematically presented in Figure 2.24. The momentum range covered is defined by the radiator used in the detector, i.e. a 15 mm thick layer of liquid C_6F_{10} : the index of refraction of this material ($n=1.2989$ at $\lambda=175$ nm) corresponds to a minimum speed $\beta_{min}=0.77$, thus to the threshold momentum $p_{th}=1.21 \cdot m$, with p in GeV/c and the mass m in GeV/c² [3, 109].

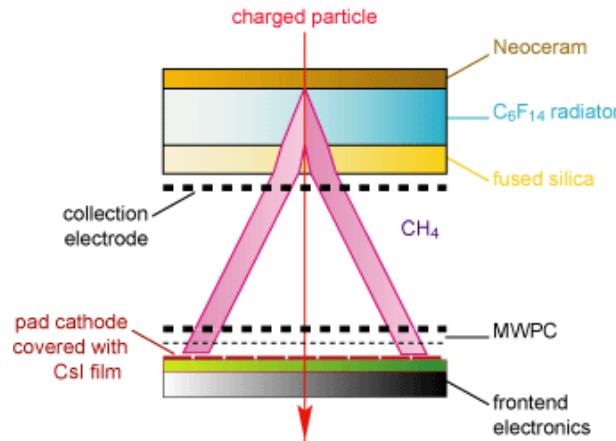


Figure 2.24: The HMPID working principle. The Cherenkov photons, emitted when a fast charged particle traverses the radiator, are detected by a photon counter, consisting of a thin layer of CsI deposited onto the pad cathode of a multi-wire proportional chamber (MWPC) [3].

The HMPID consists of seven identical modules, located on an independent support

cradle and mounted at the two o'clock position of the ALICE space frame. The seven modules ($1.5 \text{ m} \times 1.5 \text{ m}$ each) cover $-0.6 < \eta < 0.6$ in pseudo-rapidity and 57.6° in azimuth.

2.5.1.6 The Electromagnetic Calorimeters

2.5.1.6.1 The PHOton Spectrometer (PHOS) The PHOton Spectrometer (PHOS) is a high-resolution electromagnetic spectrometer covering a limited acceptance domain at central rapidity. The PHOS is capable to measure low- p_t photons emitted in the initial phase of the collision, in order to study its thermal and dynamical properties; moreover, it is designed to measure the high- p_t π^0 and γ -jet correlation in order to study the jet quenching effect. The PHOS is made of almost 18000 cells, i.e. dense scintillating crystals of lead-tungstate (PbWO_4), like the one shown in Figure 2.25, arranged in five different modules and operated at a temperature of -25°C to increase their light yield; the modules, installed on the bottom of the ALICE apparatus, 4.6 m from the interaction point, covers about 3.7% of phase space in the central region.

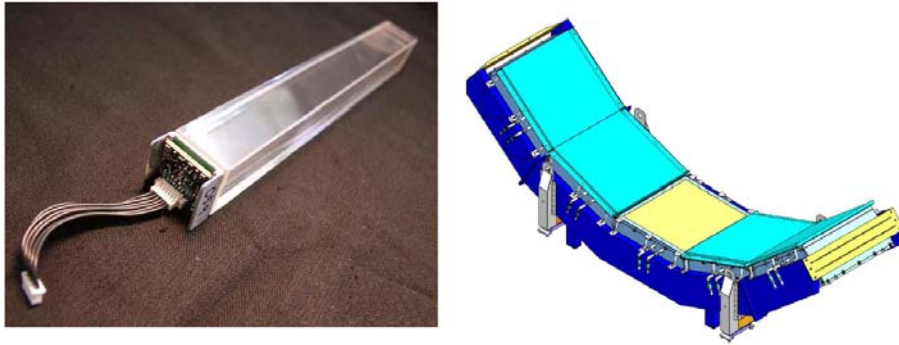


Figure 2.25: The PHOton Spectrometer: the left picture shows one of the almost 18000 lead-tungstate scintillating crystal composing the PHOS; on the right, the layout of the sub-detector, with its five modules installed on the bottom of the ALICE apparatus.

A set of multi-wire proportional chambers in front of PHOS act as a veto in order to reject charged particles. The PbWO_4 has been chosen because of its characteristic small *Molière radius* and for the sufficient light output which allows to measure the lowest energies of interest with good resolution. Its high segmentation allows to keep the cell occupancy at a manageable level of about 10-20%[3, 110].

2.5.1.6.2 The ElectroMagnetic Calorimeter (EMCal) The ElectroMagnetic Calorimeter is a Pb-scintillator sampling calorimeter with longitudinal wavelength-shifting fibres, read out via avalanche photo diodes. It measures the neutral energy component of jets, enabling full jet reconstruction in all collision systems, from p-p to Pb-Pb, photons, π^0 , and η via their decay photons like the PHOS detector and provides a fast and efficient trigger for hard jets, photons and electrons. With its cylindrical geometry, it is located adjacent to the ALICE magnet coil at 4.5 m from the beam line, approximately opposite

in azimuth to the high-precision PHOS calorimeter, covering $|\eta| < 0.7$ and $\Delta\phi = 107^\circ$. It is larger than PHOS, but with lower granularity and energy resolution[3, 111]. The detector layout can be seen in Figure 2.26.

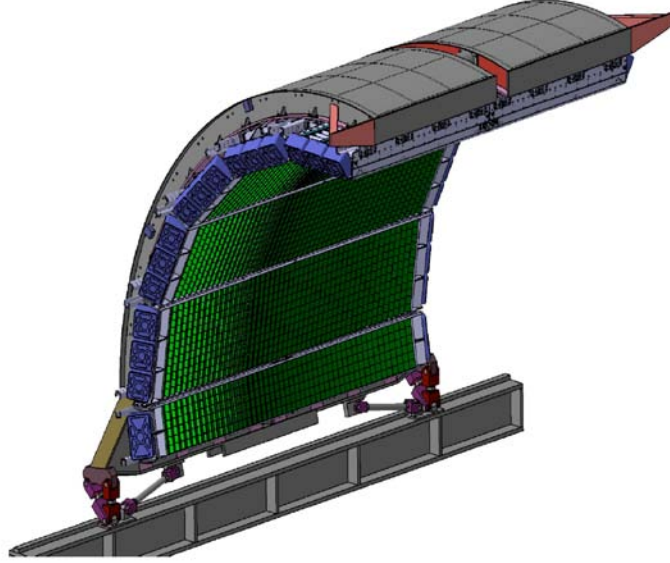


Figure 2.26: The array of EMCal Super Modules shown in their installed positions on the support structure[111].

2.5.1.7 The ALICE Cosmic Ray Detector (ACORDE)

The ALICE detector is also instrumented with a cosmic-ray detector, ACORDE, an array of plastic-scintillator counters placed on the upper surface of the L3 magnet. Together with some other ALICE detectors it will detect both single-muon and multi-muon events (called muon bundles) thus providing precise information on cosmic rays with primary energy around 10^{15-17} eV, in the region of the knee of the cosmic-ray spectrum. Another major task of ACORDE is to provide Level 0 trigger signals for commissioning, calibration and alignment procedures of some of the ALICE central detectors. A single ACORDE module consists of two 190×20 cm² scintillator counters 10 mm thick placed on top of each other and readout in coincidence by two PMTs at the end of each scintillator. A total of 60 modules are placed on top of the ALICE L3 magnet[3, 112].

2.5.2 The Muon Spectrometer

The forward muon arm is designed to detect muons in the pseudo-rapidity region $-4.0 < \eta < -2.5$, corresponding to the polar angular range 171° - 178° and it has full azimuthal coverage for muons with $p > 4$ GeV/c. It gives the possibility to study the $\mu^+\mu^-$ decay channel of the heavy-quark vector-mesons resonances like J/ψ , ψ' , Υ , Υ' , Υ'' in the same experimental condition and with a mass resolution sufficient to separate all states. The detector consists of a composite absorber to absorb hadrons and photons coming from

the interaction vertex, a high-granularity tracking system of 10 detection planes, a large dipole magnet with a 3 Tm integral field placed outside the L3 magnet, a passive muon-filter wall, followed by four planes of trigger chambers for the identification of the muons and the triggering; both the absorbers and the detectors are designed to achieve the required invariant-mass resolution of 100 MeV/c² in the 10 GeV/c² dimuon invariant-mass region, needed to resolve the Υ , Υ' , Υ'' resonances. Finally, a dense conical absorber tube provides to shield the spectrometer from secondary particles created in the beam pipe[113, 3]. The layout of the muon spectrometer is shown in Figure 2.27.

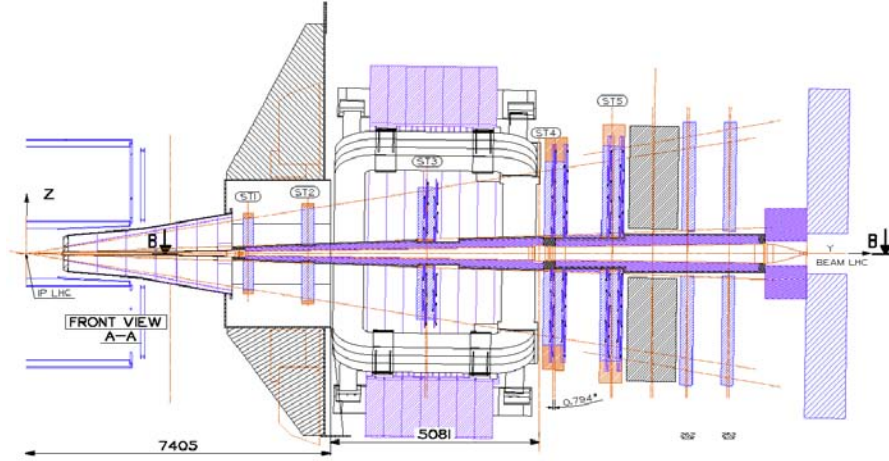


Figure 2.27: Layout of the Muon Spectrometer. The conical front absorber on the left is followed by 10 tracking stations: 4 placed between the absorber itself and the dipole magnet, two inside the magnet and four between the magnet and the muon-filter wall. Four planes of trigger chambers follow the muon filter[3].

2.5.3 Forward, Trigger and Multiplicity Detectors

2.5.3.1 The Photon Multiplicity Detector (PMD)

The PMD measures the multiplicity distribution of photons (e.g. decay products from π^0 and η) in the forward region ($2.3 < \eta < 3.7$, full azimuth) to provide estimation of the collision reaction plane on an event-by-event basis. The method used for the PMD detector makes use of the preshower technique: it consists of two planes of gas proportional counters, preceded by two lead converter plates of 3 radiation lengths each. The plane in front of the converter is used as a veto for charged particles while the information from the second plane is used to identify photons. The detector is positioned at a 3.64 m distance from the nominal interaction point (Figure 2.9)[3, 114].

2.5.3.2 The Forward Multiplicity Detector (FMD)

The Forward Multiplicity Detector (FMD), consisting in rings of silicon strip detectors located at three different positions along the beam pipe, provides charged particle mul-

tiplicity information over a large fraction of the solid angle ($-3.4 < \eta < -1.7$ and $1.7 < \eta < 5$) both in full azimuth. The five rings are located at $z = 3.2$ m, 0.83 m, 0.75 m, -0.63 m and -0.75 m. Due to its slow readout ($> 1.2 \mu\text{s}$) it cannot be used as a trigger[3, 115]. The FMD layout is shown in Figure 2.28.

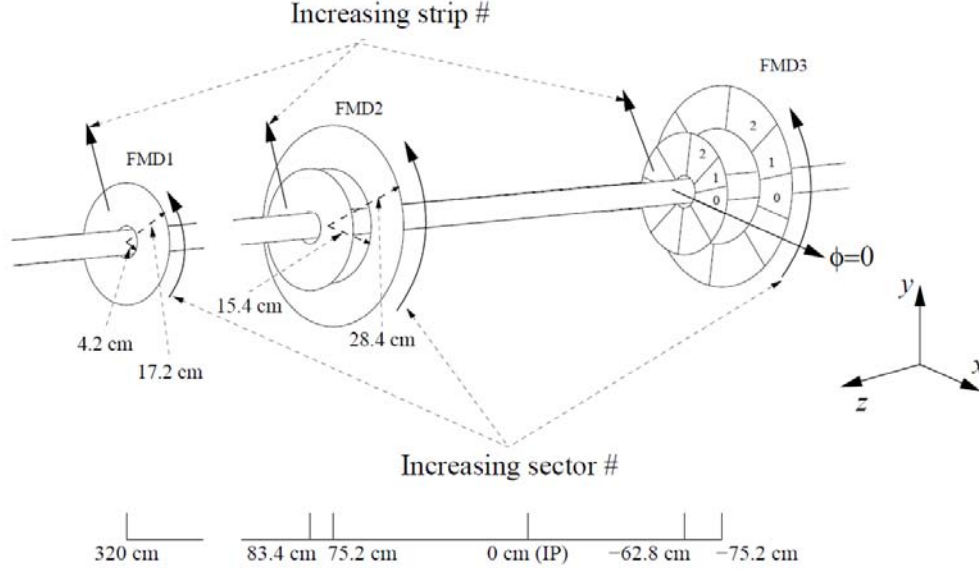


Figure 2.28: Layout of the FMD rings in the ALICE experiment. FMD3 and FMD2 are located on each side of the ITS detector while FMD1 is much further away from the interaction point (IP)[3].

Partially overlapping the SPD sensors, it provides a continuous coverage for the particle multiplicity measurement, as shown in Figure 2.29.

2.5.3.3 The V0 detector

The V0 detector is a small-angle detector consisting of two arrays of scintillator counters installed on either side of the ALICE interaction region, located at $z = 3.4$ m ($2.8 < \eta < 5.1$) and -0.9 m ($-3.7 < \eta < -1.7$). It will provide minimum bias triggers for central-barrel detectors in both pp and nucleus-nucleus collisions and will help rejecting false events induced by interactions of protons with the residual gas of the vacuum chamber. The time resolution is about 1 ns which allows beam-gas events that occurred outside of the nominal interaction region to be identified[3, 116]. The V0 layout is shown in Figure 2.30.

2.5.3.4 The T0 detector

The T0 detector was designed to generate a start-time (T0) signal for the Time-Of-Flight (TOF) detector. It measures the event time with very good precision (< 25

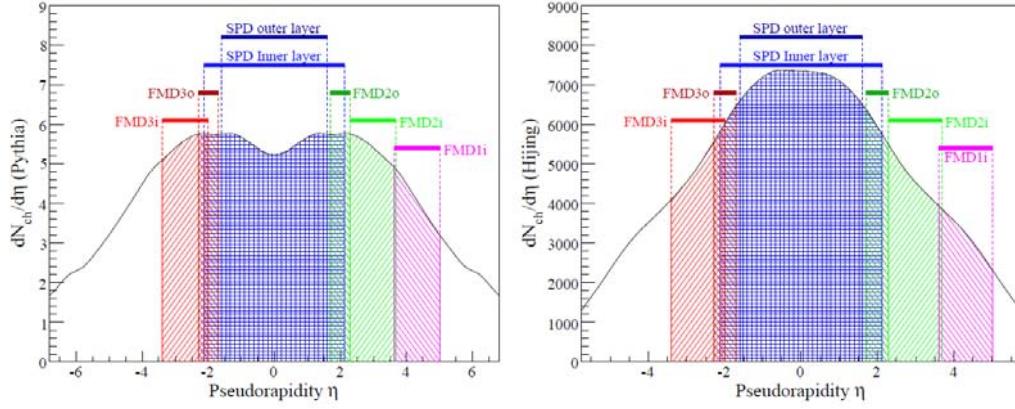


Figure 2.29: The continuous pseudorapidity coverage provided by the Forward Multiplicity Detector together with the SPD, superimposed on simulated multiplicity distributions to illustrate which regions are measured by each detector. The distributions refer to p-p events at $\sqrt{s_{NN}} = 14$ TeV in the left panel (simulated with the PYTHIA event generator) and to Pb-Pb events $\sqrt{s_{NN}} = 5.5$ TeV in the right panel (HIJING generator)[3].

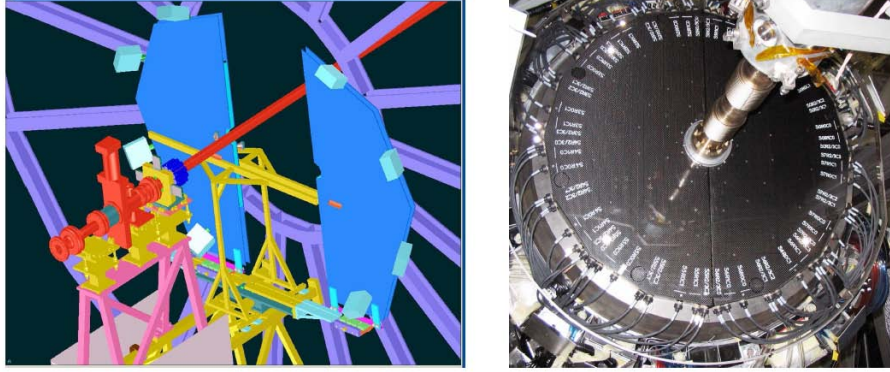


Figure 2.30: V0A 3D drawing (left) and V0C picture (right)[3].

ps). This signal is independent of the vertex position and corresponds to the real time of the collision. The T0 detector can also measure the vertex position (with 1.5 cm precision) and provide Level 0 triggers when the position is within the preset value. A vertex position outside the region where collisions should appear is used as a beam-gas rejection signal. Furthermore, the T0 detector can also send a pre-trigger to the TRD. The detector consists of two arrays of Cherenkov counters, each with 12 counters. Each Cherenkov counter is based on a fine-mesh photomultiplier tube coupled to a quartz radiator 20 mm in diameter and 20 mm thick. The two arrays are placed at 72.7 cm (T0-C) and 375 cm (T0-A) from the interaction point, respectively (Figure 2.31)[3, 116].

2.5.3.5 The Zero-Degree Calorimeter (ZDC)

The ZDC is composed of two sets of hadron calorimeters located at 116 m on either side of the Interaction Point (IP) to measure event centrality in nucleus-nucleus collisions[117].

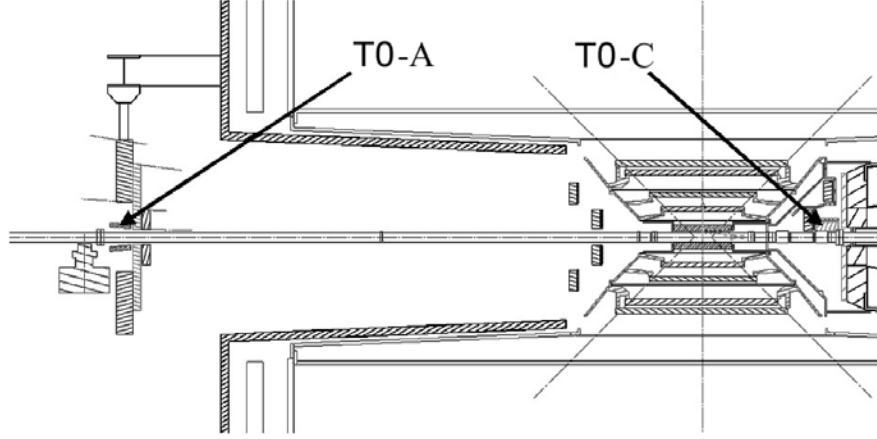


Figure 2.31: The layout of T0 detector arrays inside ALICE.[3].

In addition two small electromagnetic calorimeters (ZEM, $7 \times 7 \times 20.4 \text{ cm}^3$, $4.8 < \eta < 5.7$) are placed at about 7 m from the IP on both sides of the beam pipe, opposite to the muon spectrometer (Figure 2.32). Each ZDC set is made of two calorimeters: one for spectator neutrons (ZN, $7.04 \times 7.04 \times 100 \text{ cm}^3$, $|\eta| < 8.8$) and one for spectator protons (ZP, $12 \times 22.4 \times 150 \text{ cm}^3$, $6.5 < |\eta| < 7.5$). Since spectator protons are spatially separated from neutrons by the beam magnetic elements, the ZP is placed externally to the ongoing beam line (on the side where positive particles are deflected) while the ZN is placed between the beam pipes at 0° with respect to the beam axis. When they are not in use, the calorimeters are moved out of the beam line by a lifting platform to reduce their exposure to ionizing radiation.

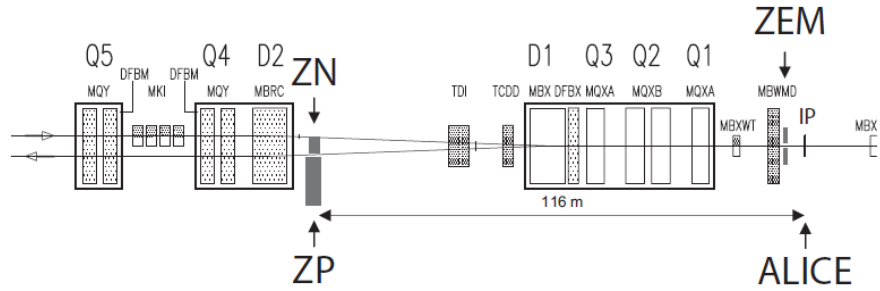


Figure 2.32: Schematic top view of the side of the ALICE beam line opposite to the muon arm. The locations of the neutron (ZN), proton (ZP) and forward electromagnetic (ZEM) calorimeters are shown. The position of the beam line dipoles (Dx) and quadrupoles (Qx) are also indicated.[3].

The hadronic ZDCs are quartz-fibre sampling calorimeters: the shower generated by incident particles in the absorber (tungsten for ZN and brass for ZC) produces Cherenkov radiation in the quartz fibres. The optical readout is divided into four independent towers. One out of two fibres is sent to a single photomultiplier (PMT), while the remaining ones are sent to the four PMTs which define the four towers. The ZEM complements

the hadronic ZDCs helping in discriminating between central and peripheral collisions. Since in very peripheral A-A collisions spectator nucleons can bound into fragments which stay in the beam pipes, they cannot be detected by the ZDCs. Therefore in very peripheral events only a small amount of energy is detected in the hadronic ZDCs, just like in central events, where the number of spectator nucleons is small. On the contrary the energy detected by the ZEM calorimeter increases monotonically with the collision centrality. Finally the ZDC can provide also a L1 trigger.

2.5.4 The Data Acquisition and The Trigger System

ALICE has a two-layer trigger architecture[118]. The low-level trigger is a hardware trigger called Central Trigger Processor (CTP). The High-Level Trigger (HLT) is implemented as a pure software trigger. The ALICE Central Trigger Processor (CTP) is designed to select events having a variety of different features at rates which can be scaled down to suit physics requirements and restrictions imposed by the bandwidth of the Data Acquisition (DAQ) system and by the High-Level Trigger (HLT). The challenge of the ALICE trigger is to make optimum use of the detectors and to perform trigger selections in an optimized way for several different running modes.

2.5.4.1 The Central Trigger Processor (CTP)

The hardware trigger combines the trigger signals of the various subdetectors to decide if an event is accepted which means that it is read out and written to disk. Several trigger levels reduce the event rate depending on the input signals. The first level, called L0, is delivered after $1.2 \mu\text{s}$, the second, called L1, after $6.5 \mu\text{s}$. The final trigger, L2, is delivered after $100 \mu\text{s}$, upon completion of the drift time in the TPC. Only after an L2 trigger the event is finally stored. Another task of the hardware trigger is to issue a pretrigger to wake up the TRD electronics which is needed in less than 900 ns after the interaction. A past-future protection ensures that events are not superimposed by too many pile-up collisions. The readout times of the different detectors vary significantly, therefore the window in which pile-up is recognized depends on the detectors that are part of the current partition as well as on the collision system. Different conditions are applied for p-p collision (with respect to Pb-Pb collision) where pile-up is always present due to the higher luminosity. However, in this case more pile-up is acceptable due to the much lower particle densities. The trigger logic acts upon numerous inputs: up to 24 L0, 24 L1, and 12 L2 input signals. Out of these inputs up to 50 trigger classes can be defined[118]. The rates of different trigger classes are very different. By definition minimum-bias triggers have the highest rate, other triggers that look for rare signals have much lower rates. Therefore, downscaling factors can be applied to the trigger classes individually, i.e. only every n^{th} event fulfilling the trigger condition is read out. The total recording rate is limited by the maximum bandwidth of data that can be recorded to disk and tape. To prevent losing precious events due to the fact that

no space is available on the temporary memory and disk buffers in a moment where a trigger that looks for a rare signal occurs, the trigger system implements an event prioritization scheme. Therefore, trigger classes are grouped into common triggers and rare triggers. In the case that the utilization of the temporary storage is above a certain value (high-water mark) only rare triggers are accepted; as soon as the utilization drops below a given low-water mark all triggers are accepted again. This scheme significantly increases the acceptance of rare events.

The CTP consists of seven different types of 6U VME boards housed in a single VME crate. The signal transmission to each detector is mediated by Local Trigger Units (LTU) which can be decoupled from the CTP for testing purposes.

2.5.4.2 The High-Level Trigger (HLT)

ALICE's software trigger, called High Level Trigger (HLT), is a farm of multiprocessor computers. The aim is about 1.000 PCs processing the data in parallel allowing an online analysis of the events. A trigger decision is derived from much more complete information than is available for the hardware trigger. Therefore, it allows for more sophisticated triggers. Examples include triggers on high-energy jets or on muon pairs. Furthermore, the HLT can significantly reduce the event size by selecting regions of interest (partial readout of subdetectors) and by further compression of the data[118].

The amount of data produced in the TPC alone in a single nucleus-nucleus collision has been estimated to be about 75 MB (assuming high charged-particle density $dN_{ch}/d\eta = 8000$ at mid-rapidity). The data rate can easily reach 25 GB/s while the DAQ archiving rate is about 1 GB/s. Therefore online processing is advisable to select relevant events and to compress data without losing their physics content. The overall physics requirements of the HLT are the following:

- accept or reject events on a detailed online analysis;
- select a physics Region-Of-Interest (ROI) within the event;
- reduce the event size without loss of physics information of the accepted and selected data.

The HLT receives a copy of the raw data and performs the detector reconstruction, partly aided by hardware coprocessors. Subsequently, the trigger decision is based on the global reconstructed event. In the same step a region of interest can be selected. In the last optional step, if the trigger decision is positive, the data is compressed. The trigger decision, partial readout information, compressed data, and the reconstruction output is subsequently processed by the DAQ. In terms of the overall DAQ architecture, data sent by HLT is treated like stemming from a subdetector.

2.5.4.3 The Data Acquisition (DAQ)

The tasks of the ALICE DAQ system is the assembly of event fragments from individual subdetectors into complete events (event building) as well as buffering and export of assembled events to permanent storage. The DAQ is designed to process a data rate of up to 1.25 GB/s in heavy-ion runs. Event building is done in two steps. Data from the subdetectors is received by Detector Data Links (DDLs) in which the D-RORCs (DAQ Readout Receiver Card) PCI-X based cards receive and assemble the event fragments into sub-events in the LDCs (Local Data Concentrators). The LDCs assemble the data into sub-events that are then shipped to Global Data Collectors (GDCs). A GDC receives all sub-events from a given event and assembles them into a complete event. Subsequently, these events are stored on a system called Transient Data Storage (TDS). At the same time the GDCs feed the recording system which eventually records the events in the Permanent Data Storage (PDS). The fully equipped DAQ setup will comprise 200 LDCs and 60 GDCs. The architecture of the data acquisition is shown in Figure 2.33.

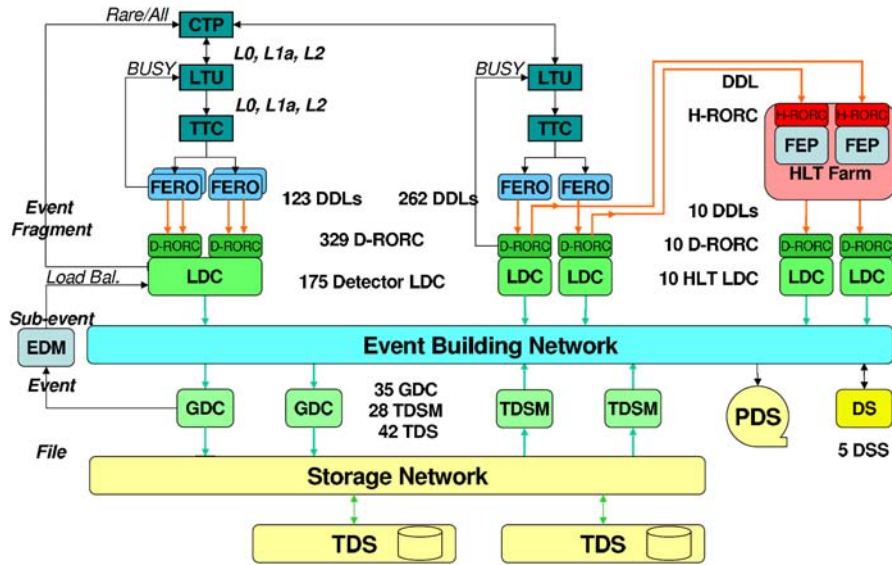


Figure 2.33: The overall architecture of the ALICE DAQ system and the interface to the HLT system[118].

ALICE can simultaneously take data in several partitions, where each partition consists of a set of subdetectors. Obviously a given subdetector can only be active in one partition at a time. The active subdetectors in a given partition are grouped into clusters for which triggers can be defined. Therefore, upon a trigger only a subset of the whole partition may be read out. Furthermore, a triggering detector does not have to be necessarily part of the partition.

2.5.5 The ALICE Offline Software Framework

The data production of the LHC experiments (about 10 - 15 PB per year) is at a new scale compared to any previous experiment. In ALICE, an average Pb-Pb event will have a size of about 13.75 MB; on average a p-p event is about 1.1 MB. For a standard running year, of the order of 10^9 p-p events and 10^8 Pb-Pb events are expected yielding a total raw data volume of 2.5 PB. The data taken with cosmics in 2008 amounts to about 300 TB. Two thirds were taken in so-called global runs with several participating subdetectors, a condition similar to real data-taking. The average size of the reconstruction output is 3 MB for a Pb-Pb event and 40 kB for a p-p event. This only includes high-level information needed for user analysis. Examples are the event-vertex position, reconstructed track parameters, and PID information. The required computing resources for the reconstruction and analysis of the raw data as well as the production of simulated events needed for the understanding of the data exceed the computing power of single institutes and even of centers like CERN. Therefore, institutes that are part of the collaboration also provide storage and computing resources. At present 80 centers contribute to ALICE's computing resources. Distribution of the data for reconstruction and analysis cannot be performed manually and this led to the need for an automated system. The concept of GRID was identified as a solution. ALICE uses the ALICE Environment (AliEn) system as a user interface to connect to a GRID composed of ALICE-specific services that are part of the AliEn framework and basic services of the Grid middleware installed at the different sites. A dedicated framework called AliRoot enables simulation and reconstruction of ALICE events to be performed. It is also the basis for any analysis performed on the data.

2.5.5.1 Dataflow

The raw data taken by the subdetectors has to be processed before be available in the form of reconstructed events for further analysis. This happens in several stages as illustrated in Figure 2.34. Data originating from the subdetectors (denoted by 1 in Figure 2.34) are processed by LDCs, global events are built by GDCs (2). The so-called publish agent registers the assembled events into the AliEn system (3) and ships them to the CERN computing center where they are stored first on disks (4) and then permanently on tapes (5) by the CASTOR system. During data-taking the subdetectors also produce conditions data that are relevant for the calibration of individual detector signals. Conditions data provides information about the detectors status and environmental variables during data-taking: inactive and noisy channel maps, distributions describing the response of a channel, temperatures and pressure in a detector, and detector configuration. Many of the conditions data could in principle be calculated from the raw data and extracted offline after data-taking. However, such an approach would require an additional step over the raw data before the reconstruction requiring not available online computing resources. Therefore, conditions data are already extracted

during data-taking. Conditions data are produced by special programs that process the raw data stream and extract the needed values. These programs work in the realm of DAQ, DCS (Detector Control System), and HLT and store their output on so-called File eXchange Servers (FXS) (6-8 in Figure 2.34).

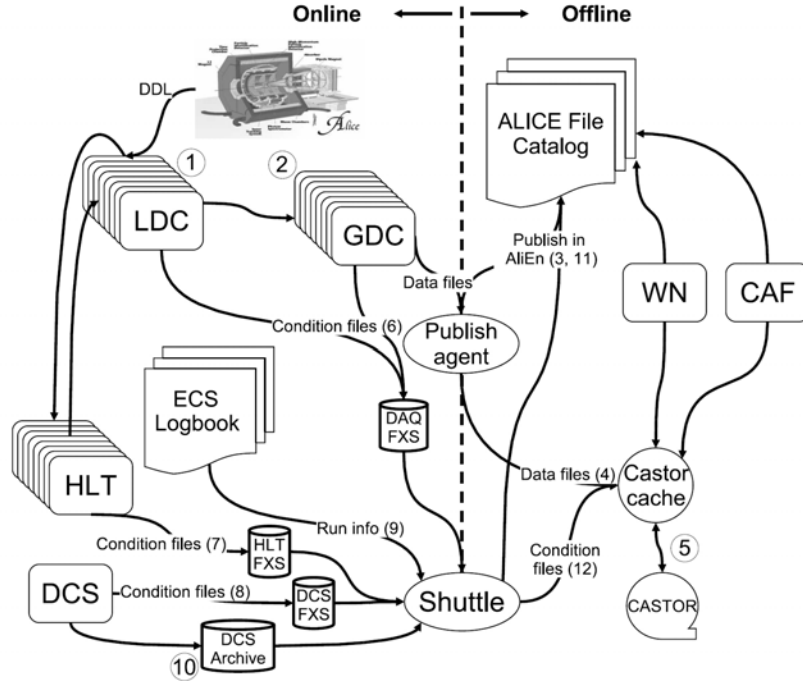


Figure 2.34: Global view of ALICE's data flow (Figure adapted from[3]).

A dedicated program called Shuttle collects these outputs and makes them available to the reconstruction. Furthermore, it retrieves information about the run from the ECS logbook (9) and collects continuously monitored values that are written by DCS into the DCS Archive (10). After processing the data, the Shuttle registers the produced condition files in AliEn (11) and stores the data in CASTOR (12). With the registration of the raw and conditions data the transition from the online to the offline environment has taken place. Online denotes all actions and programs that have to run in real time. Offline processing is the subsequent step, like for example event reconstruction, which is executed on Worker Nodes (WN) of GRID sites located around the Globe.

2.5.5.2 The ALICE Analysis Framework on the GRID: Alice Environment (AliEn)

The GRID paradigm implies the unification of resources of distributed computing centers, in particular computing power and storage, to provide them to users all over the world. It allows computing centers to offer their resources to a wider community. This allows resources in large collaborations to be shared. The huge amount of data produce by the ALICE detector (~ 2 PB per year) makes almost unavoidable the necessity of automatized procedures for the (software) reconstruction of the events and for the first

steps of the analysis, with the consequent employ of a large mass of computing resources. The worldwide distributed GRID facilities were designed to provide both the computing power and the disk space needed to face the LHC software challenge. Hence the need of a GRID-oriented analysis code. One of the main advantages in using the GRID is the possibility to analyze a large set of data by splitting a job analysis into many “clone” subjobs running in parallel on different computing nodes. The ALICE VO (Virtual Organization) is made of more than 80 sites distributed worldwide (Figure 2.35 is a snapshot of the sites in Europe).

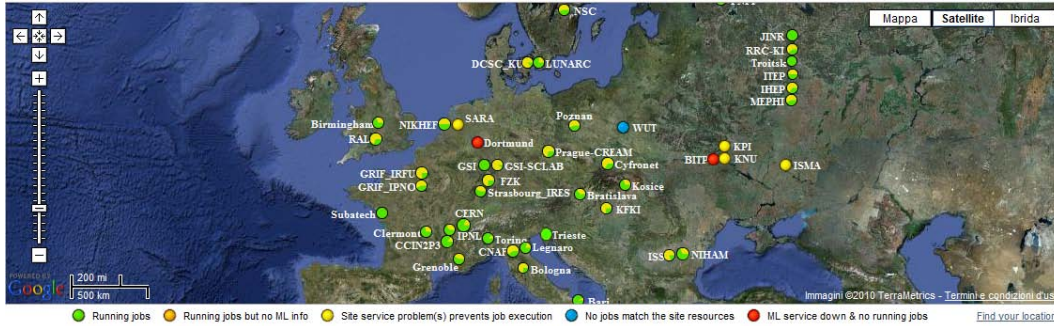


Figure 2.35: A snapshot of the ALICE VO sites in Europe. A green circle indicates that jobs are running on the sites while red and yellow circles indicate sites with problems[119].

Each site is composed of many WN, which are the physical machines where the software programs can be run. The Storage Element (SE) is responsible for managing physical files in the site and for providing an interface to mass storage. The Computing Element (CE) service is an interface to the local (WN) batch system and manages the computing resources in the site. The ALICE Collaboration has developed AliEn[120, 121] as an implementation of distributed computing infrastructure needed to simulate, reconstruct and analyze data from the experiment. AliEn provides the two key elements needed for large-scale distributed data processing: a global file system (catalogue) for data storage and the possibility to execute the jobs in a distributed environment. The analysis software, the user code and the AliRoot libraries (or par files in the case a development of the code is not deployed on the GRID), needed by each subjob to run must be specified in a JDL (Job Description Language), together with the data sample and the way to split it. The data sample is specified through a XML (eXecutable Machine Language) collection file which contains a list of the Logical File Names (LFN, the entries in the catalogue) of the files to be executed.

2.5.5.3 The AliRoot Framework

AliRoot[122, 123] is the offline framework for simulation, alignment, calibration, reconstruction, visualization, quality assurance, and analysis of experimental and simulated data. It is based on the ROOT framework. Most of the code is written in C++ with some parts in Fortran that are wrapped inside C++ code. The AliRoot development started in 1998 and it has been extensively used for the optimization of the experiment’s

design. It has been used for large-scale productions, so-called Physics Data Challenges (PDCs), where millions of events are produced. These have been used to estimate the physics performance of ALICE. Such events are also used to develop analysis procedures and to estimate the associated systematic errors, as is performed in this thesis. Finally, AliRoot is used to reconstruct events that occurred in the detector. For event simulation the framework provides the following functionality:

- **Event generation.** A collision is simulated by an event generator that is interfaced with AliRoot (e.g. Pythia[124], Phojet[125], or HIJING[126]); this step produces the *kinematics tree* containing the full information about the generated particles (type, momentum, charge, production process, originating particle, and decay products).
- **Transport.** The particles are propagated through the detector material which is modeled as realistically as possible. In this process, particles can interact with matter, decay, and create additional particles. Naturally, these particles have to be propagated through the detector as well. The total number of particles after the transport is significantly larger than the number of particles created in the initial generation step. During this process all interactions of particles with sensitive detector parts are recorded as hits that contain the position, time, and energy deposit of the respective interaction. Furthermore, track references that can be used to follow a track's trajectory, mainly needed for the debugging of the reconstruction algorithms, are stored. Programs that perform the transport and are interfaced with AliRoot are Geant3[127], Geant4[128], and Fluka[129].
- **Digitization.** If a particle produced a signal in a sensitive part (*hit*), the corresponding digital output of the detector is stored as a summable digit taking into account the detector's response function. Possible noise is then added to the summable digit and it is stored as a digit. Summable digits allow events to be merged without duplication of noise. In the last step, the data is stored in the specific hardware format of the detector (*raw data*).

At this stage the raw data corresponds to the signals that would be produced by an interaction of the same kind within the detector. The subsequent reconstruction is identical, both for simulated as well as real events. It consists of the following steps:

- **Cluster finding.** Particles that interact with the detector usually leave a signal in several adjacent detecting elements or in several time bins of the detector. In this step these signals are combined to form clusters. This allows the exact position or time of the traversing particle to be determined and reduces the effect of random noise. Overlapping signals from several particles in a single cluster are unfolded. This step is performed for each subdetector where due to the different nature of the subdetectors the implementations vary significantly.

- Track reconstruction.** The clusters are combined to form tracks that allow the track curvature and energy loss to be calculated with the aim of determining the associated momentum and particle identity. The tracking is a global task as well as an individual procedure per detector. The global central barrel tracking starts from track seeds in the TPC which are found by combining information from a few outermost pad rows under the assumption that the track originated from the primary vertex. Tracks are then followed inwards using a procedure called the Kalman filter: in each step the track, i.e. the track parameters and the covariance matrix, is propagated to the next pad row. The covariance matrix is updated adding a noise term that represents the information loss by stochastic processes such as multiple scattering and energy-loss fluctuations. If a cluster is found that fits to the track, it is added to the track, updating its parameters and the covariance matrix. Afterwards the same procedure is repeated by starting the seeding closer to the collision point. In a final step all clusters already associated to tracks are removed and the procedure is repeated without requiring that the seeds point to the primary vertex. The result, the so-called TPC-only tracks to which only TPC information contributed, is saved in the reconstruction output. Subsequently, these tracks are complemented with information from the ITS, TRD, and TOF as well as HMPID and the veto of PHOS if the track is in their acceptance, which produces so-called global tracks. Tracks can also be formed out of information from the ITS only. Tracks are represented by the parameters y , z , $\sin\phi$, $\tan\theta$ and $1/p_t$.
- Primary-vertex reconstruction.** Various information are used to find the primary-vertex position of the interaction. Examples of information, each of which is sufficient to produce a vertex position, are clusters in the SPD, tracks in the TPC, and global tracks. When a vertex position is found the tracks are constrained to it: the vertex position is used as an additional point to estimate the track parameters. The TPC-only tracks are constrained with the vertex position found with TPC-only tracks while the global tracks are constrained with the vertex position found with global tracks. Of course this constraint is only used for tracks that actually pass near the vertex.
- Secondary-vertex reconstruction.** Tracks are combined to find secondary vertices in order to reconstruct decayed particles like $\Lambda \rightarrow p\pi^-$ and photon conversions. For this purpose, opposite-sign tracks that originate sufficiently far away from the primary vertex are combined. If the closest approach and the topology of the two tracks are consistent with a decay, the pair is accepted as a potential secondary vertex.

The output of the reconstruction is called Event-Summary Data (ESD) which contains only high-level information such as the position of the event vertex, parameters of reconstructed charged particles together with their PID information, positions of secondary vertex candidates, parameters of particles reconstructed in the calorimeters, and

integrated signals of some subdetectors. These data are further reduced to the Analysis-Object Data (AOD) format. These smaller-sized objects contain only information needed for the analysis. Therefore, the transformation procedure may already contain a part of the analysis algorithm, for example track selection. Several AODs, focusing on different physics studies, can be created for a given event.

Chapter 3

Strange Resonances As Heavy Ions Physics Probe

In Chapter 1 we shown how the major goal of various heavy-ion programs is the search for a transient state of deconfined matter, the Quark-Gluon Plasma: a phase transition to this new state of matter is predicted by lattice QCD when a sufficiently high energy density ($\epsilon \gtrsim 1 \text{ GeV/fm}^3$) is reached. Strange particles yields and spectra are proposed as key probes to study excited nuclear matter and to detect the transition of (confined) hadronic matter to quark gluon matter. The relative enhancement of strange and multi-strange hadrons, as well as hadrons ratios in central heavy-ion collisions with respect to peripheral or proton induced interactions, have been suggested as possible signatures for the QGP-phase[41]. In this chapter we will see how the strange baryon resonances can be used to study some dynamical properties, in particular the freeze-out conditions, of the produced QGP fireball.

3.1 Strangeness and QGP Freeze-Out Dynamics

In the nucleus - nucleus collision, the emerging final state particles remember relatively little of their primordial source, since they had been subject to many rescattering processes during the hadronic gas stage.

Moreover for what concerns nucleus-nucleus collisions at relativistic energies, the major fraction of finally observed particles comes from decays of resonances (mesonic or baryonic) which have undergone many collisions from their point of production to the detection. The final hadron yields seem to be compatible with a hadronic gas described by the baryo-chemical potential μ_B and a temperature parameter T in a statistical model. Models take into account two sequential different kinds of freeze-out:

1. A chemical freeze-out, were the inelastic flavor changing collisions processes cease, roughly at an energy of 1 GeV per particle.

2. A later kinetic/thermal freeze-out, were also elastic processes have come to an end and the system decouples.

At the SPS energies chemical and thermal freeze-out happen sequentially at different temperatures ($T_{ch} \approx 160 - 170$ MeV, $T_{th} \approx 120$ MeV) and the system becomes colder with time.

To investigate the sequential freeze-out in heavy-ion reactions at SPS the Ultra-relativistic Quantum Molecular Dynamics model (UrQMD) is applied [130, 131]. This microscopic transport approach is based on the covariant propagation of constituent quarks and di-quarks accompanied by mesonic and baryonic degrees of freedom. The leading hadrons of the fragmenting strings contain the valence-quarks of the original excited hadron and represent a simplified picture of the leading (di)quarks of the fragmenting string.

In Figure 3.1 the time evolution of the elastic and inelastic collision rates in Pb+Pb at 160 AGeV of the SPS beams are depicted. The inelastic collision rate (full line) is defined as the number of collisions with flavor changing processes. The elastic collision rate consists of two components, true elastic processes and pseudo-elastic processes. While elastic collision do not change flavor, in the pseudo-elastic collisions the ingoing hadrons are destroyed and a resonance is formed. If this resonance decays later into the same flavors as its parent hadrons, this scattering is called pseudo-elastic.

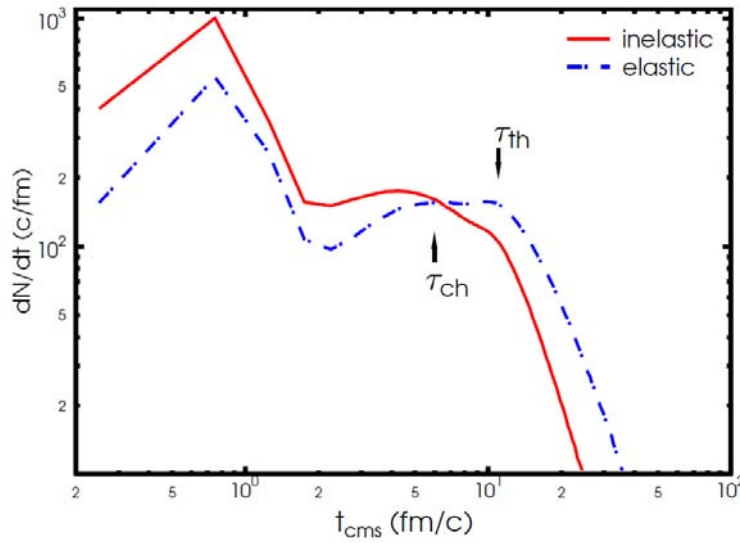


Figure 3.1: Inelastic and (pseudo-)elastic collision rates in Pb + Pb at 160 AGeV[132]. τ_{ch} and τ_{th} denote the chemical and thermal/kinetic freeze-out as given by the microscopic reaction dynamics of UrQMD.

Even if the main features revealed by this microscopic study do not contradict the idea of a chemical and thermal break-up of the source as shown in Figure 3.1, however the detailed freeze-out dynamics is much richer and by far more complicated as expected in simplified models[133]. Below a simplified schematic sequence is sketched:

1. $t < 2$ fm/c: in the initial stage of the nucleus-nucleus reaction, non-equilibrium dynamics leads to strong baryon stopping in multiple inelastic interactions, shown by huge and strongly time dependent collision rates. This stage deposits a large amount of (non-thermalized) energy and creates the first generation particles.
2. 2 fm/c $< t < 6$ fm/c: due to the high particle densities and energies, inelastic scattering processes dominate this stage of the reaction. Chemical equilibrium might be achieved due to a large number of flavour and hadro-chemistry changing processes until chemical freeze-out.
3. 6 fm/c $< t < 11$ fm/c: after the system has expanded and cooled down, elastic and pseudo-elastic collisions take over. Here, only the momenta of the hadrons change, but the chemistry of the system is mainly unaltered, leading to the kinetic freeze-out of the system.
4. $t > 11$ fm/c: finally, the reactions cease and the scattering rates drop drastically. The system breaks up.

The spectra and abundances of the resonances (such as $\Lambda(1520)$, $K^0(892)$, $\Sigma(1385)$...) can be used to study the break-up dynamics of the source between chemical and thermal freeze-out. If chemical and thermal freeze-out are not separated - e.g. due to an explosive break-up of the source - all initially produced resonances are reconstructable by invariant mass analysis of the final state hadrons. However, if there is a separation between the different freeze-outs, a part of the resonance daughters rescatter, making this resonance unobservable in the final state. Thus, the relative suppression of resonances in the final state compared to the behaviour expected from thermal estimates provides a chronometer for the time interval between the different reaction stages. This kind of study requires the acknowledge of different factors and parameters that will not all be treated in this thesis work. In particular the rescattering probability of the resonance decay products depends on the cross section of the decay products with the surrounding matter, on the lifetime of the surrounding hot and dense matter, on the lifetime of the resonance and on the specific properties of the daughter hadrons in the resonance decay channels. This leads to different “observabilities” of the different resonances. Using the estimates performed using a statistical model[134] and relating the result of the microscopic transport calculation (UrQMD) to thermal freeze-out parameters, a lifetime below 1 fm/c and a freeze-out temperature below 100 MeV are found for the microscopic source. These values obtained seem to favor a scenario of a sudden break-up of the initial hadron source, in contrast to the time evolution of the chemical and thermal decoupling as shown in Figure 3.1. It is important to note that these statistical calculations don't take into account the possible regeneration of the resonances during the elastic scattering phase.

Studies concerning the presence of a two-stages freeze-out were performed analyzing the WA97 experiment data[39, 135]. The key point in these analyses is that when sudden

QGP breakup occurs, the spectra of hadrons arise rather suddenly. Moreover, particles of different kind are produced by the same mechanism and thus are expected to have similar transverse mass⁷ m_t spectra. Because a spectrum of strange hadrons includes both directly produced, and heavy resonances decay products, it is possible to determine the freeze-out temperature and dynamical velocities of the fireball evolution solely from the study of precisely known shape of the particle spectra. In this analysis the tacit assumption done is that practically all decay products of resonances are thermally not re-equilibrated, which is equivalent to the assumption of sudden freeze out. If thermal and chemical freeze-outs are identical, these results must be consistent with earlier chemical analysis of hadron yields. The analysis were performed using the absolute yield and shape of six m_t spectra of Λ , $\bar{\Lambda}$, Ξ , $\bar{\Xi}$, $\Omega + \bar{\Omega}$, $K_s = (K_0 + \bar{K}_0)/2$, in four centrality bins. The theoretical primary particle spectra (both directly produced and parents of decay products) are derived from the Boltzmann distribution in which two velocities were introduced: a local flow velocity v of the fireball matter from where particles emerge, and an hadronization surface (breakup) velocity $v_f^{-1} \equiv dt_f/dx_f$. As expected, it was found that all hadron m_t spectra are strongly influenced by resonance decays (for what it is assumed that they are not reequilibrated in rescattering). Some of the resulting m_t spectra obtained with the cited study are shown in Figures 3.2 A and B and 3.3 A and B. The description of the shape in the four centrality cases considered is very satisfactory .

The similarity of the spectra implies that the production mechanism of Λ , $\bar{\Lambda}$, and Ξ , $\bar{\Xi}$ would be the same. This symmetry is an important cornerstone of the claim that the strange antibaryon data can only be interpreted in terms of direct particle emission from a deconfined phase. In presence of conventional hadron collision based physics, the production mechanism of antibaryons is quite different from that of baryons and a similarity of the m_t spectra is not expected. Moreover, even if QGP is formed, but an equal phase of confined particles is present, the annihilation of antibaryons in the baryon rich medium created at CERN-SPS energy would deplete more strongly antibaryon yields, in particular at small particle momenta, with the more abundant baryons remaining less influenced. This effect is not observed[136].

In Figure 3.4 the freeze-out temperature T of the m_t spectra as function of the centrality bin is shown. The horizontal lines delineate the range of results of the most recent chemical freeze-out analyses[137].

There is no indication of a significant or systematic change of T with centrality. This is consistent with the believe that the formation of the new state of matter is occurring in all centrality bins explored by the experiment WA97. The (unweighted) average of all results shown in Figure 3.4 produces a freeze-out temperature at the upper boundary of the pure chemical freezeout analysis result, $T \simeq 145$ MeV.

The magnitudes of the collective expansion velocity v and the break-up (hadronization) speed parameter v_f are shown in Figure 3.5.

In the upper part of the figure the consistency of v with earlier chemical freeze-out

⁷The transverse mass is defined as $m_t = \sqrt{m^2 + p_t^2}$ where m is the rest mass of the considered particle.

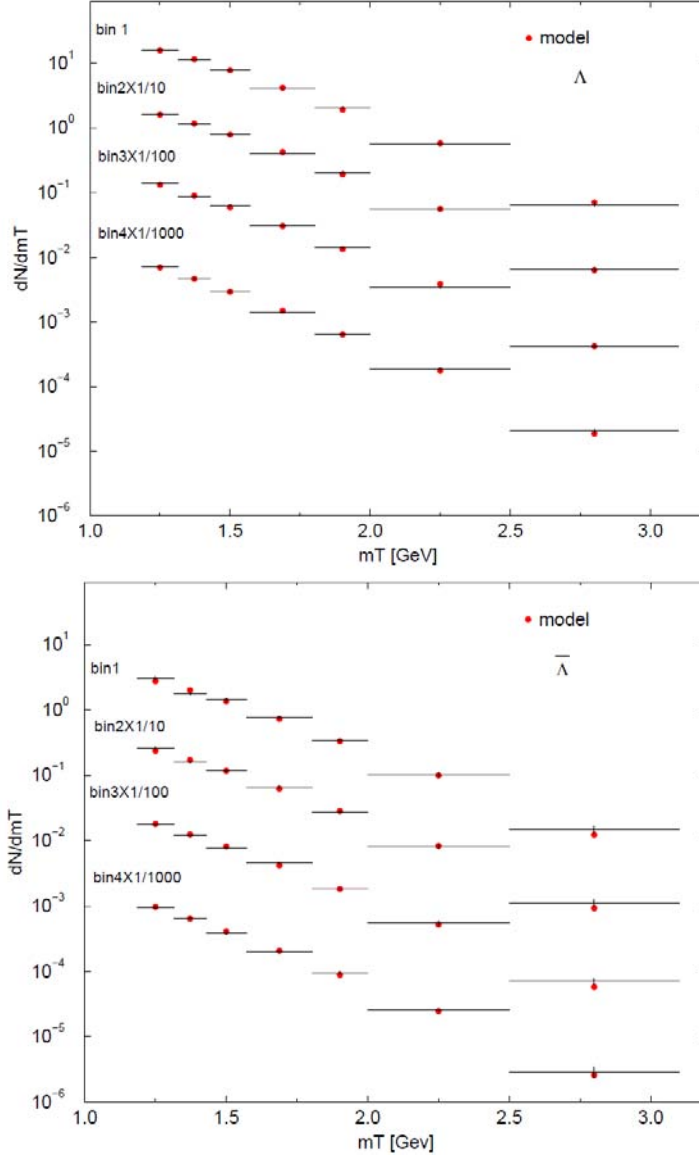


Figure 3.2: **Up - A:** Thermal analysis m_t spectra: Λ . **Down - B:** Thermal analysis m_t spectra: $\bar{\Lambda}$ [39]. The bin centrality goes from the bin number 4 (the most central) to the number 1.

analysis is evident. Even though it is flat within the experimental error, it reveals a slight but systematic increase with centrality, and thus with size of the system. This is expected, since the more central events involve a greater volume of matter, which allows more time for the development of the flow. The value of the break-up (hadronization) speed parameter $v_f^{-1} \equiv dt_f/dx_f$ shown in the top portion of Figure 3.5 is close to the speed of light and this is consistent with the picture of a sudden breakup of the fireball.

3.2 Dynamical Freeze-Out Constraint with Resonances

In recent years some studies were performed in order to explore if it is possible to experimentally determine the period of time between the fireball chemical and thermal freeze-out using the strange hadron resonances behaviour[138]. The short-lived resonances, detectable through invariant mass reconstruction[139] are natural candidates for

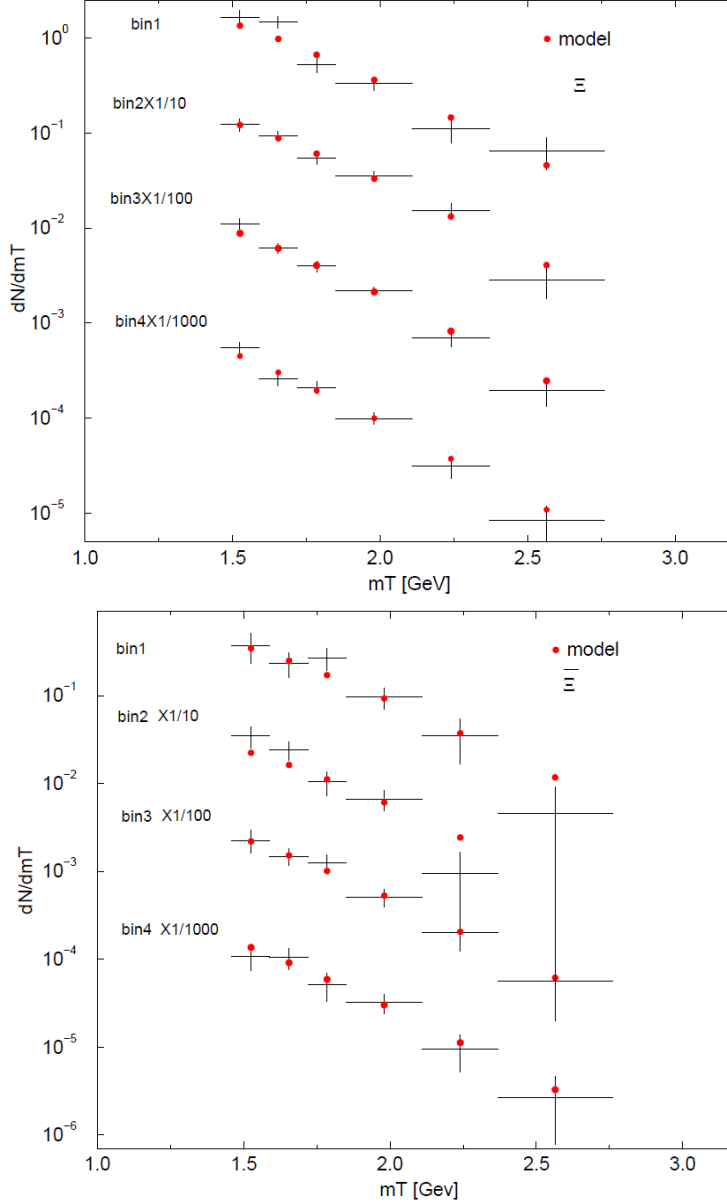


Figure 3.3: **Left - A:** Thermal analysis m_t spectra: Ξ . **Right - B:** Thermal analysis m_t spectra: $\Xi[39]$. The bin centrality goes from the bin number 4 (the most central) to the number 1.

freeze-out diagnostic since their lifetime is comparable to the hadronization timescale and to the lifetime of the interacting HG. Resonances usually have the same quark numbers as light particles, making their yield compared to the light particle independent of chemical potential. The rich variety of detected resonances includes particles with very different masses and widths, allowing us to probe both production temperatures and interaction lifetimes in detail. Figure 3.6 shows what percentage of observed light particles comes from the decays of heavier resonances (quite a few of them experimentally observable). As can be seen this resonance contribution is significant, and varies appreciably with both particle type and temperature of the production reaction.

The resonance $\Lambda(1520)$ ($\Gamma_{\Lambda(1520)} = 15.6$ MeV) has been observed in heavy-ion reactions at SPS energies. Both SPS and RHIC experiments report measurement of the $K^{*0}(892)$ signal, which has a much greater width, $\Gamma_{K^{*0}} = 50$ MeV. The $\Lambda(1520)$

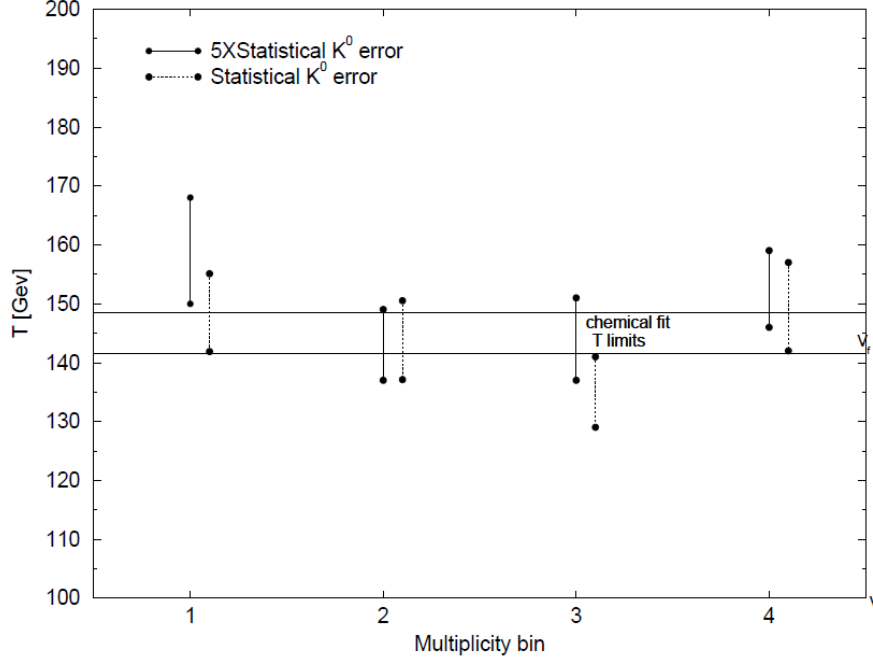


Figure 3.4: Thermal freeze-out temperature T for different centrality bins compared to chemical freeze-out analysis shown by horizontal solid lines. The bin centrality goes from the bin number 4 (the most central) to the number 1. See[39].

abundance yield is found about 2 times smaller than expectations based on the yield extrapolated from nucleon-nucleon reactions, scaled with hadron yield. This has to be compared with an increased Λ production by factor 2.5. A possible explanation for this relative suppression by a factor 5 is that the decay products (π, Λ) have re-scattered and thus their momenta did not allow to reconstruct this state in an invariant mass analysis. However, the observation of a strong K^{*0} yield signal contradicts this point of view. Another explanation is that in the nuclear matter $\Lambda(1520)$ decays faster and there is much more opportunity for the rescattering of decay products, and fewer observable resonances.

The observable yield of the resonances is thus controlled by several physical properties, such as the freeze-out temperature T , the decay width in nuclear matter Γ , and the time spent in the hadron phase after freeze-out τ . The suppressed yield can mean either a low temperature chemical freeze-out, or a long interacting phase with substantial re-scattering.

A model based on the width of the resonances $K^0(892)$, $\Lambda(1520)$, and also the (more difficult) $\Sigma(1385)$ and the decay products reaction cross-sections within an expanding fireball of nuclear matter, in order to explore their production and suppression observability, could be a further way of distinguishing between different reaction scenarios.

The $\Sigma(1385)$ is expected to be produced more abundantly than $\Lambda(1520)$ in a hadronic fireball due to its high degeneracy factor and smaller mass. Because of its shorter lifetime ($\Gamma_{\Sigma^*} = 36-39 \text{ MeV} > \Gamma_{\Lambda^*} = 15.6$), the Σ^* signal is more strongly influenced by

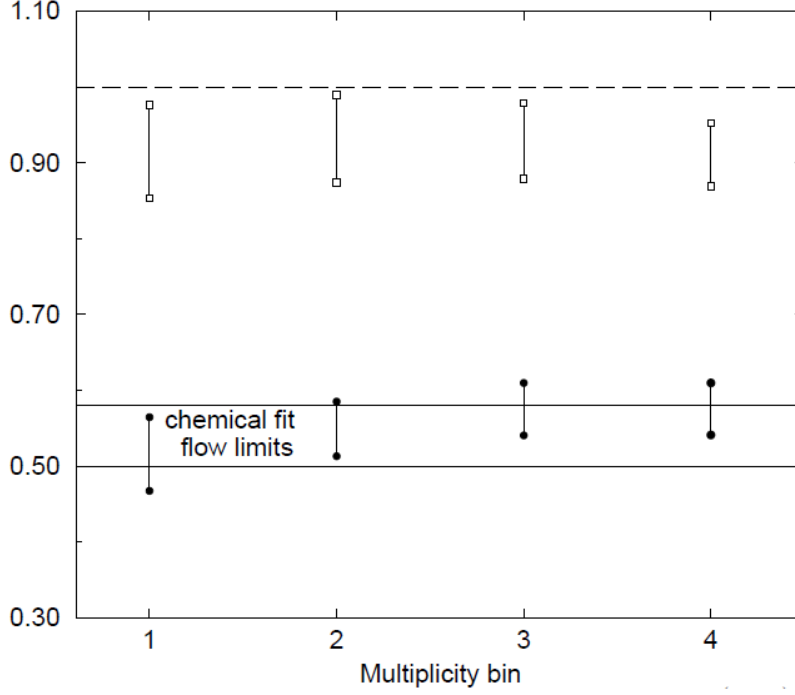


Figure 3.5: Thermal freeze-out flow velocity v (top) and break up (hadronization) velocity v_f for different centrality bins. Upper limit $v_f = 1$ (dashed line) and chemical freeze-out analysis limits for v (solid lines) are also shown. The bin centrality goes from the bin number 4 (the most central) to the number 1[39].

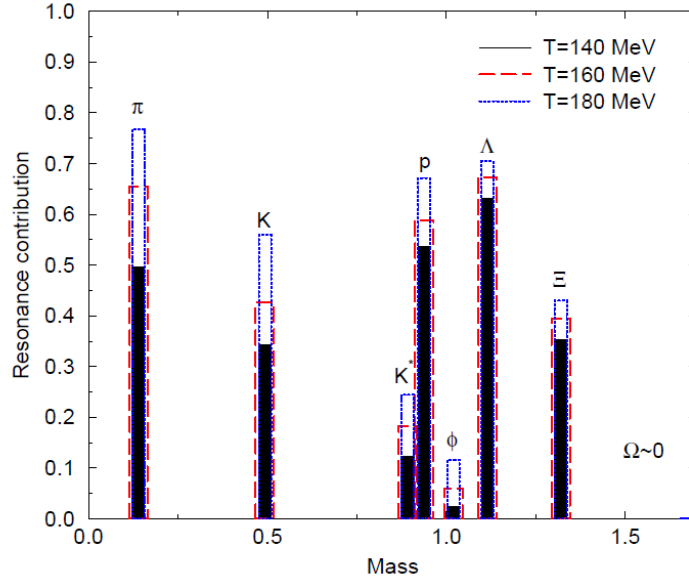


Figure 3.6: Relative resonances contribution to individual stable hadrons for three particle freeze-out temperatures[140].

final state interactions than that of $\Lambda(1520)$. Like for $K^0(892)$, one would naively expect that the observable yield of Σ^* should be suppressed by a factor 10[134].

In this model hadrons produced directly from a medium at temperature T fill the available statistical phase space which has the relativistic Boltzmann distribution shape:

$$\frac{d^2 N}{dm_t^2} \propto g \prod_{i=1}^n \lambda_i \gamma_i m_t \cosh(y) e^{-E/T} \quad (3.1)$$

where g is the statistical degeneracy, λ_i and γ_i are the fugacity⁸ and equilibrium parameters of each valence quarks, and E is the energy. When the fireball is expanding at a relativistic speed, equation 3.1 describes the energy distribution of an element of the fireball in a reference frame at rest with respect to the expansion (flow). However in this model were evaluated ratios of particles with similar masses, and interaction modes, often considered in full phase space. For this reasons to a good approximation, the flow effects largely cancel out. Similarly, for ratios of particles with the same valence quark composition, such as Σ^*/Λ , $\Lambda(1520)/\Lambda$ and, in the limit of $\lambda_u = \lambda_d$, $K^{*0}(892)/K^- (= \overline{K^{*0}}/K^+)$ the chemical factors (λ 's and γ 's) cancel out between the two states compared.

In Figure 3.7 we show the relative thermal production ratios at chemical freeze-out over the entire spectrum of rapidity and m_t (solid lines) as well a central rapidity range defined by the $y - m_t$ region covered by the WA97 experiment ($|y| < 0.5$ in the center of mass frame)(dashed lines). Looking at the graph it is possible to observe the possibility to measure the chemical freeze-out temperature by a measurement of the relative resonance yields.

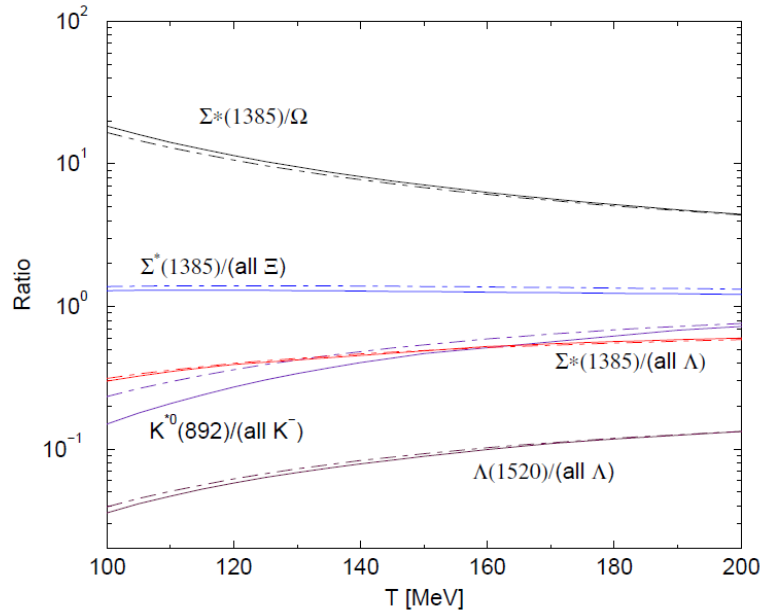


Figure 3.7: Temperature dependence of ratios of Σ^* , K^{*0} and $\Lambda(1520)$ to the total number of observed K^+ 's, Λ 's, Ξ 's and Ω 's. Branching ratios are included. Dashed lines show the result for a measurement at central rapidity $\Delta y = \pm 0.5$ [134].

A simple test of hadronization model consists in measurement of the ratio Σ^*/Ξ . If

⁸The fugacity is defined as $\lambda = e^{\mu/T}$ where μ is the chemical potential and T the temperature[38].

it is significantly smaller than unity, we should expect a re-equilibration mechanism to be present. Otherwise sudden hadronization applies.

The ratios of observed particles, however, can be considerably different from production ratios, since if the decay products rescatter before detection their identification by reconstructing their invariant mass will generally not be possible. While the lifetime of the Ξ and Ω are large enough to ensure that only a negligible portion of particles decay near enough to the fireball for rescattering to be a possibility, the lifetime of K^{*0}, Σ^* and even $\Lambda(1520)$ is instead within the same order of magnitude of the fireballs dimensions i.e. $2R/c \approx 1/\Gamma$. For this reason, a considerable number of decay products will undergo rescattering, and the estimation of this percentage is required before any meaningful parameters are extracted from the data.

Figures 3.8 and 3.9 show the dependence of the $\Lambda(1520)/\Lambda$, Σ^*/Λ and $K^{*0}(892)/K^+$ on the temperature and lifetime of the interacting phase.

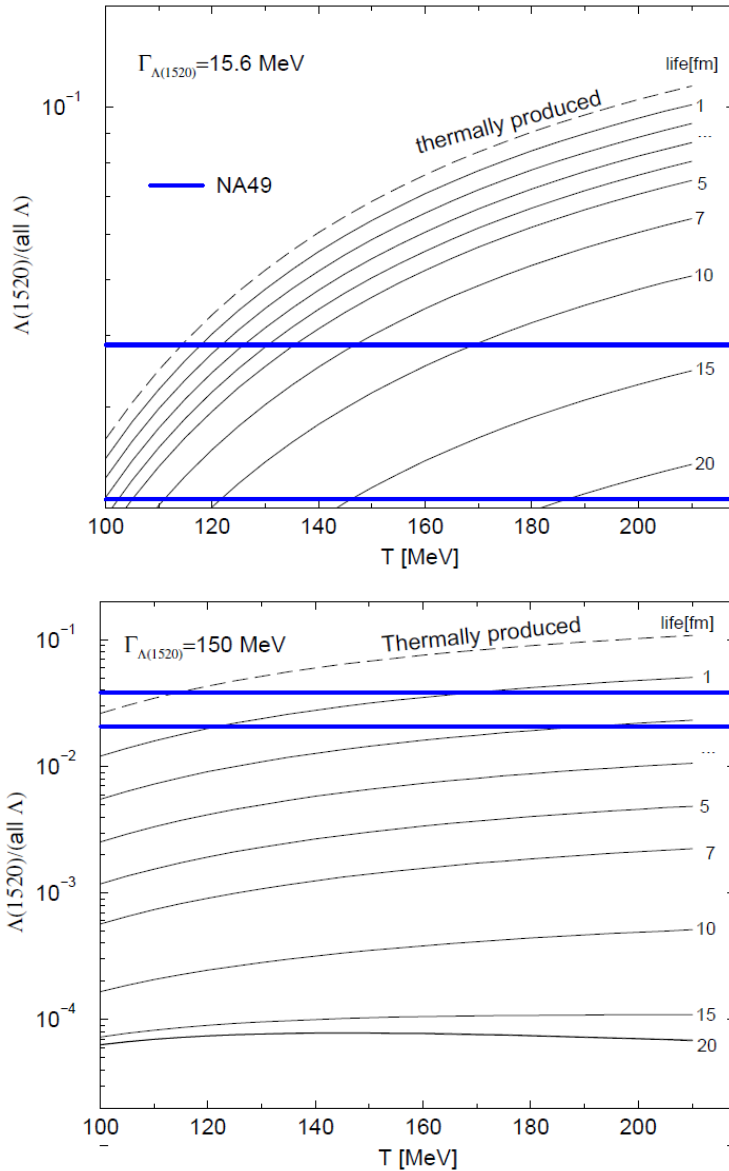


Figure 3.8: Relative $\Lambda(1520)/(\text{all } \Lambda)$ yield as function of freeze-out temperature T . Dashed - thermal yield, solid lines: observable yield for evolution lasting the time shown (1...20 fm/c) in an opaque medium. Horizontal lines: experimental limits of NA49[141]. **Up:** natural resonance width $\Gamma_{\Lambda(1520)} = 15.6$ MeV. **Down:** quenched $\Gamma_{\Lambda(1520)} = 150$ MeV[138].

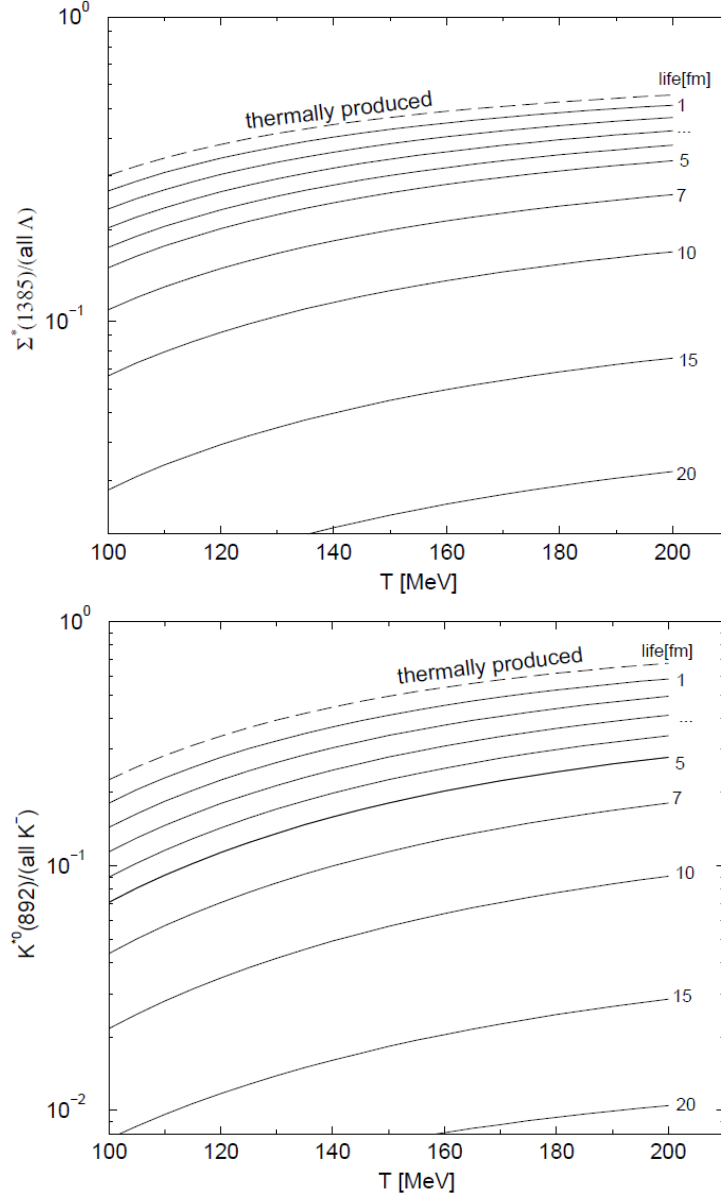


Figure 3.9: Produced (dashed line) and observable (solid lines) ratios $\Sigma^*/(\text{total } \Lambda)$ (up) and K^{*0}/K (down). The solid lines correspond to evolution after chemical freeze-out of 1, 2, 3, 4, 5, 7, 10, 15, 20 fm/c, respectively[134].

It is clear that, given a determination of the respective signals to a reasonable precision, a qualitative distinction between the high temperature chemical freeze-out scenario followed by a rescattering phase and the low temperature sudden hadronization scenario can be performed. Figures 3.8 and 3.9 demonstrate the sensitivity of strange hadron resonance production to the interaction period in the hadron phase, i.e. the phase between the thermal and chemical freeze-out. What we learn from them is that while the suppression of one of these ratios considered has generally two interpretations, as it can mean either a low temperature chemical freeze-out or a long interacting phase with substantial rescattering, the comparison of two resonances with considerably different lifetimes can be used to constrain both the temperature of chemical freeze-out and the lifetime of the interacting phase.

We can reexpress the results presented in Figures 3.8 and 3.9 representing one ratio

against the other as is seen in Figures 3.10, 3.11 and 3.12.

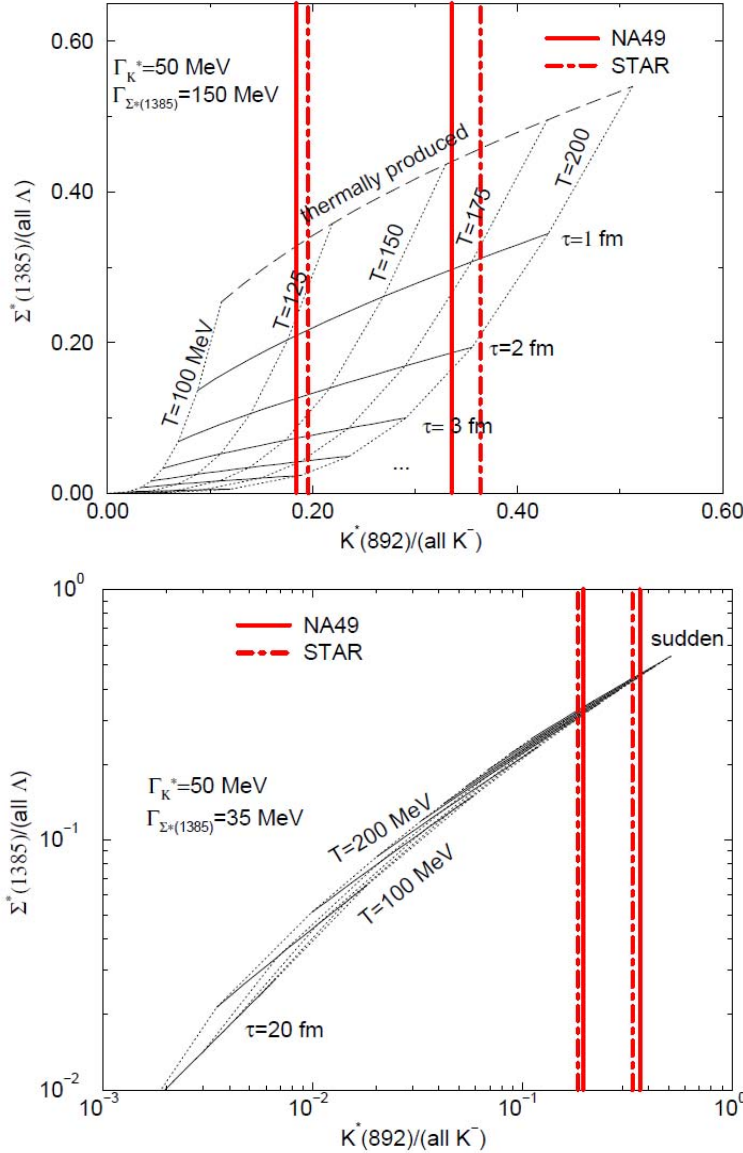


Figure 3.10: Dependence of the combined $\Sigma^*/(\text{all } \Lambda)$ with $K^0(892)/(\text{all } K)$ signals on the chemical freeze-out temperature and interacting phase lifetime. **Up:** quenched $\Gamma_{\Sigma^*} = 150$ MeV. **Down:** natural widths. Vertical lines: experimental limits of NA49[142] and STAR[138].

In all these figures we can see that from top to bottom in the grid, the lifespan in fireball increases, while from left to right the temperature of chemical particle freeze-out increases. The medium is effectively opaque, all resonances that decay in medium become unobservable. A remarkable prediction is found for the resonances Σ^* : when both the Σ^*/Λ and Σ^*/Ξ ratios become available both the temperature and the lifetime can be inferred from the Σ^* alone.

Moreover, further studies were performed in order to analyze the m_t and p_t dependence of these ratios for different freeze out temperatures[143].

Figure 3.13 shows the prediction obtained for the ratio $\Sigma(1385)/\Lambda$, at two freeze-out temperatures and flows: $T = 140$ MeV, $v_{max}/c = 0.55$ on left and $T = 170$ MeV, $v_{max}/c = 0.3$ on the right. Significant deviations from simple constant values are observed, showing the sensitivity of the ratio to the different model applied. The graphs takes

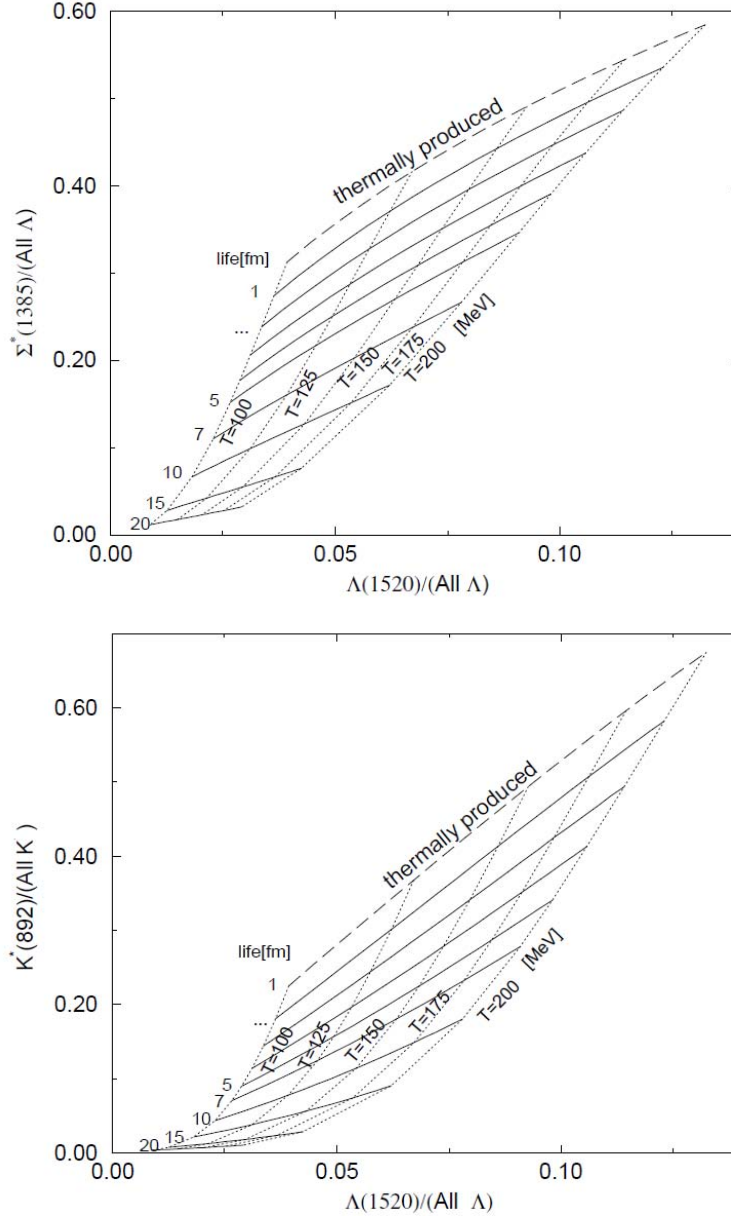


Figure 3.11: Dependence of the combined $\Sigma^*/(\text{all } \Lambda)$ with $K^0(892)/(\text{all } K)$ signals on the chemical freeze-out temperature and interacting phase lifetime. **Up:** quenched $\Gamma_{\Sigma^*} = 150$ MeV. **Down:** natural widths. Vertical lines: experimental limits of NA49[142] and STAR[138].

into account the feed down from resonances (i.e. the decay products from reconstructed $\Sigma(1385)$).

To further study the sensitivity of resonance-particle ratio to freeze-out dynamics, the (feed down corrected) ratios as a function of p_t were also considered. Comparing them with those in the Figure 3.14 it is possible to see grossly different behaviors, with many of the results coalescing. This is an expression of the fact that $\Sigma(1385)$ and Λ have dramatically different p_t at the same m_t and vice versa.

From the Figures 3.13 and 3.14 is evident that the m_t and p_t dependence of the ratios depends on the freeze-out model and, in particular, changes in temperature and flow velocity alter the ratios shape. Moreover, as previously mentioned, the presence of a long living hadronic gas rescattering phase can distort this freeze-out probe. Infact the $\Sigma(1385)/\Lambda$ ratio will be altered due to the depletion of the detectable resonances

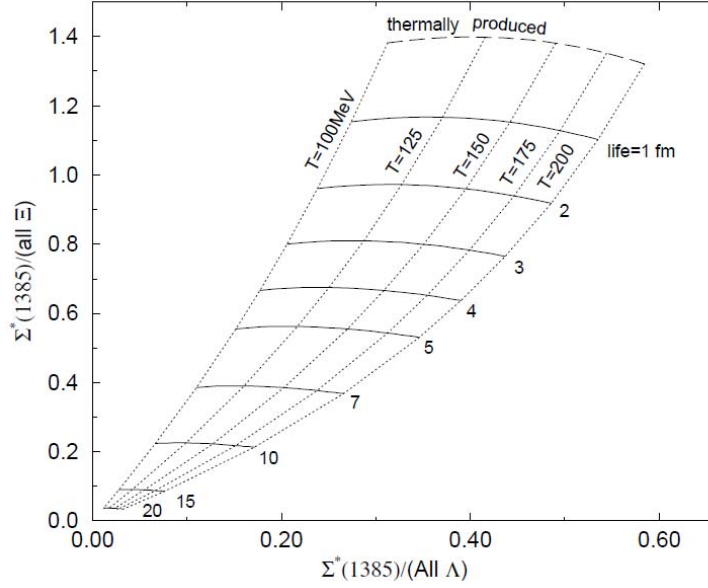


Figure 3.12: Dependence of the combined $\Sigma^*/(\text{all } \Lambda)$ and $\Sigma^*/(\text{all } \Xi)$ signals on the chemical freeze-out temperature and interacting phase lifetime[134].

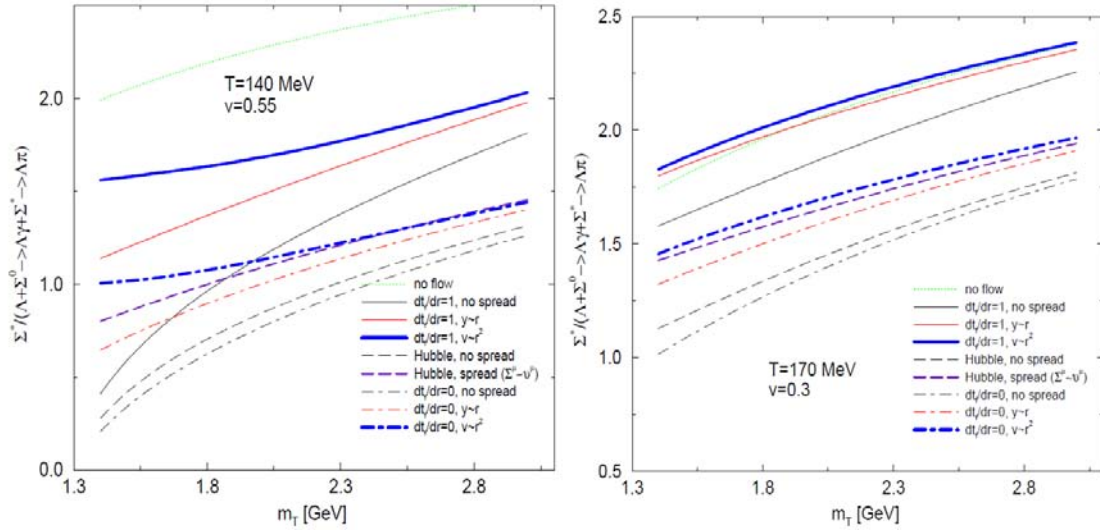


Figure 3.13: Dependence of the $\Sigma(1385)/\Lambda$ ratio on the Freeze-out model including feed down from resonances. For more details see [143].

through the rescattering of their decay products. Its dependence on m_t will be affected in a non-trivial way, since the faster resonances will have a greater chance to escape the fireball without decaying, thus avoiding the rescattering phase. Regeneration of the resonances in hadron scattering may add another m_t dependence.

A long rescattering phase would affect the Σ^* distribution and the effect would be easy to detect experimentally: 95% of Σ^* decay through the p-wave $\Sigma^* \rightarrow \Lambda\pi$ channel. However, regenerating Σ^* in a gas of Λ and π is considerably more difficult, since $\Lambda\pi$ scattering will be dominated by the s-wave $\Lambda\pi \rightarrow \Sigma^\pm$. This situation will not occur

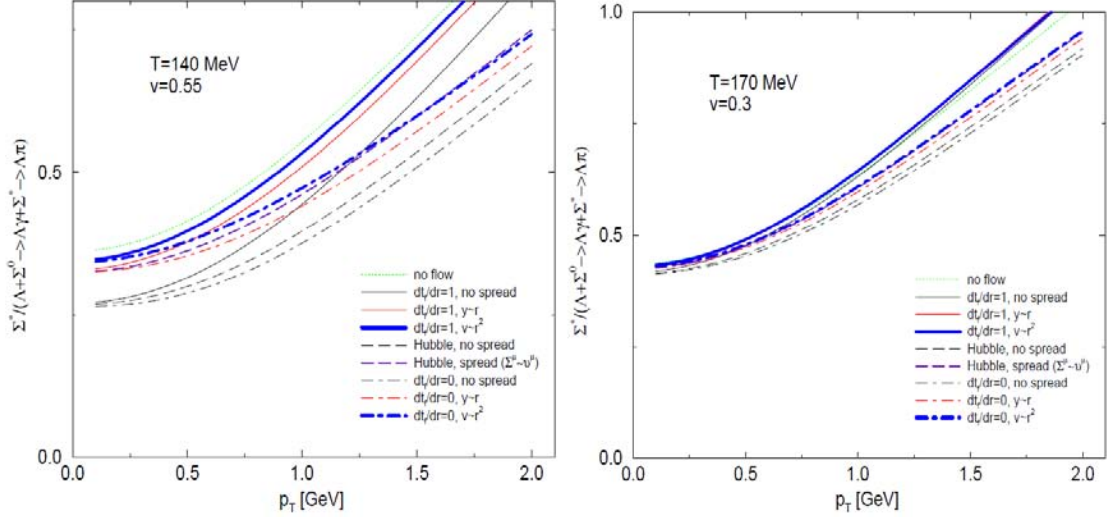


Figure 3.14: p_t dependence of $\Sigma(1385)/(\text{all } \Lambda)$ ratios, including feed down from resonances. For more details see [143].

for $K^* \leftrightarrow K\pi$, since both decay and regeneration happen through the same process, leading to a very fast reequilibration time. Since both Σ^*/Λ and K^*/K have been calculated within the thermal model (neglecting rescattering), a strongly depleted Σ^*/Λ (compared with K^*/K) suggests that a statistical freeze-out description is incomplete and an interacting hadron gas phase is also necessary[143].

3.3 Sigma(1385) Features

The $\Sigma(1385)$ is a strange resonance that exist in three charge states: Σ^{*+} , Σ^{*0} , Σ^{*-} with the respective antiparticles. Discovered in the 1960 by Margaret Alston and her group[144], it was founded to be characterized by the following quantum numbers: $S = -1$, $I (J^P) = 1 (3/2)^+$. The quark composition of the three states is $\Sigma^{*+} \rightarrow (uus)$, $\Sigma^{*0} \rightarrow (uds)$, $\Sigma^{*-} \rightarrow (dds)$. Mass and widths are summarized in Table 3.1, while its possible four decay channels are listed in Table 3.2.

$\Sigma(1385)^+$ mass m	1382.8 ± 0.4 MeV
$\Sigma(1385)^0$ mass m	1383.7 ± 1.0 MeV
$\Sigma(1385)^-$ mass m	1387.2 ± 0.5 MeV
$\Sigma(1385)^+$ full width Γ	35.8 ± 0.8 MeV
$\Sigma(1385)^0$ full width Γ	36 ± 5 MeV
$\Sigma(1385)^-$ full width Γ	39.4 ± 2.1 MeV

Table 3.1: Mass and widths of Σ^{*+} , Σ^{*0} , Σ^{*-} [6].

It is important to note that both the two most important decay channels are strong. This has two consequences: first of all the resonance peak will be quite broad, and in the data reconstruction phase will not be possible to separate the Σ^* decay vertex from

$\Sigma(1385)$ DECAY MODES	Fraction (Γ_i/Γ)	Confidence level	$\frac{p}{\text{MeV/c}}$
$\Lambda\pi$	$(87.0 \pm 1.5) \%$		208
$\Sigma\pi$	$(11.7 \pm 1.5) \%$		129
$\Lambda\gamma$	$(1.3 \pm 0.4) \%$		241
$\Sigma^- \gamma$	$< 2.4 \times 10^{-4}$	90%	173

Table 3.2: Decay channels and respective branching ratios for $\Sigma(1385)$ [6].

the interaction primary one. That means that no topological selection will be possible and the Σ^* signal can be extracted only through an invariant mass analysis.

In order to study the properties and the evolution in time of the yields of the $\Sigma(1385)$ in the nuclear medium after QGP hadronization, some theoretical studies were performed [145, 146]. In these calculations the influence of the medium on resonance lifespan and the effect of the motion of the decaying particle with respect to the thermal rest frame were taken into account. For instance in Figure 3.15 the decrease in the $\Sigma(1385)$ lifespan as a function of temperature T in the reaction $\Sigma(1385) \leftrightarrow \Lambda\pi$ is shown.

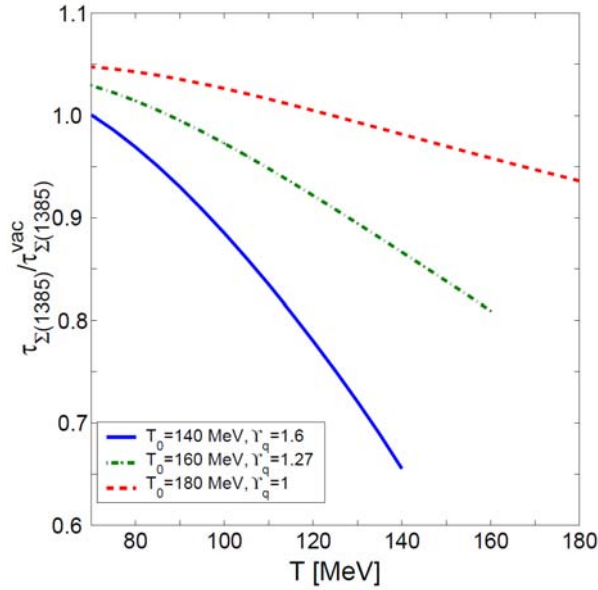


Figure 3.15: The ratio of the in medium lifespan τ_3 with the vacuum lifespan τ_0 as a function of temperature T for the reaction $\Sigma(1385) \leftrightarrow \Lambda\pi$. The dashed (red) line is for hadronization at $T_0 = 180$ MeV, $\gamma_q = 1.0$; the dot-dashed line (green) for hadronization at 160 MeV, $\gamma_q = 1.27$; solid line (blue) is for hadronization at 140 MeV and $\gamma_q = 1.6$ [145].

Much more details concerning these studies can be found in [145, 146].

3.4 Sigma(1385) studies in the STAR Experiment

In the recent years, the resonance $\Sigma(1385)$ was studied at the Relativistic Heavy Ion Collider in STAR experiment[139] in pp, pA and AA collisions at $\sqrt{s} = 200$ GeV.

The direct measurement of this resonance is not possible due to their short lifetimes (e.g. $\tau_{\Sigma^*}(1385) = 5 \text{ fm}/c$) [6].

3.4.1 Invariant Mass Analysis

The $\Sigma(1385)$ resonances are identified through the invariant mass analysis of Λ and π decay particle candidates. In particular, two methods were used to identify Σ^* 's. In the first method, the three particles mixing technique (TPM), every π is combined with every p to produce a Λ candidate. Then the Λ candidate is combined with all remaining π to get $\Sigma(1385)$. In the second method, the hybrid mixing technique (HM), $\Sigma(1385)$'s are identified by combining topologically reconstructed Λ 's with π 's. In both techniques the background is described by combining π 's from one event with the Λ 's from another event. The $\Sigma(1385)$ signal is obtained by subtracting this normalized mixed-event background from the invariant mass distribution. In Figure 3.16 the signal before and after the background subtraction for p+p, d+Au, and Au+Au collisions at $\sqrt{s_{NN}} = 200 \text{ GeV}$ is presented. Since $\Xi^- \rightarrow \Lambda \pi^-$ shares the same decay channel as $\Sigma(1385)^-$ both signals were observed in the invariant mass spectrum. The background subtracted signal is fitted with a Gaussian for Ξ and a Breit-Wigner for $\Sigma(1385)$.

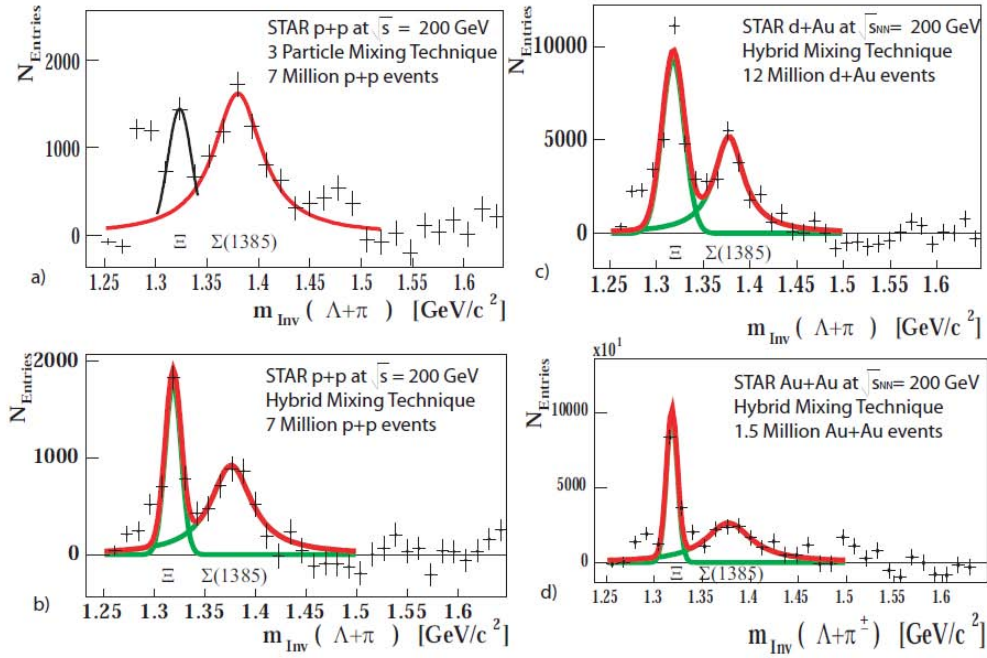


Figure 3.16: Invariant mass spectra of Ξ and $\Sigma(1385)$ after mixed-event background subtraction: (a) Invariant mass spectrum of $\Sigma(1385)$ in p+p using the three particle mixing technique. The Ξ has the same decay channel as the $\Sigma(1385)$. (b) Invariant mass spectrum in p+p using the hybrid mixing technique. With respect to the TPM technique the structure at the low M_{inv} in the background disappears with cleanly identified Λ 's. (c) Invariant mass spectrum in d+Au using the hybrid mixing technique. (d) Invariant mass spectrum in Au+Au using the hybrid mixing technique [139]

With the TPM technique, in the lower kinematic limit of the invariant mass spectrum a background structure appears (Figure 3.16-a). This initial structure increases in the d+Au collisions and totally dominates the spectrum in Au+Au collisions, due to an increase in background combinatorial statistics. Monte Carlo studies show that a partial contribution of the background structure comes from the misidentification of the Λ 's with the $\pi_{bachelor}$ and misidentification of K's as π 's. The HM technique can be used to identify $\Sigma(1385)$ with less efficiency but with a cleaner background (Figure 3.16-b,c,d). Since Λ 's can be identified more cleanly with the decay topology technique, the initial structure disappears.

3.4.2 Spectra

The transverse mass (m_t) spectra of $\Sigma(1385)^\pm$ and their antiparticles in p+p (circles) and Au+Au (stars) collisions are shown in Figure 3.17 while in Figure 3.18 for d+Au collisions.

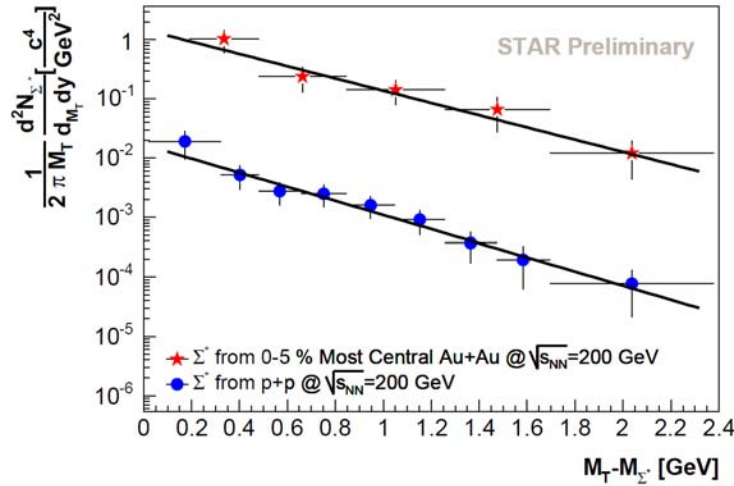


Figure 3.17: The transverse mass spectrum for $\Sigma(1385)$ drawn as stars for the 0-5% most central Au+Au and circles for p+p collisions at $\sqrt{s_{NN}} = 200$ GeV and $|y| < 0.75$ [147].

The systematic errors include the uncertainty due to bin size fluctuations, the normalization of the mixed event background and the uncertainty of the straight line fit range due to correlations in misidentified decay particles. Event and track selections were also varied. The acceptance and efficiency correction for the spectra is accomplished by embedding Monte Carlo simulated resonances into real p+p and Au+Au events. The solid lines in Figure 3.17 represent exponential fits to the data with the function directly proportional to the yield (dN/dy) and inversely proportional to the slope parameter $T^2 + m_0 T$ within the framework of a thermal model (Eq. 3.2).

$$\frac{1}{2\pi m_t} \frac{d^2 N}{dy dm_t} = \frac{dN}{dy} \frac{1}{2\pi T(m_0 + T)} \exp\left(-\frac{(m_t - m_0)}{T}\right) \quad (3.2)$$

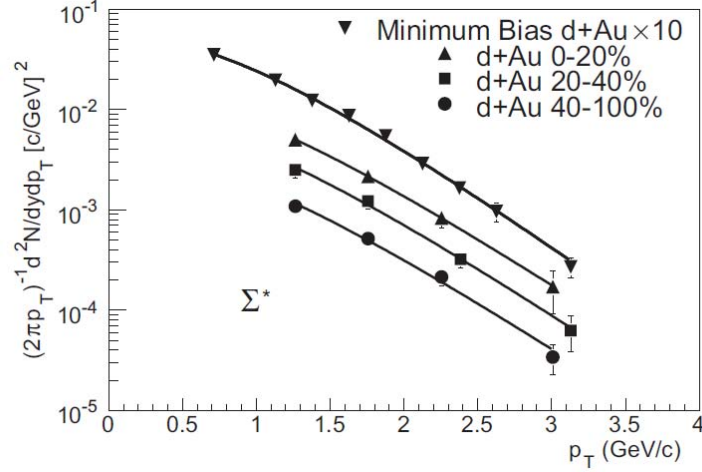


Figure 3.18: The Σ^* invariant yields as a function of p_t at $|y| < 0.75$ for minimum bias d+Au collisions and three different centralities. The lines are fits to an exponential function[148].

3.4.3 Average Transverse Momentum

The averaged transverse momentum $\langle p_t \rangle$ provides information on the shape of the particle spectra. At a given mass, the larger the $\langle p_t \rangle$, the harder the spectra are. The $\langle p_t \rangle$ is derived from the full range integration of the corresponding exponential fit. In Table 3.3 the inverse slope parameters of the exponential fit functions, the $\langle p_t \rangle$'s and the yields (dN/dy) of the summed signal of $\Sigma(1385)^\pm$ and their antiparticles are summarized, for p+p and Au+Au collisions at $\sqrt{s_{NN}} = 200$ GeV.

$\Sigma(1385)^\pm$	p+p	Au+Au
T (MeV)	358 ± 47	420 ± 84
$\langle p_t \rangle$ (GeV/c)	1.08 ± 0.15	1.2 ± 0.24
Yields (dN/dy)	$(4.66 \pm 0.98) \times 10^{-3}$	4.72 ± 1.78

Table 3.3: Temperature T, $\langle p_t \rangle$ and yield obtained from the exponential fits of the p_t spectra in Figure 3.17 for elementary p+p and 5% most central collisions. The statistical uncertainties are given and the systematic error, mostly due to the normalization and to the shape of the background, $\approx 15\%$, must be included in the given values[149].

The $\langle p_t \rangle$ of ρ^0 , K^* , Δ^{++} , Λ^* , and Σ^* as a function of $dN_{ch}/d\eta$ ⁹ compared to that of π^- , K^- , and \bar{p} for minimum bias d+Au are depicted in Figure 3.19. While the $\langle p_t \rangle$ of these hadrons are independent of centrality, as expected, they are strongly dependent on the mass of the particle. We can compare the spectra shape among particles for different systems by comparing their $\langle p_t \rangle$. Figure 3.20 shows the $\langle p_t \rangle$ of various particles for different systems, minimum bias p + p, d + Au, and central Au+Au collisions. Even though there is a strong mass dependence, the collision system dependence of the $\langle p_t \rangle$

⁹In heavy-ion physics $dN_{ch}/d\eta$ is often used as estimation of the centrality of the collision.

of these particles is not fully clarified because of the non negligible error bars. Only the \bar{p} shows a dependence when considering the Au-Au collisions with respect to the d-Au and p-p collisions. The $\langle p_t \rangle$ of particles measured in d+Au collisions lie between the $\langle p_t \rangle$ measured in p+p and Au+Au collisions, indicating a possible hardening of the spectra from p+p through d+Au to Au+Au collisions[148].

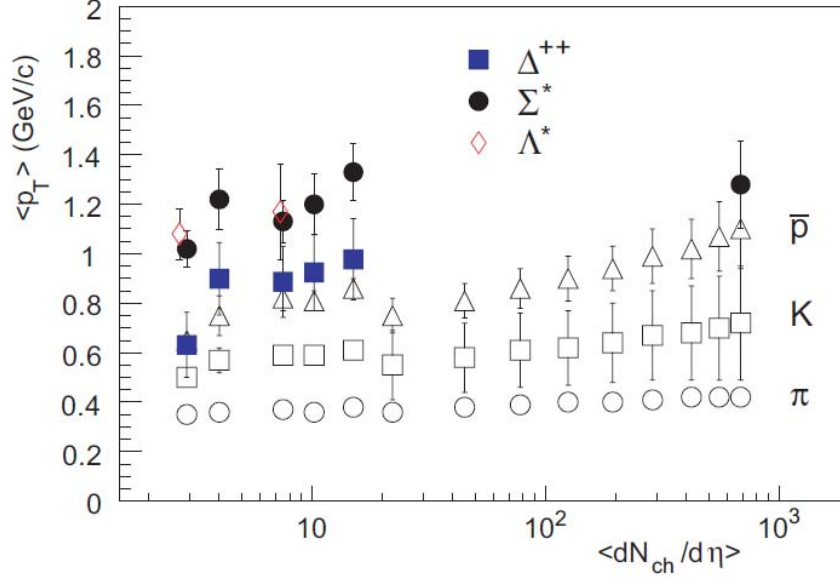


Figure 3.19: The Δ^{++} , Σ^* , and Λ^* $\langle p_t \rangle$ as a function of $dN_{ch}/d\eta$ compared to that of π^- , K^- , and \bar{p} for minimum bias p + p, minimum bias d+Au, and 0-20%, 20-40%, and 40-100% of the total d+Au cross-section. The errors shown are the quadratic sum of the statistical and systematic uncertainties[148].

The $\langle p_t \rangle$ as a function of particle mass for p+p and Au+Au collisions at $\sqrt{s_{NN}} = 200$ GeV is presented also in Figure 3.21. In this case the behavior of $\langle p_t \rangle$ vs. mass for the various particles in p+p and Au+Au collisions is compared to two parameterizations. The triangles represent the short-lived resonances and the circles indicate long-lived stable particles. The black curve is an empirical fit to the ISR π , K and p data in p+p collisions and the band is a blast wave fit using π , K and p in STAR Au+Au collisions. The STAR collaboration, extrapolating the empirical parametrization for the ISR data at $\sqrt{s} = 25$ GeV in p+p collisions to the RHIC energies, stated that this parametrization can describe the behavior of the lower mass particles, such as π , K and p, despite the fact that RHIC collision energy is one order of magnitude higher. However, they noticed that this empirical parametrization does not represent the behavior of the higher mass particles in p+p collisions. Similarly, the blast wave parametrization, which can describe the lower mass particles ($\sim 98\%$ of all the particles observed) in Au+Au collisions, fails to explain the behavior of higher mass particles.

The heavy particles in p+p and Au+Au collision show a similar behavior of $\langle p_t \rangle$. It is expected that resonances with higher transverse momentum are more likely to be re-

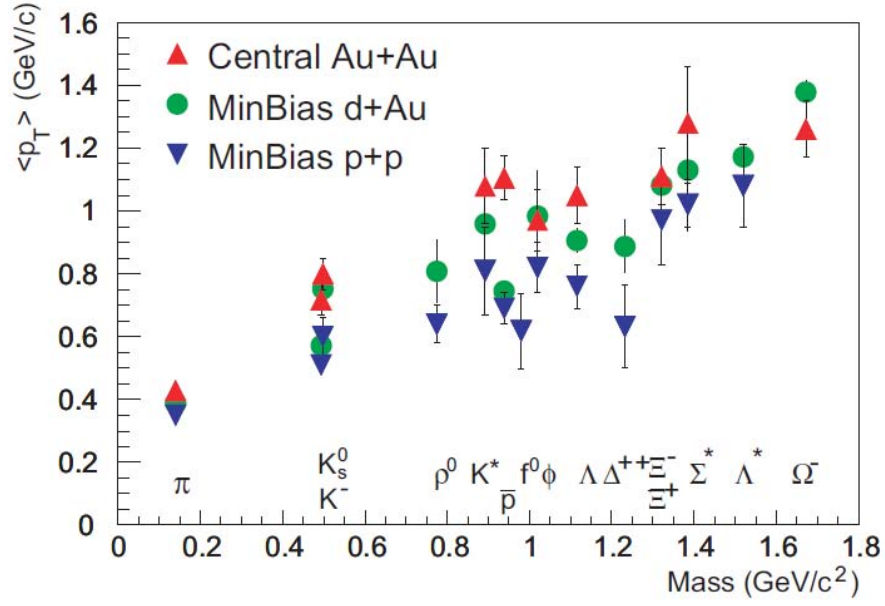


Figure 3.20: The $\langle p_t \rangle$ of various particles for different systems, minimum bias p+p, d+Au, and central Au+Au collisions. The errors shown are the quadratic sum of the statistical and systematic uncertainties[148].

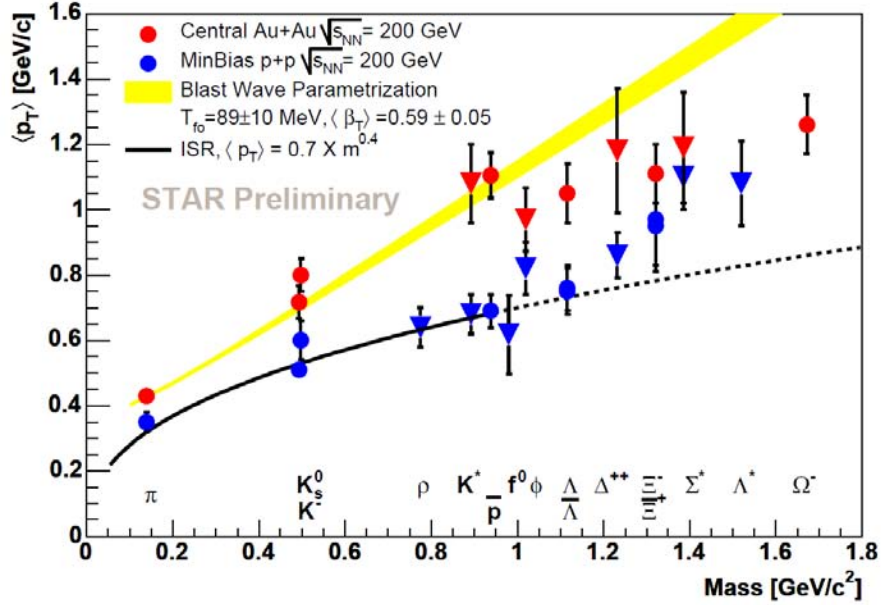


Figure 3.21: The $\langle p_t \rangle$ vs particle mass measured in p+p and Au+Au collisions at $\sqrt{s_{NN}} = 200$ GeV. While the circles represent the stable particles, triangles represent the resonances. The black curve represents the ISR parametrization from π , K and p for $\sqrt{s_{NN}} = 25$ GeV p+p collisions. The shaded band is the blast wave fit using π , K and p for Au+Au collision[147, 149].

constructed because they have longer relative lifetimes due to Lorentz contraction, which means that they are more likely to decay outside of the medium. As a consequence, their

daughter particles should interact less with the medium in Au+Au collisions. Any loss at low p_t would increase the T parameter of the p_t spectra for the central Au+Au collisions with respect to p+p collisions. However STAR collaboration didn't see any significant increase in the T parameter for $\Sigma(1385)$ from p+p to the most central Au+Au collisions within the statistical and systematic errors. But this might be due to their own p+p reference data. The higher mass particles might be produced in more violent (mini-jet) p+p collisions than the lower mass particles, so that the $\langle p_t \rangle$ for heavy particles in p+p collisions would be higher. In Au+Au collisions there is evidence that heavier particles flow radially at a lower velocity than the lighter mass particles (such as π mesons). These two independent effects in p+p and Au+Au collisions might cause the apparent merging of the $\langle p_t \rangle$ which is corroborated by the $\Sigma(1385)$ measurement.

3.4.4 Particle Ratios

The resonances production also represents an important test of thermal production and for hydrodynamics models. The ratio of resonances to their stable particles are insensitive to fugacities and phase space occupancies due to their identical valence quark composition. The thermal model accurately describes the stable particle ratios in both p+p and Au+Au collisions. The deviations observed for the resonance particles are large and must be investigated. Regeneration and rescattering are excluded in thermal models, which might suggest one explanation for why the experimental values differ from the calculations of the statistical model for most of the resonances.

The measurements of the ratios of resonances to stable particles as a function of charged particle multiplicity, which gives an estimation of the centrality of the collision, for $\Sigma(1385)$ and other resonances are presented in Figure 3.22. The observed suppression of $\Lambda(1520)/\Lambda$ and $K^*(892)/K$ from peripheral to most central Au+Au collisions compared to p+p collisions is in agreement with a rescattering scenario of the decay particles in the dense medium that causes a signal loss. The $\Sigma(1385)/\Lambda$ ratio does not show this suppression (within errors) for the 5% most central Au+Au collisions in comparison to the p+p collision environment, even though $c\tau_{\Sigma(1385)} < c\tau_{\Lambda(1520)}$, which should cause more rescattering for $\Sigma(1385)$.

In Figure 3.23 the Σ^*/Λ ratio for different colliding systems is shown. The ratios in measured d+Au collisions are in agreement with that measured in p+p collisions and do not show any suppression from p+p to Au+Au collisions either, hence they are not sensitive to the lifetime of the hadronic medium.

Resonance-to-stable-particle ratios can also be used to test microscopic (UrQMD) models, which include rescattering and regeneration in their calculations. The UrQMD model prediction in Figure 3.24 shows the collision energy dependence of the $\Sigma^\pm(1385)/\Lambda$ ratios for Au+Au collisions. The measured $\Sigma^\pm(1385)/\Lambda$ ratio is 0.295 ± 0.086 for the 5% most central Au+Au collisions, which is about a factor of 2 below the UrQMD prediction at $\sqrt{s_{NN}} = 200$ GeV (~ 0.65)[149]. The regeneration cross section assumed in UrQMD

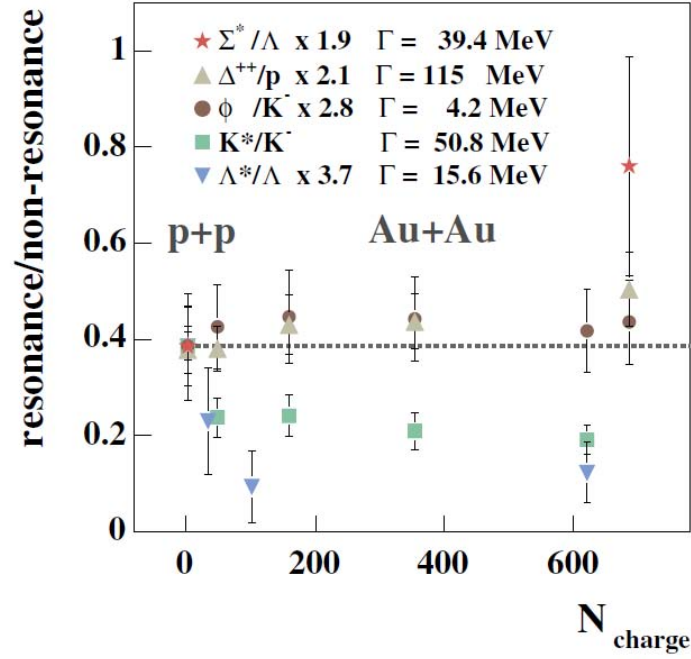


Figure 3.22: Resonance to stable particle ratios of ϕ/K^- , Δ^{++}/p , $K^*(892)/K$, $\Sigma(1385)/\Lambda$ and $\Lambda(1520)/\Lambda$ for p+p and Au+Au collisions at $\sqrt{s_{NN}} = 200$ GeV. The ratios are normalized to the ratio of $K^*(892)/K$ in p+p collisions. Statistical and systematic errors are included. The data points are scaled, using the number written in the graph, for visibility[149].

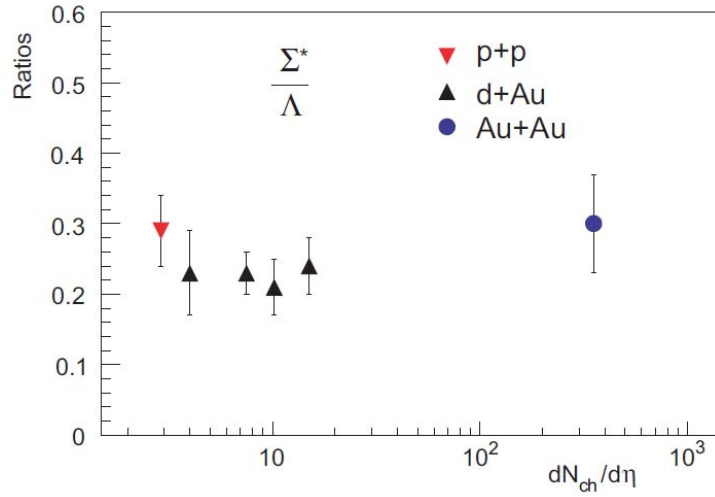


Figure 3.23: The Σ^*/Λ ratios in p + p, various centralities in d+Au, and in central Au+Au collisions as a function of $dN_{\text{ch}}/d\eta$. The errors shown are the quadratic sum of the statistical and systematic uncertainties[148].

appears to be too high and has to be revised in light of these resonance measurements.

The ratios of the yields of resonances to stable particles (at $|y| < 0.75$) as a function of the charged particle multiplicity are presented in Figure 3.25. The ratios are normalized to unity in p+p collisions in order to study variations in Au+Au relative to p+p.

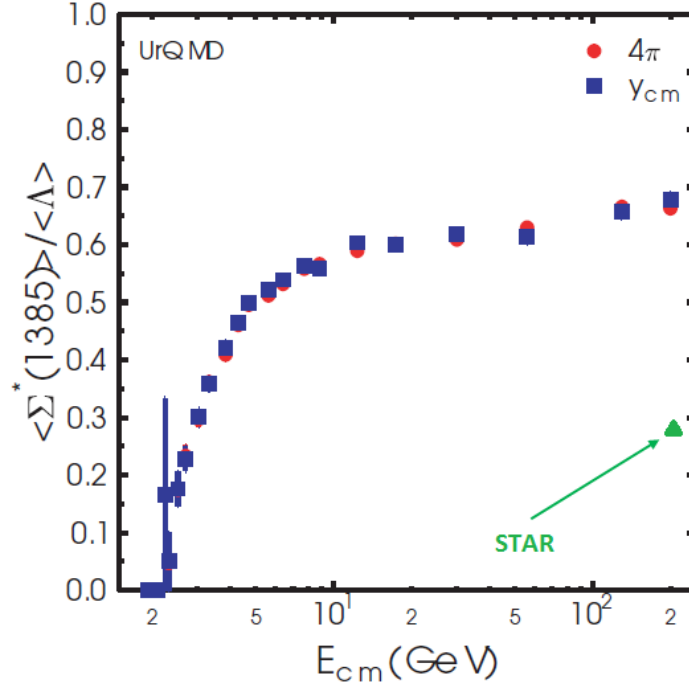


Figure 3.24: Collision energy dependence of $\Sigma^\pm(1385)/\Lambda$ ratios for Au+Au collisions predicted by the microscopic models (UrQMD). Plot from M. Bleicher[132]. The point indicated by the arrow indicates the STAR experimental value.

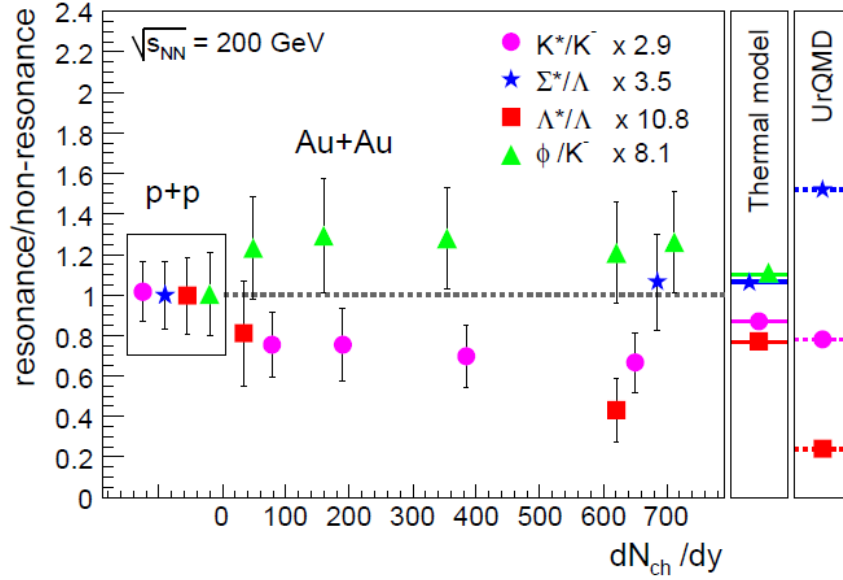


Figure 3.25: Resonance to stable particle ratios for p + p and Au + Au collisions. The ratios are normalized to unity in p + p and compared to thermal and UrQMD model predictions for central Au + Au. Statistical and systematic uncertainties are included in the error bars[150].

The STAR experiment measured also a suppression for Λ^*/Λ when comparing central Au + Au with minimum bias p + p. K^*/K^- seems to show a smaller suppression

while the Σ^*/Λ ratio are consistent with unity. In a thermal model, the measured ratios of resonance to non-resonant particles with identical valence quarks are particularly sensitive to the chemical freeze-out temperature, as all the quark content dependencies cancel out. Thermal models require a chemical freeze-out temperature in the range $T = 160 \div 180$ MeV and a baryo-chemical potential $\mu_B = 20 \div 50$ MeV in 200 GeV Au+Au collisions to describe the stable particle ratios. While these models predict the measured Σ^*/Λ ratio correctly within the errors, they yield a higher ratio than the measured Λ^*/Λ in the most central Au + Au collisions. This suggests an extended hadronic phase of elastic and pseudoelastic interactions after chemical freeze-out, where rescattering of resonance decay particles and regeneration of resonances will occur. The measured resonance yields thus depend on the time-span between chemical and kinetic freeze-out, their cross sections for re-scattering and regeneration, and their lifetimes. A thermal model using an additional pure re-scattering phase, which depends on the respective momenta of the resonance decay products, after chemical freeze-out at $T = 160$ MeV, can be fit to the data. The fit yields a hadronic lifetime of the source of $\Delta\tau = 9_{-5}^{+10}$ fm/c from the Λ^*/Λ and $\Delta\tau = 2.5_{-1}^{+1.5}$ fm/c from the K^*/K ratio. The small difference between the time spans can be explained by an enhanced regeneration cross section for the K^* in the medium. This idea is supported by the null suppression of the Σ^*/Λ . The smaller lifetime of the Σ^* compared to the Λ^* should lead to a larger signal loss due to re-scattering, thus the lack of suppression requires an enhanced regeneration probability of the Σ^* . A microscopic model calculation (UrQMD) with a typical lifespan of $\Delta\tau = 13 \pm 3$ fm/c for the re-scattering and regeneration phase, can describe K^*/K^- and Λ^*/Λ ratios approximately, but fails for the Σ^*/Λ . The measured resonance yields in heavy-ion collisions provide a tool to determine the strength of in-medium hadronic cross sections and current microscopic transport models such as UrQMD will have to be modified to account for such cross sections[150].

3.4.5 Nuclear Modification Factor

The nuclear modification factor for the $\Sigma(1385)$ in comparison to other mesons and baryons in d + Au collisions (R_{dAu}) can be found in Figure 3.26. The R_{dAu} measurements, for mesons on the left and for baryons on the right, mostly follow participant scaling at low momenta. At higher momentum, baryons show a greater enhancement over the binary scaling than the mesons¹⁰. The enhancement over binary scaling can be described by the Cronin effect, a generic term for the experimentally observed broaden-

¹⁰In nucleus-nucleus collision the production of particle at high p_t scales with the number of the elementary nucleon-nucleon collision which take place in the nucleus-nucleus collision. So, the spectra measured in the nucleus-nucleus collisions can be provided from those in pp collisions following the “binary scaling law”: $dN_{AA}/dp_t = N_{bin} \times dN_{pp}/dp_t$ where N_{bin} is the number of the elementary nucleon-nucleon collisions evaluated according to the Glauber model. If no nuclear effect is present, the nuclear modification factor is = 1 in the high p_t regime, <1 in the low p_t regime where it scale with the number of the collision participants.

ing of transverse momentum spectra at intermediate p_t in p+A collisions as compared to p+p[151] and generally attributed to the influence of multiple parton scattering through matter prior to the hard scattering that produces the observed high- p_t hadron. Therefore, the nuclear modification factor can be used to study the effects of matter on particles production.

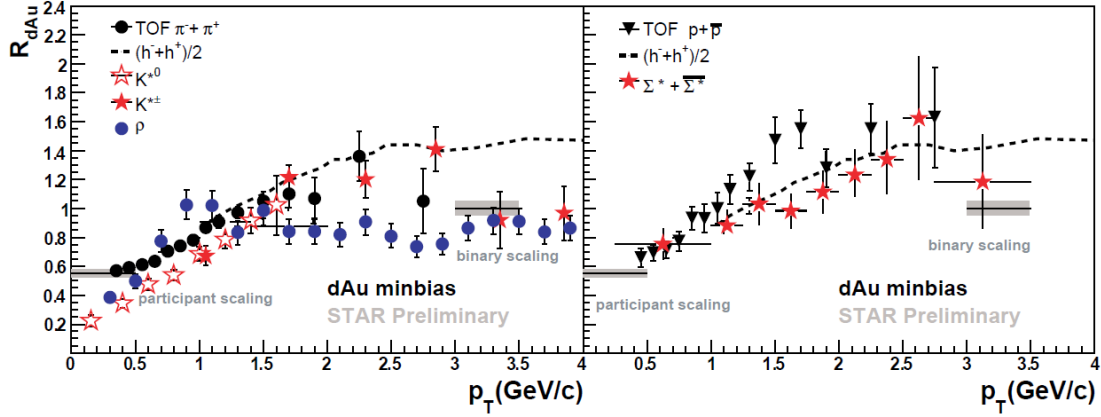


Figure 3.26: Nuclear modification factors (R_{dAu}) for the $\Sigma(1385)$ in comparison to other mesons on the left and baryons on the right in d + Au collisions[151].

Nuclear modification factors R_{CP} (ratio between the yields in central and peripheral collisions) for strange particles in Au+Au collisions are presented in Figure 3.27-a. At high p_t , the ratios exhibit a suppression from binary scaling, attributed to fast moving partons losing energy as they traverse a dense medium. Hadron production at high p_t does not follow binary scaling and is roughly consistent with participant scaling. The differences between baryons and mesons, is believed to be due to hadrons production through quark coalescence at intermediate p_t . For baryons and mesons, the suppression sets in at a different p_t . Motivated by the coalescence picture, Figure 3.27-b shows the R_{CP} ratio vs p_t/n for $\sqrt{s_{NN}} = 200$ GeV, where n is the number of valence quarks. The baryon and meson difference sets in at the same quark p_t , in agreement with the coalescence picture. Separation of the mesons and baryons is observed when the p_t of the quarks of the meson or the baryon are in the range of 0.8-1.2 GeV which corresponds to a baryon p_t range of 2.4-3.6 GeV and a meson p_t range of 1.6-2.4 GeV. If the statistical fit parameters from the ratios of the particle yields in these momentum ranges are compared to the ones from the integrated momentum range, it might be possible to determine the ranges of T and γ_s for which coalescence and recombination are applicable[152].

3.4.6 Time Scale for Au+Au collisions

In-medium effects such as elastic interactions of the decay particles with other particles in the created medium (mostly pions) may result in a signal loss. Regeneration will have the reverse effect. Microscopic model calculations (UrQMD) predict $\Lambda(1520)/\Lambda = 0.03$ and $K(892)/K^- = 0.25$. Using the measured values of $K(892)/K^-$ and $\Lambda(1520)/\Lambda$ a

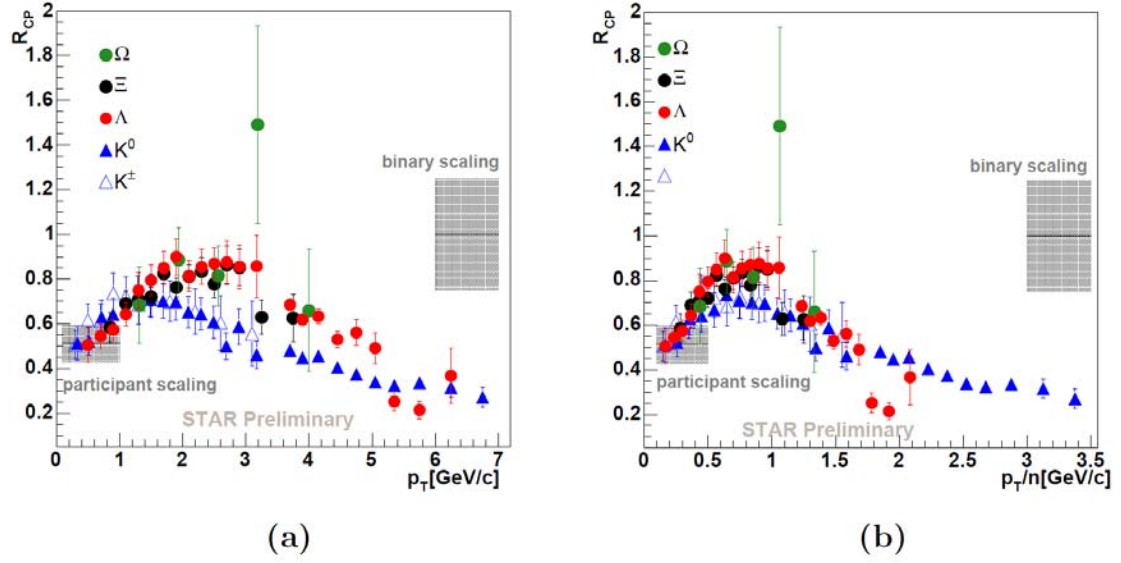


Figure 3.27: (a) R_{CP} vs p_t in Au + Au collisions at $\sqrt{s_{NN}} = 200$ GeV. (b) R_{CP} vs p_t/n in Au + Au collisions at $\sqrt{s_{NN}} = 200$ GeV for $n = 3$ for baryons and $n = 2$ for mesons. R_{CP} is calculated from 0-5% and 40-60% central Au + Au collisions[152].

thermal model, including rescattering, but no regeneration, predicts the lifetime interval between chemical and kinetic freeze-out to be >5 fm/c. The decrease of the $\Lambda(1520)/\Lambda$ and $K(892)/K^-$ ratio from p+p to Au+Au collisions occurs already for very peripheral collisions (50-80%) and remains nearly constant up to the most central collisions (5%). In terms of the lifetime of the system between chemical and thermal freeze-out, $\Delta\tau$, these result suggests the same $\Delta\tau$ for peripheral and central Au+Au collisions[142].

Chapter 4

$\Sigma(1385)$: Proton - Proton Simulations Analysis

The main goal of this thesis work is to study the strange resonance $\Sigma(1385)$ in the ALICE experiment in proton-proton collisions at $\sqrt{s} = 7$ TeV provided by the LHC. As mentioned in the Chapter 3, according to some theoretical studies, it is possible to estimate at the same time the temperature of the chemical freeze-out and the time interval between chemical and thermal freeze-out using the $\Sigma(1385)$ yields over Λ and Ξ yields ratios. In that sense it is very important to provide a very precise estimation of these quantities in heavy-ion collisions, where the QGP is expected to be created. This means that the corresponding results in proton-proton collisions play a very important role as a benchmark in a condition in which the QGP is not expected to appear and so, those values has to be very carefully provided.

In order to reach this goal a dedicated analysis procedure has to be realized. This procedure must consider many different aspects: analysis sample selection, background evaluation, signal extraction and fit, uncertainties evaluation, differential analysis in transverse momentum and (if the amount of data collected is adequate) rapidity bins, efficiencies evaluation, possible results (in terms of masses and widths) dependence from traverse momentum/mass.

Such kind of procedure was built using the official ALICE simulation/reconstruction framework AliRoot and the available proton-proton simulations provided at $\sqrt{s} = 10$ TeV. At that time simulations at $\sqrt{s} = 7$ TeV weren't available since the LHC schedule still foresaw a 10 TeV startup energy that was decreased to 7 TeV after the September 2008 incident and the consequent LHC machine safety evaluations. As soon as the first 7 TeV simulations became available, during the 2010 summer, the reconstruction procedure presented in this chapter has been checked and validated also using them. In the rest of the chapter, the results obtained also on the 7 TeV simulations will be shown as a comparison.

The event generator used to provide the particles simulation was PYTHIA while the

transport through the ALICE detector was performed using the GEANT 3 code and lastly the ROOT tools was used to built the detector geometry. Both PYTHIA and GEANT 3 are embedded in the AliRoot framework.

4.1 Data Analysis Description

4.1.1 Event Selection

The first step of the procedure is the event selection. For the aim of this work minimum bias events will be analyzed. In the ALICE context, “Minimum Bias” event means an event with at least an hit revealed in the SPD or in the V0 detector, i.e. a charged particle in the 8 pseudo-rapidity units covered by these detectors. In order to have an efficient and user-transparent event selection the AliRoot framework provides a class (called *AliPhysicsSelection*) that automatically selects the requested events just before the starting of the real physical analysis, avoiding the inclusion, for instance, of non physical data taking runs (i.e. calibration runs) or events without the interaction trigger, i.e. trigger on bunch crossings, or events flagged as beam-gas by either V0A or V0C detectors. This class can be applied both to the real and to the simulated data (even if the latter are by definition good physics events) in order to treat both of them with homogeneity. This aspect is very important in particular when we will use the number of events for the normalizations of the data. Moreover, another event selection looking at the reconstructed primary vertex is performed. Only events with a *good* primary vertex (i.e. a vertex reconstructed with the information from the complete tracks reconstructed with “ITS + TPC” or at least a vertex identified with the data from the SPD detector) will be analyzed.

4.1.2 $\Sigma(1385)$ Candidates Selection

As already written in section 3.3 the $\Sigma(1385)$ ¹¹ has two main decay channels and they are strong channels. This has two consequences: first of all it will not be possible to separate the Σ^* decay vertex from the primary interaction vertex, and secondly it will be difficult to separate the resonance peak from the background because it will be quite broad ($\Gamma > 35$ MeV). That means that no strong topological selection will be possible and the Σ^* signal can be extracted only through an invariant mass analysis.

In this study, the Σ^* resonances are identified through the invariant mass analysis of Λ and π decay particles, i.e. using only one of the possible Σ^* decay channels since it has the highest branching ratio and since, in ALICE, we are not able to identify with an acceptable efficiency the Σ ’s (needed for the second Σ^* decay channel).

The first step is therefore to identify the Λ ’s and π ’s candidates. The Λ ’s, identified by the ALICE reconstruction program are combined with all the remaining pions to get

¹¹ $\Sigma(1385)$ is also often called Σ^* and from now on, for brevity reasons, only the latter will be used.

the Σ^* . During this phase some selection criteria were applied to select them. This criteria are described in the next paragraph.

4.1.2.1 Λ 's and π 's selection criteria

The ALICE automatic general reconstruction analysis provides the identification of all the Λ (with a p_t -dependent efficiency that reach values of $\simeq 30\text{-}40\%$ [153]) but for the purpose of this analysis, it is mandatory to select, among them, those which pass a specific set of quality selection criteria. These criteria are chosen as a compromise between the requirement to have both a sample as clean as possible and a good Signal over Background ratio. The same philosophy is applied to the pions selection criteria. In order to be able to study the results coming from the application of these criteria and the tuning of the applied cuts, the procedure implemented allows us to save many different quantities and to manage them in a two-steps analysis. In this way it is possible to analyze separately the effect of the application of each single cut and its consequence on the signal significance and on efficiencies.

Since the Σ^* decay vertex is not separable from the primary vertex, the Λ 's coming from the Σ^* 's decay can be considered as primaries, and I try to select (and so reject most of the secondaries) them applying a standard ALICE p_t dependent cut in the Distance of Closest Approach (DCA) between the Λ 's and the primary vertex. This cut takes into account the resolution in the impact parameter estimation for different particle types[154]. Actually these cuts were introduced for the charged particle selection (pions, kaons and protons) while the Λ 's are not. However, the simulations tell us that the Λ 's and protons (the charged particle closer in mass) transverse momentum distributions are quite similar (Figure 4.1 left and right) and so it is reasonable to apply the proton oriented cut to the Λ 's. In Figure 4.2 (left and right) the equivalent distribution extracted from the simulations at $\sqrt{s} = 7$ TeV, from which an almost identical behavior is evident both for protons and Λ 's, are shown.

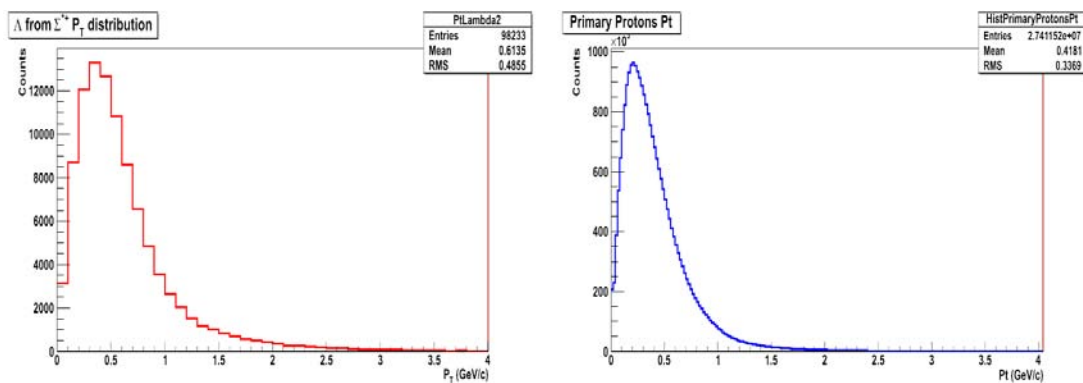


Figure 4.1: Transverse momentum distribution of Λ 's from Σ^* 's (left) and of primary protons (right) at $\sqrt{s} = 10$ TeV

Then a check is performed in order to exclude the so called “Like-Sign” Λ 's, i.e. mis-reconstructed Λ 's whose daughter assigned particles have the same charge sign. Finally

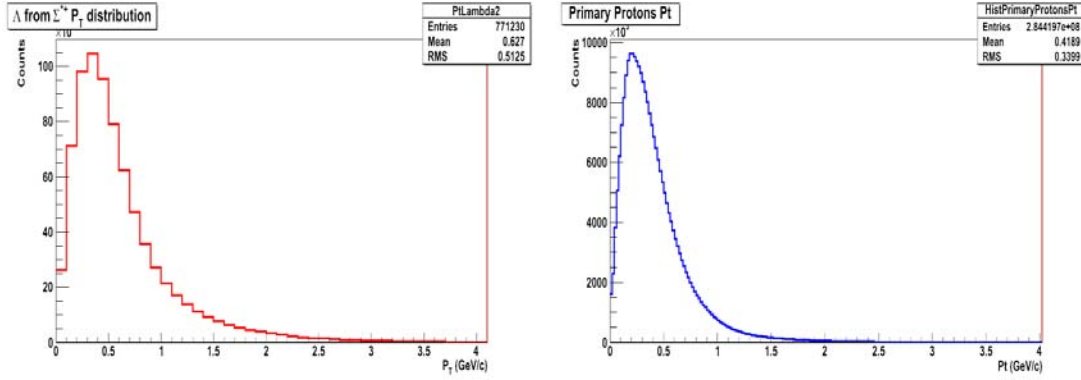


Figure 4.2: Transverse momentum distribution of Λ 's from Σ^* 's (left) and of primary protons (right) at $\sqrt{s} = 7$ TeV

a last check is performed on the Λ 's mass in order to exclude those whose reconstructed mass is too far from the PDG values. In this case, in the beginning, a very loose cut is used: the Λ 's are rejected only if their mass is $100 \text{ MeV}/c^2$ far from the PDG value. This cut will be tuned in a next analysis step.

A similar selection is then performed also for all the other event's tracks. Even for them a set of standard and dedicated selection criteria are applied. In particular, the tracks selected:

- passed a p_t dependent DCA with respect to the primary vertex cut similar to the Λ 's one, but in this case, a pion oriented cut;
- are not *kink daughter*¹²
- have a χ^2 per TPC cluster < 4 ;

These cuts, quite standard in all the ALICE analyses, are applied in the first step of the analysis procedure which performs a very preliminary filter running on the data stored on the GRID. The procedure foresees a second step in which an additional set of cuts is applied. The quantities monitored in the second analysis are described in the next paragraph.

Moreover, during the first analysis step, the track that are not already used for the Λ reconstruction are also identified, using the Particle IDentification (PID) information from the ITS, TPC and TOF detector, as possible π candidates. The PID information is saved as an additional flag that could be introduced or not, depending on how pure we want the Σ^* signal.

This last point is performed with a standard procedure as follows.

1. if the track was reconstructed with the TPC, its dE/dx is compared with a theoretical value extracted from a TPC proper Bhete-Block parameterization, under

¹²The *kinks* are topological signatures of 1-prong decays, in particular from pions and kaons. A precise description of the procedure for the *kinks* identification is described in [2].

- the hypothesis of a pion track. The track is selected if the track dE/dx value is within 5σ from the theoretical one.
2. if the track was reconstructed only with the ITS (ITS standalone), then a similar comparison is performed but with an ITS proper Bhete-Block parameterization, under the hypothesis of a pion track. The track is selected if its dE/dx value is within 4σ from the theoretical one.
 3. if also the TOF information are available and a cross check with this detector is requested, the time of flight measured by TOF is compared with a theoretical value, under the hypothesis of a pion track. The track is selected if its time of flight value is between a minimum and a maximum time value. This further control is not performed if the track has no matching between TPC and TOF.

After these selection passes, all the remaining Λ 's and π 's are combined in order to produce the Σ^* candidates. At this point not all the possible quality and kinematical cuts are applied. In order to be able to discriminate among the four Σ^* states (plus, minus and the relative antiparticles) and to be able to perform a more accurate candidates selection in the second analysis step, as mentioned, many quantities are saved both for Λ 's and π 's. In this way is it easier to apply one by one the cuts related to the different quantities and evaluate separately the effect of each of them and the consequent systematics uncertainties. Among the others, we keep quality track information (number of ITS/TPC cluster, χ^2 per ITS/TPC cluster, DCA with respect to the primary vertex...) both for the π 's and for the (anti) Λ 's and its daughters; kinematical information like (transverse) momenta, strangeness content, electric charges, (pseudo)rapidity and so on are also acquired.

If simulation data are analyzed even the Monte Carlo Truth information is saved in order to be able to evaluate the procedure self consistence and the efficiencies corrections factors that has to be applied to the data.

4.2 Data Reduction Description

4.2.1 Invariant Mass Distribution

In Figure 4.3 the Σ^{*+} total invariant mass distribution at $\sqrt{s} = 10$ TeV is shown. No cuts are applied at this level.

Starting from this distribution it is possible to evaluate the background and extract the signal as described in the following paragraphs.

4.2.2 Background Definition Techniques

Different techniques were implemented to reproduce the background below the Σ^* peak: the “Side Bands” technique and the “Event Mixing” technique.

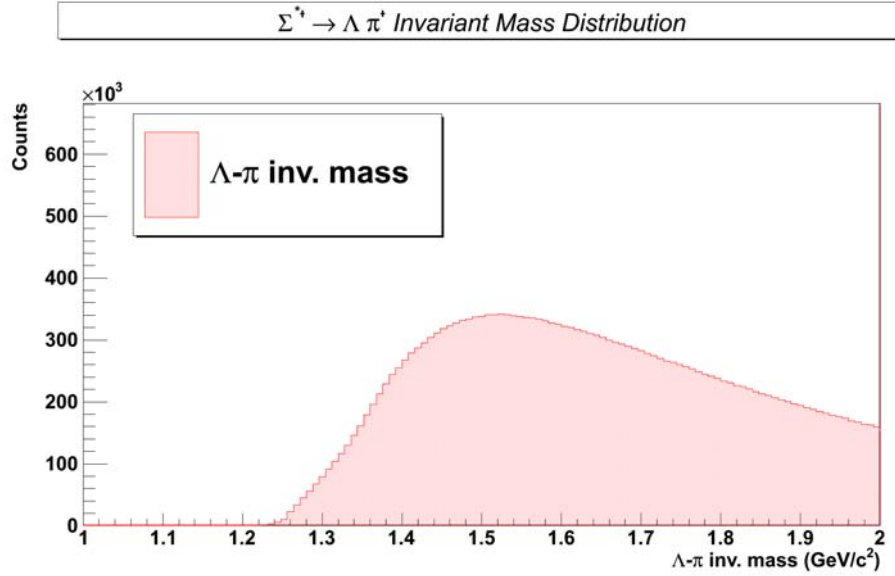


Figure 4.3: Σ^{*+} total invariant mass distribution at $\sqrt{s} = 10$ TeV.

4.2.2.0.1 Side-Bands Technique

The “Side-Bands” technique consists in a fit of the invariant mass distribution after excluding the region where the signal is supposed to appear (“exclusion region”). The “exclusion region” was chosen as centered at the Σ^* mass published in the PDG booklet (1385 MeV) and with a width equals to $3 \times \Sigma^*$ width (35 MeV). The chosen fit function is a polynomial function containing both Taylor and Laurent terms in order to be able to follow the distribution profile both at low and high invariant masses. The fitting function is then extrapolated also inside the “exclusion region”. In Figure 4.4 the Σ^{*+} total invariant mass distribution at $\sqrt{s} = 10$ TeV with the “Side Bands” fit is shown. In Figure 4.5 the equivalent distribution extracted from the simulations at $\sqrt{s} = 7$ TeV is shown. No cuts are applied at this level. As it appears from the figure, without applying any further cut the signal is totally hidden by the combinatorial background. The blue dots represent the background evaluated with the Side-Bands technique.

4.2.2.0.2 Events Mixing Technique

The “Event Mixing” technique consists in a mix of the Λ ’s from one event and the π ’s from another event in order to obtain a fully uncorrelated background. This technique foresees to be applied with particular care in the events selection. Infact in order to properly reproduce the required background it is mandatory to mix *similar events* in terms at least of particle multiplicity and vertex positions. For this reason a proper selection of the events to be mixed is needed before the applying of the procedure. The “Event Mixing” technique was successfully applied in the STAR experiments for the Σ^* signal extraction [139].

Up to now we used the “Side-Bands” technique; the “Event Mixing” technique, even

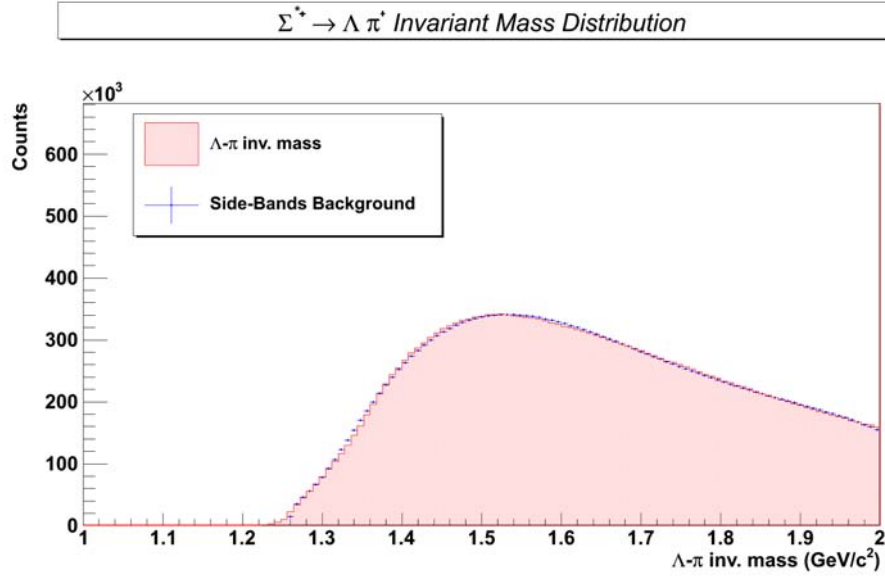


Figure 4.4: Σ^{*+} total invariant mass distribution at $\sqrt{s} = 10$ TeV. The blue dots are the background evaluated with the Side-Bands technique.

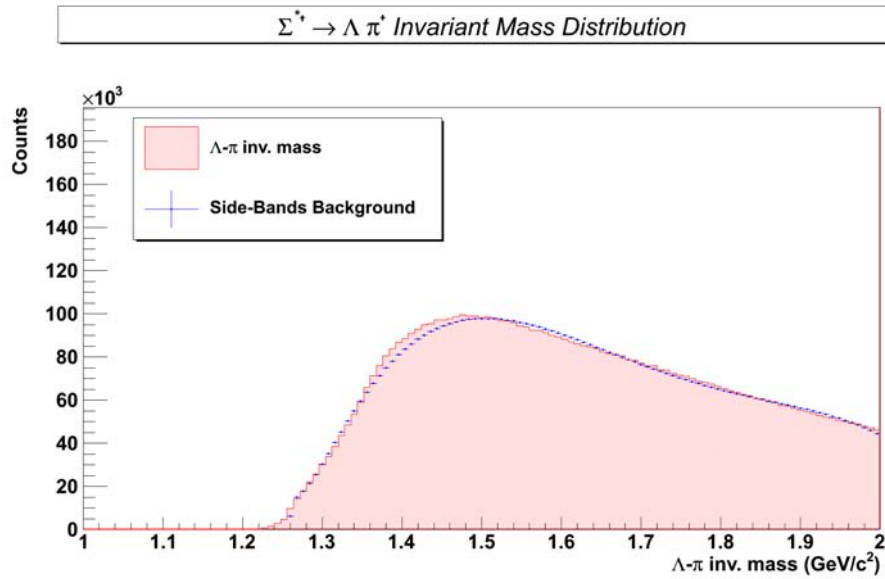


Figure 4.5: Σ^{*+} total invariant mass distribution at $\sqrt{s} = 7$ TeV. The blue dots are the background evaluated with the Side-Bands technique. The apparent bump that appears in the central region of the dynamical range considered is actually an artifact due to the Side-Bands technique.

if it appear to be very promising in providing good results, could not yet be applied in a reasonable statistic sample due to different kind of problems faced when trying to use the complete “Event Mixing Framework” on the GRID. This is why only results obtained with the “Side-Bands” technique will be shown in the following.

4.2.3 Signal Extraction

In order to extract the Σ^* signal we subtracted the background obtained with the function previously defined with the “Side-Bands” fit. In Figure 4.6 the signal after the background subtraction for pp simulations at $\sqrt{s} = 10$ TeV (52 million events analyzed) for Σ^{*+} is presented. No cuts are applied at this level and it is possible to see that in this condition it is not possible to extract any signal and the application of other cuts is mandatory. The green histogram represents the “Monte Carlo Truth” and it can be used to check the consistency of the signal extraction procedure.

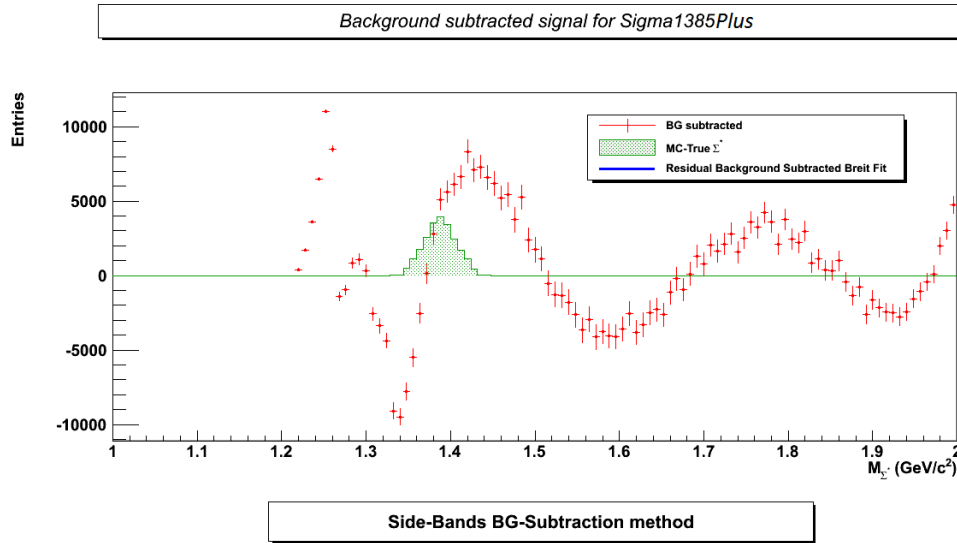


Figure 4.6: $\Lambda \pi$ signal background-subtracted for 10 TeV pp simulations. The green histogram is the Monte Carlo signal.

4.2.4 Kinematical and quality Cuts

In order to try to improve the signal over noise ratio and the signal purity, a set of kinematical and quality cuts were applied and studied. The quality cuts, applied to Λ 's and π 's involves the following quantities:

- for the Λ 's:
 1. TPC refitting of both the positive and negative daughter track
 2. number of TPC clusters per track for the positive and negative Λ 's daughter
 3. TPC χ^2 divided by the number of TPC clusters per track both for the positive and negative Λ 's daughter
 4. DCA between Λ and primary vertex
 5. Λ daughter's cosine of the pointing angle¹³

¹³The pointing angle is defined as the angle between the vector defined by the primary vertex and Λ vertex and the vector defined by the sum of the Λ daughters vectors.

6. Λ invariant mass (see Figure 4.7)

- for the π 's:
 1. TPC refitting
 2. number of TPC cluster per track
 3. TPC χ^2 divided by the number of TPC cluster per track
 4. DCA between π and primary vertex
- for the Λ - π pairs:
 1. DCA between Λ and π
 2. fiducial region¹⁴

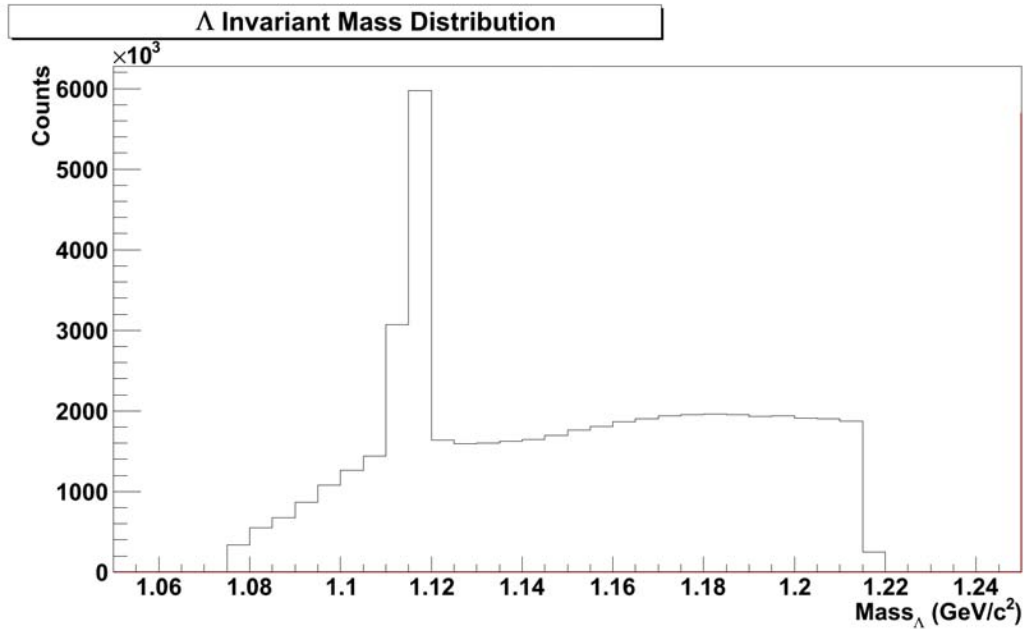


Figure 4.7: Invariant mass distribution for the Λ 's provided by the ALICE reconstruction program. The cut-off values are those putted during the first step of the analysis performed on the GRID in order to provide a preliminary selection on the Λ 's sample. Tighter selection values on the Λ 's mass are used in the second step of the analysis. See Table 4.1 and 4.3.

In order to find the best set of cuts which optimize the signal over noise ratio and the final fit results, different combinations of them were tried.

In the Tables 4.1 and 4.3 two different sets of cuts are summarized together with the results obtained with a Breit-Wigner fit of the signal in terms of mass, width, signal fit reduced χ^2 , integrated yield, and significance.¹⁵ The yield was evaluated integrating the

¹⁴The fiducial region is defined as a circle centered in the primary vertex with a radius defined by the primary vertex and the Σ^* estimated vertex.

¹⁵The significance is here defined as $\frac{S}{\sqrt{S+B}}$ where S is the signal and B the background.

fitting function in a region centered at the Σ^* PDG mass value and wide $1 \times \Sigma^*$ width per each side. These results here shown are obtained for the Σ^{*+} .

Cut	Cut Type	Mass (GeV/c ²)	Γ (MeV)	χ^2/N_{dof}	Yield	$S/\sqrt{S+B}$
0	No Cuts					
1	Λ Daug TPC refit					
2	1 + Λ Daug TPC cls > 70					
3	2 + $\chi^2/(\# \text{ TPC clusters}) < 4$					
4	3 + $1.110 < M_\Lambda < 1.122 \text{ GeV}$	1.390 ± 0.41	35 ± 3	5.3	17546 ± 867 (20262 \pm 142)	26.1 ± 1.2
5	4 + Fid Reg < 0.05 cm ²	1.386 ± 0.001	28 ± 2	2.1	16787 ± 824 (19394 \pm 139)	25.9 ± 1.2
6	5 + Λ CosPointAng > 0.99	1.386 ± 0.001	28 ± 2	2.1	16777 ± 824 (19394 \pm 139)	25.9 ± 1.2
7	6 + Λ Daug DCA < 0.2 cm	1.386 ± 0.001	28 ± 2	1.9	15390 ± 781 (17868 \pm 134)	25.1 ± 1.2
8	7 + Λ DCA < 0.4, π DCA < 0.1 cm	1.385 ± 0.001	27 ± 2	1.9	14700 ± 777 (17593 \pm 133)	24.4 ± 1.2
9	8 + $\Lambda - \pi$ DCA < 0.2 cm	1.385 ± 0.001	27 ± 2	1.8	14486 ± 775 (17549 \pm 132)	24.6 ± 1.2

Table 4.1: First example of cuts set (“purity oriented”) tried to improve the signal extraction. In brackets the Monte Carlo yield values. Lexical note: “Daug” means Daughter, “Fid Reg” Fiducial Region, “CosPointAng” Cosine of Pointing Angle.

Cut	Cut Type	Mass (GeV/c ²)	Γ (MeV)	χ^2/N_{dof}	Yield	$S/\sqrt{S+B}$
8a	7 + No Fid Reg + Λ DCA < 0.3, π DCA < 0.05 cm	1.384 ± 0.001	27 ± 3	3.5	14326 ± 740 (17086 \pm 127)	20.4 ± 1.2

Table 4.2: Second example of cuts set (“efficiency oriented”) tried to improve the signal extraction. In brackets the Monte Carlo yield values.

As it is possible to see from the values listed here both the sets of cuts allow to extract a comparable fit results while the first one apparently allow to recover more efficiency. However, this consideration is not true anymore when analyzing the 7 TeV data (see next chapter) when the first set of cuts allows to provide better fits results but losing signal extraction efficiency while the second one allows to recover some efficiency even losing a little bit of purity. So for the future it was decided to keep both of them and from now on we will call the first set of cuts “purity oriented” while the second one

“efficiency oriented”.

Other set of cuts, not listed here, were tried introducing, for instance, the PID information but it was decided not to use them since they didn’t introduced an appreciable improvement in the final fit results causing instead a statistics loss.

In Figure 4.8 the Σ^* invariant mass distribution after the application of the “purity oriented” set of cuts previously described for the 10 TeV simulations is shown, together with the signal background subtracted. In Figure 4.9 the equivalent distributions extracted from the 7 TeV simulations is shown. The signal distribution obtained was fitted with a Breit-Wigner function. In both cases a little discrepancy between the fit and the Monte Carlo signal is evident on the tails of the distribution, that seems to appear gaussian-like. This indicates that even if the Breit-Wigner is a good signal description, it is probably not the best in this case. An improvement in the fit could be provided taking into account, for instance, a convolution of a Breit-Wigner and a Gaussian distribution. At this level, the errors associated to the fit results take into account only the statistical component while the systematic one will be evaluated later.

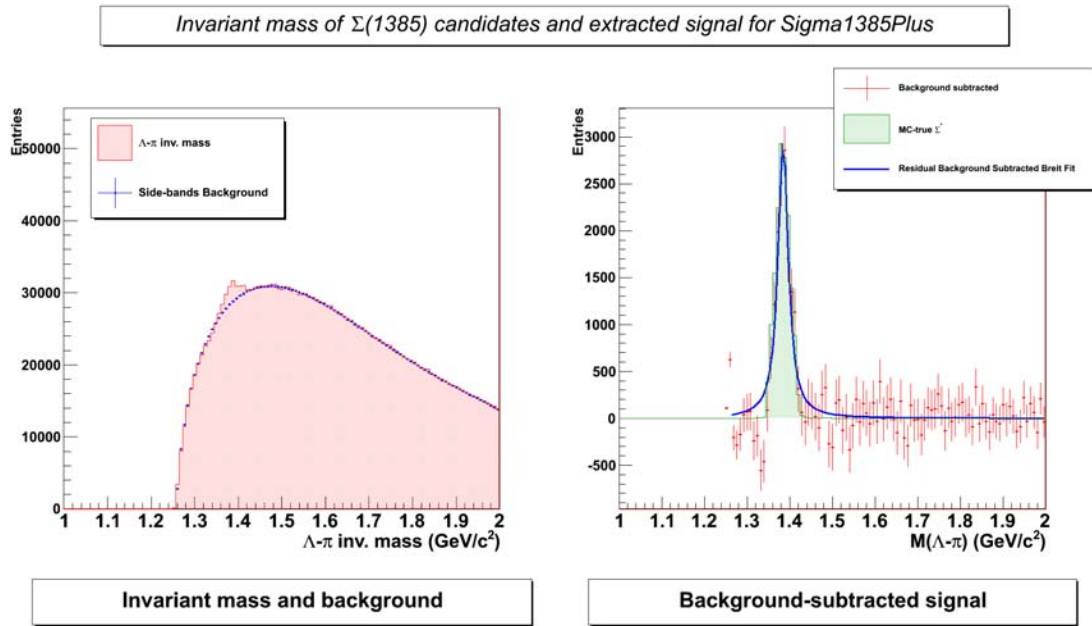


Figure 4.8: Σ^* ’s invariant mass distribution (left) and signal after background subtraction (right) after applying the “purity oriented” set of quality cuts in pp simulations $\sqrt{s} = 10$ TeV. The green histogram is the Monte Carlo signal.

The results obtained, in terms of mass and width, are in rather well agreement with the PDG values.

Moreover a set of kinematical cuts were studied in order to try further improve the signal/background ratio. In this case the cuts involve not only the Λ ’s and π ’s daughters but also the Σ^* ’s mother candidates. The cuts were developed studying the 10 TeV simulations from which I extracted the following distributions:

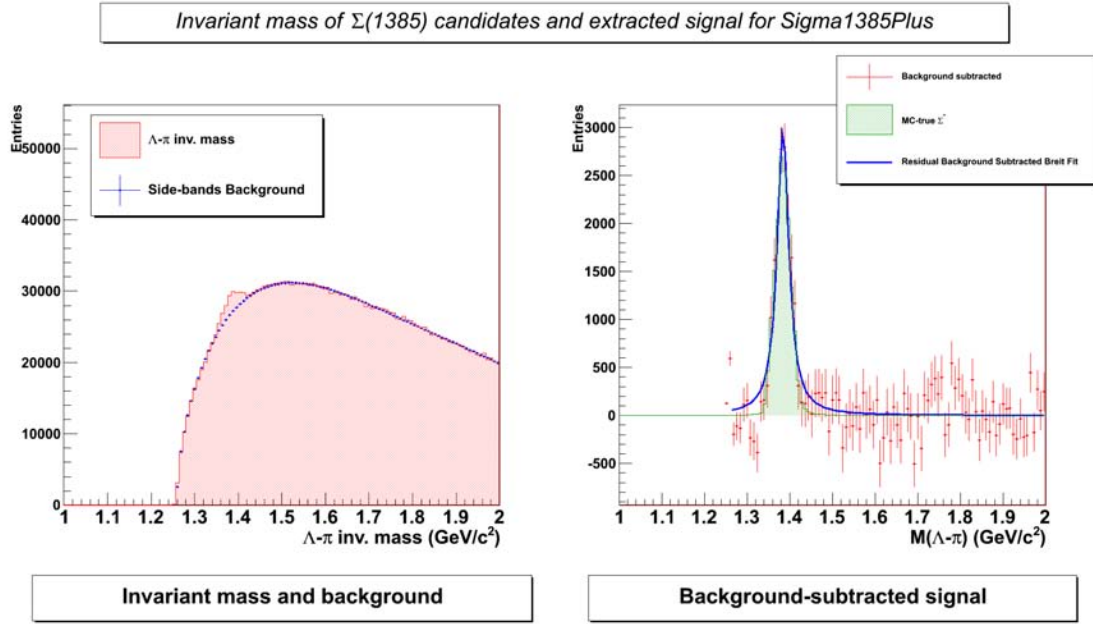


Figure 4.9: Σ^* 's invariant mass distribution (left) and signal after background subtraction (right) after applying the “purity oriented” set of quality cuts in pp simulations $\sqrt{s} = 7$ TeV. The green histogram is the Monte Carlo signal.

- Σ^* daughters cosine of the opening angle (OA)
- Λ 's momentum vs π 's momentum
- Σ^* daughters cosine of the opening angle vs Σ^* momentum

These distributions were extracted both for the *signal* and the *background*; I can separate the two contribution since I was working with simulation and so the original Monte Carlo information, concerning the real nature of a particle and its decays, is always brought out at all levels, i.e. even in the daughters information.

In Figures 4.10 and 4.11 it is possible to see the Σ^* daughters cosine of the opening angle distributions for the signal and the background respectively in the 10 TeV simulations.

The background distribution has two peaks, instead of the signal one has only one and so it is possible to cut a great part of the background selecting the $\Lambda - \pi$ pair with a proper cut on the cosine of the opening angle.

In Figures 4.12 and 4.13 it is possible to see the Λ 's momentum vs π 's momentum distributions for the signal and the background respectively in the 10 TeV simulations.

From the figures a quite good separation of the signal to the background is visible, so it is possible to try to parametrize an *exclusion area* in which the signal is not present and use this information to try to further clean the sample under analysis. This was done fitting the signal border line with a straight line function.

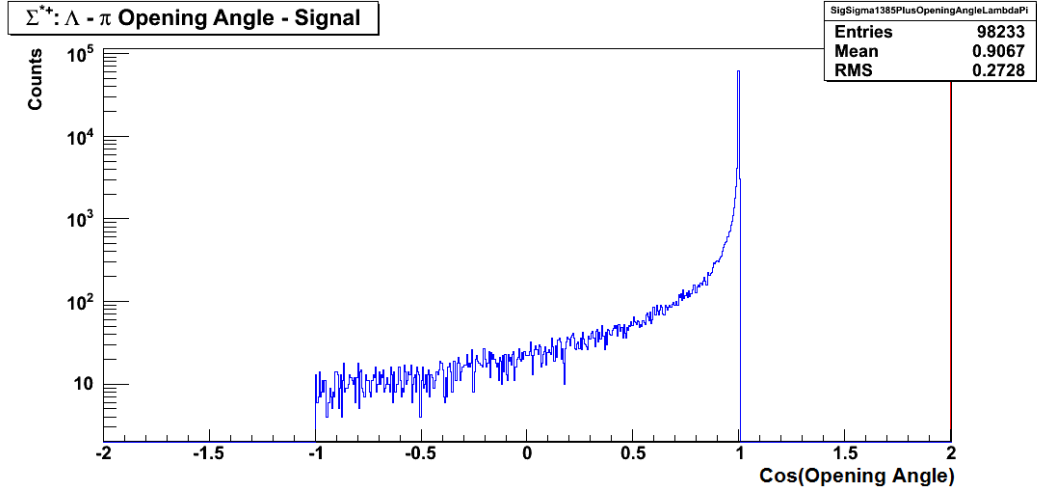


Figure 4.10: Σ^* daughters cosine of the opening angle distribution for the signal in pp simulations at $\sqrt{s} = 10$ TeV.

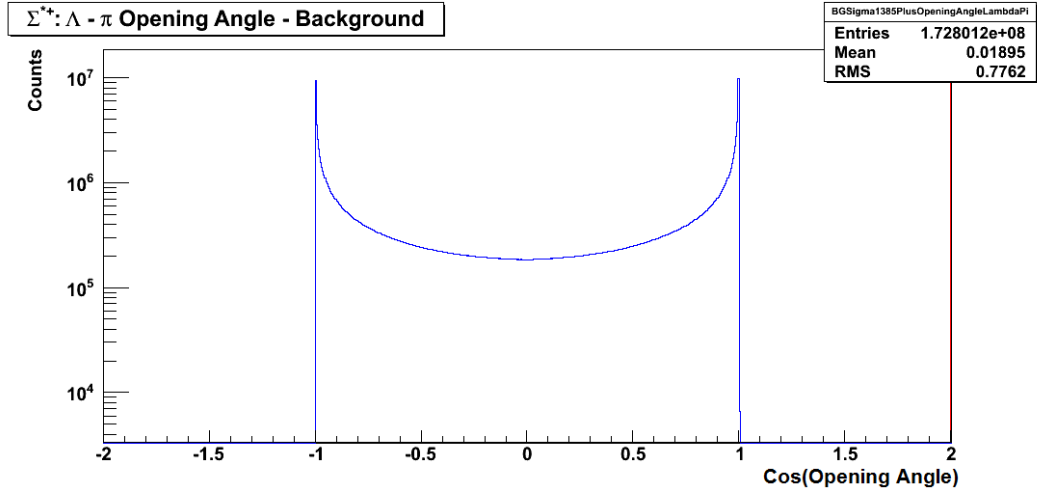


Figure 4.11: Σ^* daughters cosine of the opening angle distribution for the background in pp simulations at $\sqrt{s} = 10$ TeV.

In Figures 4.14 and 4.15 the Σ^* daughters cosine of the opening angle vs Σ^* momentum distributions for the signal and respectively for the background in the 10 TeV simulations are shown.

Also in this case, as can be inferred from the figures there is a quite good separation from the signal behaviour to the background behaviour, so it is possible to try to parametrize an *exclusion area* in which the signal is not present and use this information to clean the sample under analysis. This was done trying to find the best function which follow the signal border line.

So starting from these results, I tried to be apply these cuts:

- A. $p_\pi/p_\Lambda < (0.52 + 0.49/p_\Lambda)$
- B. $\text{Opening Angle} < \text{ArcCos} \left(1 - \frac{3.5}{p_{\Sigma^*}^2 - 1} \right)$

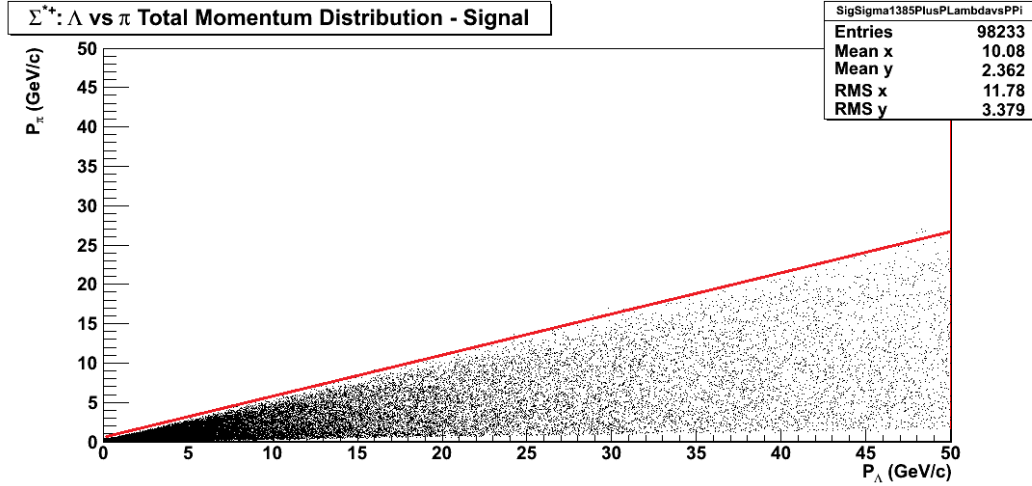


Figure 4.12: Λ 's momentum vs π 's momentum distribution for the signal in pp simulations at $\sqrt{s} = 10$ TeV. The red line represents the parameterization of the *exclusion area*.

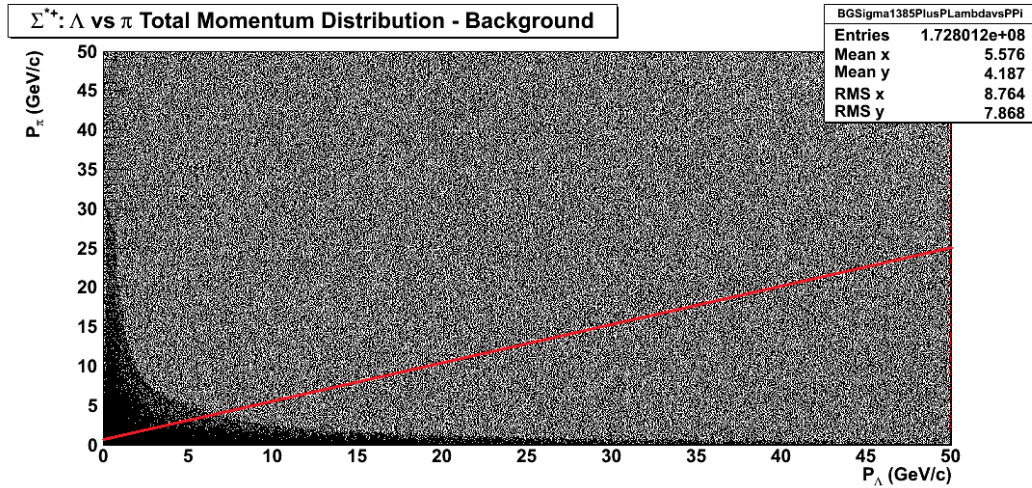


Figure 4.13: Λ 's momentum vs π 's momentum distribution for the background in pp simulations at $\sqrt{s} = 10$ TeV. The red line represents the parameterization of the *exclusion area*.

for the proton-proton simulation at $\sqrt{s} = 10$ TeV.

In Figures 4.16, 4.17 and 4.18 it is possible to see the Σ^* invariant mass distribution after the application of the kinematical cuts previously described (in addition to the quality cuts) for the 10 TeV simulations, together with the “Side-Bands” background fit, while in Table 4.3 the numerical results obtained are summarized.

Only the second kinematical cut achieves a significative improvement of the fit results with respect to those obtained without any kinematical cuts (taking into account all the 4 Σ^* particles involved in the analysis) applied. This one has then been chosen in addition to the “purity oriented” cut set. In Figure 4.19 the distribution confirming the 10 TeV results extracted from the 7 TeV simulations applying the quality cut in addition with the “ $\Lambda - \pi$ Cos(Opening Angle) vs $\Sigma^* P$ ” kinetical cut is shown.

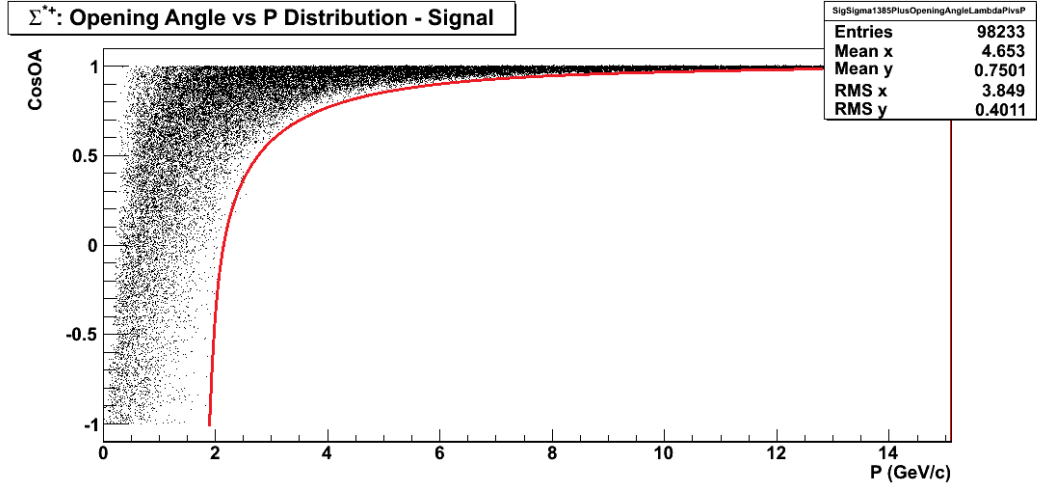


Figure 4.14: Σ^* daughters cosine of the opening angle vs Σ^* momentum distribution for the signal in pp simulations at $\sqrt{s} = 10$ TeV. The red line represents the parameterization of the *exclusion area*.

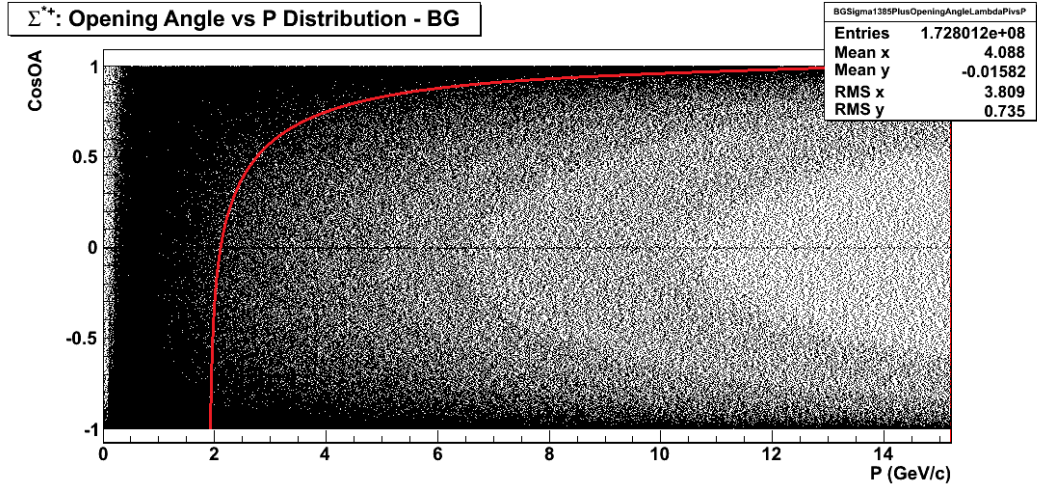


Figure 4.15: Σ^* daughters cosine of the opening angle vs Σ^* momentum distribution for the background in pp simulations at $\sqrt{s} = 10$ TeV. The red line represents the parameterization of the *exclusion area*.

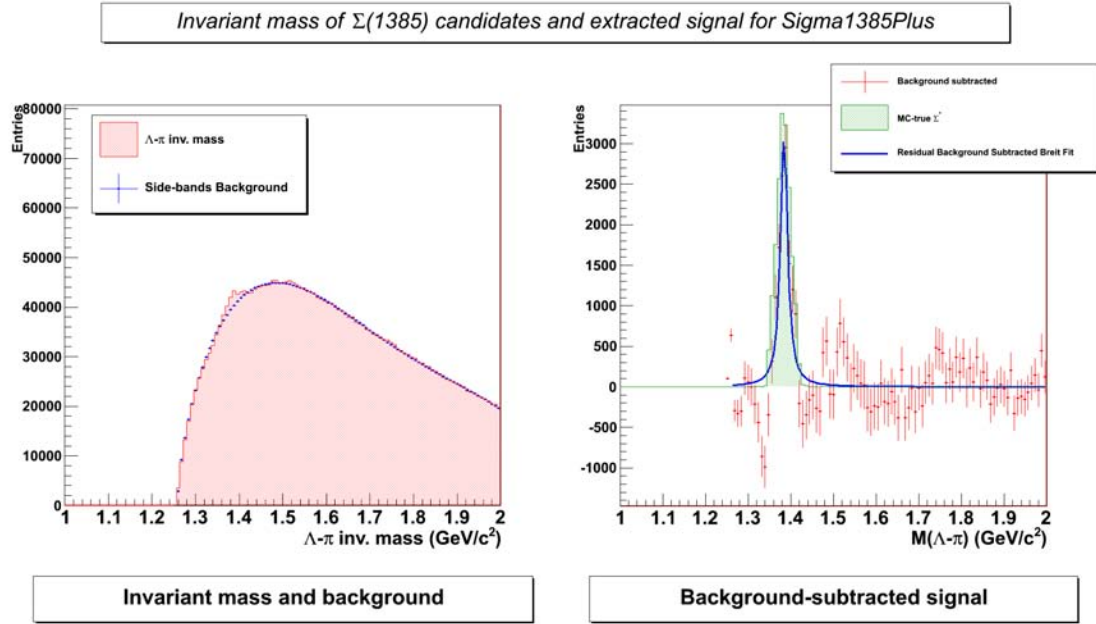


Figure 4.16: Σ^* 's invariant mass distribution and background subtracted signal after applying the Λ 's momentum vs π 's momentum cut in pp simulations at $\sqrt{s} = 10$ TeV.

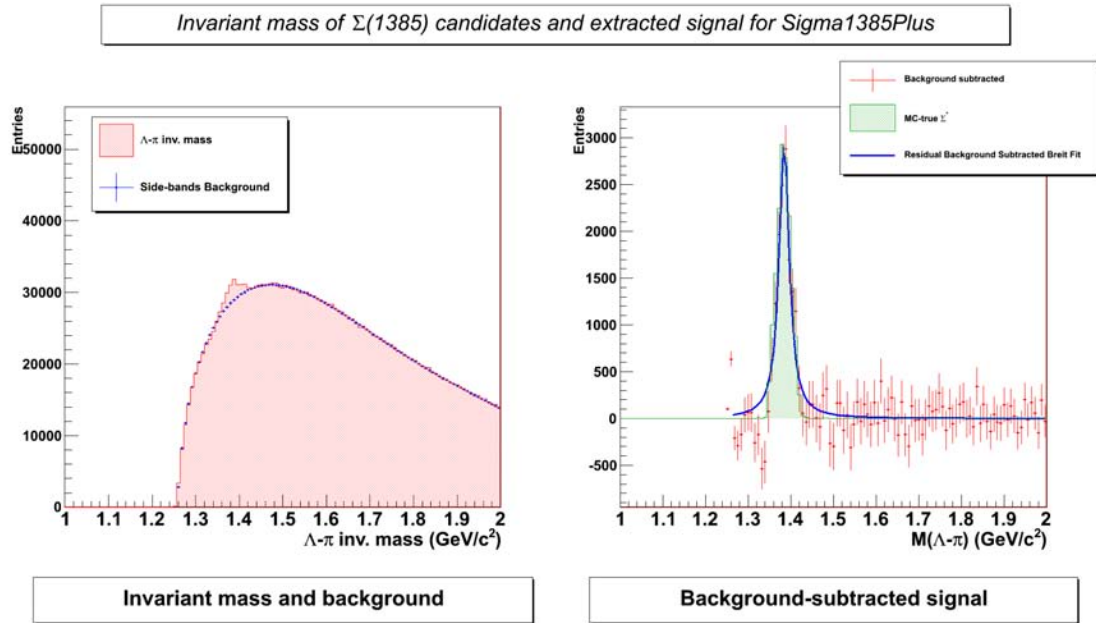


Figure 4.17: Σ^* 's invariant mass distribution and background subtracted signal after applying the Σ^* daughters cosine of the opening angle vs Σ^* momentum cut in pp simulations $\sqrt{s} = 10$ TeV.

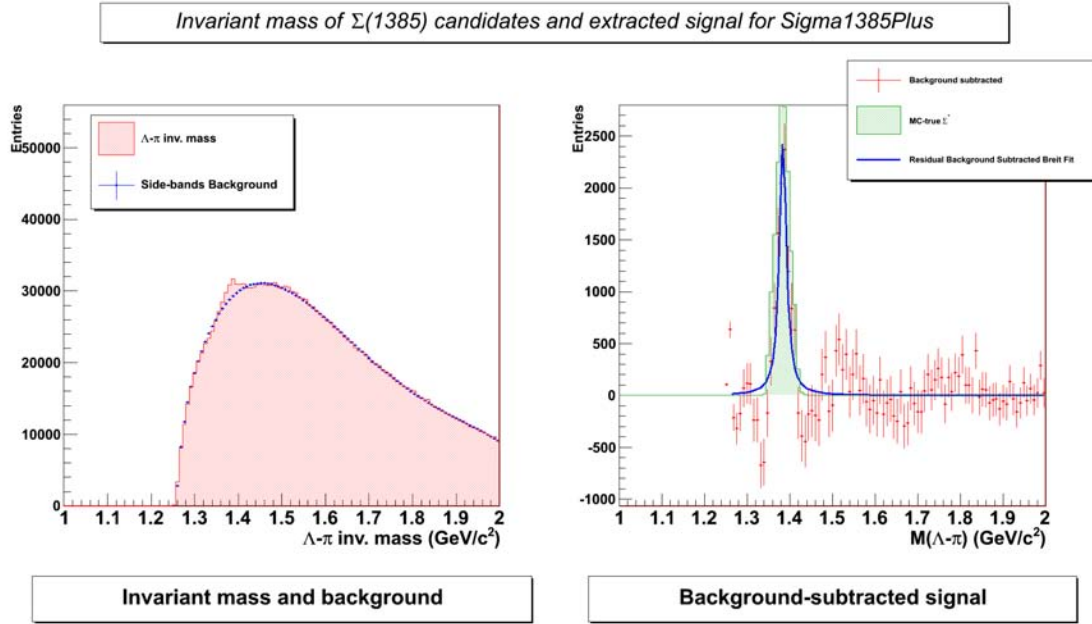


Figure 4.18: Σ^* 's invariant mass distribution and background subtracted signal after applying both the cuts previously described in pp simulations at $\sqrt{s} = 10$ TeV.

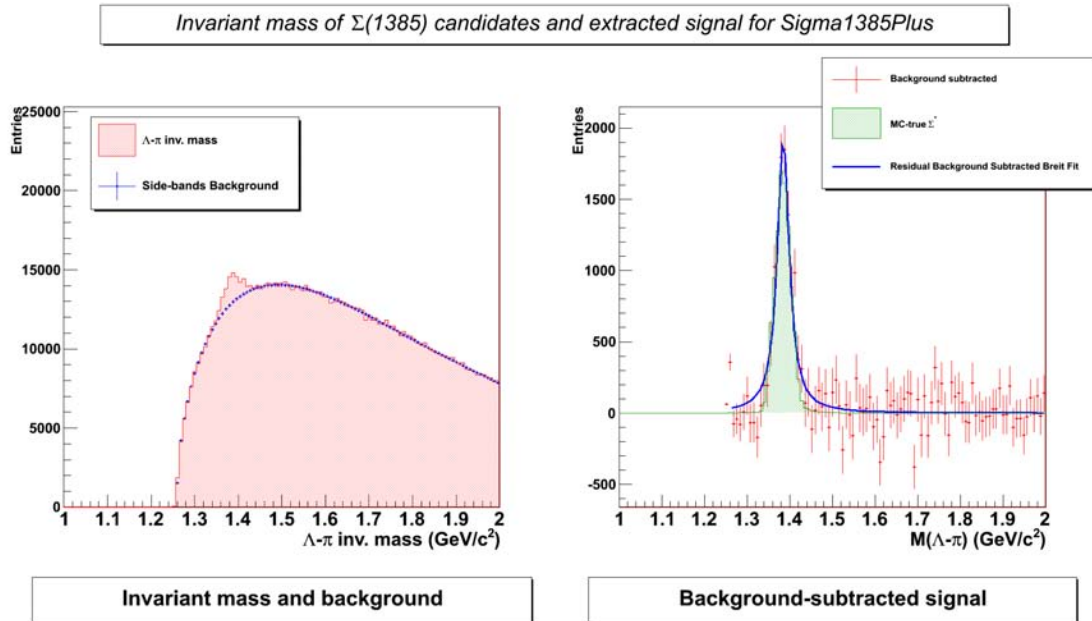


Figure 4.19: Σ^* 's invariant mass distribution and background subtracted signal after applying the Σ^* daughters cosine of the opening angle vs Σ^* momentum cut in pp simulations $\sqrt{s} = 7$ TeV.

Cut	Cut Type	Mass (GeV/c ²)	Γ (MeV)	χ^2/N_{dof}	Yield	$S/\sqrt{S+B}$
8	Quality Cuts + A.	1.385 ± 0.001	17 ± 3	3.7	9239 ± 803 (17611 \pm 133)	13.8 ± 1.2
9	Quality Cuts + B.	1.385 ± 0.001	26 ± 3	2.3	11841 ± 698 (15356 \pm 124)	21.5 ± 1.2
10	Quality Cuts + A. + B.	1.386 ± 0.001	26 ± 3	2.3	7453 ± 494 (11007 \pm 105)	19.2 ± 1.2

Table 4.3: Results obtained adding the kinematical cuts described in the text in order to improve the signal extraction. In brackets the Monte Carlo yield values.

In Table 4.4 the results, obtained with the “purity oriented” set of cuts, for all the particles involved in the analysis, provided with 52 million events at $\sqrt{s} = 10$ TeV, are summarized.

Particle	Mass (GeV/c ²)	Γ (MeV)	χ^2/N_{dof}	Yield	Significance
Σ^-	1.389 ± 0.001	37 ± 3	2.5	12440 ± 701 (14345 \pm 120)	22.4 ± 1.2
Σ^+	1.385 ± 0.001	26 ± 3	2.3	11841 ± 698 (11007 \pm 105)	21.5 ± 1.2
$\overline{\Sigma}^-$	1.392 ± 0.002	38 ± 4	2.8	11067 ± 639 (12191 \pm 110)	21.3 ± 1.2
$\overline{\Sigma}^+$	1.383 ± 0.001	30 ± 3	2.0	11398 ± 654 (13187 \pm 115)	22.4 ± 1.2

Table 4.4: All Σ^* species results obtained with the “purity oriented” cut set. In brackets the Monte Carlo yield values.

The results obtained are in good agreement with the PDG values. These set was chosen as the most pure i.e. the best in optimizing the fit results for the four particles at the same time. Moreover it is possible to reproduce, at least with the “efficiency oriented” selection, an effect seen when looking at the generated particle (and so, before the reconstruction procedure): the yield of particles production is greater than that of antiparticles, and among particles the production yield of Σ^{*+} is greater than that of Σ^{*-} . This is due to the fact that the collision initial state is a pp system and not a $p\bar{p}$ system.

Table 4.5 summarizes all the results obtained with the “efficiency oriented” set of cuts for all the particles involved in the analysis.

Again it is possible to see that both the sets of cuts allow to extract comparable results and the first one apparently allows to recover more efficiency. However, this consideration is not true anymore when analyzing the 7 TeV data. Moreover when I provided a transverse momentum differential analysis, I found that the “purity oriented” set will cause an efficiency loss at low transverse momentum values and therefore it will not be applied for these purposes.

Particle	Mass (GeV/c ²)	Γ (MeV)	χ^2/N_{dof}	Yield	Significance
Σ^-	1.390 ± 0.001	31 ± 3	3.3	11985 ± 749 (16049 \pm 127)	20.4 ± 1.2
Σ^+	1.384 ± 0.001	27 ± 3	3.5	14326 ± 740 (17086 \pm 131)	24.6 ± 1.2
$\overline{\Sigma}^-$	1.391 ± 0.002	30 ± 4	2.8	9340 ± 668 (13310 \pm 115)	17.7 ± 1.2
$\overline{\Sigma}^+$	1.384 ± 0.001	26 ± 3	3.0	10181 ± 695 (14448 \pm 120)	21.0 ± 1.2

Table 4.5: All Σ^* species results obtained with the “efficiency oriented” cut set. In brackets the Monte Carlo yield value.

4.2.5 Systematic uncertainties evaluation

The systematic component of the uncertainties associated to the fit results was evaluated varying the values of the cuts applied within a reasonable range. In particular the contribution of the systematics components can be summarized as follows:

For the “purity oriented” set:

- Degree of the polynomial fitting function: 0 GeV/c² for mass value, 3.3 MeV for width value, 10.4% for yield value.
- Width of the “exclusion region”: 0 GeV/c² for mass value, 0.5 MeV for width value, 1.9% for yield value.
- Quality cuts: 0 GeV/c² for mass value, 0.5 MeV for width value, 7.9% for yield value.
- Kinematical cuts: 0.5 GeV/c² for mass value, 1.6 MeV for width value, 11% for yield value.
- **Total:** 0.5 GeV/c² for mass value, 3.7 MeV for width value, 20.8% for yield value.

For the “efficiency oriented” set:

- Degree of the polynomial fitting function: 0.5 GeV/c² for mass value, 4 MeV for width value, 11.1% for yield value.
- Width of the “exclusion region”: 0.5 GeV/c² for mass value, 3.5 MeV for width value, 8.8% for yield value.
- Quality cuts: 0.5 GeV/c² for mass value, 0.6 MeV for width value, 8.0% for yield value.
- **Total:** 0.9 GeV/c² for mass value, 5.4 MeV for width value, 16.7% for yield value.

In both cases the systematic component dominates on the statistic one, in particular for what concern the extracted yield, and so, on the spectra. This effect is more evident for the “purity oriented” cut set that, even if it is able to provide a more pure sample

shows, at the same time, a greater sensibility to small changes in the analysis conditions. For the following differential analysis the “efficiency oriented” set will be used.

4.2.6 Transverse momentum and mass spectrum

In order to measure the p_t spectrum of the Σ^* we need to extract the signal in different p_t bins. In Figures 4.30 and 4.31 (see the end of the chapter) it is possible to see the results obtained dividing the dynamical range in seven p_t bins and extracting the signal from all of them following the previously described procedure and applying the “efficiency oriented” set of cuts. In each graph the red histogram is the signal after the background subtraction, fitted with a Breit-Wigner distribution (the blue curve) while the green histogram is the Monte Carlo signal passed through the reconstruction procedure. As we can see, a quite good signal is extracted from all the bins and it follows quite well the Monte Carlo distribution denoting the self-consistence of the procedure.

The p_t spectrum obtained in this way have to be corrected for the efficiencies before the comparison with the theoretical predictions. In order to properly correct the p_t spectra, simulations are used to evaluate the correction factors that have to be applied to the extracted yields. In Figures 4.20 and 4.21 the uncorrected and corrected transverse momentum spectra for the 10 TeV simulations are shown. In both cases the blue histogram represents the reconstructed data, while the red one represents the Monte Carlo tagged events after being passed through the reconstruction procedure. Since we are using only simulated data, of course in this way it is possible only to evaluate the self-consistence of the extraction procedure that is confirmed by the results shown. The error bars take into account both the statistical and the systematic component.

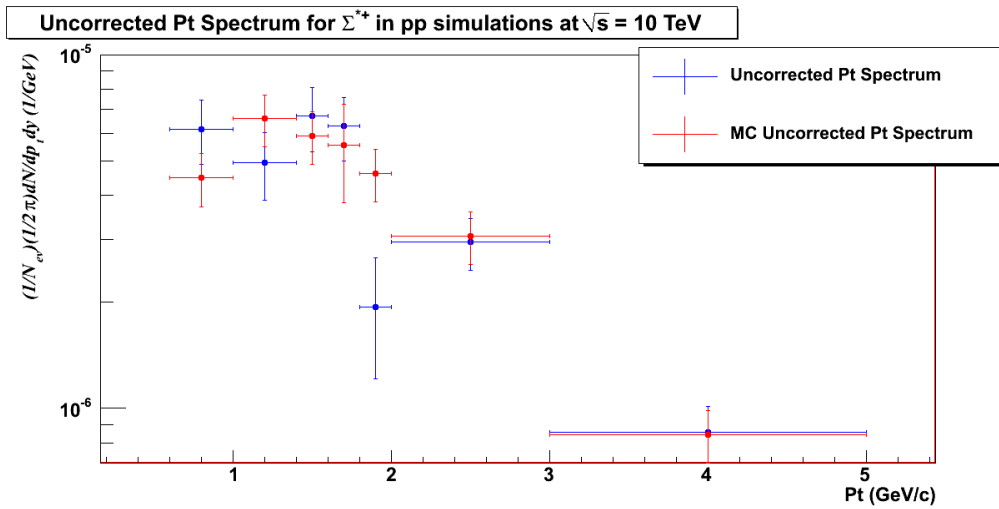


Figure 4.20: Uncorrected transverse momentum distribution for 10 TeV pp simulations. The blue histogram represents the uncorrected reconstructed yields (integrated in the interval $-2 < y < 2$) while the red one represents the uncorrected Monte Carlo yields.

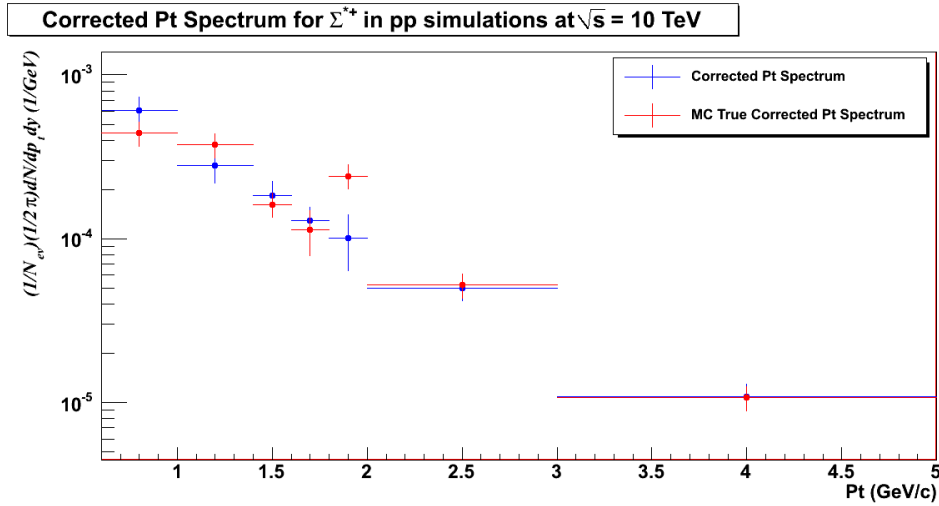


Figure 4.21: Corrected transverse momentum distribution for 10 TeV pp simulations. The blue histogram represents the reconstructed yields corrected using the correction factors obtained from the generated data while the red one represents the corrected Monte Carlo yields.

Introducing the transverse mass m_t we redo the same plot for it and the results are shown in the Figures 4.22 and 4.23.

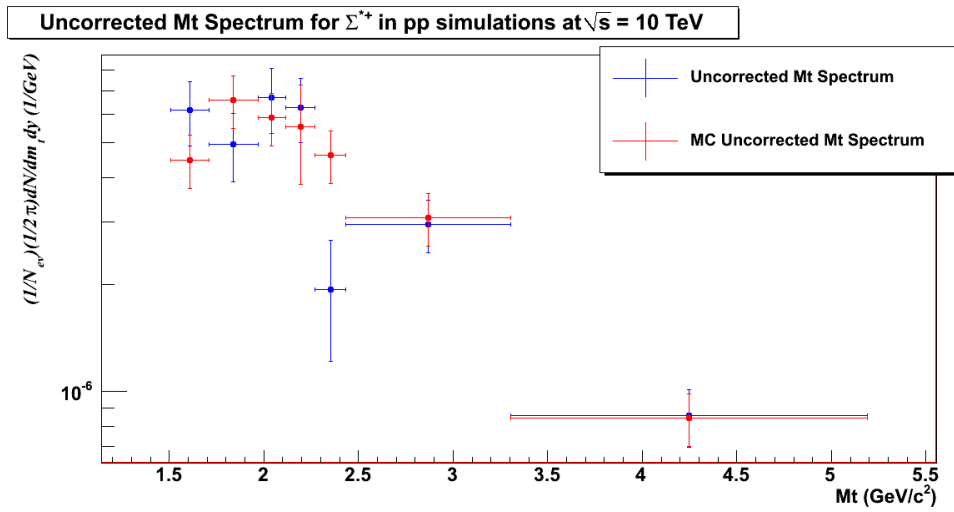


Figure 4.22: Uncorrected transverse mass distribution for 10 TeV pp simulations. The blue histogram represents the uncorrected reconstructed yields (integrated in the interval $-2 < y < 2$) while the red one represents the uncorrected Monte Carlo yields.

As it is possible to see the reconstructed spectra is in reasonable agreement with the MC one allowing in this way a further confirmation of the self-consistence of the procedure for the extraction of the signal.

The corrected distributions were fitted with the following functions in the context of thermal model particle production, as done also in other strange particle production

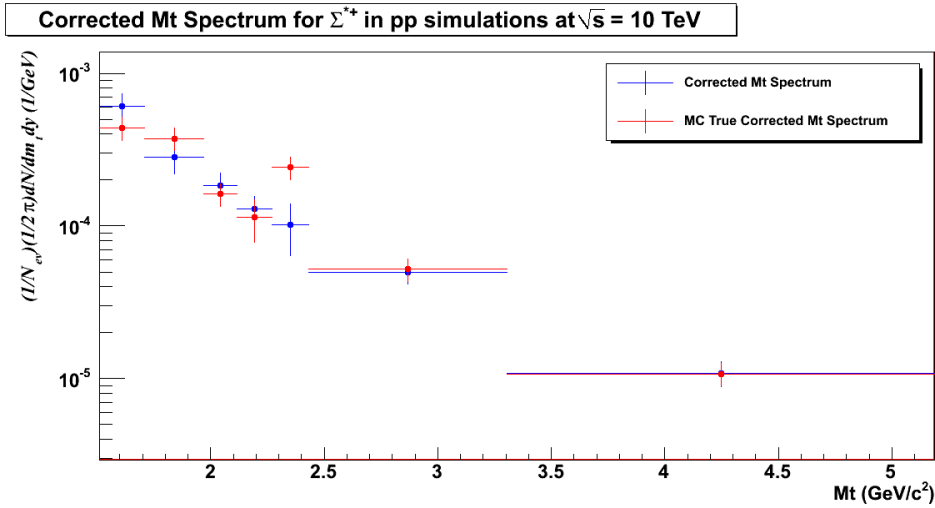


Figure 4.23: Corrected transverse mass distribution for 10 TeV pp simulations. The blue histogram represents the reconstructed yields corrected using the correction factors obtained from the generated data while the red one represents the corrected Monte Carlo yields.

analyses in ALICE:

- for the p_t spectrum:

1. $\frac{1}{2\pi} \frac{d^2N}{dydp_t} = A \times p_t \times e^{-\frac{p_t}{T}}$ (Exponential)
2. $\frac{1}{2\pi} \frac{d^2N}{dydp_t} = \frac{(n-1)(n-2)}{nT+m_{\Sigma^*}(n-2)} \times \frac{dN}{dy} \times p_t \times (1 + \frac{m_t-m_{\Sigma^*}}{nT})^{-n}$ (Levi-Tsallis)

- for the m_t spectrum¹⁶:

$$\frac{1}{2\pi} \frac{d^2N}{dydm_t} = \frac{dN}{dy} \times m_t \frac{1}{2\pi T(m_{\Sigma^*}+T)} \times \exp(\frac{-(m_t-m_{\Sigma^*})}{T}) \text{ (Exponential)}$$

The p_t exponential has two parameters: the normalization A and the inverse slope parameter T . The Levy function, already used at lower energies[155], is shown to be useful when the transverse momentum range is wide: it includes both an exponential shape for low p_t (which can be characterized by an inverse slope parameter T) and a power law component (governed by the power parameter n) for the higher p_t region. The results of these fits to the spectra, where statistical and systematic uncertainties are added in quadrature, are shown in Figures 4.24 and 4.25 where the spectra fitted with the mentioned fits function are reported.

As it is possible to see, the p_t spectrum is quite well fitted by the Levy-Tsallis in all the dynamical range considered, and by the Exponential distributions, only until intermediate p_t . As already seen by STAR the m_t spectra is quite well fitted by the Exponential distribution until intermediate m_t . From the corrected spectra it is possible to extract the mean p_t of the reconstructed particles and the temperature T of the source. The obtained values are summarized in Table 4.6:

¹⁶In this case we followed the indication from a similar analysis performed by the STAR experiment[149].

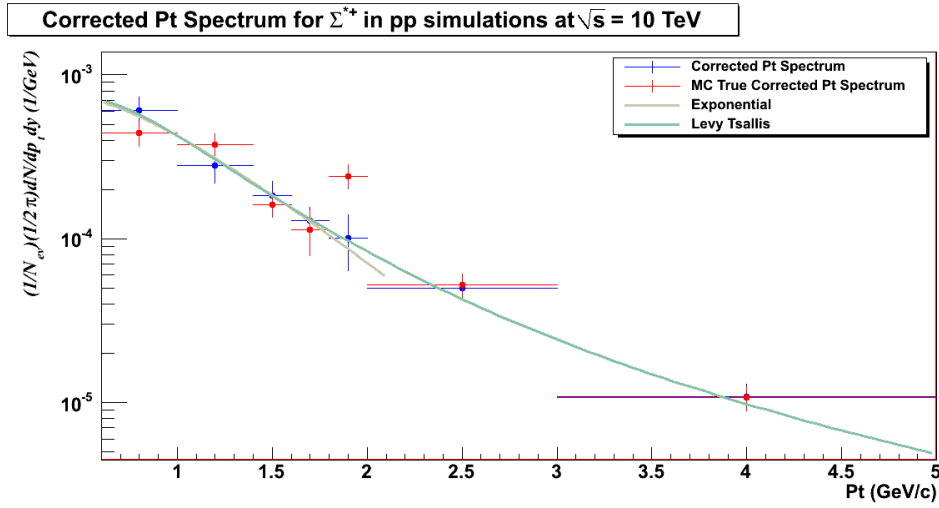


Figure 4.24: Corrected transverse momentum distribution for 10 TeV pp simulations with the corresponding fits. See text for details.

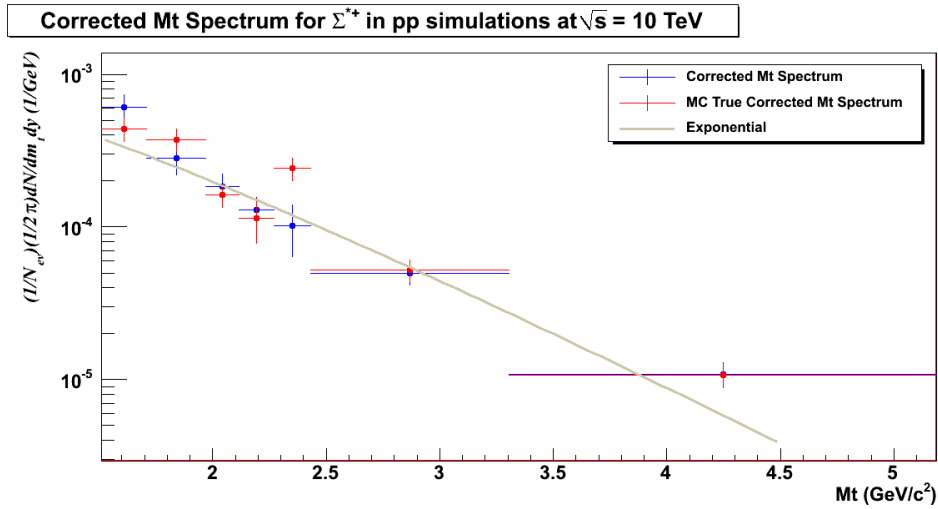


Figure 4.25: Corrected transverse mass distribution for 10 TeV pp simulations with the corresponding fits. See text for details.

The corresponding distributions provided with the simulations at $\sqrt{s} = 7$ TeV will be shown in the next chapter when they will be compared with the pp data collected at the same energy. Finally in Figure 4.26 the ratio between the PYTHIA MC data and the PYTHIA reconstructed data as function of the transverse momentum is shown.

As it is possible to see for almost all the p_t bins the ratio stands around 1 showing, as previously seen, a good efficiency of the signal extraction procedure in all the dynamical range considered.

	Exponential		Levy-Tsallis		
	$\langle p_t \rangle$	T	$\langle p_t \rangle$	T	n
	(GeV/c)	(MeV)	(GeV/c)	(MeV)	
p_t	1.120 ± 0.81	560 ± 40	1.175 ± 0.178	131 ± 51	3.43 ± 0.63
m_t	—	525 ± 42	—	215 ± 73	4.2 ± 1.2

Table 4.6: Temperature T and $\langle p_t \rangle$ obtained from the exponential and Levy-Tsallis fits of the p_t spectra and from the Exponential fit of the m_t .

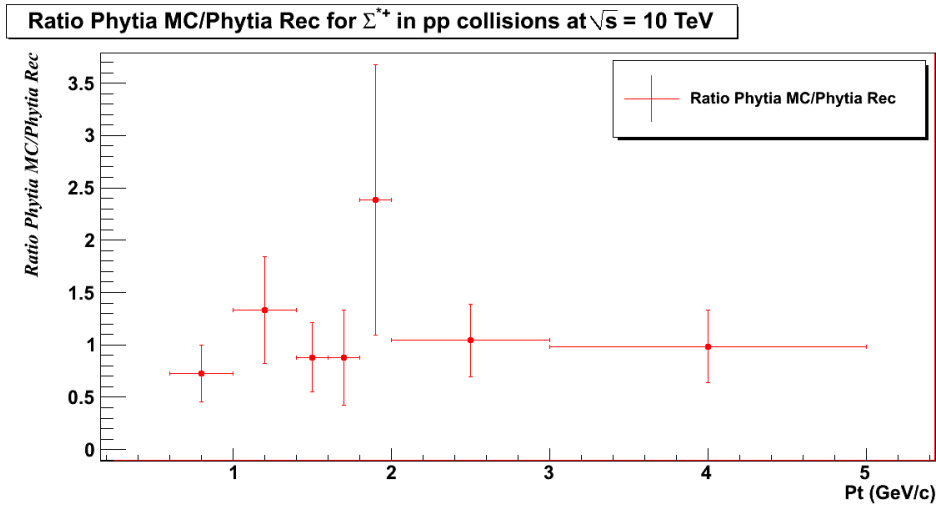


Figure 4.26: Ratio between the PYTHIA MC yields and the PYTHIA reconstructed yields.

4.2.7 Signal Significance

In Table 4.7 the significances (defined as $S/\sqrt{S+B}$) for the extracted signal obtained for the differential (in p_t) and integral analyses of 10 TeV simulations using the “efficiency oriented” cut set, are summarized. As one can see from the values reported, it was possible to extract a quite good signal in all the p_t intervals analyzed. The uncertainties here reported take into account both the statistical and the systematic component.

In Figure 4.27 it is possible to see the significance p_t dependence for the two sets of cuts tried.

Almost all the p_t bins shows, as expected, that the “efficiency oriented” cuts set increase the significance. This is not true in the last two bins (wider than the others). In this case, probably due to the wider range included and to the closeness to the dynamical range limit, a cuts release implies the introduction of more background than signal and so the net effect is a significance decrease. As shown in the next chapter this significance increasing is much more evident analyzing the 7 TeV pp data.

Table 4.7: Significances of the extracted signal for 10 TeV pp simulations both for integral and differential transverse momentum distributions ($52 \cdot 10^6$ events).

p_t range (GeV/c)	10 TeV Simulation Significances
Integral	24.6 ± 2.8
0.6-1.0	11.7 ± 1.7
1.0-1.4	9.1 ± 1.5
1.4-1.6	9.7 ± 1.6
1.6-1.8	9.2 ± 1.5
1.8-2.0	3.6 ± 1.6
2.0-3.0	14.3 ± 1.9
3.0-5.0	16.6 ± 2.1

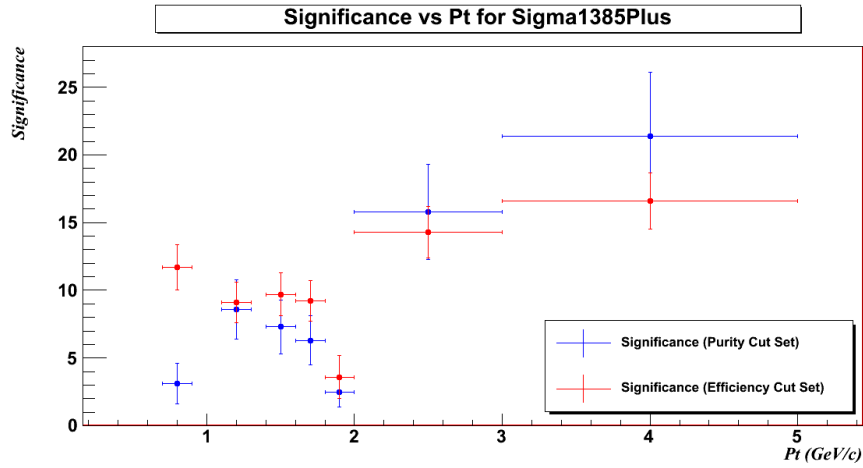


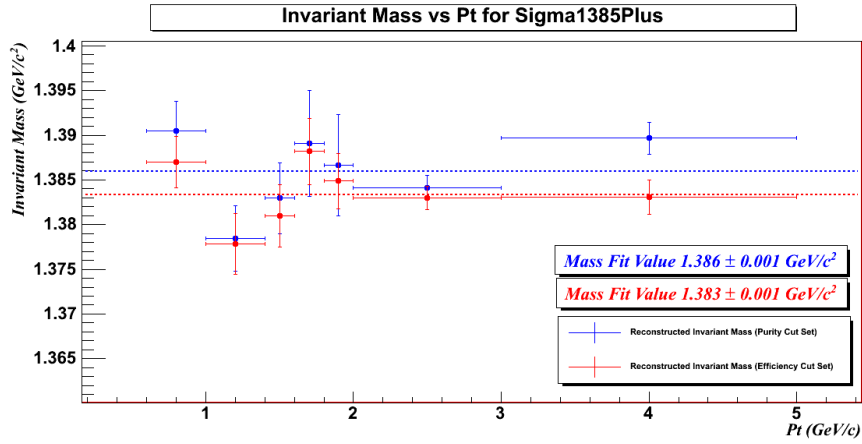
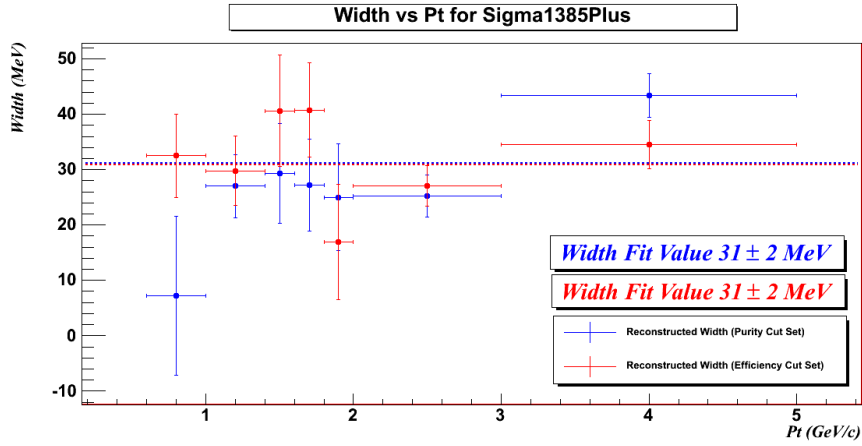
Figure 4.27: Σ^* p_t significance dependence in 10 TeV simulations.

4.2.8 Dependence of mass and width from p_t

In Figures 4.28 and 4.29 the transverse momentum dependence of Σ^* mass and width obtained with the two sets of cuts is shown.

As it can be seen from the figures even in this case the results confirms the accordance with the PDG values and no dependence from the transverse momentum is evident.

The analysis procedure described in this chapter and the results that it allows to provide are the first important step in the context of the resonance analysis in the heavy-ion collisions physics explored by ALICE. Infact, as mentioned in the Chapter 3, when both the Σ^* yield will be extracted both in pp and in PbPb collisions, the proper comparison between them and the possible resonance suppression production in PbPb collisions will allow to reach the goal of this study i.e. the determination of the time span between QGP chemical and kinetic freezeout and so a better understanding of the

Figure 4.28: Σ^{*+} p_t mass dependence in 10 TeV simulations.Figure 4.29: Σ^{*+} p_t width dependence in 10 TeV simulations.

QGP freezeout dynamics.

In the next chapter, basing on the promising results provided by the reconstruction procedure here described, I will apply it to the 900 GeV and 7 TeV data taken by the ALICE experiment.

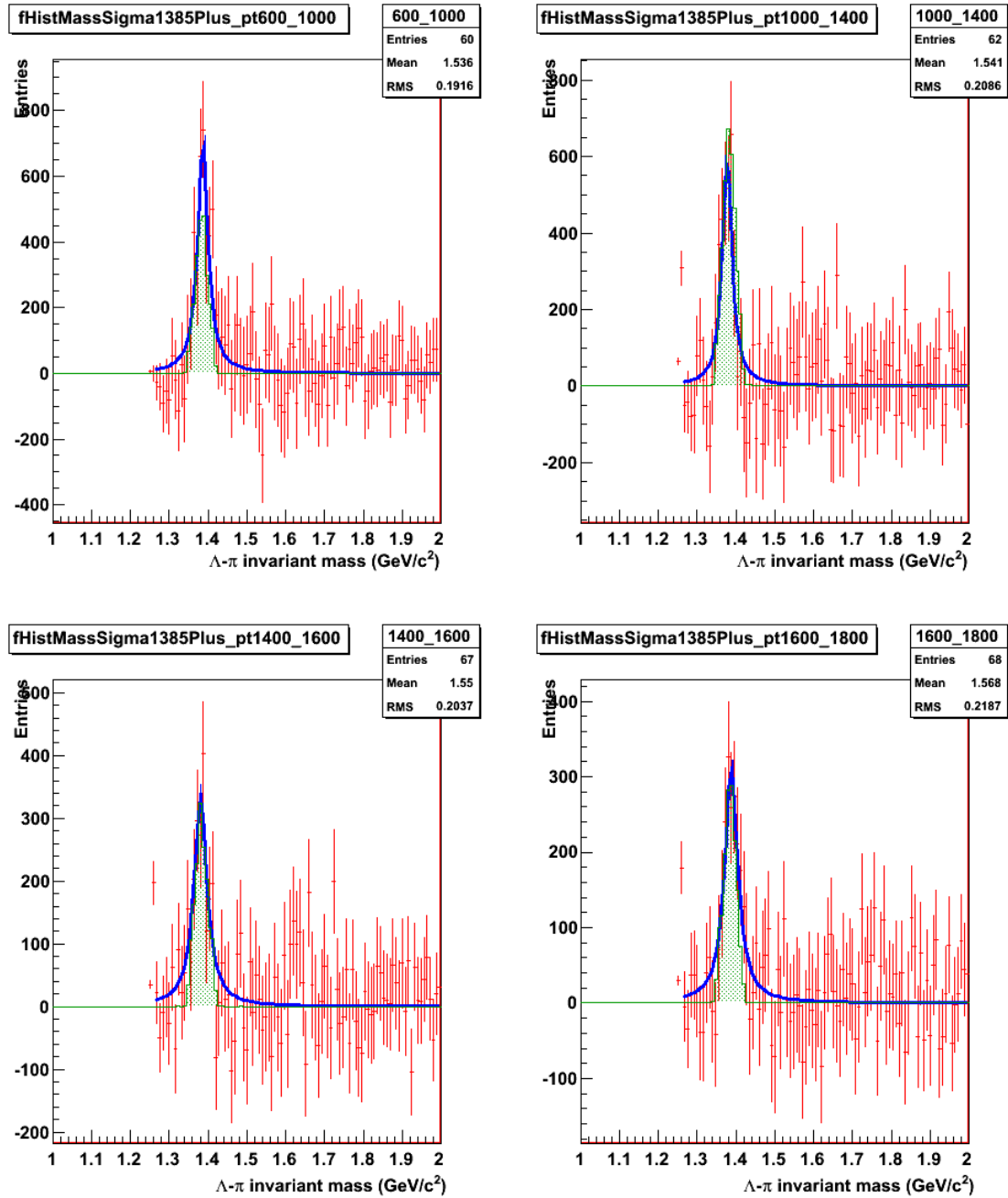


Figure 4.30: A-B-C-D. Σ^{*+} signal extracted in the 0.6-1.0, 1.0-1.4, 1.4-1.6, 1.6-1.8 GeV/c p_t bins. The red histograms represent the signal after the background subtraction fitted with a Breit-Wigner distribution (the blue curve) while the green histograms are the Monte Carlo signal passed through the reconstruction procedure.

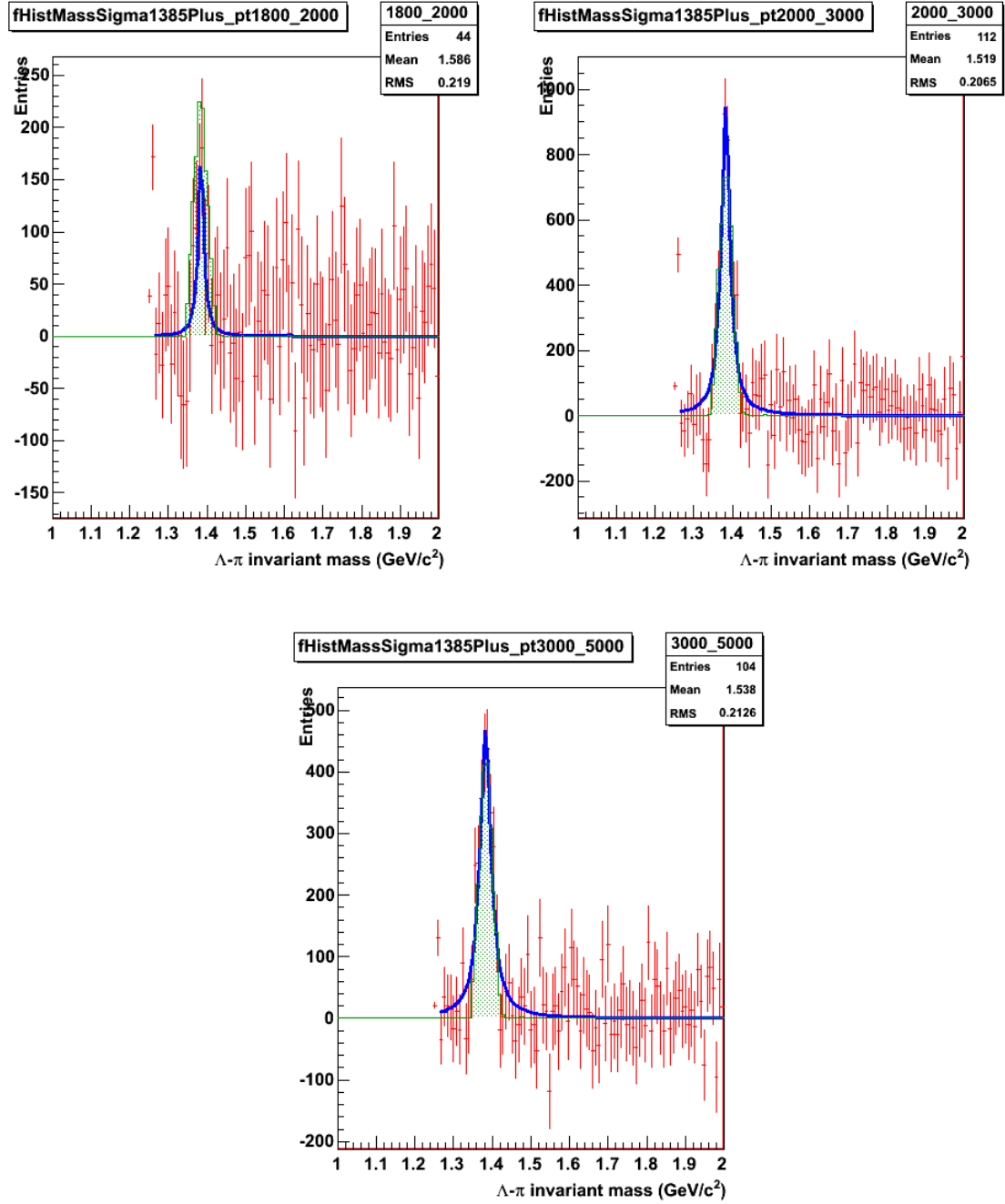


Figure 4.31: A-B-C. Σ^{++} signal extracted in the 1.8-2.0, 2.0-3.0, 3.0-5.0 GeV/c p_t bins. See caption of Figures 4.30 A, B, C, D for details.

Chapter 5

$\Sigma(1385)$: Proton - Proton Data Analysis

The analysis procedure described in the previous chapter was then applied to the 900 GeV and 7 TeV proton-proton data collected by the ALICE experiment.

5.1 900 GeV Data Analysis Description

The 900 GeV data analyzed here were collected by ALICE during April 2010. The 900 GeV statistics collected is not enough to perform a complete differential analysis (only 3 million events remained after the events selection performed on the data set available on the GRID), in terms of p_t/m_t and y , and therefore it has been possible to produce only integral analysis or data in rather wide p_t/m_t bins.

5.1.1 Invariant Mass Distribution

In Figure 5.1 the Λ - π ¹⁷ invariant mass distribution before applying any cut is shown while Figure 5.2 shows the Σ^* invariant mass distribution after the application of a dedicated set of quality cuts previously defined (left graphs). Infact, due to low statistics available, it was decided to release some of the quality cuts previously used in order to avoid to suppress the signal too much. In more details, for the 900 GeV data a more loose version of the “efficiency oriented” set of cuts will be used (Table 5.2), i.e. the cut on the Λ mass and on the DCA between Λ and π respectively and the primary vertex were released.

¹⁷In all the following figures, in order to improve the statistics, particles and respective antiparticles were put together. From now on, only the result for the $\Sigma^{*+} + \overline{\Sigma}^{*+}$ are shown, since the result for the Σ^{*-} and its antiparticles are similar.

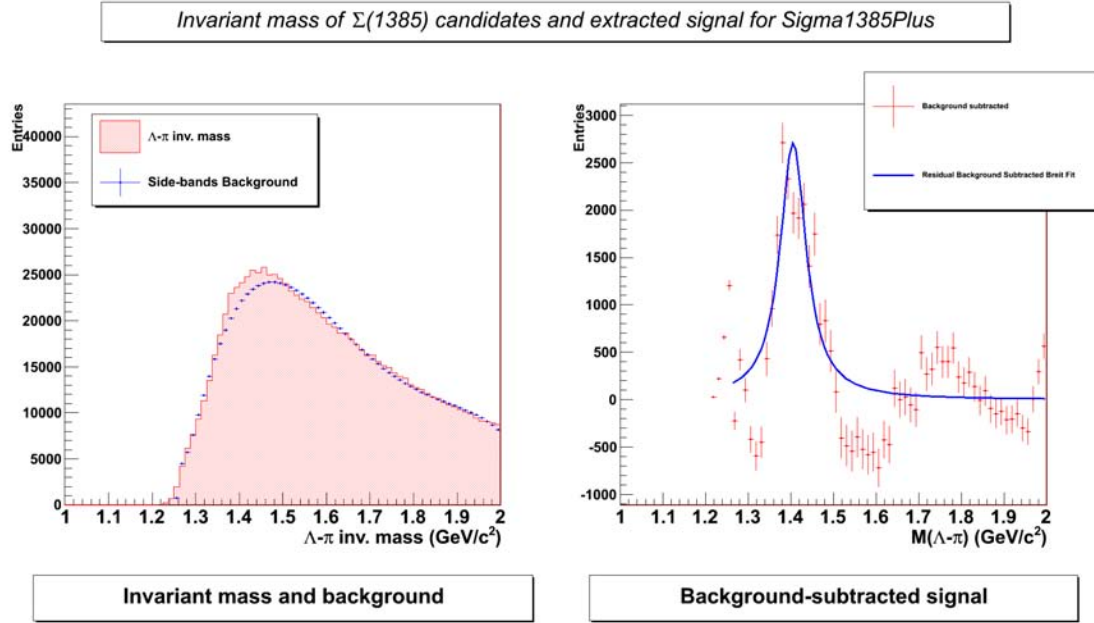


Figure 5.1: Σ^* 's invariant mass distribution and $\Lambda - \pi$ signal background-subtracted before applying the quality cuts in pp data at $\sqrt{s} = 900$ GeV.

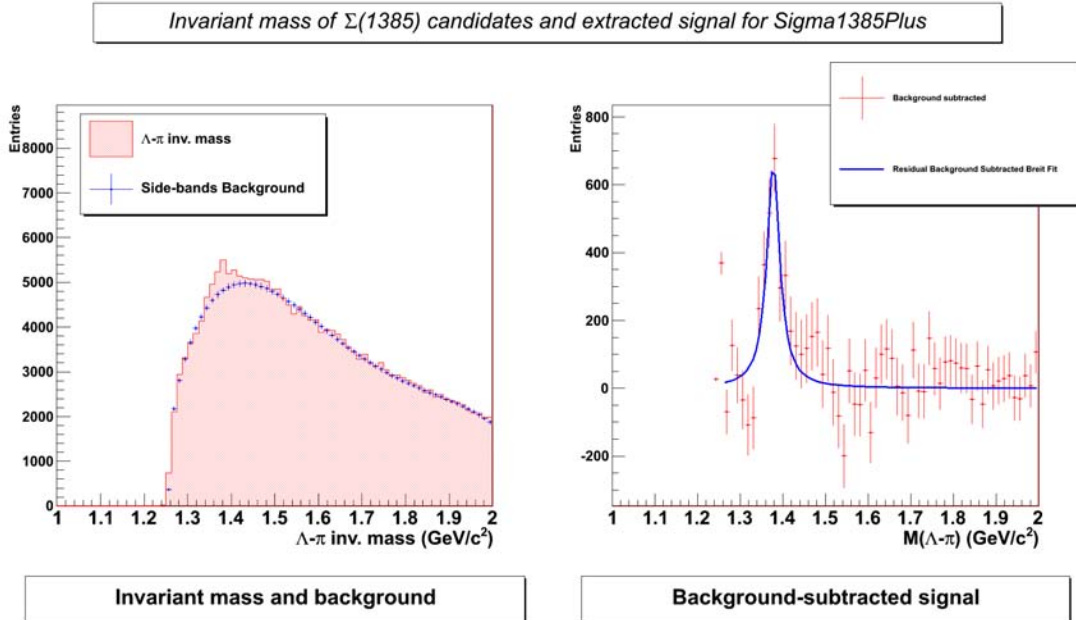


Figure 5.2: Σ^* 's invariant mass distribution and $\Lambda - \pi$ signal background-subtracted after applying the quality cuts in pp data at $\sqrt{s} = 900$ GeV.

Cut #	Cut Type	Mass (GeV/c ²)	Γ (MeV)	χ^2/N_{dof}	Yield	Significance
0	No Cuts	1.410 ± 0.004	93 ± 8	5	5122 ± 338	20.5 ± 1.7
1	Λ Daugh TPC refit	1.410 ± 0.004	93 ± 8	5	5122 ± 338	20.5 ± 1.7
2	$1 + \Lambda$ Daugh TPC cls > 70	1.413 ± 0.004	93 ± 8	4.6	4226 ± 310	18.4 ± 1.2
3	$2 + \chi^2/(\# \text{ TPC clusters}) < 4$	1.413 ± 0.004	92 ± 8	4.5	4191 ± 309	18.2 ± 1.3
4	$3 + 1.100 < M_\Lambda < 1.130 \text{ GeV}$	1.378 ± 0.004	39 ± 11	1.3	1452 ± 183	9.9 ± 1.2
5	$4 + \Lambda \text{ CosPointAng} > 0.99$	1.374 ± 0.004	31 ± 10	1.2	988 ± 173	7.3 ± 1.2
6	$5 + \Lambda \text{ Daugh DCA} < 0.2 \text{ cm}$	1.373 ± 0.004	29 ± 10	0.97	879 ± 151	7.2 ± 1.2

Table 5.1: Σ^{*+} results obtained with the modified “efficiency oriented” cut set.

Putting together Σ^{*+} and $\overline{\Sigma}^{*+}$, Σ^{*-} and $\overline{\Sigma}^{*-}$ respectively:

Particle	Mass (GeV/c ²)	Γ (MeV)	χ^2/N_{dof}	Yield	Significance
$\Sigma^{*+} + \overline{\Sigma}^{*+}$	1.377 ± 0.003	39 ± 7	1.5	2137 ± 216	12.5 ± 1.2
$\Sigma^{*-} + \overline{\Sigma}^{*-}$	1.393 ± 0.003	39 ± 8	1.2	1921 ± 208	11.5 ± 1.2

Table 5.2: $\Sigma^{*+} + \overline{\Sigma}^{*+}$ and $\Sigma^{*-} + \overline{\Sigma}^{*-}$ results obtained with the modified “efficiency oriented” cut set.

5.1.2 Signal Extraction

In order to define the background and to extract the signal, the “Side-Bands” technique was applied. The signal was fitted with a Breit-Wigner function and the results are shown in Figure 5.1, before applying the quality cuts and in Figure 5.2 after their application (right graphs). The results obtained, in terms of mass and width, even with the low statistics available, are still in agreement, within the errors, with the PDG values. The errors associated to the fit results take into account only the statistical component. The systematic one will be evaluated later.

5.1.3 Kinematical Cuts

Some simulation as anchor runs for the 900 GeV data were provided and then studied in order to try to extract a set of kinematical cuts. In Figures 5.3 and 5.4 it is possible to see the Σ^* daughters cosine of the opening angle distributions for the signal and the background respectively in the 900 GeV simulations.

In Figures 5.5 and 5.6 the Λ ’s momentum vs π ’s momentum distributions for the signal and the background respectively in the 900 GeV simulations is shown.

In Figures 5.7 and 5.8 the Σ^* daughters cosine of the opening angle vs Σ^* momentum distributions for the signal and the background respectively in the 900 GeV simulations is shown.

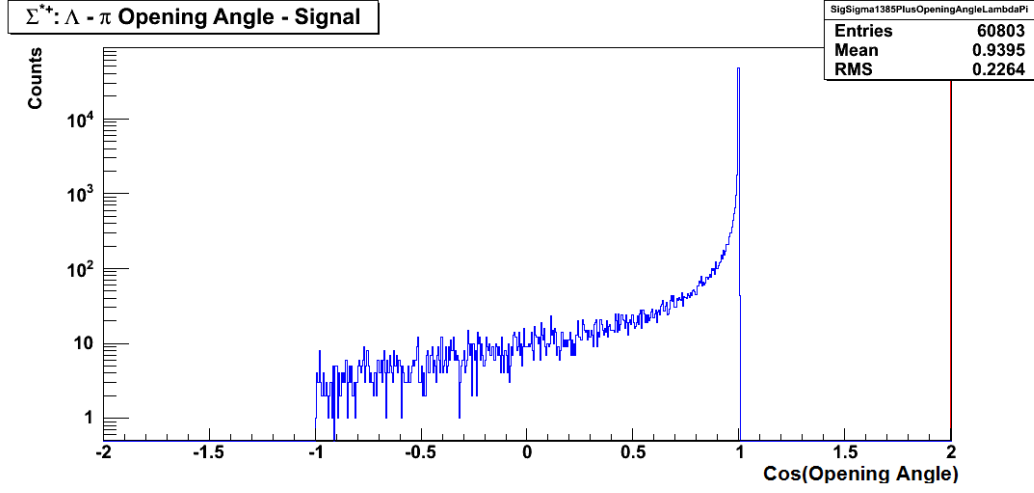


Figure 5.3: Σ^* daughters cosine of the opening angle distribution for the signal in pp simulations at $\sqrt{s} = 900$ GeV.

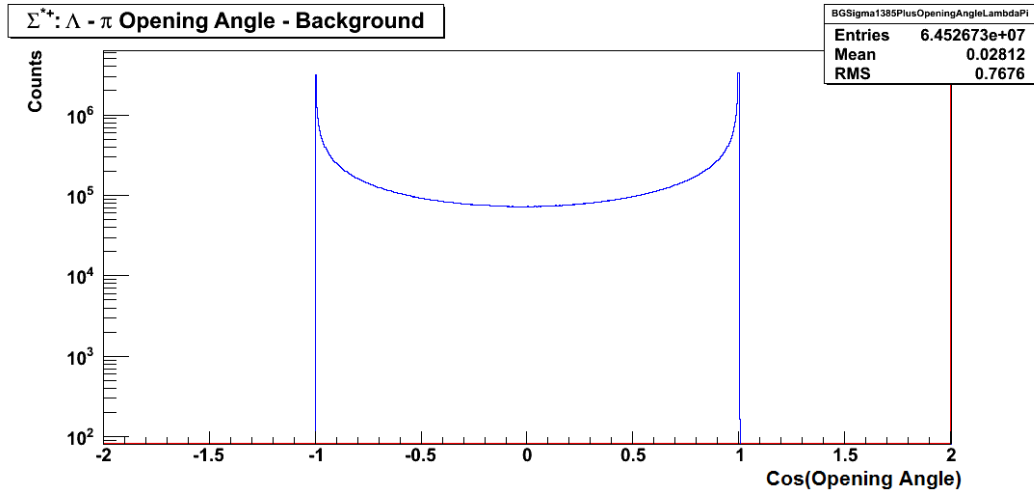


Figure 5.4: Σ^* daughters cosine of the opening angle distribution for the background in pp simulations at $\sqrt{s} = 900$ GeV.

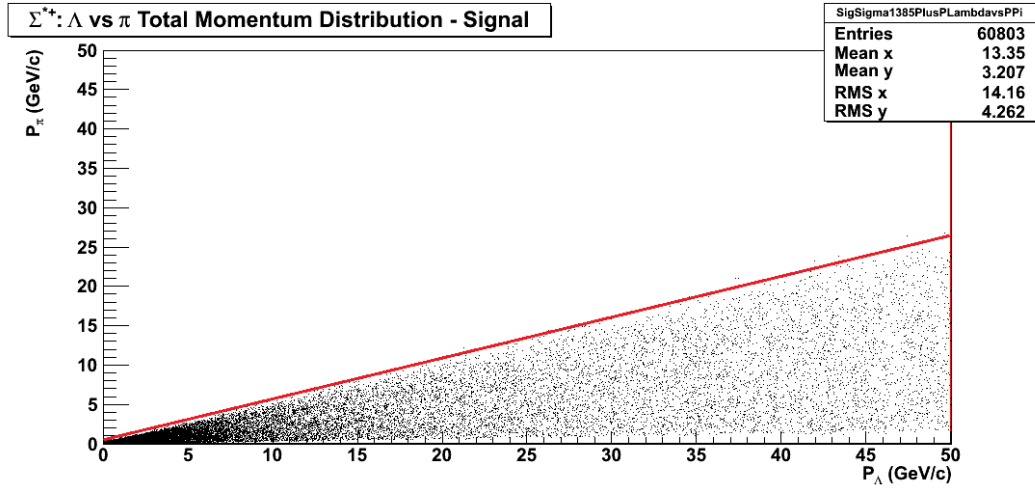


Figure 5.5: Λ 's momentum vs π 's momentum distribution for the signal in pp simulations at $\sqrt{s} = 900$ GeV. The red line represents the parameterization of the *exclusion area*.

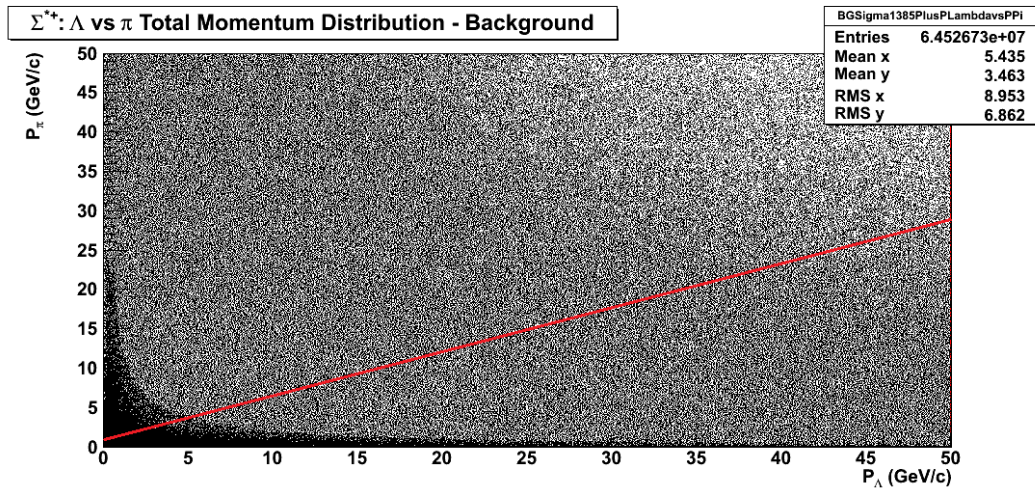


Figure 5.6: Λ 's momentum vs π 's momentum distribution for the background in pp simulations at $\sqrt{s} = 900$ GeV. The red line represents the parameterization of the *exclusion area*.

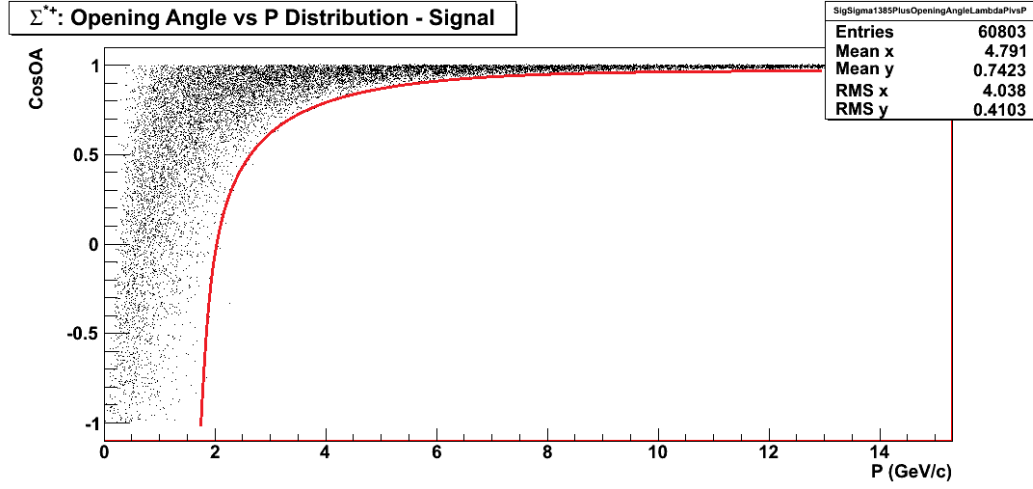


Figure 5.7: Σ^* daughters cosine of the opening angle vs Σ^* momentum distribution for the signal in pp simulations at $\sqrt{s} = 900$ GeV. The red line represents the parameterization of the *exclusion area*.

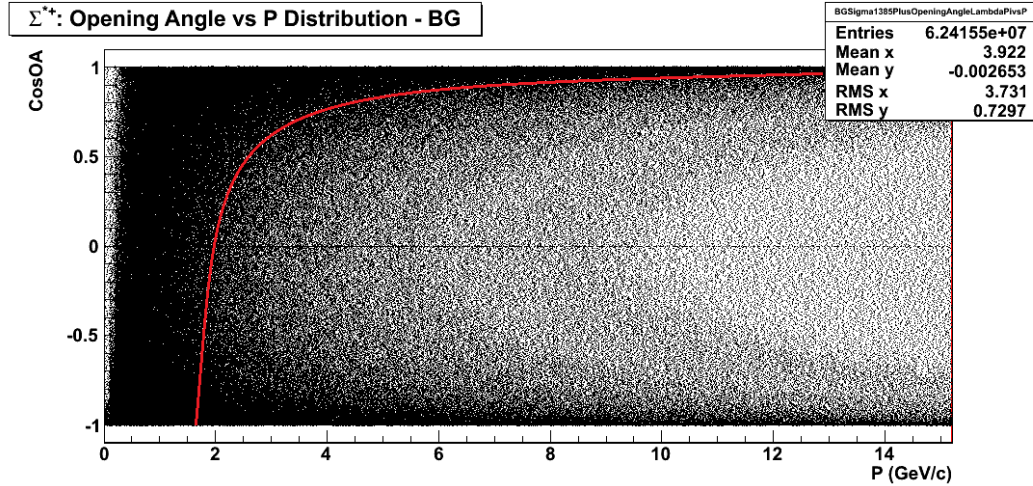


Figure 5.8: Σ^* daughters cosine of the opening angle vs Σ^* momentum distribution for the signal (Left) and the background (Right) in pp simulations at $\sqrt{s} = 900$ GeV. The red line represents the parameterization of the *exclusion area*.

However, since the background parametrization procedure doesn't work anymore after the application of these selections, it was not possible to apply any cut related to these distributions. As a consequence, for the 900 GeV analysis it was decided to keep a less pure sample but at least able to provide a signal with reasonable significance.

5.1.4 Systematic uncertainties evaluation at $\sqrt{s} = 900$ GeV

The systematic component of the errors associated to the fit results was evaluated varying the values of the cuts applied within a reasonable range. In particular the contribution of the systematics components can be summarized as follows:

- Degree of the polynomial fitting function: 0.5 GeV/c² for mass value, 1.5 MeV for width value, 4.1% for yield value.
- Width of the “exclusion region”: 0 GeV/c² for mass value, 3 MeV for width value, 6.9% for yield value.
- Quality cuts: 2 GeV/c² for mass value, 2.5 MeV for width value, 16.1% for yield value.
- **Total:** 2.1 GeV/c² for mass value, 4.2 MeV for width value, 18.5% for yield value.

5.1.5 Transverse momentum and mass spectrum

In Figure 5.9 it is possible to see the results obtained dividing the dynamical range in three p_t bins and extracting the signal from all of them following the previously described procedure.

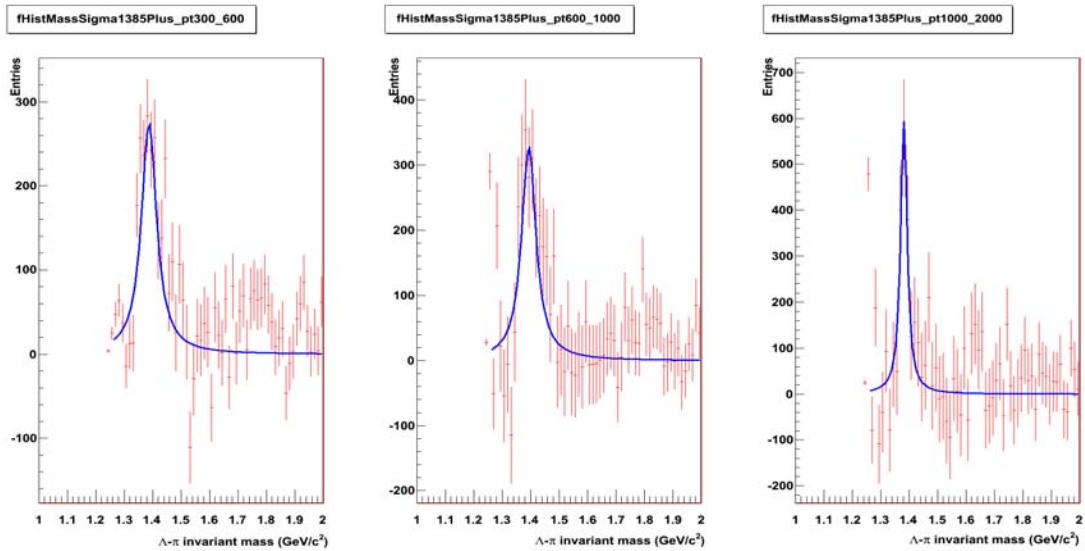


Figure 5.9: $\Sigma^{*+} + \Sigma^{*+} + \Sigma^{*-} + \Sigma^{*-}$ signal extracted in the 0.3-0.6, 0.6-1.0, 1.0-2.0 GeV/c p_t bins. The red histograms are the signal after the background subtraction fitted with a Breit-Wigner distribution (the blue curve) in pp simulations at $\sqrt{s} = 900$ GeV.

In each graph the red histogram is the signal after the background subtraction fitted with a Breit-Wigner distribution (the blue curve). A quite good signal is extracted from all the bins.

The uncorrected transverse momentum and mass spectra are shown in Figures 5.10 and 5.11. As previously reported, the statistics wasn't high enough to attempt a fine differential analysis, and so the dynamical range was divided only in three p_t/m_t sub-ranges. In order to further increase the statistics, all particles and respective antiparticles were treated together.

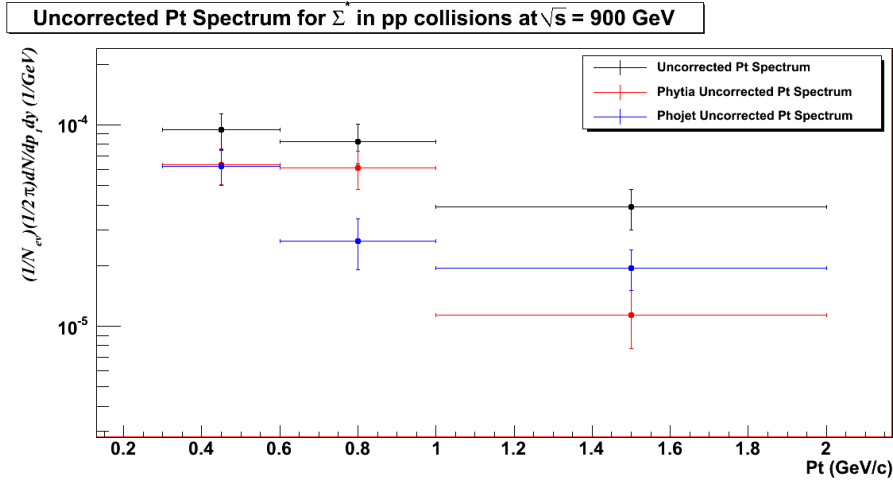


Figure 5.10: Uncorrected transverse momentum distribution for 900 GeV pp data. The black points are the 900 GeV uncorrected spectrum while the red points are the PHYTIA uncorrected spectrum and the blue points the Phojet uncorrected spectrum.

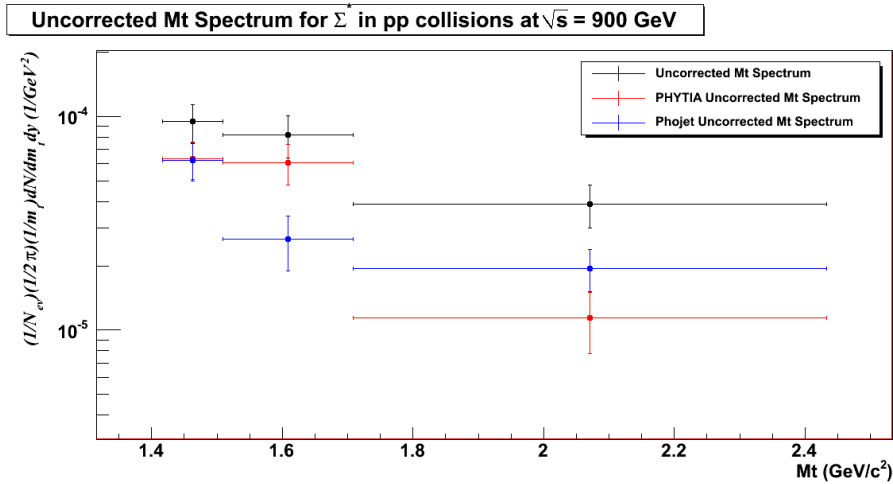


Figure 5.11: Uncorrected transverse mass distribution for 900 GeV pp data. The black points are the 900 GeV uncorrected spectrum while the red points are the PHYTIA uncorrected spectrum and the blue points the Phojet uncorrected spectrum.

In order to obtain the corrected spectra dedicated simulations produced using PYTHIA and Phojet as event generators were analyzed. The spectra corrected using the PYTHIA anchor runs simulations are shown in Figures 5.12 and 5.14, while those corrected with PHOJET are shown in the Figures 5.13 and 5.15. As a comparison, in each graph, also the model generated distribution is shown.

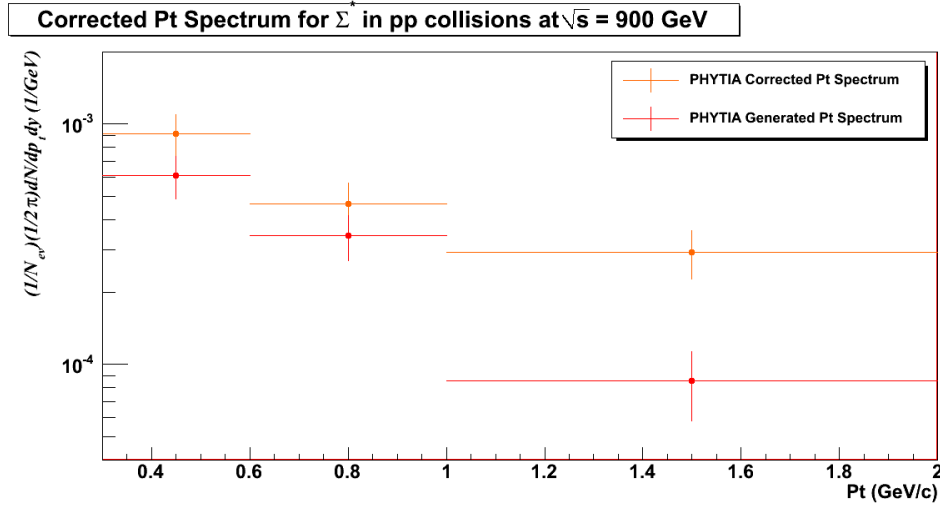


Figure 5.12: Corrected transverse momentum distribution for 900 GeV pp data obtained with the PYTHIA anchor runs simulations. The orange points are the corrected spectrum while the red points are the PYTHIA generated spectrum.

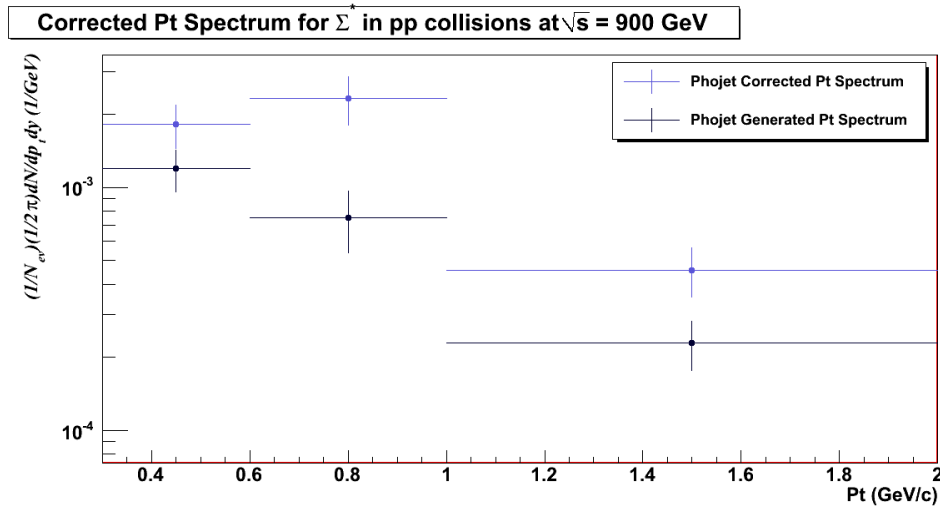


Figure 5.13: Corrected transverse momentum distribution for 900 GeV pp data obtained with the PHOJET anchor runs simulations. The blue points are the corrected spectrum while the dark blue points the are Phojet generated spectrum.

Both the generators underestimate the data as expected[153, 156] and need to be better tuned but proved to be useful for the efficiencies evaluations.

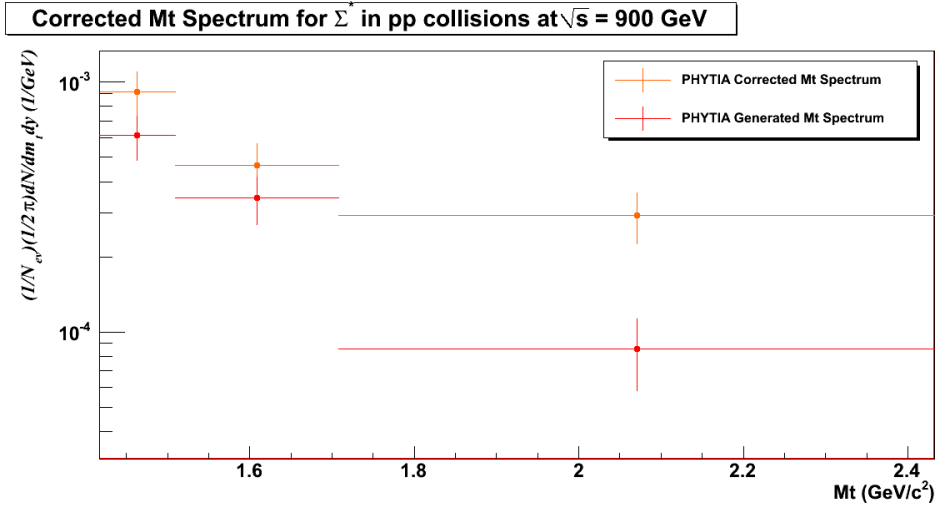


Figure 5.14: Corrected transverse mass distribution for 900 GeV pp data obtained with the PHYTHIA anchor runs simulations. The orange points are the corrected spectrum while the red points are the PHYTHIA generated spectrum.

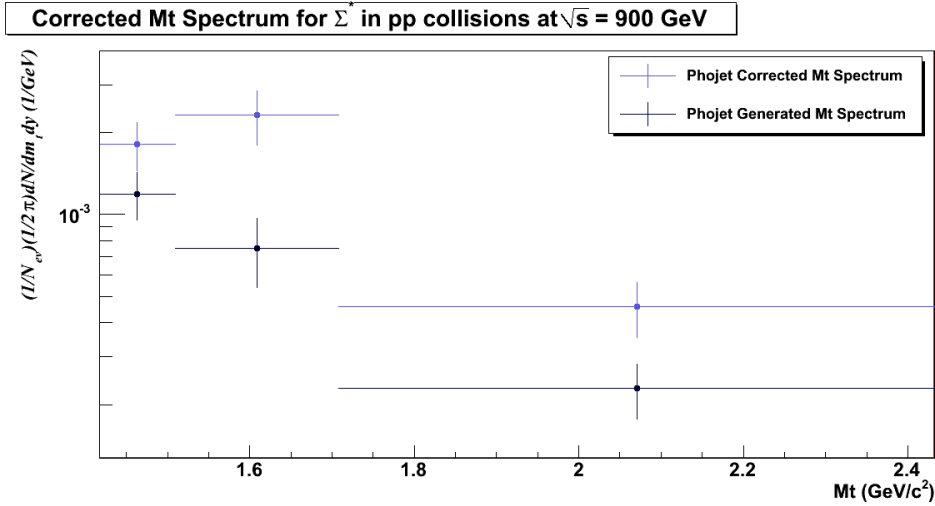


Figure 5.15: Corrected transverse mass distribution for 900 GeV pp data obtained with the PHOJET anchor runs simulations. The blue points are the corrected spectrum while the dark blue points are the Phojet generated spectrum.

Since, at the moment, there are no strong reasons to prefer one of the two generators, we decided, in a very preliminary way, to take, as efficiency correction factor, the mean value between the two generators. In Figures 5.16 and 5.17, the p_t and the m_t spectra corrected as just mentioned. The half difference between the PHYTHIA and Phojet correction factors is taken as systematic errors associated to the models.

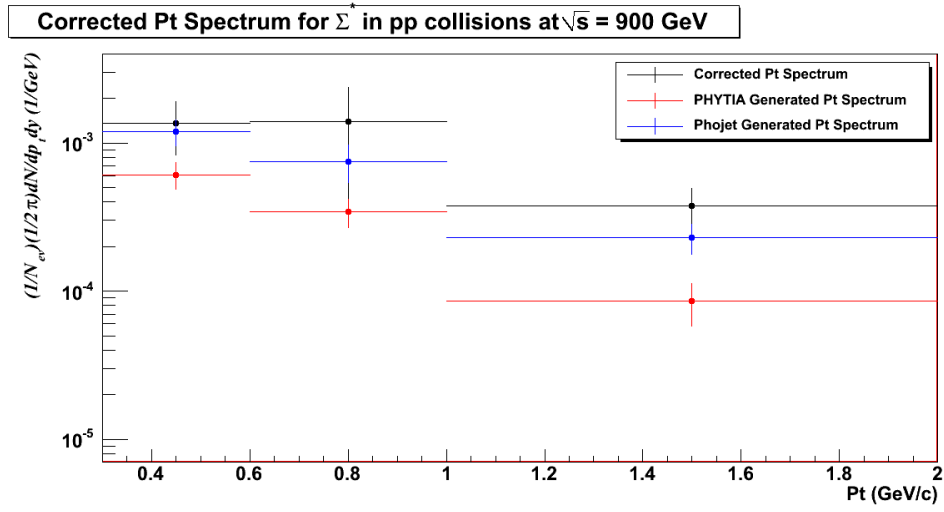


Figure 5.16: Transverse momentum distribution for 900 GeV pp data corrected taken, as efficiency correction factor, the mean value between the two generators. The black points are the corrected spectrum, the red points are the PHYTIA generated spectrum while the blue points are the Phojet generated spectrum.

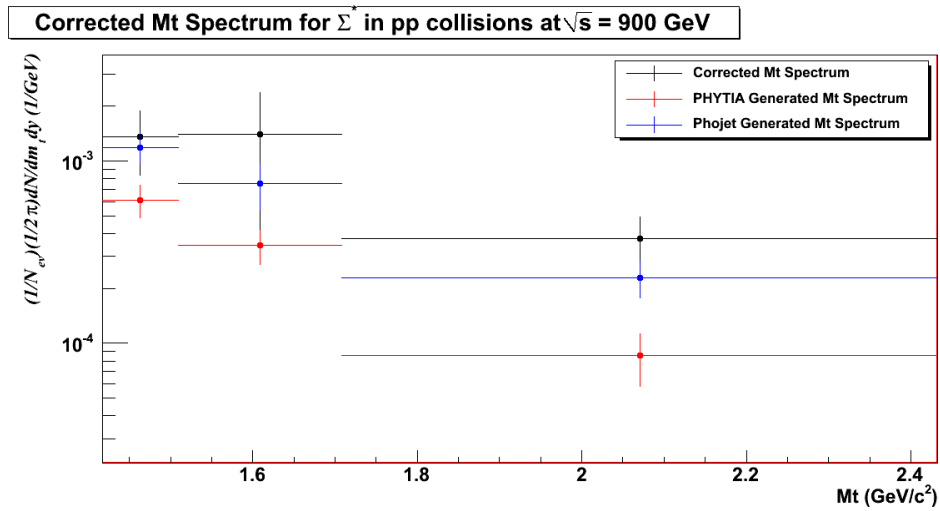


Figure 5.17: Transverse mass distribution for 900 GeV pp data corrected taken, as efficiency correction factor, the mean value between the two generators. The black points are the corrected spectrum, the red points are the PHYTIA generated spectrum while the blue points are the Phojet generated spectrum.

The corrected distribution was fitted both with an exponential and with a Levy-Tsallis distribution as explained in the previous chapter. The results are shown in Figures 5.18, 5.19, 5.20, 5.21, 5.22, 5.23 and summarized in Table 5.3 for what concern the spectrum corrected using the mean of the two generators.

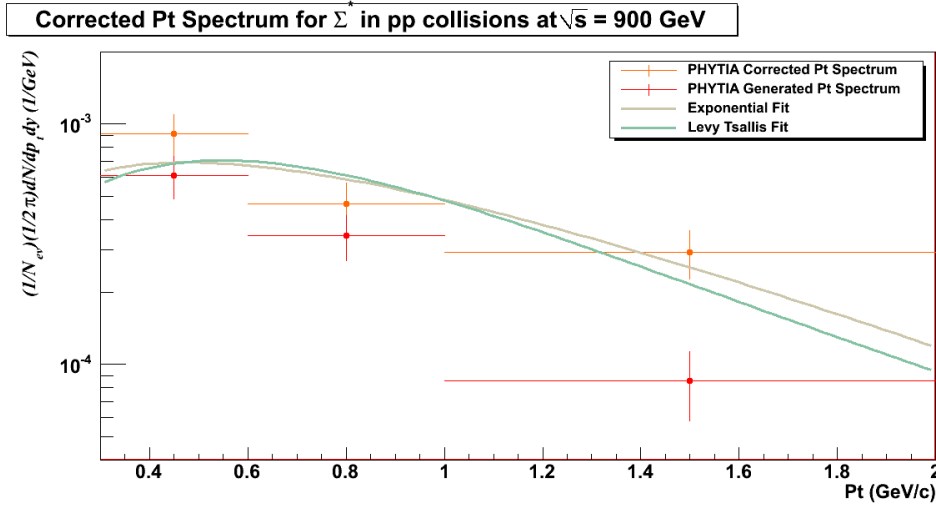


Figure 5.18: Corrected transverse momentum distribution for 900 GeV pp data obtained with the PYTHIA anchor runs simulations fitted with an exponential and a Levy-Tsallis distribution. The orange points are the corrected spectrum while the red points are the PYTHIA generated spectrum.

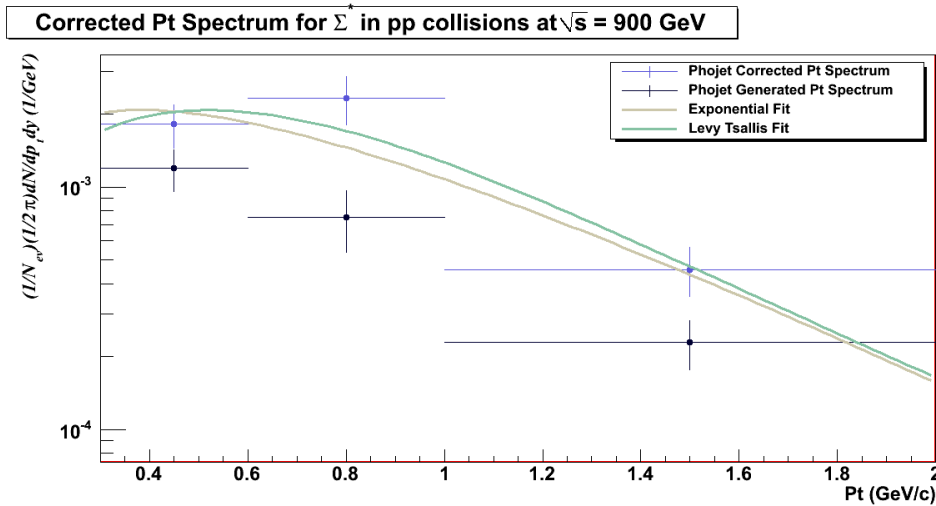


Figure 5.19: Corrected transverse momentum distribution for 900 GeV pp data obtained with the PHOJET anchor runs simulations fitted with an exponential and a Levy-Tsallis distribution. The blue points are the corrected spectrum while the dark blue points are the Phojet generated spectrum.

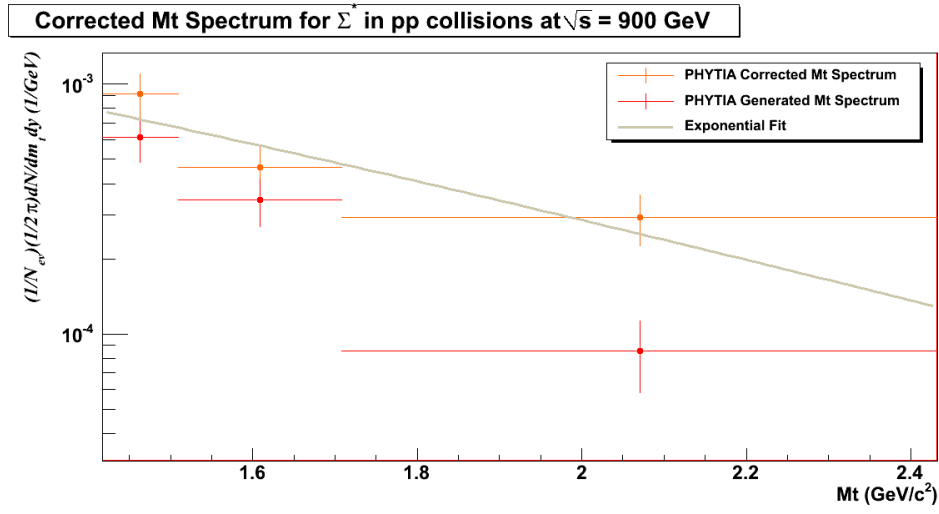


Figure 5.20: Corrected transverse mass distribution for 900 GeV pp data obtained with the PYTHIA anchor runs simulations fitted with an exponential distribution. The orange points are the corrected spectrum while the red points are the PYTHIA generated spectrum.

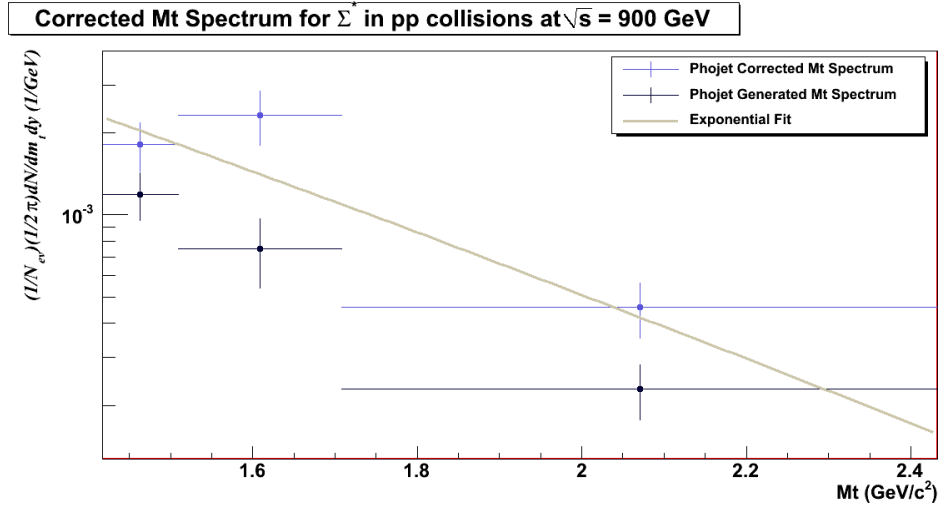


Figure 5.21: Corrected transverse mass distribution for 900 GeV pp data obtained with the PHOJET anchor runs simulations fitted with an exponential distribution. The blue points are the corrected spectrum while the dark blue points the Phojet generated spectrum.

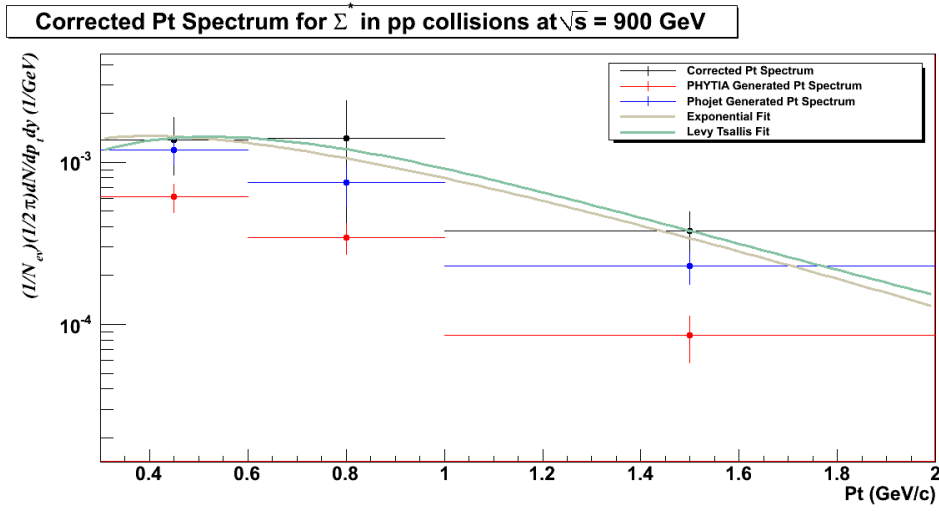


Figure 5.22: Transverse momentum distribution for 900 GeV pp data corrected taken, as efficiency correction factor, the mean value between the two generators and fitted with an exponential and a Levy-Tsallis distribution. The black points are the corrected spectrum, the red points are the PHYTIA generated spectrum while the blue points are the Phojet generated spectrum.

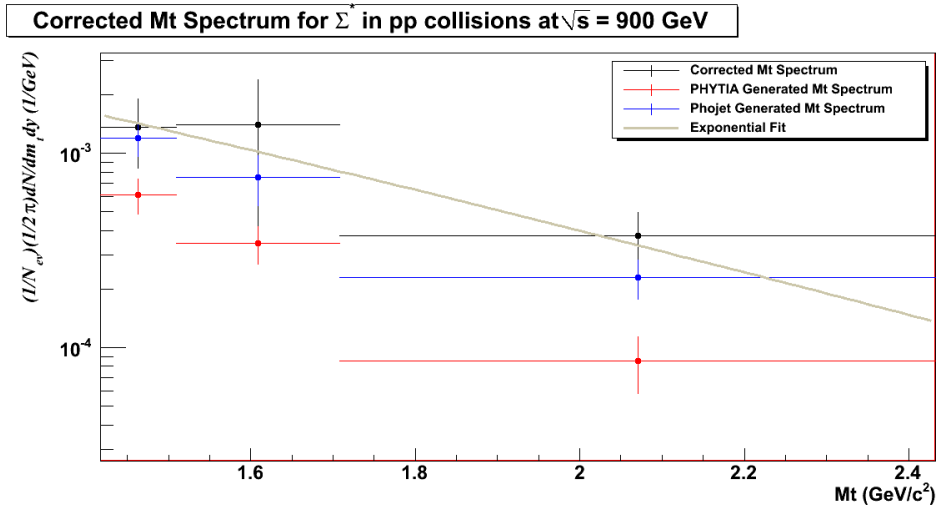


Figure 5.23: Transverse mass distribution for 900 GeV pp data corrected taken, as efficiency correction factor, the mean value between the two generators and fitted with an exponential distribution. The black points are the corrected spectrum, the red points are the PHYTIA generated spectrum while the blue points are the Phojet generated spectrum.

Spectrum	Exponential Fit		Levy-Tsallis Fit		
	$\langle p_t \rangle$ (GeV/c)	T (MeV)	$\langle p_t \rangle$ (GeV/c)	T (MeV)	n
p_t	0.793 ± 0.166	396 ± 83	0.891 ± 0.134	165 ± 36	5.53 ± 3.74
m_t	–	348 ± 110	–	–	–

Table 5.3: Temperature T, $\langle p_t \rangle$ and yield obtained from the exponential and Levy-Tsallis fits of the p_t spectrum and from the Exponential fit of the m_t spectrum, both for the PYTHIA and the Phojet corrected spectra.

As evident from the figures both the exponential and the Levy distribution are able to fit the graphs and the results they provide are quite in agreement.

This results can be roughly compared with those obtained by the STAR collaboration (see Table 3.3) in pp collisions at $\sqrt{s} = 200$ GeV. Within the errors they are compatible both for the $\langle p_t \rangle$ and temperature T values.

Finally in the Figures 5.24 and 5.25 the ratio between data and the simulations provided with PYTHIA and Phojet and the reconstruction the efficiency as function of the transverse momentum are shown respectively.

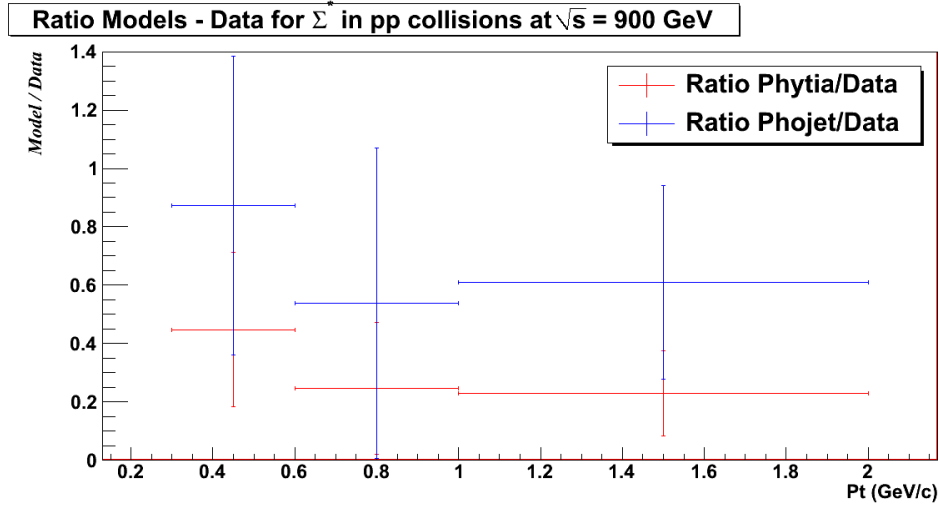


Figure 5.24: Ratio between the PYTHIA (Phojet) generated yields and the yield reconstructed from data.

As evident form the graphs, even if the error bars are quite big, both the generators underestimate quite significantly the Σ^* production.

The efficiency corrections also in this are obtained by analyzing Monte Carlo (MC) events in exactly the same way as for the real events. A dependence is found on the generators used (PYTHIA and Phojet). Therefore the corrections presented here are obtained taking the mean value of the two generators corrections and taking into ac-

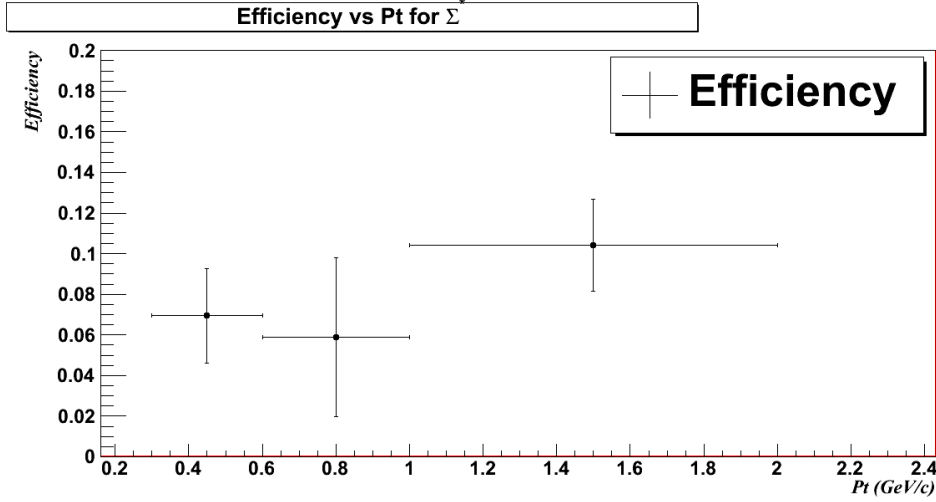


Figure 5.25: Reconstruction efficiency as function of the transverse momentum. It is evaluated using both PYTHIA and Phojet, taking, as efficiency correction factor, the mean value of the two generators corrections. The associated uncertainty is evaluated taking the half-difference of the values provided by the two generators.

count, as systematic uncertainties, the half-difference of the values provided by the two generators. As evident from the figure, the efficiency is very limited, especially at low p_t , because of the acceptance of the detector.

5.1.6 Signal Significance

In Table 5.4 the significances for the extracted signal obtained for the differential and integral analyses of 900 GeV data, are summarized. The errors take into account both the statistical and the systematic component.

Table 5.4: Significances of the extracted $\Sigma^{*+} + \overline{\Sigma}^{*+}$ (integral distribution) and $\Sigma^{*+} + \overline{\Sigma}^{*+} + \Sigma^{*-} + \overline{\Sigma}^{*-}$ (differential transverse momentum distribution) signal for 900 GeV pp data, $3.3 \cdot 10^6$ events).

p_t range (GeV/c)	900 GeV Data Significances
Integral	12.5 ± 3.1
0.3 - 0.6	15.0 ± 3.0
0.6 - 1.0	9.6 ± 2.5
1.0 - 2.0	6.4 ± 1.9

5.1.7 Dependence of mass and width from p_t

In Figures 5.26 and 5.27 the transverse momentum dependence of Σ^* mass and width is shown.

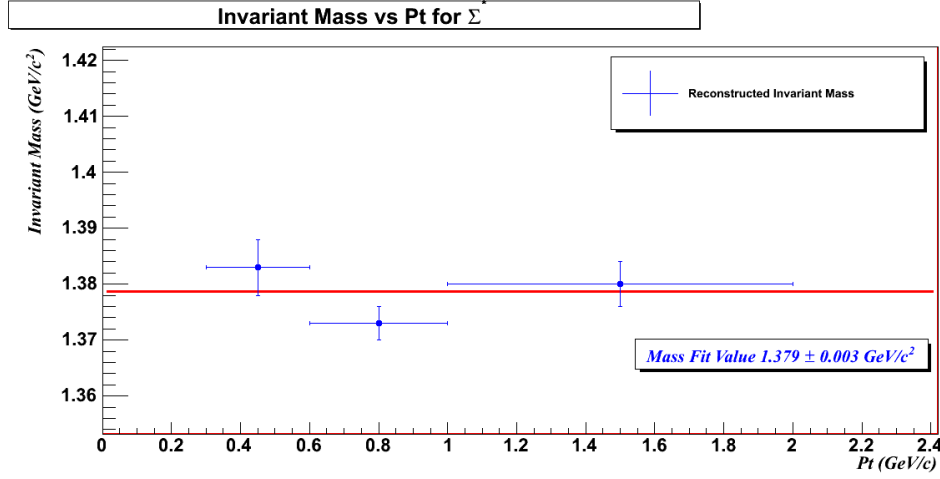


Figure 5.26: $\Sigma^{*+} + \overline{\Sigma}^{*+}$ p_t mass dependence in 900 GeV pp data.

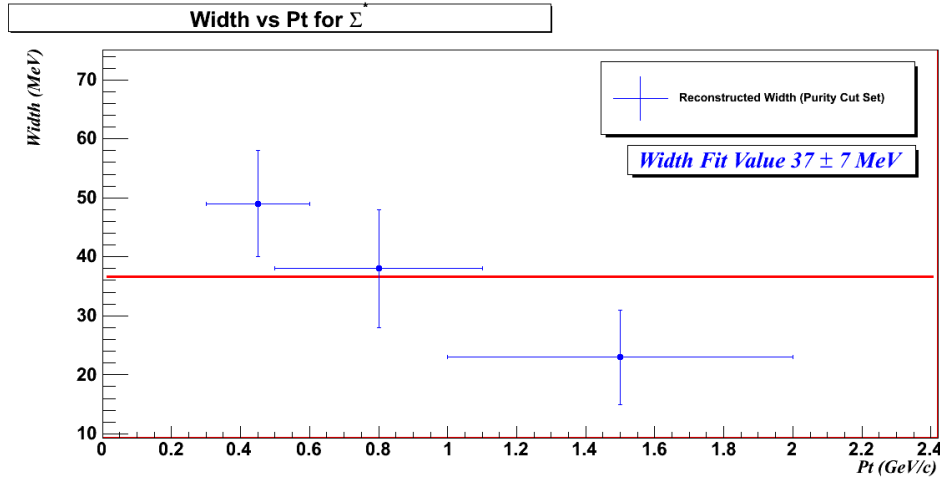


Figure 5.27: $\Sigma^{*+} + \overline{\Sigma}^{*+}$ p_t width dependence in 900 GeV pp data.

As it can be seen from the figures the values are compatible with the PDG values although with sizable errors. Due to the very poor sample in terms of available p_t bins and to the not small error bars, it is not possible to determine a possible mass or width p_t dependence.

5.2 7 TeV Data Analysis Description

The 7 TeV data analyzed here were collected by the ALICE experiment during May 2010. The 7 TeV statistics collected is adequate to perform a more complete differential analysis, at least in terms of p_t .

5.2.1 Invariant Mass Distribution

In Figure 5.28 the $\Lambda\pi$ ¹⁸ invariant mass distribution without applying any cut is shown. In Figure 5.29 instead the Σ^* invariant mass distribution after the application of the “efficiency oriented” cuts set previously described for the 10 TeV simulations is shown (left graphs).

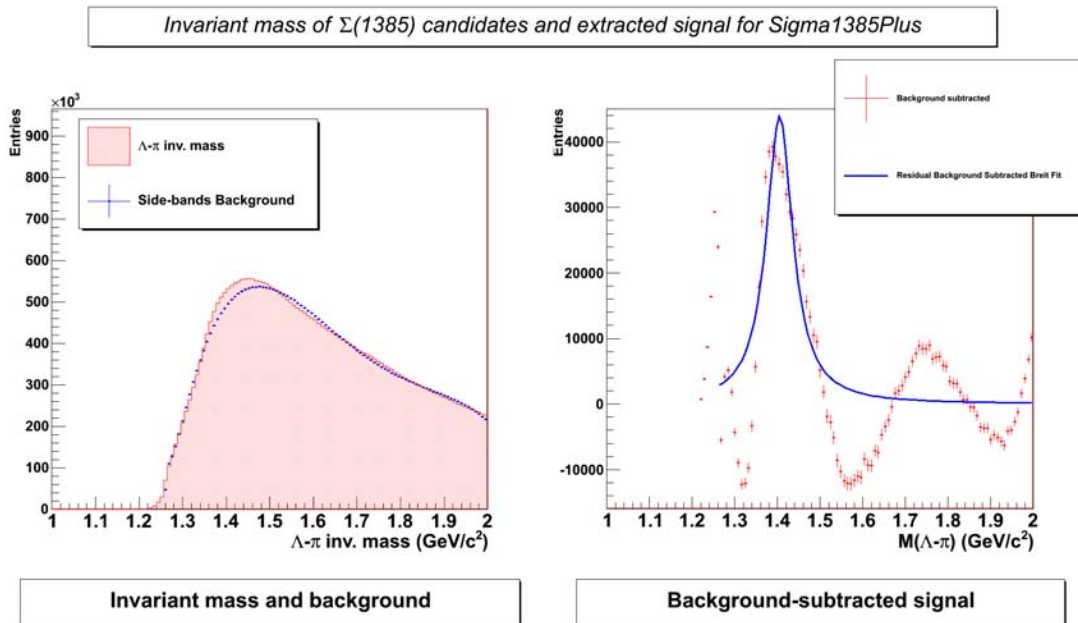


Figure 5.28: Σ^* 's invariant mass distribution and signal background subtracted before applying the quality cuts in pp data at $\sqrt{s} = 7$ TeV.

5.2.2 Signal Extraction

In order to define the background and to extract the signal, the “Side-Bands” technique was applied. The signal was fitted with a Breit-Wigner function and the results are shown in Figure 5.28 and 5.29 before and after the application of the “efficiency oriented” cuts set (right graphs).

The 7 TeV data analysis confirms that the “purity oriented” set of cuts allows to obtain a signal sample quite pure but losing a non negligible efficiency (see Table 5.5) while the “efficiency oriented” allows to recover efficiency even losing a bit of purity in

¹⁸In all the following figures only the result for the Σ^{*+} are shown, but the result for the Σ^{*-} and their antiparticles are similar.

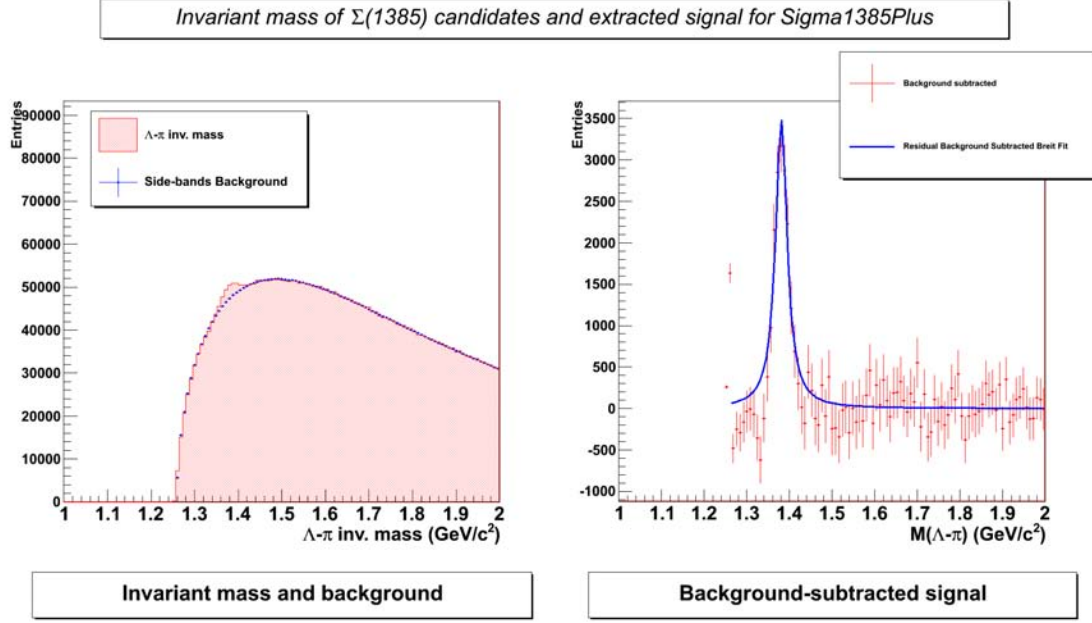


Figure 5.29: Σ^* 's invariant mass distribution and signal background subtracted after applying the “efficiency oriented” quality cuts in pp data at $\sqrt{s} = 7$ TeV.

the fit results. These numbers are obtained using a subsample of the 7 TeV available statistic (12 million of events).

Cut	Cut Type	Mass (GeV/c ²)	Γ (MeV)	χ^2/N_{dof}	Yield	Significance
0	No Cuts	1.402 ± 0.001	71 ± 2	47.6	110394 ± 1716	86.5 ± 1.3
1	Λ Daugh TPC refit	1.402 ± 0.001	68 ± 2	47.6	110394 ± 1716	86.5 ± 1.3
2	1 + Λ Daugh TPC cls > 70	1.404 ± 0.001	70 ± 2	40.6	89328 ± 1580	76.8 ± 1.3
3	2 + $\chi^2/(\# \text{ TPC clusters}) < 4$	1.404 ± 0.001	70 ± 2	40	88847 ± 1578	76.5 ± 1.3
4	3 + $1.110 < M_\Lambda < 1.122$ GeV	1.383 ± 0.001	37 ± 4	8.5	15552 ± 816	24.4 ± 1.2
5	4 + Fid Reg < 0.05 cm ²	1.385 ± 0.002	42 ± 5	2.1	8781 ± 575	19.3 ± 1.2
6	5 + Λ CosPointAng > 0.99	1.386 ± 0.002	38 ± 5	2.1	7550 ± 559	17.2 ± 1.2
7	6 + Λ Daugh DCA < 0.2 cm	1.385 ± 0.001	38 ± 5	2.1	6720 ± 521	16.4 ± 1.2
8	7 + Λ DCA < 0.4, π DCA < 0.1 cm	1.385 ± 0.002	36 ± 5	1.97	5775 ± 504	14.6 ± 1.2
9	8 + $\Lambda - \pi$ DCA < 0.2 cm	1.384 ± 0.002	35 ± 6	2.01	5564 ± 501	14.1 ± 1.2

Table 5.5: Σ^{*+} results obtained with the “purity oriented” cuts set tried to improve the signal extraction.

The results obtained, in terms of mass and width, are in agreement with the PDG values. The errors associated to the fit results take into account only the statistical component. The systematic one will be evaluated later.

Cut	Cut Type	Mass (GeV/c ²)	Γ (MeV)	χ^2/N_{dof}	Yield	Significance
8a	7 No Fid Reg + Λ DCA < 0.3, π DCA < 0.05 cm	1.381 ± 0.002	34 ± 4	4.2	9614 ± 614	19.8 ± 1.2

Table 5.6: Σ^{*+} results obtained with the “efficiency oriented” cuts set tried to improve the signal extraction.

5.2.3 Kinematical Cuts

Some simulation as anchor runs for the 7 TeV data were provided and then studied in order to extract a set of kinematical cuts. In Figures 5.30 and 5.31 it is possible to see the Σ^* daughters cosine of the opening angle distributions for the signal and the background respectively in the 7 TeV simulations.

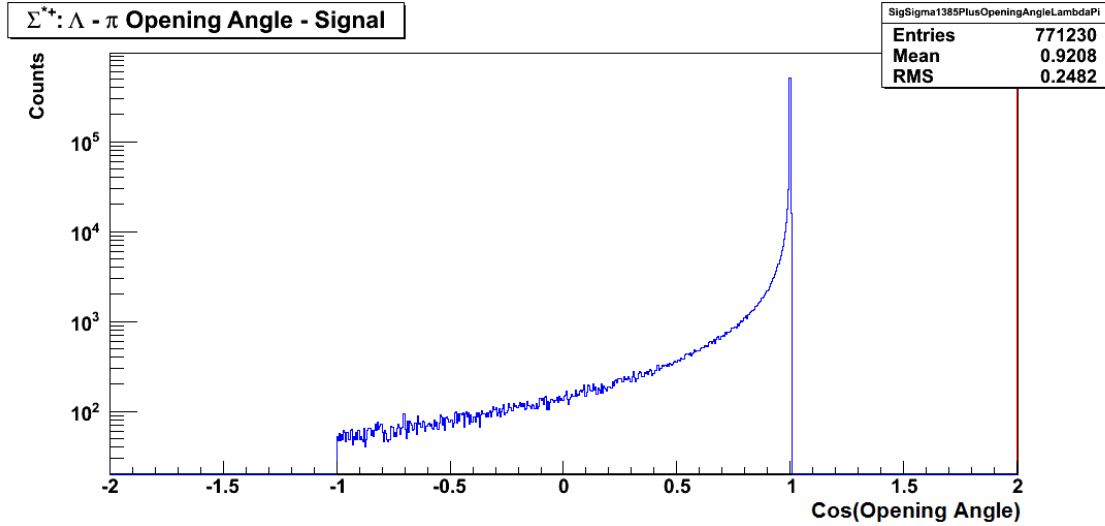


Figure 5.30: Σ^* daughters cosine of the opening angle distribution for the signal in pp simulations at $\sqrt{s} = 7$ TeV.

In Figures 5.32 and 5.33 it is possible to see the Λ 's momentum vs π 's momentum distributions for the signal and the background respectively in the 7 TeV simulations.

In Figures 5.34 and 5.35 it is possible to see the Σ^* daughters cosine of the opening angle vs Σ^* momentum distributions for the signal and the background respectively in the 7 TeV simulations.

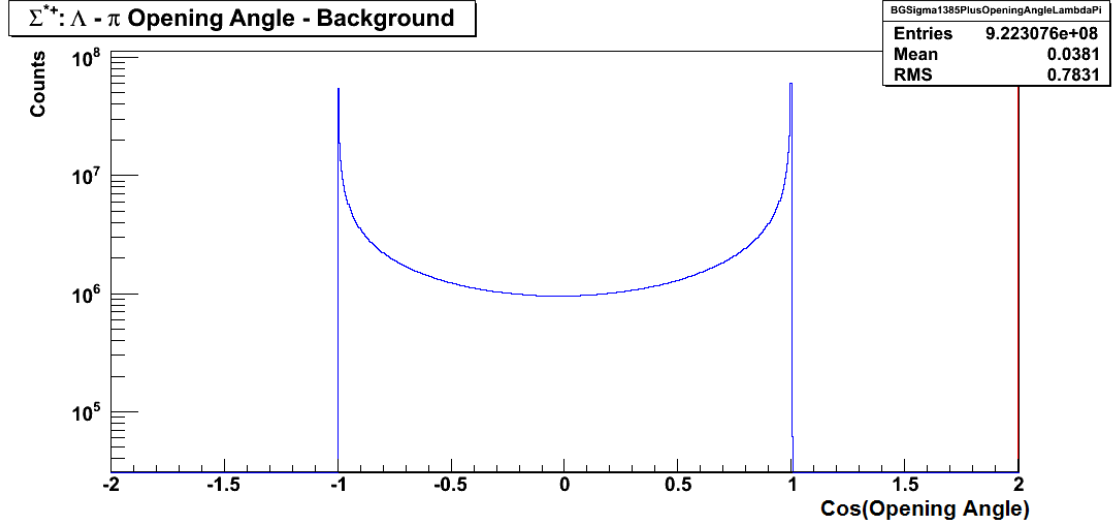


Figure 5.31: Σ^* daughters cosine of the opening angle distribution for the background in pp simulations at $\sqrt{s} = 7$ TeV.

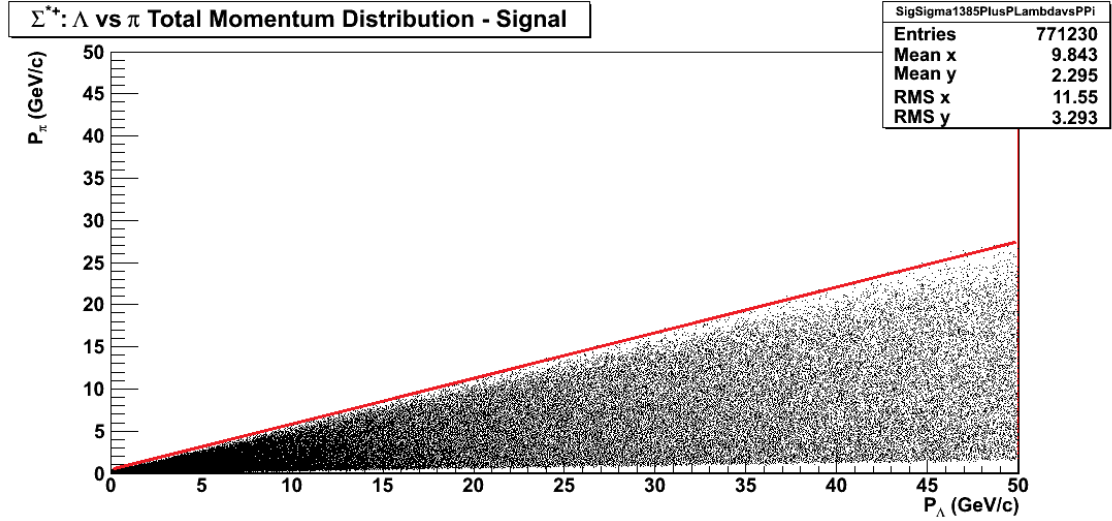


Figure 5.32: Λ 's momentum vs π 's momentum distribution for the signal in pp simulations at $\sqrt{s} = 7$ TeV. The red line represents the parameterization of the *exclusion area*.

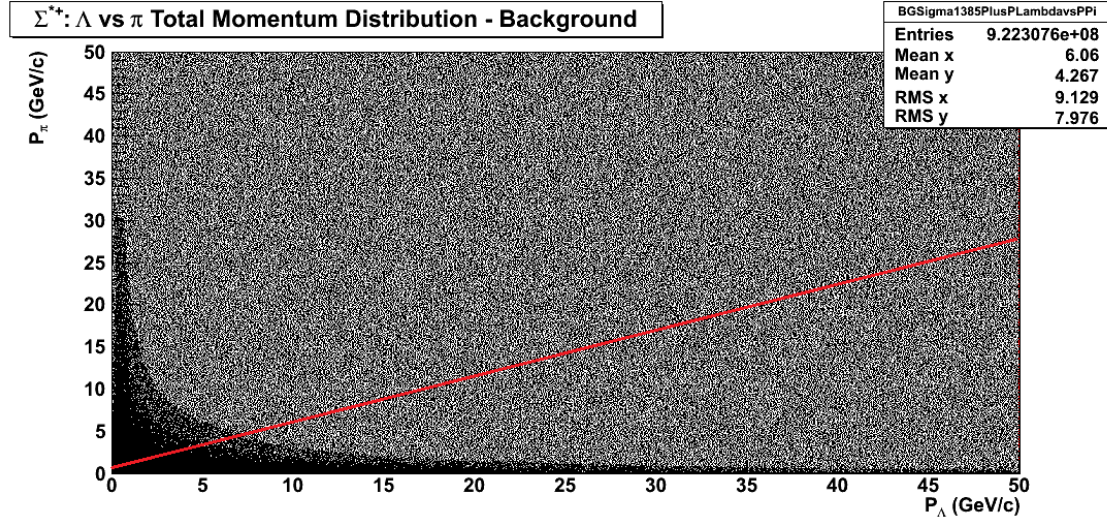


Figure 5.33: Λ 's momentum vs π 's momentum distribution for the background in pp simulations at $\sqrt{s} = 7$ TeV. The red line represents the parameterization of the *exclusion area*.

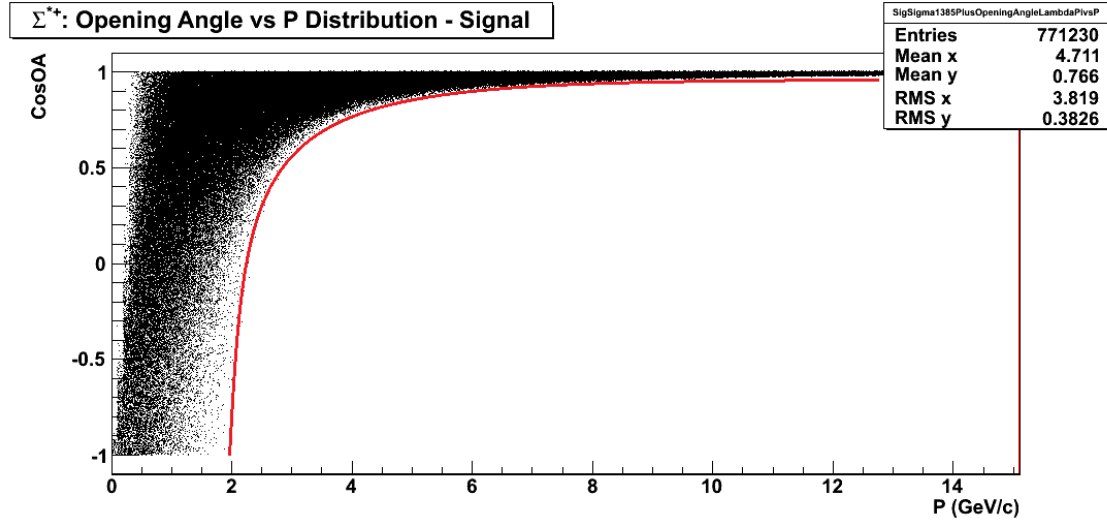


Figure 5.34: Σ^* daughters cosine of the opening angle vs Σ^* momentum distribution for the signal in pp simulations at $\sqrt{s} = 7$ TeV. The red line represents the parameterization of the *exclusion area*.

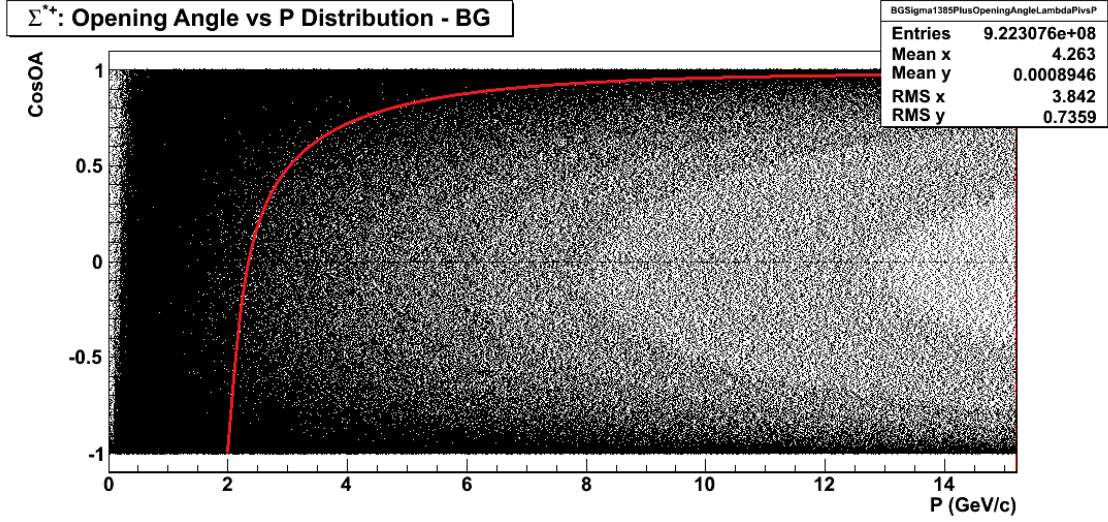


Figure 5.35: Σ^* daughters cosine of the opening angle vs Σ^* momentum distribution for the signal in pp simulations at $\sqrt{s} = 7$ TeV. The red line represents the parameterization of the *exclusion area*.

As already seen studying the trend in the 10 TeV simulations, a quite good separation from the signal behaviour to the background behaviour is evident, so it is possible to try to parameterize an *exclusion area* in which the signal is not present and use this information to clean the sample under analysis. This was done trying to find the best function which follows the signal border line.

So based on these results, the cuts I applied, are:

- A. $p_\pi/p_\Lambda < (0.545 + 0.350/p_\Lambda)$
- B. Opening Angle $< \text{ArcCos} \left(1 - \frac{2}{p_{\Sigma^*}^{1.74-2.16}} \right)$

for the proton-proton simulation at $\sqrt{s} = 7$ TeV.

The Figures 5.36, 5.37 and 5.38 show the Σ^* invariant mass distribution after the application of the kinematical cuts.

As it is possible to see from the figures and from the Table 5.7, and as already noticed in the simulations, only the second kinematical cut improves significantly the results with respect to those obtained without any kinematical cuts applied (taking into account all the 4 Σ^* particles involved in the analysis) and so only this one could possibly be used.

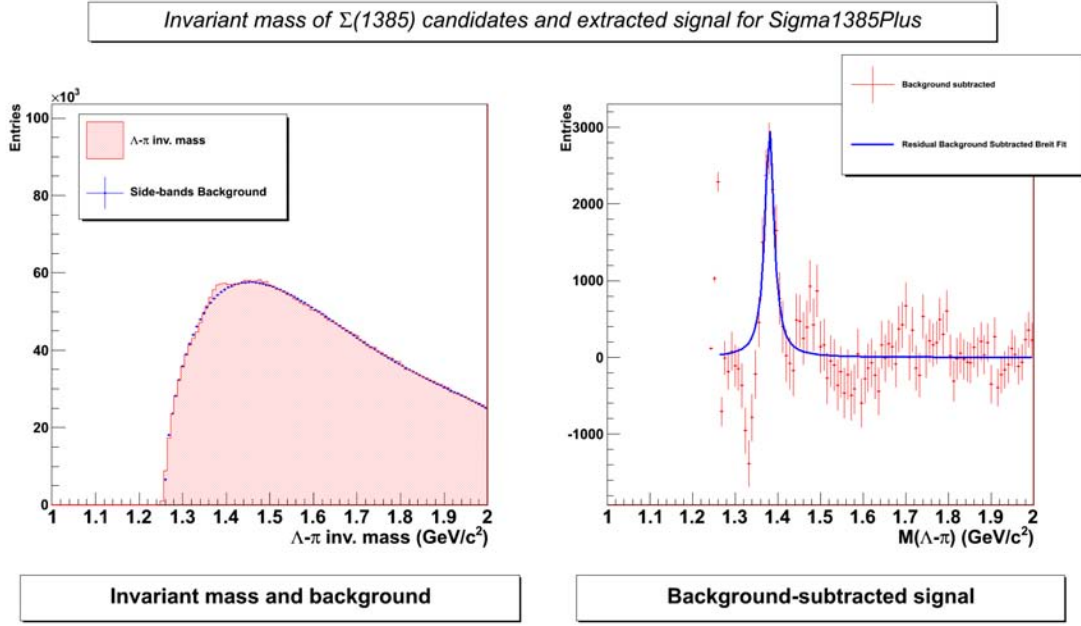


Figure 5.36: Σ^* 's invariant mass distribution after applying the the Λ 's momentum vs π 's momentum cut in pp data at $\sqrt{s} = 7$ TeV.

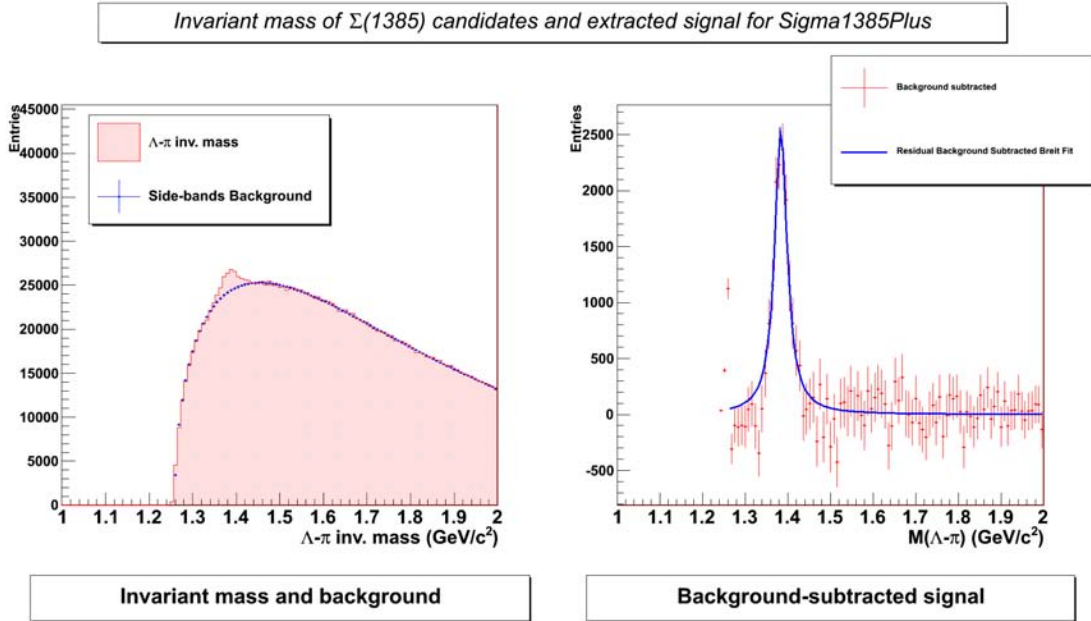


Figure 5.37: Σ^* 's invariant mass distribution after applying the the Σ^* daughters cosine of the opening angle vs Σ^* momentum cut in pp data at $\sqrt{s} = 7$ TeV.

5.2.4 Global Results

The Table 5.8 summarizes the results, obtained with the “purity oriented” set of cuts for all the particles involved in the analysis, and provided with 30 million of events collected at $\sqrt{s} = 7$ TeV.

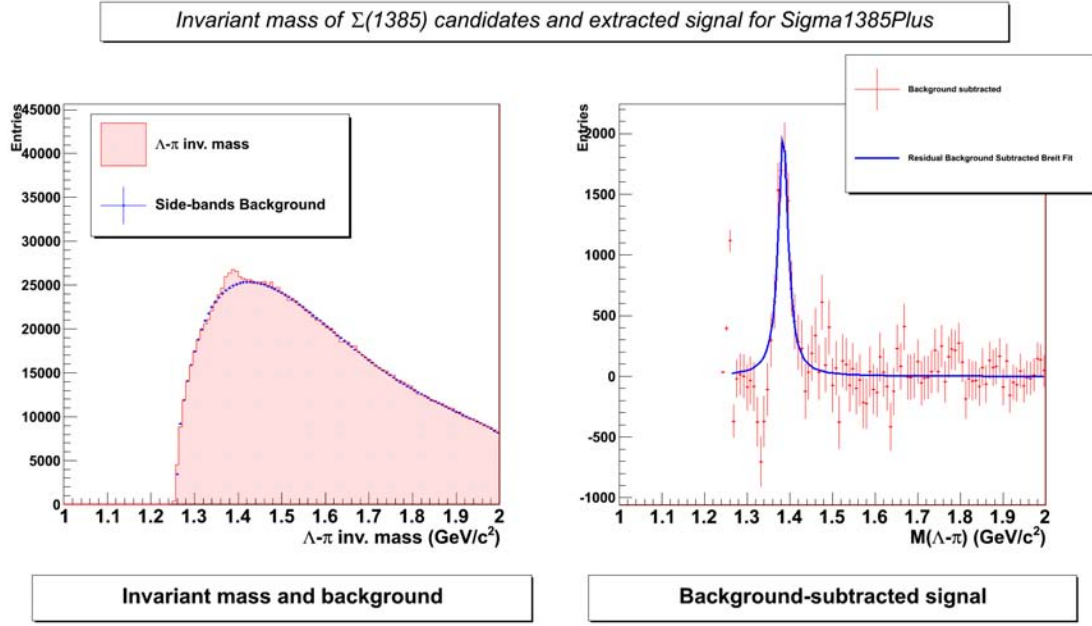


Figure 5.38: Σ^* 's invariant mass distribution after applying both the kinematical cuts previously described in pp data at $\sqrt{s} = 7$ TeV.

Cut	Cut Type	Mass (GeV/c ²)	Γ (MeV)	χ^2/N_{dof}	Yield	$S/\sqrt{S+B}$
8	Quality Cuts + A.	1.391 ± 0.003	27 ± 6	2.1	3633 ± 517	9.2 ± 1.3
9	Quality Cuts + B.	1.387 ± 0.003	36 ± 5	1.4	4420 ± 349	16.1 ± 1.2
10	Quality Cuts + A. + B.	1.388 ± 0.002	34 ± 7	1.5	2441 ± 343	9.0 ± 1.2

Table 5.7: Results obtained adding the kinematical cuts described in the text in order to improve the signal extraction.

The results obtained are in quite good agreement with the PDG values, and a behaviour already seen in the simulation in here reproduced i.e. due to the pp initial state more particle than antiparticle are produced and, among particle, more Σ^{*+} than Σ^{*-} are produced in the collisions.

The Table 5.9 summarizes the results, obtained with the “efficiency oriented” set of cuts for all the particles involved in the analysis.

Again for the following differential analysis the “efficiency oriented” cut set was chosen.

5.2.5 Systematic uncertainties evaluation at $\sqrt{s} = 7$ TeV

The systematic contribution to the errors associated to the fit results was evaluated varying the values of the cuts applied within a reasonable range. In particular the contribution of the systematics components can be summarized as follows:

Particle	Mass (GeV/c ²)	Γ (MeV)	χ^2/N_{dof}	Yield	Significance
Σ^-	1.388 ± 0.002	37 ± 3	1.7	10865 ± 576	23.9 ± 1.2
Σ^+	1.384 ± 0.001	36 ± 3	1.9	12247 ± 583	26.6 ± 1.2
$\overline{\Sigma}^-$	1.385 ± 0.002	37 ± 4	1.8	9963 ± 566	22.2 ± 1.2
$\overline{\Sigma}^+$	1.383 ± 0.002	34 ± 3	1.8	9983 ± 564	22.5 ± 1.2

Table 5.8: All Σ^* species results obtained with the “purity oriented” cut set.

Particle	Mass (GeV/c ²)	Γ (MeV)	χ^2/N_{dof}	Yield	Significance
Σ^-	1.385 ± 0.001	28 ± 3	8.3	18203 ± 979	23.4 ± 1.3
Σ^+	1.379 ± 0.001	33 ± 2	8.8	23197 ± 971	30.0 ± 1.2
$\overline{\Sigma}^-$	1.381 ± 0.001	33 ± 3	8.3	19390 ± 952	30.0 ± 1.2
$\overline{\Sigma}^+$	1.380 ± 0.001	33 ± 2	8.2	23725 ± 940	31.7 ± 1.2

Table 5.9: All Σ^* species results obtained with the “efficiency oriented” cut set.

For the “purity oriented” set:

- Degree of the polynomial fitting function: 0 GeV/c² for mass value, 3 MeV for width value, 11.8% for yield value.
- Width of the “exclusion region”: 0 GeV/c² for mass value, 1 MeV for width value, 2.9% for yield value.
- Quality cuts: 0.5 GeV/c² for mass value, 0.5 MeV for width value, 24.2% for yield value.
- Kinematical cuts: 1 GeV/c² for mass value, 2.5 MeV for width value, 18.8% for yield value.
- **Total:** 1.1 GeV/c² for mass value, 4 MeV for width value, 33.0% for yield value.

For the “efficiency oriented” set:

- Degree of the polynomial fitting function: 0.5 GeV/c² for mass value, 4.5 MeV for width value, 18.7% for yield value.
- Width of the “exclusion region”: 0 GeV/c² for mass value, 2 MeV for width value, 8.9% for yield value.
- Quality cuts: 0.5 GeV/c² for mass value, 2.5 MeV for width value, 2.6% for yield value.
- **Total:** 0.7 GeV/c² for mass value, 5.5 MeV for width value, 21.0% for yield value.

In both cases the systematic component dominates on the statistic one, in particular for what concern the extracted yield, and so, on the spectra. This effect, as previously seen analyzing the 10 TeV simulations, is more evident for the “purity oriented” cut set that even if able to provide a more pure sample it is, at the same time, more sensible to small changes in the analysis conditions. The “efficiency oriented” set will be used for following differential analysis.

5.2.6 Transverse momentum and mass spectrum

In Figures 5.58 and 5.59 (see the end of this chapter) the results obtained dividing the dynamical range in seven p_t bins and extracting the signal from all of them following the previously described procedure and applying the “efficiency oriented” set of cuts are shown. In each graph the red histogram is the signal after the background subtraction fitted with a Breit-Wigner distribution (the blue curve). A quite good signal is extracted from each chosen bins. The uncorrected transverse momentum and the transverse mass spectra are shown in Figures 5.39 and 5.40. In each graph the black dots represents the uncorrected spectrum extracted from the data while the red and the blue dots are the spectra extracted analyzing the anchor runs produced in order to extract the efficiency correction factor with PYTHIA and Phojet respectively. In order to increase the statistic Σ^{*+} and $\bar{\Sigma}^{*+}$ are put together.

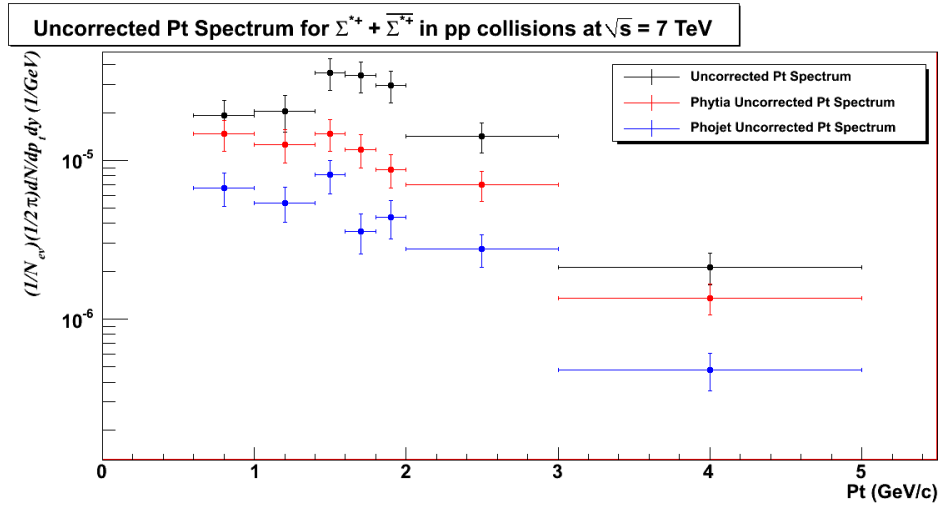


Figure 5.39: Uncorrected transverse momentum distribution for 7 TeV pp data. The black dots represents the spectrum extracted from the data, the red and the blue dots are the spectra extracted from the anchor runs with PYTHIA and Phojet respectively.

Finally the corrected spectra are shown in Figures 5.41, 5.42, 5.43, 5.44.

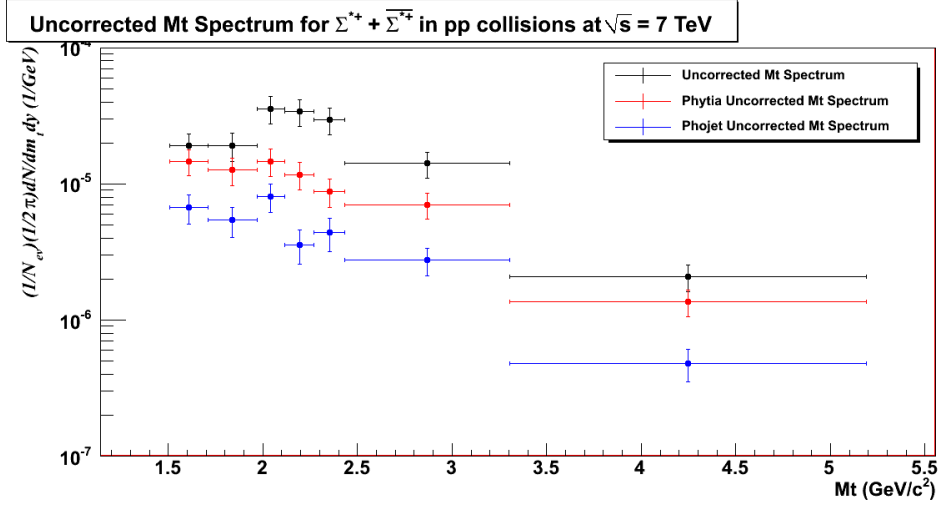


Figure 5.40: Uncorrected transverse mass distribution for 7 TeV pp data. The black dots represents the spectrum extracted from the data, the red and the blue dots are the spectra extracted from the anchor runs with PYTHIA and Phojet respectively.

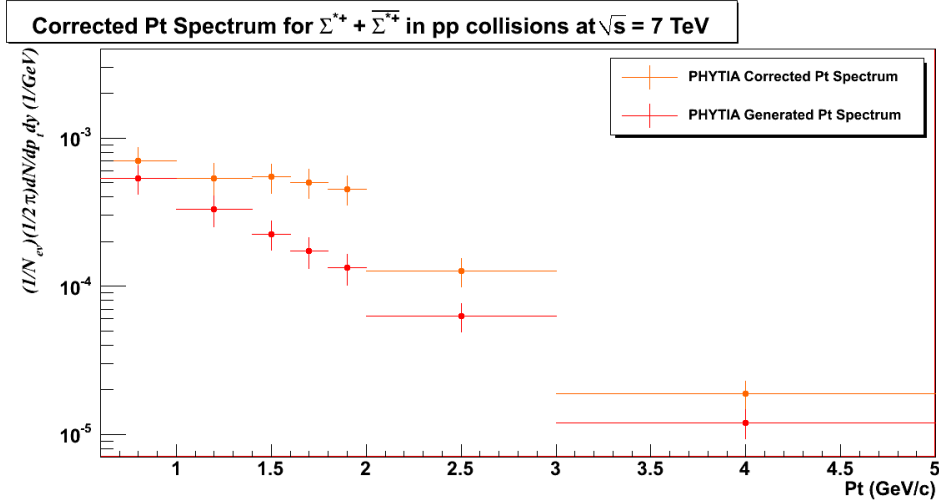


Figure 5.41: Corrected transverse momentum distribution for 7 TeV pp data. The orange dots represents the spectrum extracted form the data corrected with the PYTHIA anchor runs, while the red dots are the PYTHIA generated spectrum.

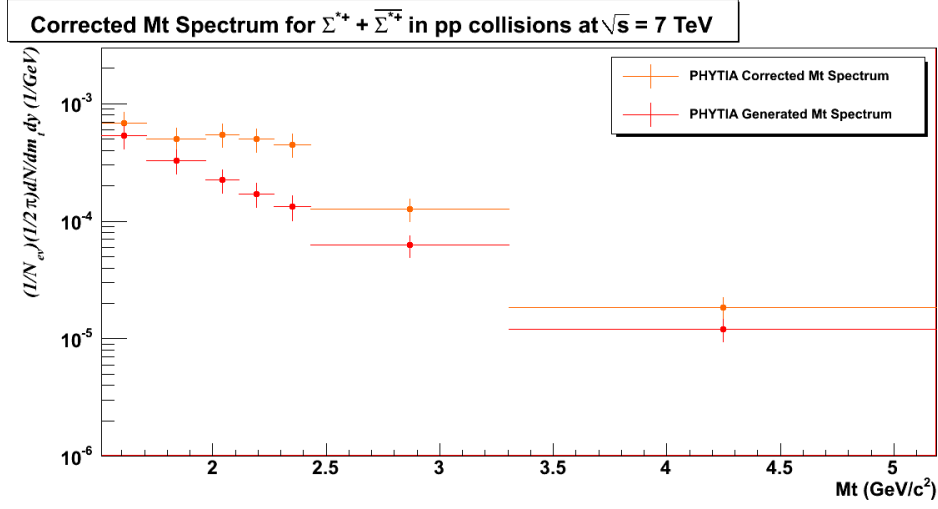


Figure 5.42: Corrected transverse mass distribution for 7 TeV pp data. The orange dots represents the spectrum extracted from the data corrected with the PYTHIA anchor runs, while the red dots are the PYTHIA generated spectrum.

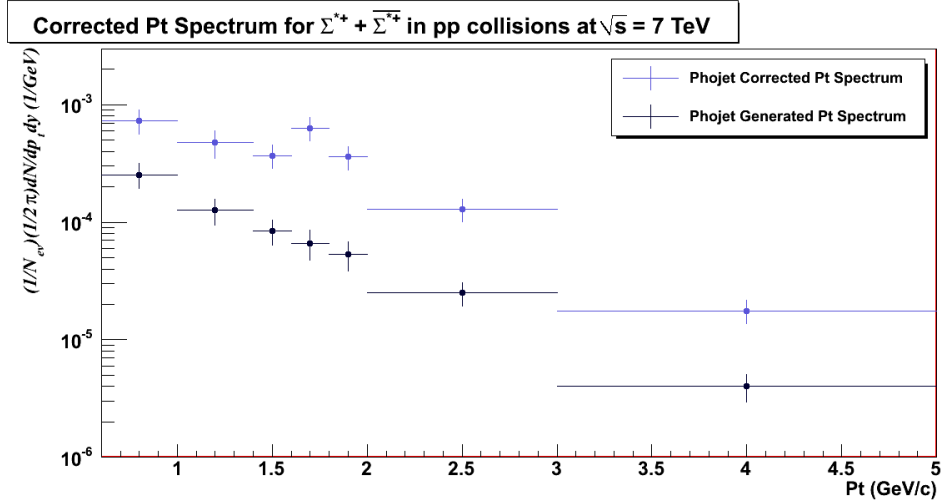


Figure 5.43: Corrected transverse momentum distribution for 7 TeV pp data. The blue dots represents the spectrum extracted from the data corrected with the Phojet anchor runs, while the dark blue dots are the Phojet generated spectrum.

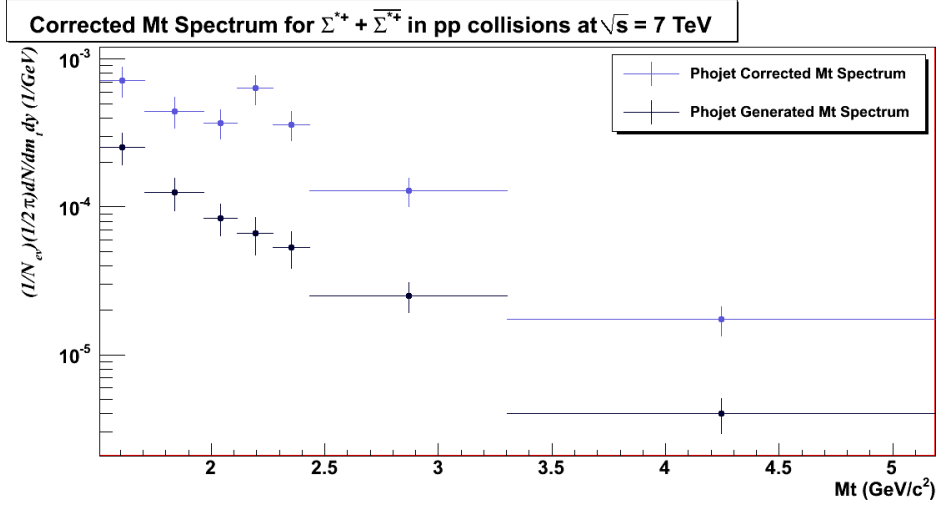


Figure 5.44: Corrected transverse mass distribution for 7 TeV pp data. The blue dots represents the spectrum extracted from the data corrected with the Phojet anchor runs, while the dark blue dots are the Phojet generated spectrum.

As observed also in the 900 GeV data the distributions generated both with PYTHIA and Phojet underestimate the data, as expected[156]. However, as previously mentioned both of them proved to be useful for the efficiencies evaluation and of course these models have to be tuned in the next future taking into account these results together with the others provided at these energies.

Again since, at the moment, there are no strong reasons to prefer one of the two generators, we decided, in a very preliminary way, to take, as efficiency correction factor, the mean value between the two generators. In Figures 5.45 and 5.46, the p_t and the m_t spectra corrected as just mentioned. The half difference between the PYTHIA and Phojet correction factors is taken as systematic errors associated to the models.

As described in the previous chapter, the corrected distribution was fitted with an Exponential (both p_t and m_t spectrum) and a Levy functions (only p_t spectrum).

The results of these fits applied to the spectra, where statistical and systematic uncertainties are added in quadrature, are shown in Figures 5.47, 5.48, 5.49, 5.50, 5.51 and 5.52.

As it is possible to see, the p_t spectrum is reasonably fitted by the Levy-Tsallis and the Exponential distributions throughout the dynamical range considered and as already noticed by STAR the m_t spectra is reasonably fitted by the Exponential distribution. From the corrected spectra it is possible to extract the mean p_t of the reconstructed particles and the temperature T of the source. The obtained values are summarized in the Table 5.10 for what the spectra corrected with the two generators combination.

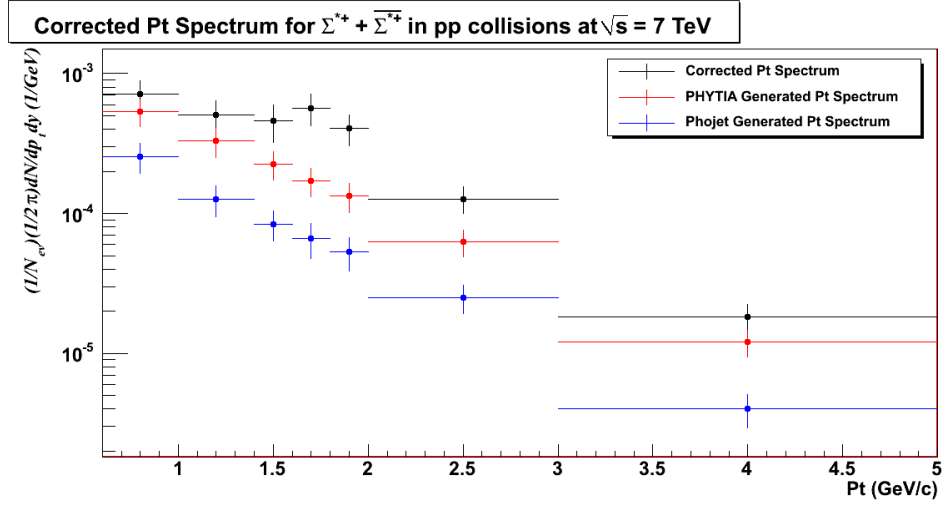


Figure 5.45: Transverse momentum distribution for 7 TeV pp data corrected taken, as efficiency correction factor, the mean value between the two generators. The black points are the corrected spectrum, the red points are the PYTHIA generated spectrum while the blue points are the Phojet generated spectrum.

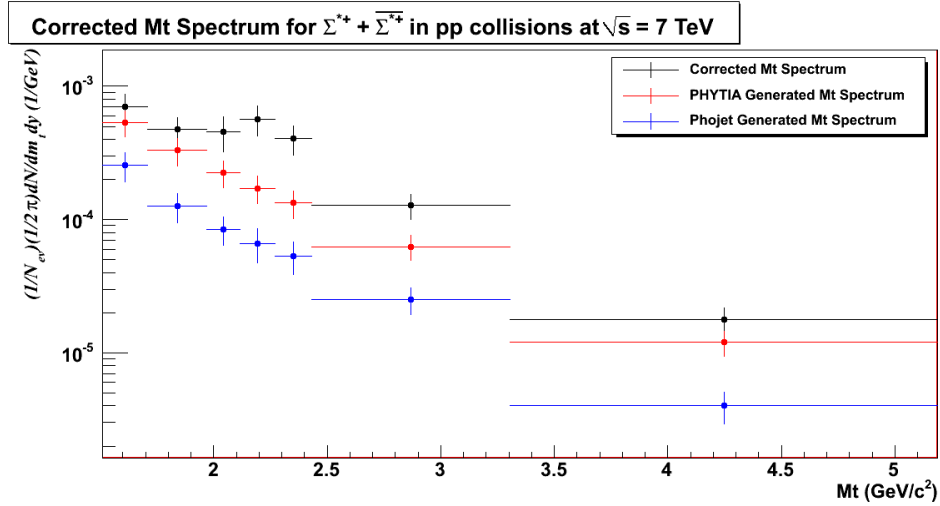


Figure 5.46: Transverse mass distribution for 7 TeV pp data corrected taken, as efficiency correction factor, the mean value between the two generators. The black points are the corrected spectrum, the red points are the PYTHIA generated spectrum while the blue points are the Phojet generated spectrum.

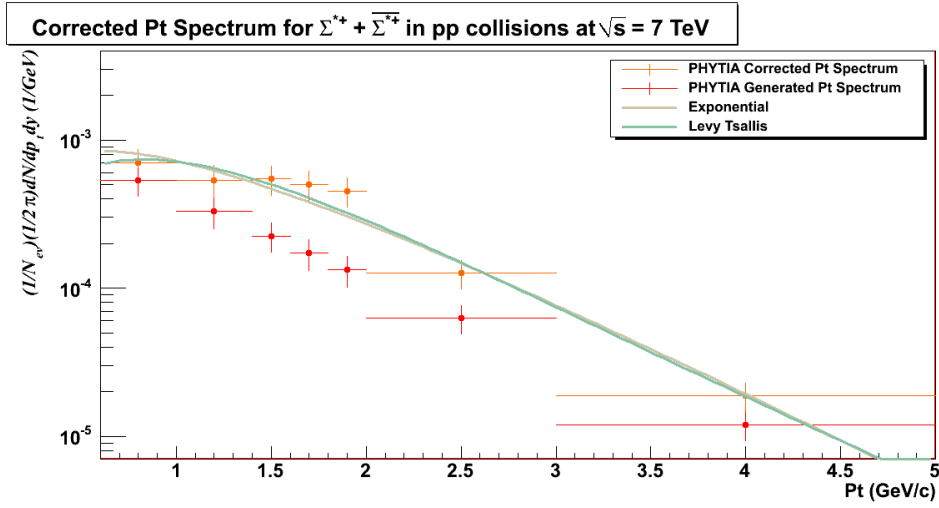


Figure 5.47: PYTHIA Corrected transverse momentum distribution for 7 TeV pp data with the corresponding fits. See text for details.

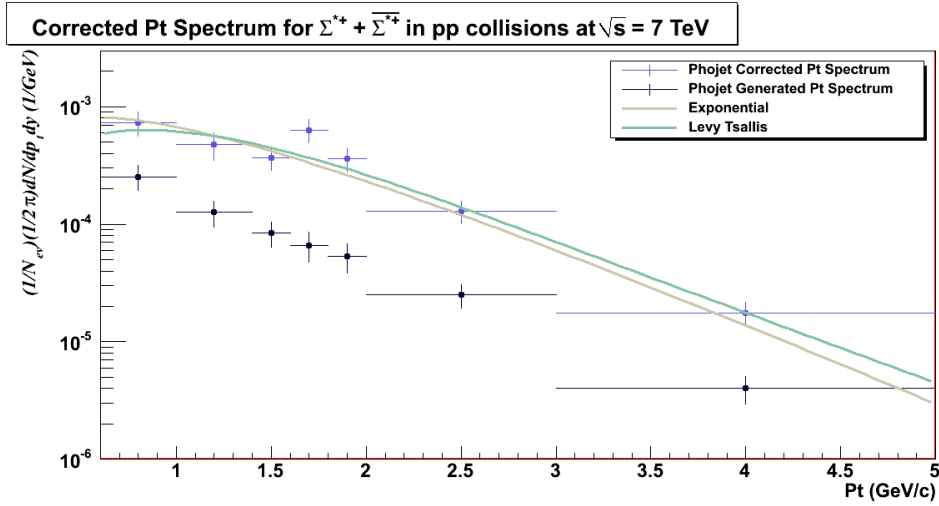


Figure 5.48: Phojet Corrected transverse momentum distribution for 7 TeV pp data with the corresponding fits. See text for details.

Spectrum	Exponential Fit		Levy-Tsallis Fit		
	$\langle p_t \rangle$ (GeV/c)	T (MeV)	$\langle p_t \rangle$ (GeV/c)	T (MeV)	n
p_t	1.131 ± 0.059	566 ± 29	1.272 ± 0.064	406 ± 28	20.1 ± 6.3
m_t	—	520 ± 31	—	—	—

Table 5.10: Temperature T and $\langle p_t \rangle$ and obtained from the exponential and Levy-Tsallis fits of the p_t spectrum and from the Exponential fit of the m_t spectrum.

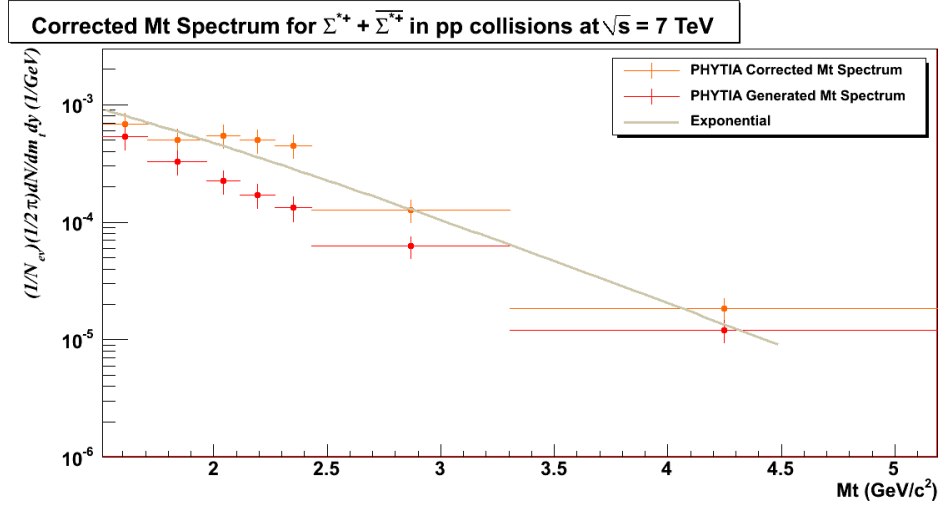


Figure 5.49: PYTHIA Corrected transverse mass distribution for 7 TeV pp data with the corresponding fits. See text for details.

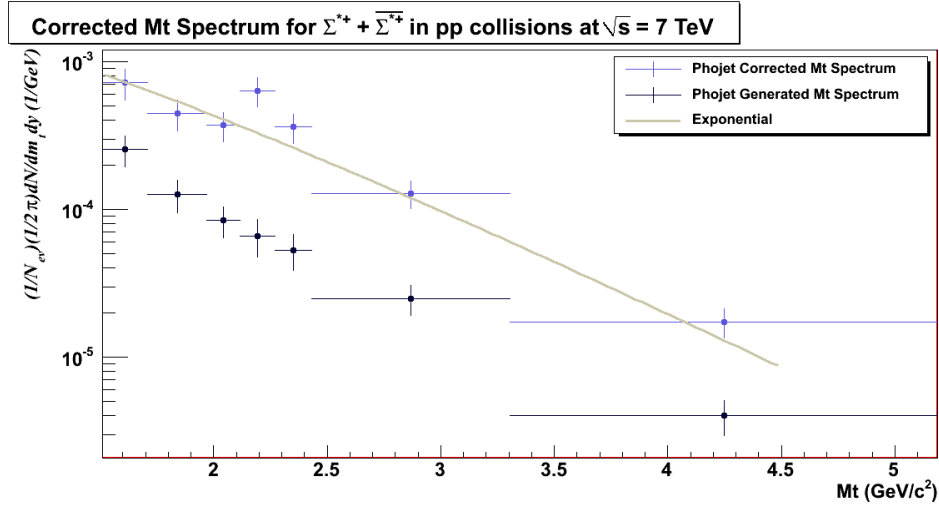


Figure 5.50: Phojet Corrected transverse mass distribution for 7 TeV pp data with the corresponding fits. See text for details.

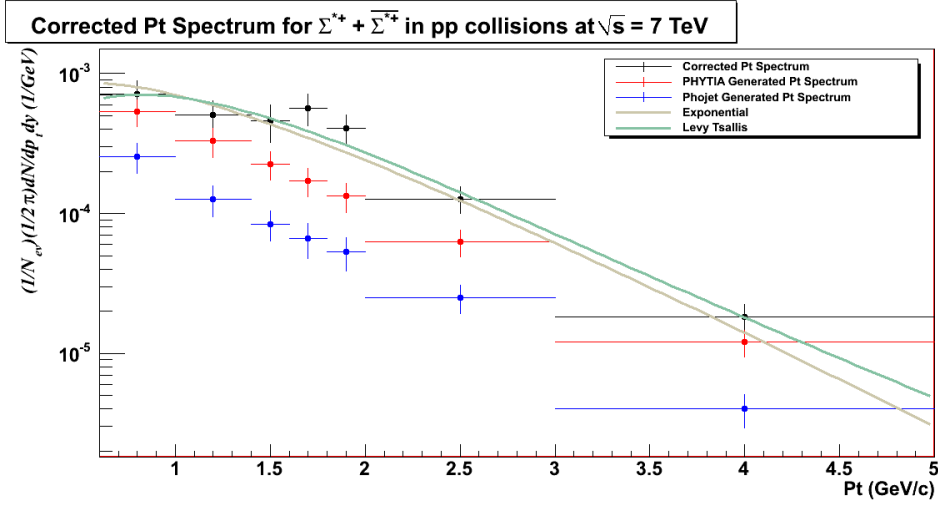


Figure 5.51: Transverse momentum distribution for 7 TeV pp data corrected taken, as efficiency correction factor, the mean value between the two generators and fitted with an exponential and a Levy-Tsallis distribution. The black points are the corrected spectrum, the red points are the PHYTIA generated spectrum while the blue points are the Phojet generated spectrum.

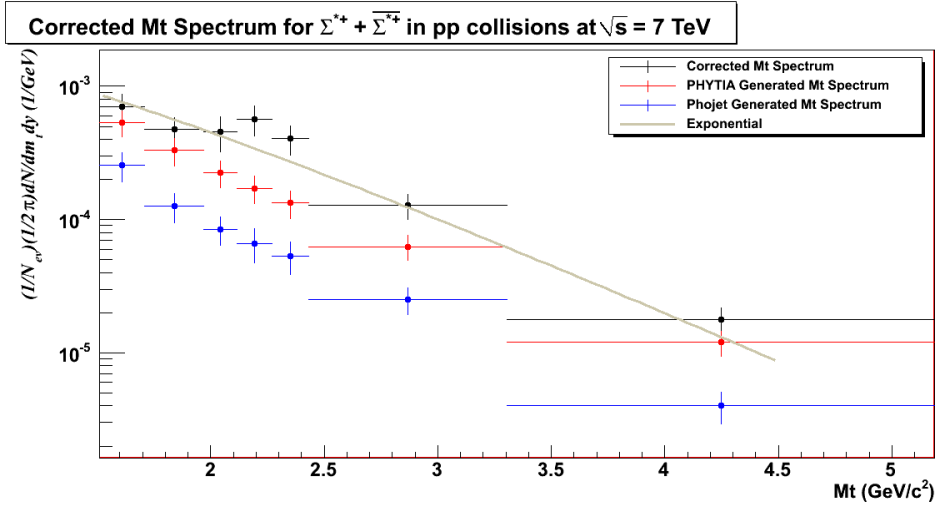


Figure 5.52: Transverse mass distribution for 7 TeV pp data corrected taken, as efficiency correction factor, the mean value between the two generators and fitted with an exponential distribution. The black points are the corrected spectrum, the red points are the PHYTIA generated spectrum while the blue points are the Phojet generated spectrum.

Finally in the Figures 5.53 and 5.54 the ratio between data and the simulations provided with PYTHIA and Phojet and the reconstruction efficiency as function of the transverse momentum are shown respectively.

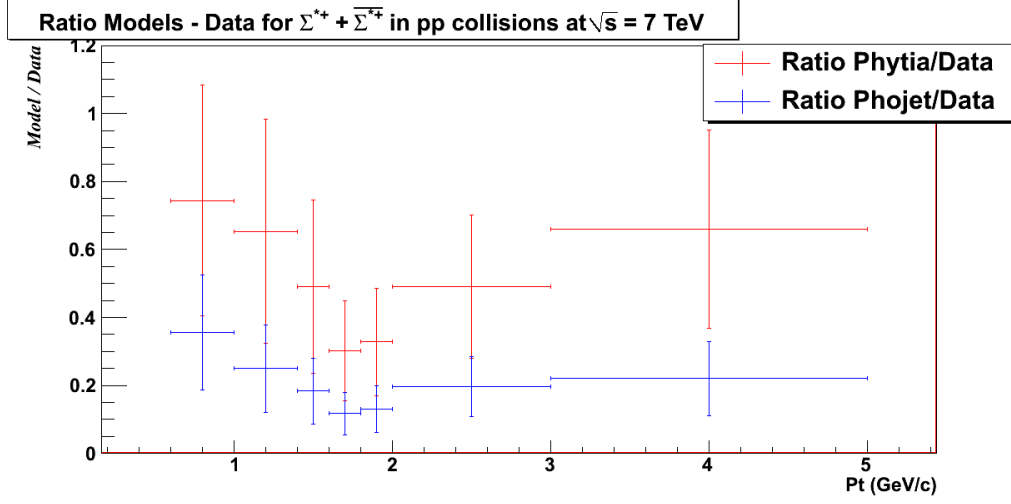


Figure 5.53: Ratio between the PYTHIA and Phojet generated spectra and the reconstructed data.

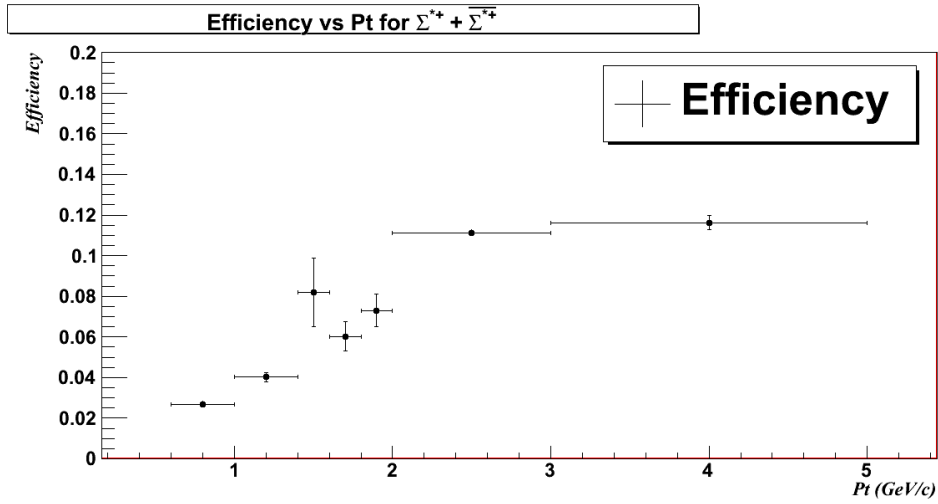


Figure 5.54: Reconstruction efficiency as function of the transverse momentum. It is evaluated using both PYTHIA and Phojet, taking, as efficiency correction factor, the mean value of the two generators corrections. The associated uncertainty is evaluated taking the half-difference of the values provided by the two generators.

As it is possible to see both PYTHIA (especially at intermediate p_t) and Phojet (in the whole dynamical range considered) highly underestimate the data, as already observed for the 900 GeV data.

The efficiency corrections also in this are obtained by analyzing Monte Carlo (MC)

events in exactly the same way as for the real events. A dependence is found on the generators used (PYTHIA and Phojet). Therefore the corrections presented here are obtained taking the mean value of the two generators corrections and taking into account, as systematic uncertainties, the half-difference of the values provided by the two generators. As evident from the figure, the efficiency is limited, especially at low p_t , because of the acceptance of the detector.

The reader must take into account that results just shown has not to be considered as final at all. The analysis, infact, is still ongoing and, in particular, some improvement, that was not possible to include in this thesis, are foreseen for the next future such as, a narrowing of the rapidity interval considered in order to take into account the rapidity region in which the detector efficiency is the best.

5.2.7 Signal Significance

In Table 5.11 the significances (defined as $S/\sqrt{S+B}$) for the extracted signal obtained for the differential (only in p_t) and integral analyses of 7 TeV data, are summarized. The uncertainties here reported take into account both the statistical and the systematic component.

Table 5.11: Significances of the extracted signal for 7 TeV pp data (both for integral and differential transverse momentum distribution, $3 \cdot 10^7$ events).

p_t range (GeV/c)	7 TeV Data Significances.
Integral	30.0 ± 5.4 .
0.6 - 1.0	12.3 ± 2.5 .
1.0 - 1.4	11.4 ± 2.4 .
1.4 - 1.6	16.9 ± 3.2 .
1.6 - 1.8	17.5 ± 3.3 .
1.8 - 2.0	16.4 ± 3.1 .
2.0 - 3.0	26.1 ± 4.8 .
3.0 - 5.0	14.8 ± 2.9 .

The significance p_t dependence for the two sets of cuts considered is shown in Figure 5.55.

Almost all the p_t bins shows, as expected, that the “efficiency oriented” cuts set increase the significance. As mentioned in the previous chapter this effect is much more evident with the data than with the simulations.

5.2.8 Dependence of mass and width from p_t

In Figures 5.56 and 5.57 the transverse momentum dependence of Σ^* mass and width for the two sets of cuts considered is shown. An apparent increase of mass and width is

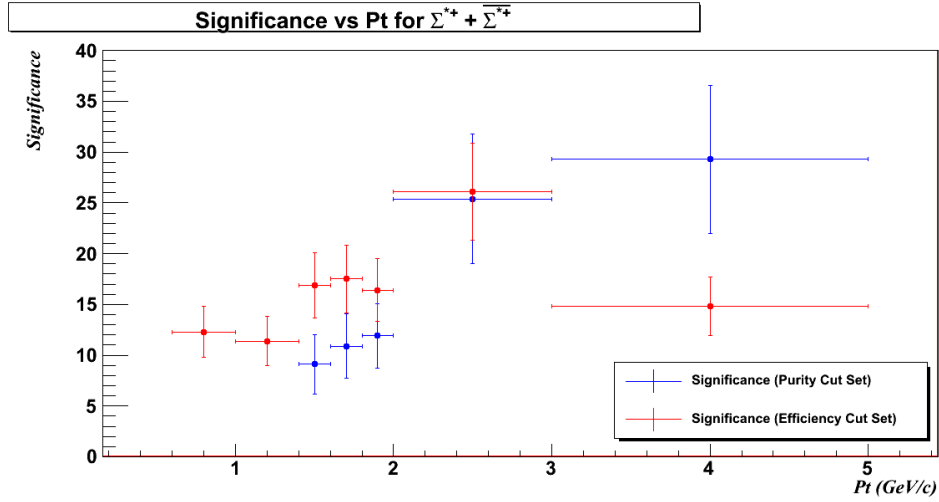


Figure 5.55: $\Sigma^{*+} + \overline{\Sigma}^{*+}$ p_t significance dependence in 7 TeV pp collisions data. The missing blue points corresponds to p_t bins not reconstructable with the “purity oriented” cut set.

present for the data managed with the “purity oriented” set of cuts, while this behaviour disappear for the data managed with the “efficiency oriented” set of cuts. Even in this case the fit results confirms the accordance with the PDG values.

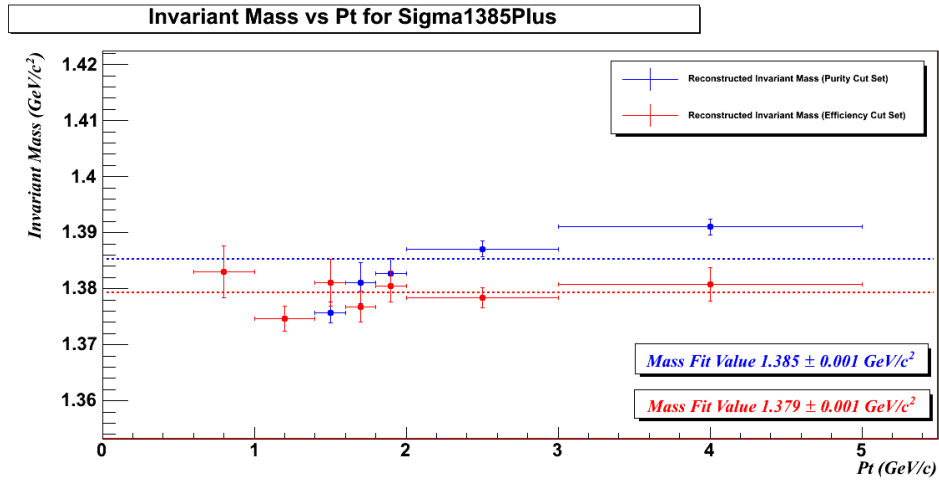


Figure 5.56: Σ^{*+} p_t mass dependence in 7 TeV pp collisions data. The missing blue points corresponds to p_t bins not reconstructable with the “purity oriented” cut set.

The analysis and the results presented and discussed in this chapter are only the first step needed in order to perform the possible studies on the QGP dynamic evolution described in the Chapter 3. The results provided with the Σ^* have, infact, to be considered together with those obtained with other strange resonances (like K^* , Λ^* and so on) in order to have a well established reference set of starting points for the next comparison with the PbPb data, for instance in order to determine the resonance absorption degree

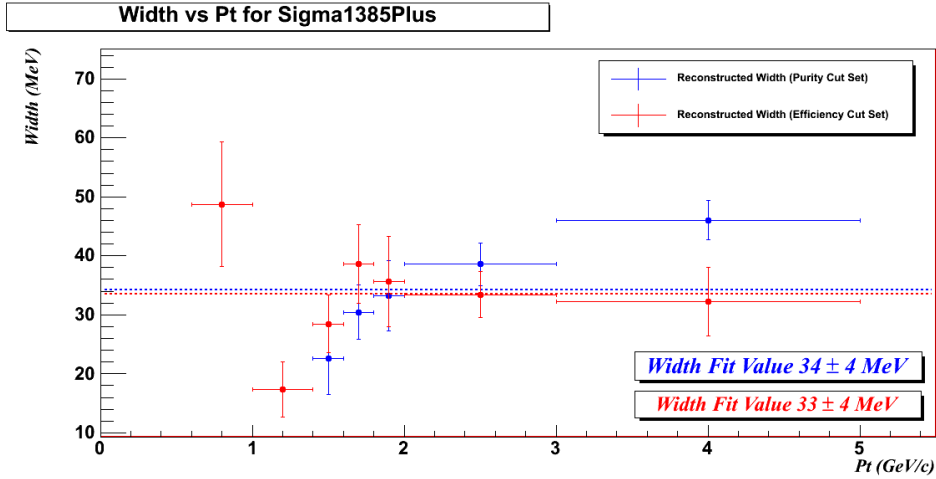


Figure 5.57: $\Sigma^{*+} p_t$ width dependence in 7 TeV pp collisions data. The missing blue points corresponds to p_t bins not reconstructable with the “purity oriented” cut set.

during the interacting hadron gas phase between the chemical and kinematical QGP freezeout. For these reasons, the work presented in this thesis has not to be considered as an end in itself but as a needed phase to provide essential tools for one of next goal of ALICE in the study of PbPb events recently collected at LHC.

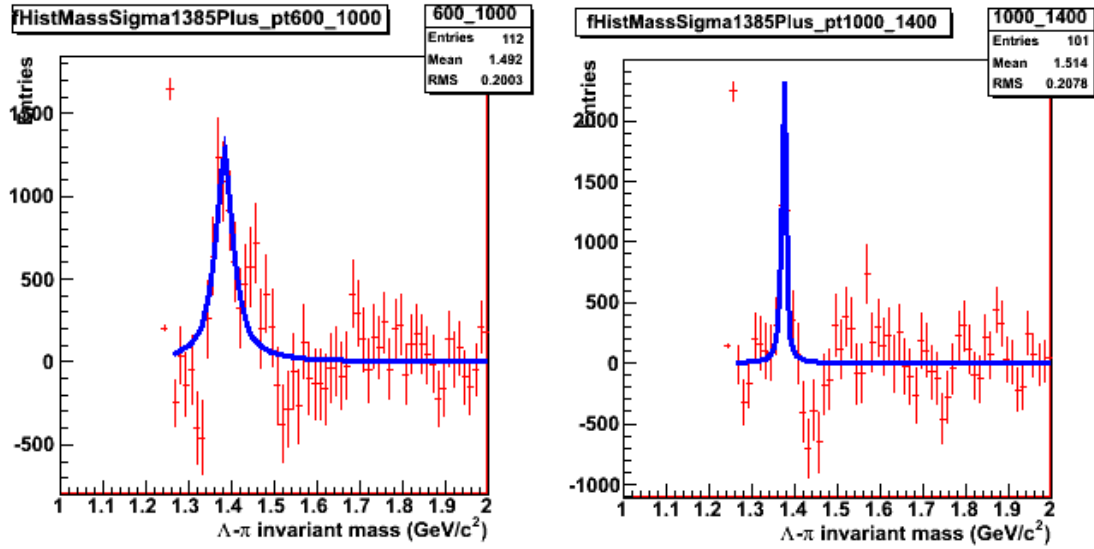


Figure 5.58: $\Sigma^{*+} + \overline{\Sigma}^{*+}$ signal extracted in the 0.6-1.0 and 1.0-1.4 GeV/c p_t bins. The red histograms represent the signal after the background subtraction fitted with a Breit-Wigner distribution (the blue curve).

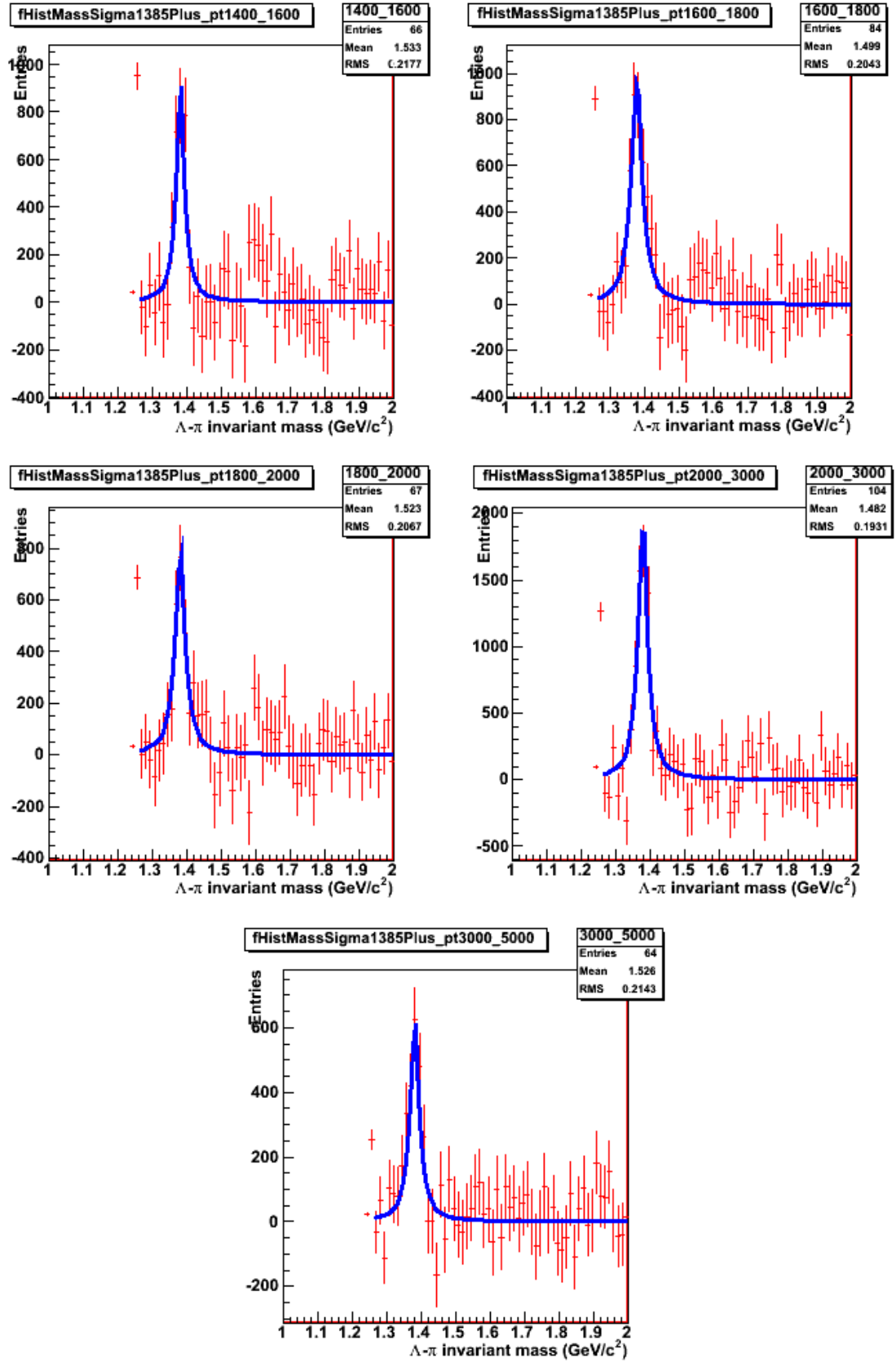


Figure 5.59: $\Sigma^{*+} + \overline{\Sigma}^{*+}$ signal extracted in the 1.4-1.6, 1.6-1.8, 1.8-2.0, 2.0-3.0 and 3.0-5.0 GeV/c p_t bins. See previous figure caption for details.

Conclusions

The main physics goal of the ALICE experiment is the creation and the investigation of the properties of the strongly-interacting matter in the framework of before never reached conditions of so high energy density ($> 10 \text{ GeV/fm}^3$) and high temperature ($\gtrsim 0.2 \text{ GeV}$). This state of the nuclear matter is called Quark-Gluon Plasma. Due to its short lifetime, the QGP is studied looking at several different kind of physical observables in the final state, the so called “hard and soft probes”. The studies on the QGP started in the '80 first with the SPS experiments and then at RHIC.

Among the different topics related to the physics of the Quark-Gluon Plasma and investigated by the ALICE experiment, the analysis of the strange resonances is one of the most important, in order to study the dynamics of the evolution of the QGP during the fireball expansion and cool-down. In recent years some studies were performed in order to explore if it is possible to experimentally determine the period of time between the fireball chemical and kinetic freeze-out using the strange hadron resonances behaviour. The short-lived resonances, detectable through an invariant mass reconstruction, are natural candidates for freeze-out diagnostics since their lifetime is comparable to the hadronization timescale and the lifetime of the interacting Hadron Gas. If chemical and kinetic freeze-out are not separated, all initially produced resonances are reconstructable otherwise if a time separation is present, part of the resonance daughters rescatter in the interacting phase and the resonance will not be observable anymore in the final state. In this way the relative suppression of resonances in the final state, compared to the behaviour expected, provides a chronometer for the time interval between the different reaction stages. An accurate determination of the resonances yields could therefore provide a distinction between different hadronization scenarios. The rich variety of detectable resonances includes particles with very different masses and widths, allowing to probe the production phase (the chemical freeze-out) temperature and interaction lifetimes in detail.

The ALICE experiment, thanks to its very composite, complex and efficient detector is able to explore these aspects in deep detail.

Goal of this thesis is the study and the reconstruction of the strange resonance $\Sigma(1385)$ in proton-proton collisions since it is crucial for the tuning of the existing models and is an important benchmark for the subsequent lead-lead collisions analysis. Some theoretical studies found a remarkable prediction for the $\Sigma(1385)$ resonance: when both the Σ^*/Λ and Σ^*/Ξ ratios become available both the temperature of the thermal freeze-out and the lifetime of the interacting hadron gas phase can be inferred from the Σ^* alone. In the recent past the $\Sigma(1385)$ was studied in pp and Au-Au collisions at $\sqrt{s} = 200 \text{ GeV}$ in the STAR experiment at RHIC.

This work started with the analysis of the ALICE pp simulation at $\sqrt{s} = 10 \text{ TeV}$ in

order to build a dedicated signal extraction procedure. The $\Sigma(1385)$ was reconstructed in its strong $\Lambda \pi$ decay channel, i.e. only one of the possible $\Sigma(1385)$ decay channels since it has the highest branching ratio and due to the now insufficient efficiency in Σ 's identification (needed for the second $\Sigma(1385)$ decay channel). The signal extraction procedure includes the background evaluation with the so called "Side-Bands" technique and the application of a specific set of quality and kinematic cuts in order to increase the Signal over Background ratio. Much effort was spent in order to fix the best set of cuts which allow, at the same time, to extract a quite pure signal without losing too much efficiency. In more details, two sets of cuts were tried, one "purity oriented" and one "efficiency oriented", the latter used for the differential analysis. The procedure was validated again on the 7 TeV simulation, and it was applied on the pp data collected by the experiment at $\sqrt{s} = 900$ GeV and 7 TeV. The results obtained, in terms of mass and width of the $\Sigma(1385)$ are in agreement with the PDG values. The amount of data collected at 900 GeV enabled the analysis of the dynamical range in three p_t intervals. The statistics collected at 7 TeV was much higher and enough to perform a better differential analysis dividing the dynamical range in seven p_t intervals. The extracted spectra at both energies were corrected for the efficiencies using some dedicated simulations provided with two different generators, PYTHIA and Phojet, and a combination of both and then compared with the Monte Carlo distributions. As expected both the generators underestimate the $\Sigma(1385)$ yield both at 900 GeV and 7 TeV reflecting the necessity to tune the models at these energies taking into account, among the others, also the results obtained in this analysis. The spectra were then fitted, in the context of a thermal production model with an exponential and a Levy-Tsallis distribution as already done in other strangeness related analyses in ALICE and also in the STAR experiment. From the spectra it was possible to extract the information on the temperature of the source and the $\langle p_t \rangle$ in the dynamical range considered. A first, very preliminary, comparison with the results obtained by the STAR experiment was performed. Comparable values both for T and $\langle p_t \rangle$ were found comparing the data at 200 GeV and 900 GeV while a sensible increase was spotted moving to the 7 TeV data. The collected data at 7 TeV are enough to measure the Σ^*/Λ and Σ^*/Ξ ratios in pp collisions, which play a very important role both in models renormalization and as benchmark for the subsequent measurement of the same ratios in PbPb collisions.

The analysis work presented in this thesis is, of course, the starting point for an analysis that starting from the pp data will find its main goal on the PbPb data collected during November-December 2010, and those which will be collected during the next years by ALICE. The analysis in heavy-ion collisions will be much more critical due to the higher combinatorial background and therefore needs a very strong signal extraction procedure together proper set of cuts. The results that will be provided in terms of Σ^*/Λ and Σ^*/Ξ ratios has to be compared with those coming from other resonances, in order to be able to discriminate among different QGP evolution and freezeout models as mentioned in the motivations.

Bibliography

- [1] ALICE Collaboration, *ALICE: Physics Performance Report, Volume I*, 2004 J. Phys. G: Nucl. Part. Phys. 30 1517
- [2] ALICE Collaboration, *ALICE: Physics Performance Report, Volume II*, 2006 J. Phys. G: Nucl. Part. Phys. 32 1295.
- [3] ALICE Collaboration, *The ALICE experiment at the CERN LHC*, 2008 JINST 3 S08002
- [4] S.L. Glashow, *Partial-symmetries of weak interactions*, Nuclear Physics 22: 579-588 1961
S. Weinberg, *A Model of Leptons*, Physical Review Letters 19: 1264-1266 1967
A. Salam, *Elementary Particle Physics: Relativistic Groups and Analyticity*, Eighth Nobel Symposium. Stockholm: Almquist and Wiksell. pp. 367. 1968
P.W. Higgs, *Broken Symmetries and the Masses of Gauge Bosons*, Physical Review Letters 13: 508-509 1964
- [5] F. Karsch, E. Laermann, A. Peikert, *The Pressure in 2, 2+1 and 3 Flavour QCD*, Phys. Lett. B 478 (2000) 447-455
- [6] C. Amsler et al. (Particle Data Group), PL B667, 1 (2008) (URL: <http://pdg.lbl.gov>)
- [7] P.W. Higgs, *Broken Symmetries and the Masses of Gauge Bosons*, Physical Review Letters 13: 508-509 1964
- [8] M.E. Peskin and D.V. Schroeder, *An Introduction to Quantum Field Theory*, Addison Wesley (1995)
- [9] F. Halzen and A.D. Martin, *Quarks and Leptons*, John Wiley and Sons (1984)
- [10] À. Mócsy, F. Sannino, K. Tuominen, *Confinement versus Chiral Symmetry*, Phys. Rev. Lett. 92 (2004)
- [11] V. Koch, *Introduction to Chiral Symmetry*, Laurence Berkeley National Laboratory, (1995)

- [12] H. Satz, *Colour Deconfinement in Nuclear Collisions*, Rept.Prog.Phys. 63 (2000) 1511
- [13] E. Shuryak, *Physics of the first three fermis in high energy heavy ion collisions*, Nucl. Phys. A 566 559c-562c (1994)
- [14] H. Satz, *Phase Transition in QCD*, Nucl. Phys. A 681 (2001) 3-21
- [15] S. Gottlieb, *Lattice calculation of the quark gluon plasma*, Journal of Physics: Conference Series 78 (2007) 012023
- [16] R. Hagedorn, *Multiplicities, p_T distributions and the expected hadron \rightarrow quark-gluon phase transition*, TH.3684-CERN
- [17] N. Cabibbo, G.Parisi, *Exponential Hadronic Spectrum and Quark Liberation*, Phys. Lett. B 59 pp. 67-69 (1975)
- [18] F. Karsch, *Properties of the Quark Gluon Plasma: A Lattice Perspective*, Nucl. Phys. A 783 (2007) 13c-22c
- [19] K. G. Wilson, *Confinement of quarks*, Phys. Rev. D 10, 2445-2459 (1974)
- [20] J. D. Bjorken, *Highly relativistic nucleus-nucleus collisions: The central rapidity region*, Phys. Rev. D, Vol. 27, No. 1 (1983) 140-150
- [21] U. Heinz, *The Little Bang: Searching for quark-gluon matter in relativistic heavy-ion collisions*, Nucl. Phys. A 685 414-431 (2001)
- [22] H. Satz, *The Search for the QGP: A Critical Appraisal*, Nucl. Phys. Proc. Suppl. 94 (2001) 204-218
- [23] The ALICE Collaboration, *Charged-particle multiplicity measurement in proton-proton collisions at $\sqrt{s} = 7$ TeV with ALICE at LHC*, Eur. Phys. J. C DOI: 10.1140/epjc/s10052-010-1350-2 and references therein.
- [24] The ALICE Collaboration, *Charged-particle multiplicity density at mid-rapidity in central Pb-Pb collisions at $\sqrt{s_{NN}} = 2.76$ TeV*, and references there in, Phys. Rev. Lett. 105, 252301 (2010)
- [25] S. Margetis et al. [NA49 Collaboration], *Transverse Energy Production in Pb + Pb²⁰⁸ Collisions at 158 GeV per Nucleon*, Phys. Rev. Lett. 75 (1995) 3814.
- [26] B.I. Abelev et al. [STAR Collaboration], *Systematic measurements of identified particle spectra in pp, d+Au, and Au+Au collisions at the STAR detector*, Phys. Rev. C 79 (2009) 034909
- [27] J. Adams et al. [STAR Collaboration], *Experimental and theoretical challenges in the search for the quark gluon plasma: The STAR Collaboration's critical assessment of the evidence from RHIC collisions*, Nucl. Phys. A 757 (2005) 102-183

- [28] R. Snellings for the STAR and ALICE Collaborations, *Anisotropic flow from RHIC to the LHC*, Eur. Phys. J. C 49 (2007) 87-90
- [29] J. Adams et al. [STAR Collaboration], *Particle-type dependence of azimuthal anisotropy and nuclear modification of particle production in Au+Au collisions at $\sqrt{s_{NN}} = 200$ GeV*, Phys. Rev. Lett. 92 (2004) 052302
- [30] J. Adler et al. [STAR Collaboration], *Pion Interferometry of $\sqrt{s_{NN}} = 130$ GeV Au+Au Collisions at RHIC*, Phys. Rev. Lett. 87 (2001) 082301
- [31] A. Adare et al. [PHENIX Collaboration], *Scaling properties of azimuthal anisotropy in Au+Au and Cu+Cu collisions at $\sqrt{s_{NN}} = 200$ GeV*, Phys. Rev. Lett. 98, 162301 (2007)
- [32] R. A. Lacey and A. Taranenko, *What do elliptic flow measurements tell us about the matter created in the little Bang at RHIC?*, PoS CFRNC2006, 021 (2006)
- [33] The ALICE Collaboration, *Elliptic flow of charged particles in Pb-Pb collisions at 2.76 TeV*, Phys. Rev. Lett. 105, 252302 (2010)
- [34] U. Heinz, *Concepts of heavy-ion physics*, Prepared for European School of High-Energy Physics (ESHEP 2002), Pylos, Greece, 25 Aug - 7 Sep 2002. Published in Pylos 2002, High-energy physics 127-178
- [35] The ALICE Collaboration, *Midrapidity Antiproton-to-Proton Ratio in pp Collisions at $\sqrt{s} = 0.9$ and 7 TeV Measured by the ALICE Experiment*, Phys. Rev. Lett. Vol.105, No.7, (2010)
- [36] F. Beccattini and G. Pettini, *Strange quark production in a statistical effective model*, Phys. Rev. C 67 015205 (2003)
- [37] J. Cleymans and K. Redlich, *Unified Description of Freeze-Out Parameters in Relativistic Heavy Ion Collisions*, Phys. Rev. Lett. 81 (1998) 5284-5286
- [38] J. Letessier, J. Rafelski, *Hadrons and Quark Gluon Plasma*, Cambridge Monographs on Particle Physics, Nuclear Physics and Cosmology (No. 18), 2002
- [39] G. Torrieri, J. Rafelski, *Search for QGP and Thermal Freeze-out of Strange Hadrons*, New J. Phys. 3 12 (2001)
- [40] G. Torrieri, *Phenomenology of Strangeness enhancement in heavy ion collisions*, J. Phys. G 36 064007 (2009)
- [41] J. Rafelski, B. Müller, Phys. Rev. Lett. 48 (1982) 1066;
J. Rafelski, B. Müller, Phys. Rev. Lett. 56 (1986) 2334, Erratum;
P. Koch, B. Müller, J. Rafelski, Phys. Rep. 142 (1986) 167

- [42] M. K. Mitrovski et al. [NA49 Collaboration], *Strangeness production at SPS energies*, J. Phys. G 32, S43 (2006)
- [43] E. Andersen et al. [WA97 Collaboration], Phys. Lett. B 449, 401 (1999)
T. Virgili et al. [NA57 Collaboration], *arXiv:hep-ex/0405052*
- [44] A. R. Timmins and for the STAR Collaboration, *Overview of Strangeness Production at the STAR Experiment*, J. Phys. G 36 064006 (2009)
- [45] F. Antinori et al, *New results from the NA57 experiment*, proc. *The XXXVI-IIIth Rencontres de Moriond "QCD and High Energy Hadronic Interactions"*, (2003)
- [46] B.I. Abelev et al, *Enhanced strange baryon production in Au+Au collisions compared to p+p at $\sqrt{s} = 200$ GeV*, Phys. Rev. C 77 044908 (2008)
- [47] B. Hippolyte for the ALICE Collaboration, *Strange prospects for LHC energies*, Eur. Phys. J. C 49 (2007) 121-124
- [48] S. Wheaton, J. Cleymans, M. Hauer, *THERMUS – A Thermal Model Package for ROOT*, Comput. Phys. Commun. 180 84-106, 2009
- [49] G. Torrieri, S. Jeon, J. Letessier, J. Rafelski, *SHAREv2: fluctuations and a comprehensive treatment of decay feed-down*, Comput. Phys. Commun. 175 635-649, 2006
- [50] R. Vernet, *Prospects for strangeness measurements in ALICE*, Phys. Atom. Nucl. 71 1523-1534, 2008
- [51] E. L. Feinberg, *Direct Production of Photons and Dileptons in Thermodynamical Models of Multiple Hadron Production*, Nuovo Cimento A 34, 391 (1976)
- [52] T. Peitzmann, M. H. Thoma, *Direct Photons from Relativistic Heavy-Ion Collisions*, Phys. Rept. 364 (2002) 175-246
- [53] H. Satz, *Quarkonium Binding and Dissociation: The Spectral Analysis of the QGP*, Nucl. Phys. A 783 249-260, 2007
- [54] The NA50 Collaboration, *A new measurement of J/ψ suppression in Pb-Pb collisions at 158 GeV per nucleon*, Eur. Phys. J. C 39 335-345, 2005
- [55] M. C. Abreu et al. (NA50), *Evidence for deconfinement of quarks and gluons from the J/ψ suppression pattern measured in Pb-Pb collisions at the CERN-SPS*, Phys. Lett. B 477, 28 (2000).
- [56] R. Arnaldi for the NA60 collaboration., *Anomalous J/ψ suppression in In-In collisions at 158 GeV/nucleon*, Nuclear Physics A 774 (2006) 711-714
- [57] F. Karsch, D. Kharzeev and H. Satz, *Sequential charmonium dissociation*, Phys. Lett. B 637 (2005)

- [58] H. Pereira Da Costa for the PHENIX Collaboration, *PHENIX results on J/ψ production in Au+Au and Cu+Cu collisions at $\sqrt{s_{NN}} = 200$ GeV*, Nucl.Phys. A 774 747-750, 2006
- [59] J. D. Bjorken (1982), *Energy Loss of Energetic Partons in Quark - Gluon Plasma: Possible Extinction of High p_T Jets in Hadron - Hadron Collisions*, FERMILAB-PUB-82-059-THY
- [60] M. Gyulassy, I. Vitev, X.-N. Wang, and B.-W. Zhang, *Jet Quenching and Radiative Energy Loss in Dense Nuclear Matter*, arXiv:nucl-th/0302077v2 2003
- [61] A. Kovner and U. A. Wiedemann, *Gluon Radiation and Parton Energy Loss*, arXiv:hep-ph/0304151v1 (2003)
- [62] X.-N. Wang and M. Gyulassy, *Gluon shadowing and jet quenching in A+A collisions at $\sqrt{s} = 200A$ GeV*, Phys. Rev. Lett. 68, 1480-1483 (1992)
- [63] X.-N. Wang, *Effect of Jet Quenching on High- p_T Hadron Spectra in High-energy Nuclear Collisions*, Phys. Rev. C 58, 2321 (1998)
- [64] R. Baier, D. Schiff, and B. G. Zakharov, *Energy loss in perturbative QCD*, Ann. Rev. Nucl. Part. Sci. 50 (2000) 37-69
- [65] S. S. Adler et al. [PHENIX Collaboration], *Common Suppression Pattern of η and π^0 Mesons at High Transverse Momentum in Au+Au Collisions at $\sqrt{s_{NN}} = 200$ GeV*, Phys. Rev. Lett. 96, 202301 (2006)
- [66] John Adams et al. (STAR Collaboration), *Evidence from d+Au measurements for final state suppression of high p_T hadrons in Au+Au collisions at RHIC*, Phys. Rev. Lett. 91, 072304, 2003
- [67] John Adams et al. (STAR Collaboration), *Azimuthal anisotropy and correlations in the hard scattering regime at RHIC*, Phys. Rev. Lett. 90, 032301 (2003)
- [68] John Adams et al. (STAR Collaboration), *Disappearance of back-to-back high p_T hadron correlations in central Au+Au collisions at $\sqrt{s_{NN}} = 200$ GeV*, Phys. Rev. Lett. 90, 082302 (2003)
- [69] S. Salur for the STAR Collaboration, *Searching for Jets in Heavy Ion Collisions*, Proceedings of the 24th Winter Workshop on Nuclear Dynamics, South Padre Island, Texas, 5-12 April 2008
- [70] J. Putschke for the STAR Collaboration, *First fragmentation function measurements from full jet reconstruction in heavy-ion collisions at $\sqrt{s_{NN}} = 200$ GeV by STAR*, Eur. Phys. J. C 61 (2009) 629-635

- [71] S. Salur for the STAR Collaboration, *First Direct Measurement of Jets in $\sqrt{s_{NN}} = 200$ GeV Heavy Ion Collisions by STAR*, Eur. Phys. J. C 61 761-767, 2009
- [72] P.M. Jacobs and M. van Leeuwen, *High p_T in Nuclear Collisions at the SPS, RHIC, and LHC*, Nucl. Phys. A 774 (2006) 237-246
- [73] Jürgen Schukraft (CERN) , “*Little Bang*” *The first 3 weeks...*, Talk at “First results from Heavy Ion collisions at the LHC (ALICE, ATLAS, CMS)” - CERN 02/12/2010
- [74] B. A. Cole on behalf of the ATLAS Collaboration, *Observation of a Centrality-Dependent Dijet Asymmetry in Lead-Lead Collisions with the ATLAS Detector*, Talk at “First results from Heavy Ion collisions at the LHC (ALICE, ATLAS, CMS)” - CERN 02/12/2010
- [75] B. Wyslouch on behalf of CMS Collaboration , *PbPb collisions in CMS*, Talk at “First results from Heavy Ion collisions at the LHC (ALICE, ATLAS, CMS)” - CERN 02/12/2010
- [76] R. Hanbury Brown and R. Q. Twiss, *A test of a new type of stellar interferometer on Sirius*, Nature 178 (1956) 1046
- [77] S. Pokorski, *Gauge Field Theories*, Cambridge University Press, 2nd edition (2000)
- [78] R. D. Pisarski, *Phenomenology of the Chiral Phase Transition*, Phys. Lett. B 110 (1982) 155.
- [79] S. Damjanovic (for the NA60 Collaboration), *First measurement of the rho spectral function in nuclear collisions*, Eur. Phys. J C 49 235-241, 2007
- [80] S. Damjanovic et al. (NA60 Collaboration), *NA60 results on the rho spectral function in In-In collisions*, Nucl. Phys. A 783 327-334, 2007
- [81] NASA Cosmic Background Explorer (COBE), URL <http://lambda.gsfc.nasa.gov/product/cobe/>
- [82] L. Stodolsky, *Temperature Fluctuations in Multiparticle Production*, Phys. Rev. Lett. 75, 1044 (1995)
- [83] S. Mrowczynski, *Hadronic matter compressibility from event-by-event analysis of heavy-ion collisions*, Phys. Lett. B 430 (1998) 9-14
- [84] E.V. Shuryak, *Event-by-event analysis of heavy ion collisions and thermodynamical fluctuations*, Phys.Lett. B 423 (1998) 9-14

- [85] M. Asakawa, U. Heinz, B. Muller, *Fluctuation Probes of Quark Deconfinement*, Phys. Rev. Lett. 85 2072-2075, 2000
- [86] S.Jeon, V.Koch, *Charged Particle Ratio Fluctuation as a Signal for QGP*, Phys. Rev. Lett. 85 (2000) 2076-2079
- [87] K.J. Eskola, K. Kajantie, P.V. Ruuskanene and K. Tuominen, *Scaling of transverse energies and multiplicities with atomic number and energy in ultrarelativistic nuclear collisions*, Nucl. Phys. B 570 (2000) 379
- [88] K. Kajantie, *Physics of LHC (theory)*, Nucl. Phys. A 715 (2003) 432c
- [89] V.N. Gribov, L.N. Lipatov, *Deep inelastic $e p$ scattering in perturbation theory*, Sov. J. Nucl. Phys. 15 (1972) 438 and 675
G. Altarelli, G. Parisi, *Asymptotic freedom in parton language*, Nucl. Phys. B 126 (1977) 298
Yu.L. Dokshitzer, *Calculation of the Structure Functions for Deep Inelastic Scattering and $e^+ e^-$ Annihilation by Perturbation Theory in Quantum Chromodynamics*, Sov. Phys. JETP 46 (1977) 641
- [90] Proceedings of the workshop “HERA and the LHC A workshop on the implications of HERA for LHC physics”, DESY-PROC-2005-001 (2005), DESY-PROC-2009-002 (2008).
- [91] K.J. Eskola et al., *Nuclear Parton Distributions in the DGLAP Approach*, International Journal of Modern Physics E 12 (2003) 177-195
- [92] <http://aliceinfo.cern.ch/index.html>
- [93] Lyndon Evans and Philip Bryant, *LHC Machine*, Lyndon Evans and Philip Bryant (editors) 2008 JINST 3 S08001
- [94] ATLAS Collaboration, *The ATLAS Experiment at the CERN Large Hadron Collider*, 2008 JINST 3 S08003
- [95] CMS Collaboration, *The CMS experiment at the CERN LHC*, 2008 JINST 3 S08004
- [96] The LHCb Collaboration, *The LHCb Detector at the LHC*, 2008 JINST 3 S08005
- [97] The LHCf Collaboration, *The LHCf detector at the CERN Large Hadron Collider*, 2008 JINST 3 S08006
- [98] The TOTEM Collaboration, *The TOTEM Experiment at the CERN Large Hadron Collider*, 2008 JINST 3 S08007
- [99] P. Lebrun, *Interim Summary Report on the Analysis of the 19 September 2008 Incident at the LHC*, CERN EDMS document no. 973073, ver. 1, <https://edms.cern.ch/document/973073/1> (2008)

- [100] B. Pastircak, J. Vrlakova, A. Morsch, M. Tavlet, *Radiation zoning calculations for ALICE experiment Update*, ALICE-INT-2009-008 version 1.0
- [101] A. Kluge et al., *The ALICE Silicon Pixel Detector System (SPD)*, Topical Workshop on Electronics for Particle Physics, Prague, Czech Republic, 03 - 07 Sep 2007, pp.143-147
- [102] S. Beolè et al, *The ALICE silicon drift detectors: Production and assembly*, Nuclear Instruments and Methods in Physics Research A 582 (2007) 733-738
- [103] G. Contin, *The Silicon Strip Detector (SSD) for the ALICE experiment at LHC: construction, characterization and charged particles multiplicity studies.*, PhD Thesis - Università degli Studi di Trieste, 2009
- [104] The ALICE Collaboration, *Production of pions, kaons and protons in pp collisions at $\sqrt{s} = 900$ GeV with ALICE at LHC.*, in publications at European Physical Journal.
- [105] J. Almea et al., *The ALICE TPC, a large 3-dimensional tracking device with fast readout for ultra-high multiplicity events*, arXiv:1001.1950v1 [physics.ins-det]
- [106] C. Lippmann, *The ALICE Transition Radiation Detector*, SNIC Symposium, Stanford, California - 3-6 April, 2006
- [107] R. Preghenella, *The Time-Of-Flight detector of ALICE at LHC: construction, test and commissioning with cosmic rays*, PhD Thesis - Università degli Studi di Bologna, 2009
- [108] <http://www.bo.infn.it/alice-tof-hw/public/VolumeINFN/TOFinfo.html>
- [109] L. Molnar, *The ALICE HMPID detector ready for collisions at the LHC*, Nucl. Instrum. Meth A 595 27-30, 2008
- [110] D. C. Zhou (for the ALICE Collaboration), *PHOS, the ALICE-PHOTon spectrometer*, J. Phys. G: Nucl. Part. Phys. 34 S719 2007
- [111] U. Abeysekara et al., *ALICE EMCAL Physics Performance Report*, submitted to the U.S. Department of Energy, arXiv:1008.0413v1
- [112] A. Fernández, S. Kartal, C. Pagliarone, *ACORDE a Cosmic Ray Detector for ALICE*, Proceedings of the International Conference: New Trends in High-Energy Physics, Crimea, 2006
- [113] G. Martinez for the ALICE Collaboration, *The Muon Spectrometer of the ALICE experiment*, Nucl. Phys. A 749 (2005) 313-319
- [114] The ALICE Collaboration, *Addendum to the Technical Design Report of the Photon Multiplicity Detector (PMD)*, CERN-LHCC 2003-038

- [115] C. H. Christensen et al, *The ALICE Forward Multiplicity Detector*, Nucl. Phys. A 774 919-922 2006.
- [116] The ALICE Collaboration, *Technical Design Report on Forward Detectors: FMD, T0 and V0*, CERN-LHCC-2004-025
- [117] G. Puddu et al., *The zero degree calorimeters for the ALICE experiment*, Nuclear Instruments and Methods in Physics Research A 581 (2007) 397-401
- [118] The ALICE Collaboration, *Technical Design Report of the Trigger Data Acquisition High-Level Trigger and Control System*, CERN-LHCC-2003-062
- [119] From ALICE Monitoring with MonALISA <http://pcalimonitor.cern.ch>
- [120] P. Buncic, J. F. Grosse-Oetringhaus, A. J. Peters, P. Saiz, *The Architecture Of The AliEn System*, Computing in High Energy Physics and Nuclear Physics 2004, Interlaken, Switzerland, 27 Sep - 1 Oct 2004, pp.951
- [121] <http://alien2.cern.ch/>
- [122] <http://aliceinfo.cern.ch/Offline/>
- [123] The ALICE Collaboration, *The ALICE Offline Bible*
- [124] T. Sjostrand et al., *High-energy-physics event generation with PYTHIA 6.1*, Comput. Phys. Commun. 135 (2001) 238.
T. Sjostrand, L. Lonnblad and S. Mrenna, *PYTHIA 6.2: Physics and manual*, arXiv:hep-ph/0108264 (2001). Version in use by ALICE: V6.214 with “ATLAS tune”
- [125] R. Engel, *Photoproduction within the two-component dual parton model. 1. Amplitudes and cross-sections*, Z. Phys. C 66 (1995) 203.
R. Engel and J. Ranft, *Hadronic photon-photon interactions at high energies*, Phys. Rev. D 54 (1996) 4244.
- [126] M. Gyulassy and X. N. Wang, *HIJING 1.0: A Monte Carlo program for parton and particle production in high-energy hadronic and nuclear collisions*, Comput. Phys. Commun. 83, 307 (1994).
- [127] R. Brun, R. Hagelberg, M. Hansroul and J. C. Lassalle, *Geant: Simulation Program for Particle Physics Experiments. User Guide and Reference Manual*, CERN-DD-78-2-REV (1978).
<http://wwwasd.web.cern.ch/wwwasd/geant/index.html>
- [128] S. Agostinelli et al. [GEANT4 Collaboration], *GEANT4: a Simulation Toolkit*, Nucl. Instrum. Meth. A 506 (2003) 250
<http://geant4.cern.ch/>

- [129] A. Fasso et al., *The physics models of FLUKA: Status and recent development*, Conference Proceedings of Computing in High-Energy and Nuclear Physics (CHEP 03), La Jolla, California, arXiv:hep-ph/0306267 (2003).
<http://www.fluka.org/fluka.php>
- [130] M. Bleicher, E. Zabrodin, C. Spieles, S.A. Bass, C. Ernst, S. Soff, L. Bravina, M. Belkacem, H. Weber, H. Stöcker, W. Greiner, J. Phys. G 25 (1999) 1859
- [131] S.A. Bass, M. Belkacem, M. Bleicher, M. Brandstetter, L. Bravina, C. Ernst, L. Gerland, M. Hofmann, S. Hofmann, J. Konopka, G. Mao, L. Neise, S. Soff, C. Spieles, H. Weber, L.A. Winckelmann, H. Stöcker, W. Greiner, C. Hartnack, J. Aichelin, N. Amelin, Progr. Nucl. Phys. 41 (1998) 225
- [132] Marcus Bleicher, *Probing hadronization and freeze-out with multiple strange hadrons and strange resonances*, Nuclear Physics A 715 (2003) 85-94
- [133] Marcus Bleicher, Jörg Aichelin, *Strange resonance production: probing chemical and thermal freeze-out in relativistic heavy ion collisions*, Physics Letters B 530 (2002) 81-87
- [134] Giorgio Torrieri, Johann Rafelski, *Strange hadron resonances as a signature of freeze-out dynamics*, Phys. Lett. B 509 (2001) 239
- [135] Johann Rafelski, Giorgio Torrieri, Jean Letessier, *Strangeness And QGP Freeze-Out Dynamics*, Presented at XXVI Rencotres de Moriond, March 17-24, 2001 Les Arcs, France
- [136] F. Antinori et al., WA97 Collaboration Eur. Phys. J. C 14, 633, (2000), and private communication.
- [137] J. Letessier and J. Rafelski, Int. J. Mod. Phys. E 9, 107, (2000), and references therein.
- [138] Johann Rafelski, Jean Letessier, Giorgio Torrieri, *Strange hadrons and their resonances: a diagnostic tool of QGP freeze-out dynamics*, Phys. Rev. C 64: 054907, 2001; Erratum. ibid. C65:069902, 2002 and references therein.
- [139] Sevil Salur for STAR Collaboration, *$\Sigma(1385)$ Resonance Studies With STAR At $\sqrt{s_{NN}} = 200$ GEV*, NATO Science Series 2: V166 S665-S667, 2004
- [140] Giorgio Torrieri, Johann Rafelski, *Hadron resonances probes of QGP*, Nukleonika 49 (2004) S109-S114
- [141] Ch. Markert, PhD thesis, available at na49info.cern.ch/cgi-bin/wwwd-util/NA49/NOTE?257;
- [142] Christina Markert for the STAR collaboration, *Strange Resonance Production in $p+p$ and $Au+Au$ Collisions at RHIC Energies*, J. Phys. G 30 (2004) S1313-S1316

- [143] Giorgio Torrieri, Johann Rafelski, *Statistical Hadronization Probed by Resonances*, Phys. Rev. C 68 (2003) 034912
- [144] Margaret Alston et al., *Resonance in the $\Lambda \pi$ System*, Phys. Rev. Lett. 5, 520-524 (1960)
- [145] Inga Kuznetsova and Johann Rafelski, *Resonance Production in Heavy Ion Collisions: Suppression of $\Lambda(1520)$ and Enhancement of $\Sigma(1385)$* , Phys. Rev. C 79: 014903, 2009
- [146] Inga Kuznetsova and Johann Rafelski, *Enhanced Production of Δ and $\Sigma(1385)$ Resonances*, Phys. Lett. B 668: 105-110, 2008
- [147] Sevil Salur for STAR Collaboration, *$\Sigma(1385)$ Results and Status of the Θ^+ in STAR*, J. Phys. G 31 (2005) S179-S186
- [148] The STAR Collaboration, *Hadronic resonance production in $d+Au$ collisions at $\sqrt{s_{NN}} = 200$ GeV at RHIC*, Phys. Rev. C 78: 044906, 2008
- [149] Sevil Salur, *$\Sigma(1385)$ results with STAR*, Eur Phys J C 40, s03, 9-13 (2005)
- [150] The STAR Collaboration, *Strange baryon resonance production in $\sqrt{s_{NN}} = 200$ GeV $p + p$ and $Au + Au$ collisions*, Phys. Rev. Lett. 97: 132301, 2006
- [151] Sevil Salur (for the STAR Collaboration), *Baryonic Resonance Studies with STAR*, J. Phys. G32 (2006) S469-S472
- [152] Sevil Salur (for the STAR Collaboration), *Statistical Models and STAR's Strange Data*, Proc. 22nd Winter Workshop on Nuclear Dynamics (2006)
- [153] ALICE Collaboration, *Strange particle production in proton-proton collisions at $\sqrt{s} = 0.9$ TeV with ALICE at the LHC*, arXiv:1012.3257v1
- [154] <https://twiki.cern.ch/twiki/bin/view/ALICE/SelectionOfPrimaryTracksForPp2009DataAnalysis>
- [155] STAR Collaboration, B. I. Abelev et al., Phys. Rev. C75, (2007) 064901.
- [156] H.Ricaud, A.Kalweit, A.Maire, *Study of strange particle production in pp collisions with the ALICE detector*, Proceeding SQM (2009) arXiv:1003.4609v1

Ringraziamenti

Giunto al termine di questi tre anni, sento di essermi lasciato alle spalle un'esperienza estremamente importante sotto il profilo umano e scientifico. Un capitolo della mia vita si chiude e se apre un altro spero altrettanto intenso ed interessante. Prima di intraprendere la strada che il futuro ha in serbo per me, mi volto indietro per un attimo e non posso far a meno di notare che sono davvero molte le persone che devo ringraziare per essermi state vicino in questo lungo periodo e senza le quali indubbiamente non sarei qui.

Prima di tutto vorrei ringraziare chi mi ha aiutato a portare a termine questa tesi. Grazie quindi ad Enrico Fragiaco con il quale ho svolto la maggior parte del lavoro e con cui ho trascorso lunghe ore di interessanti e proficue discussioni di fisica (senza le quali questa tesi non sarebbe quello che é) e non solo. Grazie al mio supervisore, Giacomo Margagliotti che ha avuto la straordinaria pazienza di sobbarcarsi la lettura e la correzione di questa tesi. Grazie per i consigli che l'hanno migliorata per le dritte che l'hanno valorizzata. Un grazie a Paolo Camerini che, pur continuamente soffocato da impegni di ogni genere, ha sempre trovato il tempo per lavorare e discutere insieme, consigliare o anche solo per scambiare qualche battuta. Ad Enrico, Giacomo e Paolo va anche un sentito ringraziamento per l'amicizia sempre dimostratami e che hanno reso piacevole lavorare nel gruppo in questi tre anni.

Grazie a tutti i componenti (passati e presenti) del Gruppo III, Nevio, Paolo-Maria, Kaori, Stefano, Marco, Raffaele. Spero di poter lavorare con voi ancora a lungo!

Grazie ad Alberto Pulvirenti per i preziosi consigli che hanno dato una svolta al lavoro di questa tesi. Quella birra ti sta aspettando!

Un ringraziamento speciale al nucleo storico della Camera Pulita, Mino e Sasha. Non ci sono parole adeguate per descrivere la mia riconoscenza verso di voi e l'importanza che ha per me la vostra amicizia e la vostra presenza. Il mio sogno é un giorno rimettere insieme questo gruppo e ricostruire quell'atmosfera fantastica che si respirava durante i mesi passati insieme in laboratorio. Grazie di tutto, siete impareggiabili!

Grazie a Ramona, new entry del gruppo di Trieste, ma con la quale si é sin da subito instaurato un rapporto di intesa. Grazie per avermi prestato un bella fetta delle tue risorse GRID per le analisi che altrimenti non sarei stato in grado di fare.

Come non ringraziare poi tutti gli amici in ALICE conosciuti in questi anni: Andrea (sono sempre 29!!), Rossella, Mariella, Carmelo, Cristina, Grazia, Emanuele, Sergey,

Francesco, Livio, Fiorella, Costanza, Francesco, Paola, Daniele, Valerio, Martino... spero di non aver dimenticato nessuno... Le ore passate con voi dentro e fuori da ALICE sono state tra le piú piacevoli in assoluto. Ragazzi, siete grandi!!

Un enorme grazie a tutti i miei coinquilini (passati, presenti, veri ed acquisiti) di via Coroneo 29, ed in special modo alle mie ragazze Ilenia, Dalila e Giorgia. Questi anni con voi sono stati davvero unici anche se ogni tanto un po' turbolenti. Siete stati per me come dei fratelli piú piccoli e in qualche modo é stato bello vedervi ambientare in un mondo che vi era del tutto nuovo. Ma adesso che siete "cresciuti" dovrete camminare da soli. Fate i bravi, mi raccomando!

Un pensiero speciale va alla mia famiglia, a mia madre, a mio padre, a mia sorella, a nonna Rosa che resiste caparbiamente ed ai nonni che non ci sono piú, per il supporto, l'affetto e l'aiuto che mi avete dimostrato e mi dimostrano senza condizioni giorno dopo giorno. Senza di voi, i vostri sacrifici, il vostro lavoro, non potrei essere qui. Il debito che ho con voi é tale da non poter mai essere ripagato ma vorrei che questo traguardo possa rappresentare un segno, per quanto piccolo, della mia riconoscenza.

Infine il mio ringraziamento piú grande e profondo va a colei che ha riportato il sole nella mia vita, ridando luce ai miei giorni piú grigi. Grazie di esistere Elisa, grazie per la tua bellezza, il tuo sorriso, le tue parole, per ogni tuo piccolo gesto e per ogni momento passato insieme. Non trovo aggettivi adeguati per esprimerti la fortuna che sento di aver avuto nel conoscerti. Una fortuna che forse non merito. Non so davvero come farei se tu non ci fossi. Questa tesi é dedicata a te cui va il mio affetto senza limiti.